Photoluminescence and Charge Carrier Dynamics of Perovskite Nanocrystals

A Thesis Submitted for the Degree of
Doctor of Philosophy

by

Mr. Somnath Das

School of Chemistry

University of Hyderabad

Hyderabad- 500 046

India

December 2022

Dedicated to

‘My Family’

“Talk to yourself at lest once in a day, otherwise you may miss a meeting with an excellent person in this world”

Swami Vivekananda

“There is a huge amount of freedom that comes to you when you take nothing personally”

Don Miguel Ruiz

Contents

STATEMENT

I, **Somnath Das**, hereby declare that the matter embodied in the thesis entitled **"Photoluminescence and Charge Carrier Dynamics of Perovskite Nanocrystals"** is the result of investigations carried out by me in the School of Chemistry, University of Hyderabad, India under supervision of **Prof. Anunay Samanta**.

In keeping with the general practice of reporting scientific investigations, acknowledgements have been made wherever the work described is based on the finding of other investigations. Any omission or error that might have crept is regretted.

University of Hyderabad, India

December 2022

Somnath Das

School of Chemistry
UNIVERSITY OF HYDERABAD
HYDERABAD-500046, INDIA

Phone: (work) +91 40 2313 4813, +91 40 2301 2341
(lab): +91 40 2313 4913
Fax: +91 40 2301 1594
Email: anunay@uohyd.ac.in OR anunay.samanta@gmail.com
URL: http://chemistry.uohyd.ac.in/~as/

Professor Anunay Samanta
School of Chemistry

CERTIFICATE

This is to certify that the thesis entitled **"Photoluminescence and Charge Carrier Dynamics of Perovskite Nanocrystals"** submitted by **Mr. Somnath Das** bearing the registration number **16CHPH41** in partial fulfilment of the requirements for the award of Doctor of Philosophy (Ph.D.) in the School of Chemistry, University of Hyderabad, India under my supervision and guidance. This thesis is free from plagiarism and has not been submitted previously in part or full to this or other University/Institution for any degree or diploma. Further, the student has following publications before submission of the thesis for adjudication and has produced evidences for the same in the form of reprints.

Parts of the thesis have been published in the following publications:

1. **S. Das**, A. De and A. Samanta, *J. Phys. Chem. Lett.* **2020,** *11*, 1178-1188. **(Chapter 3)**

2. **S. Das** and A, Samanta, *ACS Energy Lett.* **2021**, *6*, 3780–3787. **(Chapter 4)**

3. **S. Das** and A. Samanta, *Nanoscale* **2022**, *14*, 9349-9358. **(Chapter 5)**

4. **S. Das,** M. Hossain and A. Samanta, (manuscript submitted). **(Chapter 6)**

The student has made presentation in the following conferences:

1. Breaching the Perovskite Red Wall: Phase Stable and Highly Luminescent Red/NIR-Emitting All-inorganic and Hybrid Perovskite NCs. **ChemFest-2022, 19th Annual In-house Symposium of the School of Chemistry**, University of Hyderabad, Hyderabad, India in April 22-23, 2022. ***(Poster and Oral)***

2. Phase Stable and Highly Luminescent Red/NIR-Emitting All-inorganic and Hybrid Perovskite NCs. **16th DAE-BRNS Biennial Trombay Symposium on Radiation &**

Photochemistry (TSRP-2022, Online), Bhaba Atomic Research Centre (BARC), Mumbai, India in January 12-15, 2022. **(Short oral)**

3. Breaching the Perovskite Red Wall: Phase Stable and Highly Luminescent Red/NIR-Emitting All-inorganic and Hybrid Perovskite NCs. **11th Asian Photochemistry Conference (APC 2021, Online)**, South Korea in October 31-November 4, 2021. **(Oral)**

4. Synthesis of Highly Luminescent $APbBr_3$ (A = Cs, MA and FA) Perovskite Nanocrystals: A 'Three-precursor' Approach. **International Conference on Nano Science and Technology (ICONSAT 2020)**, S N Bose National Centre for Basic Sciences, Kolkata, India in March 5-7, 2020. **(Poster)**

5. Violet- and Green-Emitting Perovskite Nanocrystals with Enhanced Photoluminescence Efficiency and Stability. **15th DAE-BRNS Biennial Trombay Symposium on Radiation & Photochemistry (TSRP-2020)**, Bhaba Atomic Research Centre (BARC), Mumbai, India in January 3-7, 2020. **(Poster)**

Further, the student has passed the following courses towards the fulfilment of coursework requirement for Ph.D. degree:

Sl. No.	Course Code	Title	Credits	Status
1.	CY801	Research Proposal	3	Pass
2.	CY802	Chemistry Pedagogy	3	Pass
3.	CY805	Instrumental Methods-A	3	Pass
4.	CY806	Instrumental Methods-B	3	Pass
5.	CY501	Spectroscopic Methods for Structure Elucidation	3	Pass

Anunay Samanta
Thesis Supervisor

PROF. ANUNAY SAMANTA
SCHOOL OF CHEMISTRY
UNIVERSITY OF HYDERABAD
HYDERABAD - 500 046

Dean
School of Chemistry
University of Hyderabad

Dean
SCHOOL OF CHEMISTRY
University of Hyderabad
Hyderabad-500 046

Acknowledgements

Frankly speaking, I never thought I would come to a position like this and I was little doubtful about my Ph.D. journey at the beginning. However, my association with some outstanding peoples and brilliant minds stretches my abilities and made this journey smooth, kept me spirited throughout the past five and half years. Surely, it wouldn't have been possible without those important 'figures' and it is indeed difficult for me to express digitally how much I owe to these peoples for what I am today.

First and foremost my sincere gratitude to the principal architect of this thesis work, my Sir, Prof. Anunay Samanta, for his faith on me and granting me this opportunity to work under his supervision. Simply, one cannot have a better guide than our Sir. I am grateful to his guidance, encouragement, cooperation, inputs and giving me the freedom to work in the laboratory. I will not forget his efforts to resolve the complexities related to my enrolment to the University, without which I could not be a part of the School of Chemistry (SoC). It has been a great learning experience for me how to put best efforts in every single work irrespective of its merit. His passion for science, planning for effective utilization of time, work-life balance and enthusiastic nature have been great examples to me and no doubt a bonus in my learning, wish I can execute ten percent of it in future. The kind of mental support I had received from Sir in my tough Covid-19 'quarantine period' is priceless. Occasional interaction with Madam, Boni di and Ani da especially during lab or house parties has been very relaxing as well as learning experiences to me.

I would like to thank the former and present dean/s and all the faculty members for their help and allowing me to use the infrastructure and instrumental facilities of SoC. Here, I specially mention my doctoral committee members, Prof. M. J. Swamy and Prof. S. K. Das Sir for their generous cooperation and encouragement throughout the programme. The Centre for Nanotechnology is thankfully acknowledged for extending their TEM facility in the initial days of the programme. In this context, continuous help from the non-teaching stuffs of SoC, specially from Mr. Venkat, Mr. Abraham, Ms. Radhika (school office) and Ms. Geetha for various official works, Dr. M. Durga Prasad, Mr. Rajesh for TEM imaging, Mr. Durgesh Kumar Singh and Mr. Mahindar for NMR measurements, Mr. Sunil and Mr. Vinay Kumar for the FESEM and PXRD measurements, respectively has been absolute helpful to facilitate my research work.

The financial support from SERB and MHRD are thankfully acknowledged. I specially thank UGC for my Ph.D. fellowships.

It would have been extremely difficult without getting cooperation of engineers from LSS to ensure smooth functioning of the instruments. I sincerely thank Radhika (UGC Cell), Shiva, Naresh, Shrinivas and Kumar for sharing many of my own official work in many times. I acknowledge the prompt services of the glassware and chemical suppliers with related essentials in lab. Life becomes so smooth for all of you.

I am grateful to Dr. Pralay Kumar Santra from Centre for Nano and Soft Matter Sciences (CeNS), Bangalore for extending his facility in fabricating LED. Modasser from CeNS and Dipanjan from ACRHEM has been more than a collaborator to me. I enjoyed a lot working with them. I thank Anil anna, Surya anna and Abhijit da from Prof. Aswini Nangia's lab for their generous help in multiple times related to PXRD measurement and

other stuff. I am also thankful to Hema and Debu (from Prof. Samar K. Das Sir's lab) for their kind help in some occasions.

I cannot forget the contribution of my school teachers starting from primary to higher secondary levels. All of them have been the building blocks of my today's journey. I am fortunate enough that, I have been blessed by some exceptional professors during my graduate and post-graduate studies. I shall always remember the valuable inputs of S.P.B Sir, P.S.S Sir and R.P Sir in my graduate studies. Here I specially mention Rizabul Sir and Sukriti Sir, whom have been more than private tutor to me. I am thankful to my post-graduate project mentor Prof. T. K. Mukherjee for his careful guidance.

It is simply hard to describe how much I am thankful to the 'AS group' members, not just academically but also in many aspects of life. Navendu da has been an amazing senior to me. Your very polite behaviour did not even force me to think of your seniority in the lab at the timing of joining. It has made me flexible to reach you for anything (academic and personal) without any hesitation not only in my initial days but also even today. Sudipta da is someone I had followed since my graduation time. Your frank yet sincere opinion is invaluable and made me clear to decide many aspect of this journey. I will always cherish some light-hearted moments between us. Sneha di has extraordinary communication, teaching and management skills which I guess everyone wants to adopt. It's been always informative to discuss with you on many topics including instrumentation, travel, restaurants, food and so on. Saddam da is someone I feel more close to my own thinking. You rectified me on several occasions for my silly mistakes which I now realize how crucial those moments were. I shall cherish our close association forever, after all we both are 'Biryani lover'. I genuinely thank Apurba da for guiding me in initial hands-on experience on various instruments, designing experiments, scientific discussions and taking time to go through manuscripts. I shall always remember our early moments and your manners to me. Thanks to Tasnim di for her help in few occasions. My association with Sumanta is something beyond lab mate. Apart from research, our time-to-time out-of-the-box discussion indeed educated me on several other things. Working with Rajesh has been a nice experience to me. I enjoyed occasional discussion with Ramavath anna and thanks for your multiple help. I shall cherish the funny conversations with Alila even in her limited presence to the lab. Interaction with super-seniors specially Ravi anna, Chandu anna and Ashoke anna has always been informative and joyful. Finally you all have been fabulous senior/friend to me and I consider myself fortunate to be associated with you all in this beautiful 'AS group'. Value of team work, dealing with failures, human nature is something I have learnt from this family. If unknowingly I made any of you unhappy at any stage, I sincerely apologize for that and pardon me with your own virtue if you can.

I am lucky to have a tremendous group of lovely friends surrounding me during this time. Quality moments spent with Subham, Anupam, Sarada, Sumanta, Suman da, Soutrick, Alamgir, Nilu da, Alim da, Tausif, Rabiul and Surya has been an absolute relaxation in stringent journey. I will always cherish the moments we shared during many 'Saturday night' celebrations for multiple reasons. Here I specially mention Daradi, a friend who have been always there for any help, suggestion and support. I will remember the interaction with seniors like Bappa da, Arijit da (Math), Subha da, Arijit da (Chem), Anirban da, Sugata da, Suman da, Rudra da, Kaushik da, Golu da, Kallol da, Senthil

anna, Ankit bhaiya, Kuntal da, Nitai da, Rajendra anna, Ramesh anna, Tanmay da, Mou di, Sabari di, Shipra di, Shameeta di and Moumita di in many occasions. I cherish my bonding with Ph.D. batch mates specially Hema, Ravi, Subham (dutta), Hafizur, Sabbir, Sashikant, Shyam, Isfaq, and Mujahid. I valued my association with Arghadip, Somratan, Debu, Arunabha, Abhijit, Olivia, Somdatta, Shampita, Sampurna, Arkadeb and Joydev.

My Covid-19 quarantine period (April, 2021) has learned me a lot about the value of life and drives me to think of its meaning in different perspective. The kind of help I had received in that isolation time from Anupam, Sarada, Sumanta, Suman da, Alim da and Subham is something can never be paid off. I also thank Shreyasi for her effective suggestions which kept me less exhausted during and post Covid time.

Let me take this opportunity to express how deeply I owe to my best friends Sarada and Anupam in this journey. Our association especially during the tough pandemic time has been priceless. Both of you had been an absolute support for me in this time. A special mention to Sarada for her unconditional support in the recent past, particularly during many ups and downs related to my health. Thank you both of you.

It will be tough for me to stay away from the campus Saraswati puja, Diwali and Mahalaya celebrations in the coming days. The same is true for many competitive events, even though I had very limited participation (rather merely a spectator). I am definitely going to miss these events in the future.

The moments I shared with friends in B.Sc. and M.Sc. times will always remain close to my heart. I am fortunate to have friends like Manotosh, Shubhadeep, Monojit, Mainak and Sourav (from B.Sc.) and Jonu, Ritu, Ajay, Bhaswati di and Rahul (from M.Sc.). I valued my deep association with Arpan da with whom I had spent a year as a master's project trainee and learned basics about research. I have so many memorable precious moments will you all, which I found absolute treasure for future.

My childhood friends Anup, Sudipta and their families has always been a mighty support in this journey. I can't express how much I owe these two families. The indirect financial assistance of Sudipta and his family during my higher secondary studies is something I shall remember forever.

It would not be possible for me to come so far without the support of my family. Any word would be less to justify their sacrifice and I don't want to let them down with 'thank you' either. The enormous support at any stage I received from all my family members is invaluable. The sacrifices of my father, mother and uncle are unparallel. Here I specially mention my grandfather, who had been my first teacher and guided in my childhood days and his training has shaped me largely of what I am today. The supports that I received from relatives are quite indispensable too.

Finally, I believe this journey has made me competent in many aspects of life which again helps me to grow-up as an individual one. Now on verge of this long incredible chapter, I must say that many people have contributed in their own ways. If I have missed any of them, I sincerely apologize and express my outmost gratitude to all.

Somnath
December, 2022

List of Publications

Publication from Thesis Chapters

1. S. Das, A. De and A. Samanta, Ambient Condition Mg^{2+}-Doping Producing Highly Luminescent Green- and Violet-Emitting Perovskite Nanocrystals with Reduced Toxicity and Enhanced Stability. *J. Phys. Chem. Lett.* **2020,** *11*, 1178-1188. **(Chapter 3)**
2. S. Das and A, Samanta, Highly Luminescent and Phase-Stable Red/NIR-Emitting All-Inorganic and Hybrid Perovskite Nanocrystals. *ACS Energy Lett.* **2021**, *6*, 3780–3787. **(Chapter 4)**
3. S. Das and A. Samanta, On direct synthesis of high quality $APbX_3$ ($A = Cs^+$, MA^+ and FA^+; $X = Cl^-$, Br^- and I^-) nanocrystals following a generic approach. *Nanoscale* **2022**, *14*, 9349-9358. **(Chapter 5)**
4. S. Das, M. Hossain and A. Samanta, Exceptionally Stable and Intense Violet Emitting $CsPbCl_3$ Nanocrystals Obtained Directly: A Paradigm of L-type Surface Passivation. **(Chapter 6,** manuscript submitted**)**

Other Publications

5. S. Mondal, S. Das, and Musti J. Swamy, Macromolecular Crowding Significantly Affects the Conformational Features and Carbohydrate Binding Properties of CIA17, a PP2-type Lectin from Coccinia indica. *Biochemistry* **2022**, *61*, 2344-2357.
6. S. Mondal, S. Das, S. Paul, S. Barik, and Musti J. Swamy, Low-pH Molten Globule-Like Form of CIA17, a Chitooligosaccharide-Specific Lectin from the Phloem Exudate of Coccinia indica, Retains Carbohydrate-Binding Ability. *J. Phys. Chem. B* **2022**, *126*, 4049–4060.
7. R. K. Gautam, S. Das and Prof. A. Samanta, Room-Temperature Treatment with Thioacetamide Yielding Blue- and Green-Emitting $CsPbX_3$ Perovskite Nanocrystals with Enhanced Photoluminescence Efficiency and Stability. *ChemNanoMat.* **2022**, *8*, e202200029.
8. R. K. Gautam, S. Das and Prof. A. Samanta, Can Sulfur-Containing Small Systems Enhance the Photoluminescence and Stability of the Blue-, Green- and Yellow-Emitting Perovskite Nanocrystals? A Case Study with Sodium Thiosulfate. *J. Phys. Chem. C* **2021**, *125*, 24170–24179.

9. S. Paul, T. Ahmed, **S. Das** and A. Samanta, Effect of Lead:Halide Precursor Ratio on the Photoluminescence and Carrier Dynamics of Violet- and Blue-Emitting Lead Halide Perovskite Nanocrystals. *J. Phys. Chem. C* **2021**, *125*, 23539–23547.
10. N. Mondal, A. De, S. Seth, T. Ahmed, **S. Das**, S. Paul, R. K. Gautam and A. Samanta, Dark Excitons of the Perovskites and Sensitization of Molecular Triplets. *ACS Energy Lett.* **2021**, *6*, 588–597.
11. A. De, **S. Das**, and A. Samanta, Hot Hole Transfer Dynamics from $CsPbBr_3$ Perovskite Nanocrystals. *ACS Energy Lett.* **2020**, *5*, 2246–2252.
12. A. De, **S. Das**, N. Mondal and A. Samanta, Highly Luminescent Violet- and Blue-Emitting Stable Perovskite Nanocrystals. *ACS Materials Lett.* **2019**, *1*, 116-122.
13. N. Mondal, A. De, **S. Das**, S. Paul and A. Samanta, Ultrafast Carrier Dynamics of Metal Halide Perovskite Nanocrystals and Perovskite-composites. *Nanoscale* **2019**, *11*, 9796-9818.
14. A. Bhattacharya, **S. Das**, and T. K. Mukherjee, Insights into the Thermodynamics of Polymer Nanodot–Human Serum Albumin Association: A Spectroscopic and Calorimetric Approach. *Langmuir* **2016**, *32*, 12067–12077.

Presentations

Oral Presentations

1. Breaching the Perovskite Red Wall: Phase Stable and Highly Luminescent Red/NIR-Emitting All-inorganic and Hybrid Perovskite NCs. **ChemFest-2022, 19th Annual In-house Symposium of the School of Chemistry**, University of Hyderabad, Hyderabad, India in April 22-23, 2022.
2. Phase Stable and Highly Luminescent Red/NIR-Emitting All-inorganic and Hybrid Perovskite NCs. **16th DAE-BRNS Biennial Trombay Symposium on Radiation & Photochemistry (TSRP-2022, Online)**, Bhaba Atomic Research Centre (BARC), Mumbai, India in January 12-15, 2022. **(Best Oral Awarded)**
3. Breaching the Perovskite Red Wall: Phase Stable and Highly Luminescent Red/NIR-Emitting All-inorganic and Hybrid Perovskite NCs. **11th Asian Photochemistry Conference (APC 2021, Online)**, South Korea in October 31-November 4, 2021.

Poster Presentations

1. Synthesis of Highly Luminescent $APbBr_3$ (A = Cs, MA and FA) Perovskite Nanocrystals: A 'Three-precursor' Approach. **International Conference on Nano Science and Technology (ICONSAT 2020)**, S N Bose National Centre for Basic Sciences, Kolkata, India in March 5-7, 2020.
2. Violet- and Green-Emitting Perovskite Nanocrystals with Enhanced Photoluminescence Efficiency and Stability. **ChemFest-2020, 17th Annual In-house Symposium of the School of Chemistry**, University of Hyderabad, Hyderabad, India in February 27-28, 2020.
3. Violet- and Green-Emitting Perovskite Nanocrystals with Enhanced Photoluminescence Efficiency and Stability. **15th DAE-BRNS Biennial Trombay Symposium on Radiation & Photochemistry (TSRP-2020)**, Bhaba Atomic Research Centre (BARC), Mumbai, India in January 3-7, 2020.

CHAPTER 1

Introduction

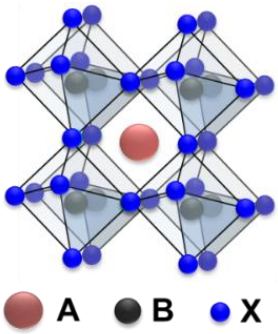

Overview

This chapter starts with a discussion on the importance of unconventional energy sources in today's perspective and the role of semiconductors in this regard. A general overview of the optical and electronic properties of bulk semiconductors and their nanoscale analogues (i.e. NCs) is presented with particular focus on newly emerged lead-halide 'perovskite NCs' around which this thesis work revolves. A brief history of their journey since appearance in 1893 till date in the field of energy has been discussed. Salient characteristics of the perovskites NCs such as crystal structure and formability criteria, exciton fine structure, composition dependent bandgap tunability, surface termination and ligand chemistry, defect formation and optical properties have been discussed. The importance of B-site doping in perovskites and basic information on charge transfer processes in semiconductors are outlined. Finally, reasons of their structural and optical instability and possible ways to counter these challenges have also been pointed out.

1.1. Preface

Modern world has been facing lots of challenges and continuously growing demand of energy is one such big problem which will be even more severe in the coming days. Rapid deterioration of conventional energy sources is a big concern in this regard. Therefore unconventional (renewable) energy sources, which are highly abundant yet not much expensive to convert into energy, are of great significance in saturating energy demand for everyone and a viable way of dealing with the possible energy crisis. Solar energy is the most abundant renewable energy source that can be used with full potential worldwide. Indeed, the most popular silicon solar cell has been in the industry since early 1977 and an efficiency exceeding 26.5% has been witnessed thus far.[1] Despite their many advantages, silicon solar cells are quite expensive even today and a matter of economic burden considering their large scale production and consequent application. The lead-halide perovskite solar cells, which came much late (in 2009), attracted worldwide attention owing to their easy and inexpensive fabrication with fascinating efficiencies of over 26% and 31% (with Si tandem) even being a late contender in the field.[1] However, such materials are also not free from limitations hindering their utility in photovoltaics that will be discussed thoroughly in this thesis. In a similar fashion we came across a long way starting from sodium vapor bulb to more effective tungsten bulbs and currently we are simply living in a world of light-emitting diodes (LEDs) consisting of semiconducting materials. The major advantage that these LEDs bring is maximum brightness with the expense of least energy, thanks to their unique electronic properties. The perovskites being semiconductor in nature are no exception. However, their ideal electronic and optical properties are of paramount importance for their utilization with full potential in photovoltaic and optoelectronic applications. The thesis mainly focuses on probing the optical properties of perovskites (in nano-dimension) employing a number of spectroscopic and microscopic tools and designing new strategies for best utilization of the systems in light-emitting and absorbing applications.

1.2. Semiconductors: Bulk Solids to Nanocrystals

In atoms we talk about atomic orbitals which have discrete energy levels. In first approximation, we use these atomic orbitals in linear combinations either in hybridized or un-hybridized forms to generate bonding and anti-bonding molecular orbitals (MO) for molecules (Figure 1.1.A). Again molecules also have discrete energy levels. Now, more the number of atomic orbitals used to generate MO, smaller is the energy gap between

those bonding and anti-bonding levels of molecules. Consequently, if there are several bonding/anti-bonding molecular orbitals, the energy gap between them decreases. Therefore, if we keep increasing the number of atoms, the energy gap between bonding or antibonding MO further decreases and eventually it will become zero. In such a scenario, there will be no discrete energy levels, rather it will be continuous energy bands and the low energy band is called valence band (VB) and the higher energy band as conduction band (CV). This is the characteristic feature of bulk solids and the energy gap between the VB and CB is known as band gap (E_g) of the material. Note that, based on Eg, solids can be classified as conductor ($E_g \approx 0$), semiconductor ($E_g < 3$) and non-conductor ($E_g > 3$).[2] However, here we will focus solely on semiconductor, which is the subject matter of this thesis. Now if we consider the reverse process i.e. what will happen to the band structures if a solid is broken down into smaller particles? There will come a time when the characteristics continuous energy bands of solids will be no longer continuous and they will split into discrete energy levels (Figure 1.1.B).[3] It means such small systems have a certain E_g, and at the same time within the bands they exhibit discrete energy levels. This phenomenon is observed in semiconductor nanocrystals (NCs) having moderate E_g values. Hence, we can say that the NCs essentially bridge the characteristics of molecules and bulk solids.

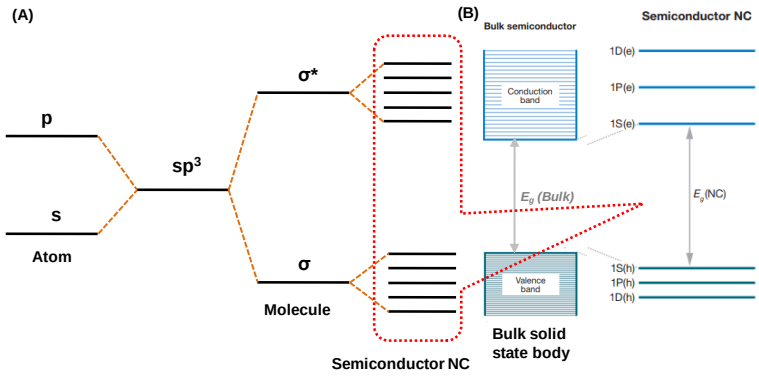

Figure 1.1. *(A) Discrete energy levels in atoms, molecules and semiconductor NCs. (B) Continuous VB and CB of bulk solid which converts into discrete atom like state when size of the system decreases. Figure (B) reproduced from reference 3.*

The semiconductor NCs are nanometer sized crystalline particles consisting of ~100-10000 atoms. They can be made of only elements like Si, Ge or compounds of II-VI or III-V like CdSe, InP etc. When semiconductor NCs are exposed to energy equal to or higher than E_g in the form of light or heat, an electron from the VB gets excited and

promoted to the CB leaving behind a positively charged hole in the VB.[3] In laboratory generally formation of such electron-hole pair in semiconductors is achieved through optical excitation of the NCs. The photogenerated electron and hole can be free depending on their mutual distance and can be mobilized easily in presence of an external electric field to get a current. However, when the electron and hole pair are electrostatically bound, they are in the lowest energy state and is known as exciton.[4] This electrically neutral charge pair can diffuse together within the crystalline structure of the NCs and often called quasi-particle. The binding energy (R^*) of excitons can vary widely depending on dielectric constant of the parent system. For example, in organic systems having low dielectric constant, R^* is usually in the range of ~0.1 – 1 eV and such excitons are known as Frenkel excitons.[5] Inorganic nanocrystalline systems have high dielectric constant values resulting in low R^* values (~10 – 100 meV) of excitons, known as Wannier-Mott excitons. Recombination of excited electron with the hole in VB eventually decimates the exciton with concomitant emission of a photon in a radiative manner or heat through non-radiative recombination. Assuming excitons equivalent to neutral 3D H-atom model, the calculated excitonic energy under the influence of Coulomb potential in zero magnetic field can be expressed as[6]

$$E_n = E_g - \frac{R_y}{n^2} + \frac{\hbar^2 k^2}{2(m_e^* + m_h^*)}$$

where E_n is the energy of n^{th} excitonic level, R_y is Rydberg constant, $\hbar$ is reduced Planck's constant, k is wavenumber and m_e^* and m_h^* represent the effective mass of the excited electron and hole, respectively. It is worth mentioning that R^* and dielectric constant of the system is related by the following equation[6-8]

$$R^* = \frac{R_y \mu}{m_0 \varepsilon_r^2}$$

where μ represents reduced mass of the carriers, m_0 is free electron mass and ε_r corresponds to relative dielectric constant. Note that, R* and ε_r are inversely related to each other, and hence, inorganic semiconductors having high values of ε_r usually falls in the category of Wannier-Mott excitons with low R* values.

There is a separation distance between the electron-hole probability distribution of an exciton which is known as exciton Bohr radius (a_0). It depends on the composition of the semiconductor NC and can vary between 1-100 nm. For example, a_0 of the CdSe NCs is ~9.6 nm, while the same is 1.05 nm for CdTe NCs.[4, 9] When the size of a semiconductor NC is smaller than a_0 of the material, the electron-hole wave function becomes spatially confined and the NC is said to be in the 'quantum confined' regime

with increased energy of the exciton.[4] Therefore it can be said that, an exciton is strongly confined when size of the particle is equal or lower than a_0 of the system, and confinement leads to an increase in E_g of the NCs apart from more pronounced intra-band energy levels in VB and CB edges of the NCs (Figure 1.2.A).[10] Thus smaller the size higher will be E_g of the NCs resulting in blue-shift of excitonic transitions. A typical example of size-dependent evolution of photoluminescence (PL) of CdSe NCs over a wide range of visible spectrum is shown below (Figure 1.2.A).[10] A change in size of the NCs from 6.0 to 2.0 nm leads to huge blue-shift in the absorption and PL spectra of the NCs due to quantum confinement effect, resulting in a drastic change in emission from red to blue region of the visible spectrum.

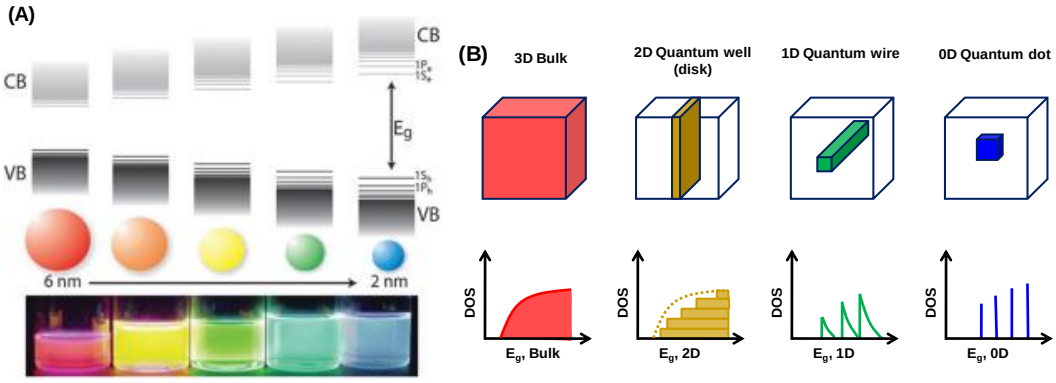

Figure 1.2. *(A) Schematic representation of quantum confinement effect on E_g and intra-band energy levels of the VB and CB of CdSe NCs upon reduction in size from 6 to 2 nm. The lower panel exhibits digital images of the colloidal NCs of different sizes under UV light. Reproduced from reference 9. (B) Schematic representation of quantum confined nanostructures of different shapes (upper panel). The evolution of density of states (DOS) and E_g of the systems are also shown (lower panel).*

The degree of quantum confinement can also vary along different directions relying on the shape of the NCs. The NCs having size much higher than a_0 of the material is essentially a 3D (bulk like) system where in all the three directions (i.e. along x, y and z axis) the dimension of the NCs are way larger than a_0. Since quantum confinement is a size-dependent property, therefore reduction in size of such 3D NCs in any direction (keeping size in other two directions constant) imparts confinement on the excitons along that axis.[11] As shown in Figure 1.2.B (upper panel), depending on the direction of spatial confinement the NCs can be categorized 3D (bulk, no confinement), 2D (quantum well or quantum disk, confined in any one direction), 1D (quantum rod or quantum wire,

confined in any two directions) and 0D (quantum dot, confined in all three directions).[11, 12] As the degree of confinement increases, E_g of the system increases and the intra-band energy levels becomes more discrete (Figure 1.2.B, lower panel). In effective mass approximation, considering an exciton is confined in a spherical volume of crystallite, Brus for the first time theoretically calculated the relation between E_g and size (R) of quantum confined NCs (taking CdSe and CdS as examples), which can be expressed by the following equation.[13]

$$E_g(QD) = E_g(Bulk) + \frac{h^2}{8R^2}\left(\frac{1}{m_e^*} + \frac{1}{m_h^*}\right) - \frac{1.786e^2}{\varepsilon R}$$

where E_g (QD) and E_g (Bulk) correspond to band-gap of the quantum confined and bulk systems, respectively. R is the radius of the systems, h is Planck's constant, and e represents the charge of the electron. Though the above equation satisfactorily describes the bulk and confined systems, spatial correlation of exciton was not accounted into the above effective mass approximation. Later, Kayanuma modified the Brus equation by considering spatial correlation effect of exciton and can be represented as follows.[14]

$$E_g(QD) = E_g(Bulk) + \frac{h^2}{8R^2}\left(\frac{1}{m_e^*} + \frac{1}{m_h^*}\right) - \frac{1.786e^2}{\varepsilon R} - 0.248E_{Ry}^*$$

The 1st term in right hand side of the above equation is the band-gap of bulk material. The 2nd additive term represents additional energy due to quantum confinement effect. Note that lower the value of R, higher will be the value of E_g (QD). The 3rd subtractive term corresponds to Columbic interaction energy between the electron-hole pair and sometimes neglected owing to high ε of inorganic semiconductor NCs. The numerical value associated in this term arises from the electron-hole wavefunction overlap integral and it can be different for different systems. The final subtractive term denotes spatial correlation of exciton and significant only for systems with low ε values as E_{Ry}^* is inversely related with it by the following equation.[11, 14]

$$E_{Ry}^* = 13605.8\frac{1}{\varepsilon}\left(\frac{m_0}{m_e^*} + \frac{m_0}{m_e^*}\right)^{-1}$$

The quantum confinement induced change in PL color of NCs has been extensively exploited in numerous applications ranging from LEDs, lasers, in vivo and in vitro imaging and other biological applications. The current nanoworld would not be as demanding as it is today if semiconductor NCs did not show such size tunable interesting optical and electronic properties.

1.3. The Perovskites

1.3.1. A Brief Journey

The calcium titanium oxide ($CaTiO_3$) mineral, which was discovered in the Ural Mountains of Russia by Gustav Rose in 1839, was named as "Perovskite" after Russian mineralogist Lev Perovski. The solids having similar crystal structure to that of $CaTiO_3$, are known as perovskites having general chemical formula of ABX_3 where A and B are cations with A larger than B and X is an anion usually oxide or halide. The lead-halide perovskites (LHPs) which are the subject matter of this thesis were first reported much late in 1893 by Wells as bulk system with compositions like Cs_4PbX_6, $CsPbX_3$ and $CsPb_2X_5$.[15] In early 1900s they start to attract the attention of scientific communities which led to the elucidation of their detailed structural characteristics by Weber.[16-18] Studies like magnetic properties, photoconductivity were the major focuses with such bulk perovskites in early times.[19] It is worth mentioning in this context that, the first work on LHPs from India was in 1969 demonstrating anti-ferroelectric properties of $CsPbCl_3$ compositions.[20] Subsequently, LHPs had been used as sensitizer in dye-sensitized solar cell. However, it was later realized that apart from increasing absorption cross section in such solar cells, they intrinsically possess impressive charge transport properties. The potential application of LHPs in optical and electronic devices starts to unveil in late 1990s and early 2000s.[21, 22] Specifically, after the pioneering work of Miyasaka and coworkers in 2009,[23] the utility of LHPs as visible light sensitizers in solar cells came into limelight to the world energy researchers and a power conversion efficiency (PCE) of over 26% is achieved using LHPs till date.[1] Bulk LHPs are great in solar energy conversion, however they are weakly luminescent and not suitable for light-emitting applications. Efforts in making these systems with bright emission started since then. After some incremental work in this direction in 2014,[24] the real breakthrough was made by Kovalenko and co-workers in 2015 where colloidal $CsPbX_3$ NCs were first reported with bright emission having PL quantum yield (PLQY) of ~50-90%.[25] In the same year, Zhang et al. introduced another new approach of achieving brightly luminescent organic LHP NCs even at room-temperature (RT).[26] Since then the popularity of the LHP NCs has skyrocketed as a newly emerged promising material of the 21st century with great potential in a range of applications of optoelectronics to photovoltaics and more recently even in photocatalysis.[27, 28]

1.3.2. Crystal Structure of the Perovskites

As mentioned earlier, the generic chemical formula of perovskite is ABX_3, where the monovalent A cation can be Cs^+ or Rb^+ for all-inorganic and methylammonium (MA^+) or formadinium (FA^+) for organic-inorganic hybrid perovskites. B is a bivalent cation and can be Pb^{2+} or Sn^{2+} or Ge^{2+} and X is an anion like oxide or halide (Cl^-, Br^-, I^- or a combination of them).[27-29] However in line with the content of this thesis we will restrict our discussion here on LHPs only. It is important to mention that, for double or vacancy ordered perovskites an exception from the ABX_3 formula is not uncommon though (Figure 1.3.A).[29] In a perovskite cubic unit cell, the A cations occupy at the corners while the B cation remains in centre of the unit cell. The X anions reside at the face-centered position of the cube. Thus the B ions are octahedrally coordinated with six X, forming a corner shared $[BX_6]^{4-}$ units and the A ions reside in the empty cuboctahedral voids of the crystal structure (see Figure 1.3.A).[29, 30] It is important to note that since the cuboctahedral voids are formed by corner sharing arrangement of the $[BX_6]^{4-}$ octahedral units, the A-site cation is under size constrains and it largely controls the stability of a 3D perovskite structure. For example, ethylammonium (EA^+) being larger in size than both MA^+ and FA^+, no hybrid perovskite based on EA^+ is reported till date and much larger

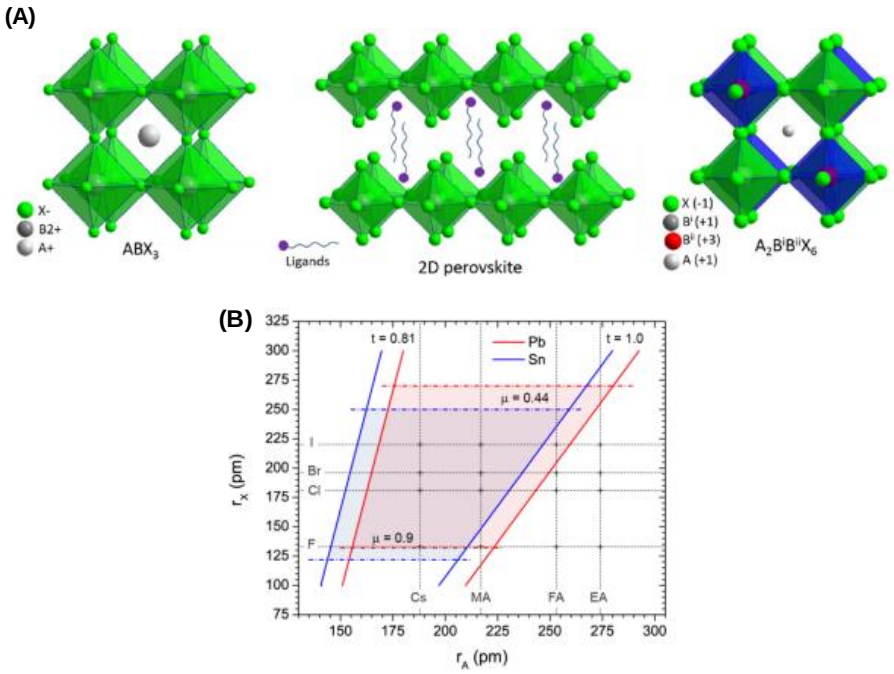

Figure 1.3. *(A) Schematic representation of cubic ABX_3 perovskite, 2D perovskite and double perovskites. Reproduced from reference 27. (B) Formability space (red shaded area) of LHPs as a function of ionic radii of A- and X-site ions. Figure (B) reproduced from reference 31.*

size facilitates the formation of 2D layered perovskite structures (Figure 1.3.A).[27] A composition dependent semiempirical parameter, known as Goldschmidt tolerance factor (t), can be considered to predict the formability and consequent stability of the 3D perovskite structures as follows [32]

$$t = \frac{r_A + r_X}{\sqrt{2}(r_B + r_X)}$$

Here 'r' corresponds to ionic radii of the corresponding constituents. Typically, 't' value of most of the 3D LHPs lies in the range of $0.81 \leq t \leq 1.0$ and a value over 1 or below 0.8 usually gives rise to 1D hexagonal or non-perovskite structures.[31] The octahedral factor (μ), expressed as $\mu = r_B/r_X$ indicates the formability of $[BX_6]^{4-}$ units and empirically falls in the range of $0.44 \leq \mu \leq 0.9$. Considering both 't' and 'μ' an allowed space for the formability (and stability) of 3D perovskites can be drawn and shown as a red-shaded area in the 2D plot of 'A' and 'X' ionic radii (Figure 1.3.B).[31] If combination of the above two parameter values for a particular system lies within the shaded region formation of a perovskite structure can be expected and when it falls well outside these limits a non-perovskite structure results. It is however important to note that the concept of 't' was initially proposed for the metal-oxide perovskites and hence the allowed ranges are accurate for more electronegative oxide and fluoride based systems.[32] The heavier halides (like Br and I) being less electronegative, show deviation from the empirical ranges particularly with the organic A-site cations. For example, all FA-based LHPs form cubic 3D structure even though t >1.[33] Interestingly, despite having a 't' value close to the allowed value of 1.0, the $FAPbI_3$ (t = 1.03) is unstable,[34] while $FAPbBr_3$ (t = 1.08) and $FAPbCl_3$ (t = 1.09) form stable 3D structure.[35] Hence, the upper boundary of 't' for the LHPs is still not well defined and stable LHPs with A-site organic cations are found to have t>1.0 leaving questions for the future studies.

1.3.3. Optical Properties of the Perovskite NCs

Since the invention of perovskite NCs in 2015,[25] a giant leap of research on these NCs has been witnessed worldwide. Fascinating optical and electronic properties such as defect tolerance nature, high PLQY, narrow emission bandwidth, broad and intense absorption, composition and size dependent emission tenability have brought them in forefront of energy research in recent time.[27, 28] The band structure of the perovskite NCs is quite different from that of the conventional metal chalcogenides QDs, making them even more attractive in real applications. The band gap in conventional semiconductors like CdSe, GaAs etc. are usually formed between bonding (σ) and antibonding (σ^*)

orbitals *vis-à-vis* to VB and CB, respectively (Figure 1.4.A).[36] Hence, the dangling orbitals due to point defect appear as non-bonding states within the band gap of such conventional QDs and contribute to non-radiative recombination of photogenerated charge carriers. However, in LHPs, the band gap is formed between two anti-bonding orbitals, thus non-bonding defect states are either shallow in nature or completely enclosed within their band structures (Figure 1.4.A).[36] This makes the LHPs much more 'defect tolerant' over the conventional semiconductors,[36, 37] and hence, the radiative recombination mostly remains unperturbed in LHP NCs resulting in much higher PLQY (up to ~100%) compared to the conventional QDs. It is further reported that the VB

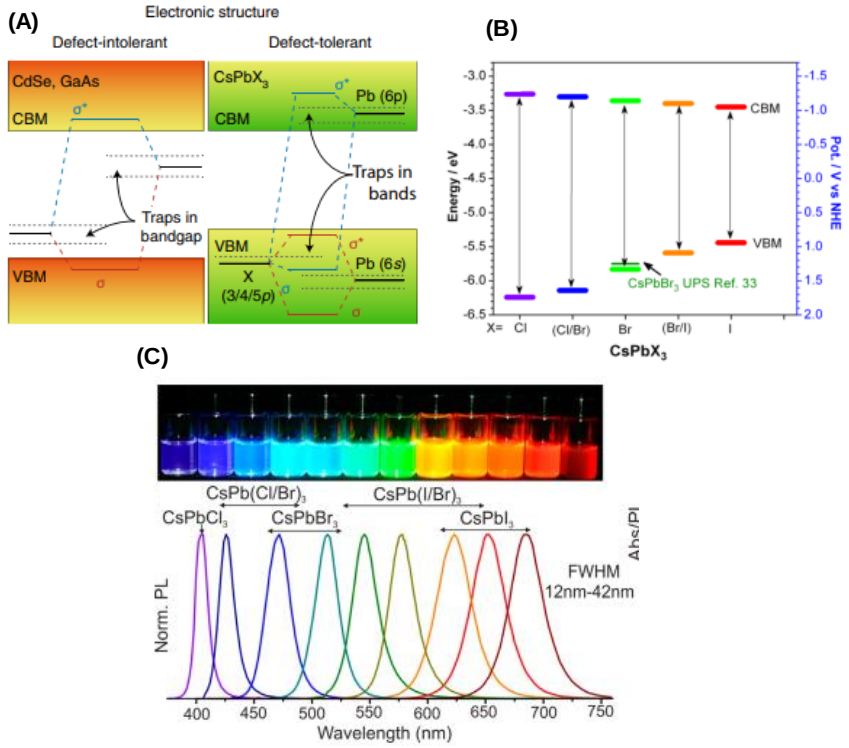

Figure 1.4. *(A) A comparison of electronic band structures of the metal chalcogenide QDs to that of the LHP NCs. (B) Change in energy of VBM and CBM of the $CsPbX_3$ NCs with different halides. (C) PL spectra of the $CsPbX_3$ NCs with different halide composition. The upper panel shows digital photographs of their colloidal solutions under UV light (365 nm) NCs. Figure (A), (B) and (C) are adopted from Reference 36, 38 and 25.*

maxima (VBM) of LHPs are mainly composed of anti-bonding mixing of X np and Pb 6s atomic orbitals with major contribution from X np orbitals.[36, 38] Hence, a change in halogen from I (5p) to Cl (3p) *via* Br (4p) decreases corresponding energy of the np

orbital leading to a reduced energy of the VBM (Figure 1.4.B).[38] On the other hand, the CB minima (CBM) is associated with anti-bonding coupling of Pb 6p and X np orbitals with predominant contribution from Pb 6p atomic orbitals. As spin-orbit coupling constant in LHPs is nearly constant (~1.1 eV),[39] extent of hybridization plays a major role in determining the energy of CBM. If we move from X = I to Cl *via* Br, the Pb-X bond length decreases, which in turn increases the orbital overlap of the Pb 6p and X np orbitals leading to a shift of the CBM towards higher energy.[38] Thus if we tune the halide ion composition from I to Cl (*via* Br) in $APbX_3$ NCs, the band gap increases and thereby the absorption and PL maxima of the NCs change from red to violet (*via* green) region of the visible spectrum (Figure 1.4.C).[25, 38] It is therefore evident that the optical and electronic properties of LHP NCs are predominately governed by the $[PbX_6]^{4-}$ octahedral units. Although, the A-site cation doesn't have much influence on the electronic band structure of LHPs, a small increase in size of cations like moving from Cs^+ to MA^+ to FA^+ slightly expands the crystal structure, which slightly decreases the band gap of the NCs and leads to a small red-shift of the absorption and emission spectra of the NCs. Furthermore, like conventional QDs, LHP NCs also exhibit size-dependent optical properties. For example, it is reported that, a change in size of the green-emitting $CsPbBr_3$ NCs from ~9.5 to 3.7 nm, results in blue-shift its PL spectrum from ~510 to 467 nm due to quantum confinement effect (a_0 of $CsPbBr_3$ NCs is ~7 nm[25]) of the NCs.[40] Thus perovskite NCs exhibit size and composition dependent attractive optical properties with broad absorption and bright and narrow (fwhm of ~10-50 nm) emission over the entire visible window making them indeed a coveted material in the 21st century for a wide range of optical applications.

1.3.4. Exciton Fine Structure

It is already mentioned that in LHP NCs the CB has a predominate contribution of the Pb 6p orbital, thus VB and CB of such NCs has 's' and 'p' type symmetry, respectively.[38] Presence of heavy atom (lead), facilities spin-orbit coupling in these systems leading to splitting of the six-fold degenerate CB into a doubly degenerate (J_e = 1/2, m_J = ±1/ 2) lower energy state and four-fold degenerate (J_e = 3/2, m_J = ±3/2, ±1/2) higher energy state.[41, 42] Therefore, the lowest energy exciton can be considered as a hole in any one of the two-fold degenerate VB state (J_h = S_h = 1/2, m_S = ±1/2) and the excited electron in any one of the low lying two-fold degenerate CB states. Further, electron-hole exchange interaction splits the band-edge excitonic states, into exciton fine structure with a three-

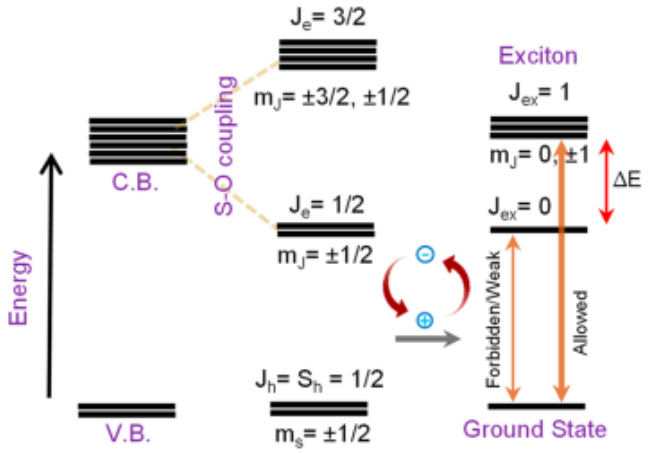

Figure 1.5. *Schematic representation of exciton fine structure of 3D cubic LHPs considering contributions of spin-orbit coupling and electron-hole exchange interaction. Adopted from reference 45.*

fold degenerate optically allowed (bright) state (J_{ex} = 1, m_J = 0, ±1) and one optically passive (dark, J_{ex} = 0) state (Figure 1.5.).[42, 43] It is to be noted that, this splitting is valid as far as the system is symmetric, a lower order or distorted crystal can further lift the degeneracy of the band-edge states.[41] Thus three bright (spin allowed) and one dark (spin forbidden) recombination pathways for photogenerated electrons are possible in LHPs.[44, 45] It is to be noted that although the dark state lies below the bright state for metal chalcogenide QDs, the positioning of these states in LHP NCs is a matter of debate.[46, 47] However, we will not go into this as it is beyond the scope of the thesis. Moreover, since the spacing between the bright and dark state is typically < 10 meV, individual transitions from the allowed states are not observed at RT with thermal energy over 25 meV. Hence, a simplified picture of excitonic recombination between VB and CB is normally considered for RT studies.

1.3.5. Surface Characteristics of the Perovskite NCs

Large surface-to-volume ratio of nanomaterials not only makes their exterior a dominant player in physical and chemical properties but also imparts in their colloidal stability. As size of a NC decreases, surface area of the systems increases and thereby the number of atoms at the surface increases.[4] Now if we think practically, there will be a termination of each NC and such terminal faces are made of the constituent atoms of the NCs. Therefore, clearly the atoms present at the terminal faces of any NCs are incompletely

bonded and the unbound orbitals are directed outside the crystal. These unpassivated orbitals are known as 'dangling orbitals' and in nano-dimension they are highly abundant owing to the presence of large number of atoms at the surface.[4] Since NCs are highly faceted, large density of dangling orbitals collectively forms an energy band structure within the band gap of the NCs. Further, they can reduce the overlap between electron-hole pair, facilitating nonradiative recombination of the charge carriers.[4, 37] However, as discussed in section 1.3.3, such energy levels are mostly shallow in nature particularly in LHP NCs and have much less impact compared to the metal chalcogenide QDs.[36] Later we will see that contribution of such shallow energy levels towards nonradiative processes is not negligible and this has large impact on optical properties of the perovskite NCs. In practice, however, such dangling orbitals are passivated by long organic ligands [usually oleic acid (OA) and oleylamine (OAm) for perovskite NCs],[25] which not only minimize the inter-band surface states but also helps maintaining structural integrity and colloidal solubility of the NCs in non-polar medium.

In bulk perovskites, the halogen to lead ratio (i.e. X/Pb) is close to 3.0. However, this ratio varies for the NCs and theoretically considering the upper and lower limits of X/Pb value, surface termination possibilities of the $CsPbX_3$ NCs can be represented in two ways (Figure 1.6.A).[48] The CsX-terminated surface consists of $CsPbX_3$ core terminated by PbX_2 inner cell and CsX outer cell, represented as $[CsPbX_3](PbX_2)\{CsX\}$. On the other hand, the PbX_2-terminated surface consists of $CsPbX_3$ core terminated by CsX inner shell and PbX_2 outer shell, denoted as $[CsPbX_3](CsX)\{PbX_2\}$.[48] In reality, however, the NCs are terminated with long-chain organic ligands like oleylammonium-oleate, which provide them colloidal integrity apart from acting as surface passivator.[49] Hence considering ligand capping, in realistic model, surface termination can be represented as $[CsPbX_3](PbX_2)\{AX'\}$, where A is monovalent cation like oleylammonium or Cs^+ and X is an anion like oleate or halide (Figure 1.6.B, right).[48] Ligand density largely depends on the steric hindrance and the equilibrium between NCs surface and solution. It is important to note here that $\{PbX_2'\}$ type termination is quite impossible in reality as firstly, about 2.5 times higher ligand density (than in other model) will cause severe steric hindrance in the ligand shell and secondly, this would break octahedral coordination of Pb.[49] Moreover, in many earlier studies it has been shown that $[CsPbX_3](PbX_2)\{AX'\}$ is the most relevant surface termination for the LHP NCs. However, there are few instances where it is shown that PbX_2-terminated $CsPbX_3$ NCs with high structural stability are also possible.[50, 51]

As already mentioned, OA and OAm are primarily used as surface capping ligands for efficient surface passivation and to disperse the NCs in non-polar solvents like toluene, hexane etc.[25] Hence, a question may arise, what is the binding motif of such ligands on NCs surface? Before answering the question, it is important to take note of the acid-base equilibrium between OA and OAm, leading to formation of oleylammonium (OAm^+) through deprotonation of OA, which in turn converts into oleate ions.[52] It has been reported that, OAm^+ ligands adsorbed on the surface of the NCs through H-bonding interaction with surface halides (Figure 1.6.C).[53] The positively charged ligand can also occupy some of the surface exposed A-sites through substitution of some surface cations

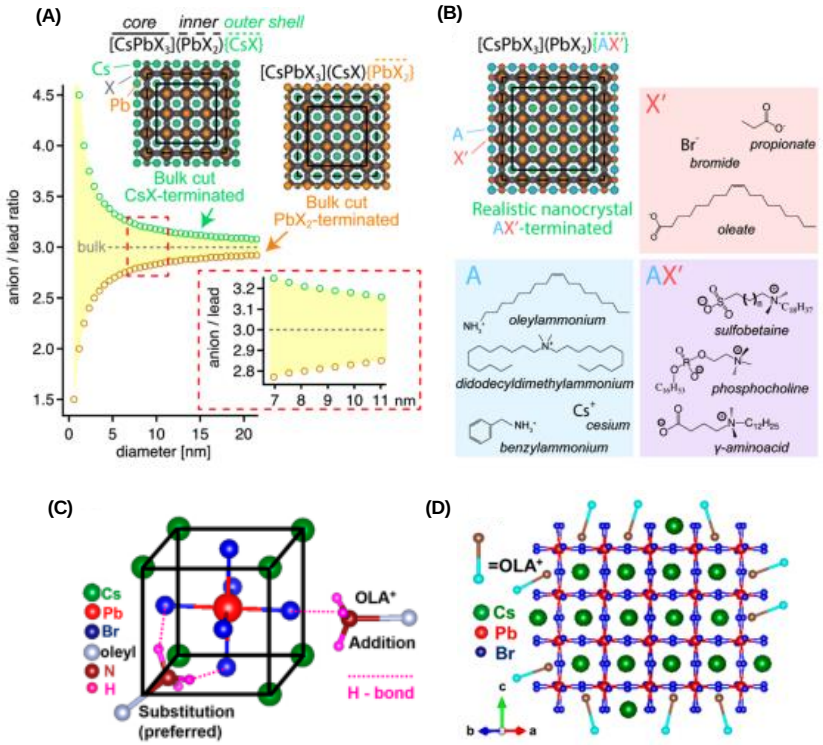

Figure 1.6. *(A) Schematic representations showing the possible surface terminations of $CsPbX_3$ NCs. (B) The realistic surface termination model with the common cationic and anionic surface ligands. Adopted from reference 48. (C) Schematic showing the possible binding of OAm+ on the surface of $CsPbBr_3$ NCs. (D) An atomistic model of substitution of OAm^+ in some surface Cs^+ sites. Adopted from reference 53.*

(Figure 1.6.C).[53] In such cases, the ammonium moiety of OAm^+ can form additional H-bond with the surrounding X atoms compared to simple addition of the ligands. Therefore, substitution of OAm^+ is thermodynamically more favorable in LHP NCs

(Figure 1.6.D). The role of OA (or oleate) is somewhat debatable with some reports showing its binding at the surface while some do not.[49, 53] However, OA (or oleate) is required for maintaining a balance in acid-base equilibrium with OAm and thus it contributes to the colloidal stability and desired optical properties of the NCs.

1.3.6. Defect and its Impact on the Perovskite NCs

Although it has been shown earlier that the trap or defect states in LHP NCs are mostly benign due to their shallow nature,[36] a sub-unity PLQY of the NCs however suggests that they still impart a detrimental effect on their optical properties.[27, 54] The point defect, which arises primarily due to vacancies at A- or X-sites owing to low formation energy are highly abundant and forms shallow defects in perovskite NCs (Figure 1.7.A).[36] Deep traps from the interstitial and/or anti-site defects are however less common in LHP NCs as the constituting ions in perovskite lattice are difficult to misplace from their lattice sites.[36] The OAm^+ ligands bound to the surface of such NCs are highly dynamic in nature as they are associated with surface halogens by weak H-bonding interaction.[49] Such weak bonding of OAm^+ facilitates its desorption from the surface as oleylammonium halide (OAm^+X^-) ion pair, forming halide vacancies (V_X) at the surface.[52] Note that, it is quite unfavorable for the OAm^+ ligands to dissociate as independent solvated ion in a non-polar media like hexane/toluene and since oleate is absent at the surface they pull out the surface halides (X^-) resulting in formation of halide-vacancy (V_x) related point defects.[52, 55] Again, large surface-to-volume ratio in nano-dimension makes the surface halide vacancies (under-coordinated lead atom in other word) predominant source of defects, facilitating non-radiative recombination of photogenerated charge carriers leading to sub-unity PLQY of the NCs.[54] Alivisatos and co-workers both experimentally and theoretically have shown that the impact of halide vacancies on the electronic structure of LHP NCs is not identical.[55] The detrimental effect of chloride-vacancies (V_{Cl}) on the optical properties (like PLQY) of the $CsPbCl_3$ NCs is much more pronounced compared to the bromide- and iodide-vacancies (V_{Br} and V_I, respectively) in $CsPbBr_3$ and $CsPbI_3$ NCs (Figure 1.7.B).[55] This is because the chloride-vacancies (V_{Cl}) in $CsPbCl_3$ NCs are highly localized deep trap states, while the corresponding V_{Br} and V_I in $CsPbBr_3$ and $CsPbI_3$ NCs are shallow in nature (Figure 1.7.C).[55] For this reason, PLQY of $CsPbCl_3$ is typically in the range of 0.5-5%, while it is above 50% for both $CsPbBr_3$ and $CsPbI_3$ NCs.[27, 54] However, sub-unity experimental PLQY of these two systems indicates that the bromide- and iodide-based NCs are still not trap-free and have other issues.

Being a soft lattice, LHP NCs are highly susceptible towards crystal disorder which eventually creates defects in these systems. For example, due to large size of iodine, the volume of a $[PbI_6]^{4-}$ octahedral unit is large and hence they created large cuboctahedral voids where the smaller A-site cations like Cs^+ reside. This results in slight tilting of the lead-halide octahedral units towards the void space of cuboctahedral sites.[54, 56] This is known as 'octahedral tilting' and such crystal distortion not only contributes to

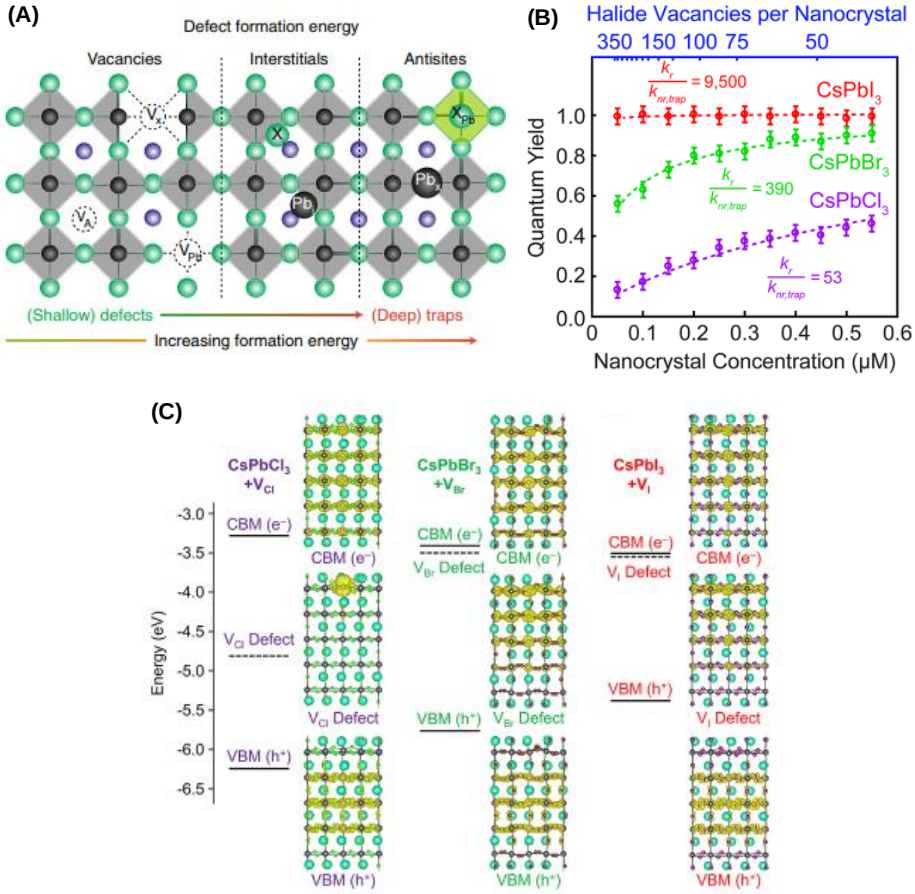

Figure 1.7. *(A) Schematic representation of typical point defects in LHP NCs. Adopted from reference 36. (B) Impact of halide-vacancies on the PLQY of $CsPbX_3$ NCs. (C) Possible electronic structures and associated charge density distribution due to halide-vacancy related defects in LHP NCs. Figures (B) and (C) are adapted from reference 55.*

inter band-gap trap states but also destabilizes the iodide-based NCs.[54] Again, in the case of $CsPbCl_3$ NCs it has been reported that the V_{Cl} and local structural distortion collectively create short-range disorder in the lattice that deteriorates optical properties and stability of such NCs through formation of deep-trap (defect) states.[57] However, partial substitution (doping) of smaller sized metal cations in place of lead can partially

rectify such crystal disorder and improve optical properties and stability of the NCs.[56] Moreover, soft and ionic characteristics of the perovskite lattice lead to structural dynamics (shift from equilibrium position) of the lead-halide lattice even at RT leading to a strong coupling between the photogenerated excitonic wave function and ionic displacement of the lattice, known as polaron.[36] These polarons are known to screen Coulombic potential and have a detrimental effect on the optical properties of the LHP NCs.[36, 58]

1.3.7. Doping in Perovskite NCs

Doping or alloying is considered to be an excellent strategy for tuning the optical and electronic properties of semiconductor NCs. In case of LHP NCs, doping also contributes to the optical and phase stability of the systems.[28, 54, 56] Typically all the three constituents (i.e. A, B and X) of $APbX_3$ type LHP NCs can be doped for different purposes.[27] However, we will restrict our discussion here mostly to Pb-site doping since it is one of the major theme of this thesis. There are essentially two ways to incorporate small amount of impurity or foreign element to partially substitute Pb in achieving doped NCs (Figure 1.8.A). Firstly, addition of desired metal salt of the dopant in precursor solution during the synthesis of LHP NCs (*in situ*) usually leads to formation of doped NCs.[59] Secondly, due to soft crystallite nature, doping in LHP NCs can be executed post-synthetically even at RT, provided Pb-X and M-X bond energies of the host and guest, respectively are comparable.[60] However, there are many instances where no evidence of doping was found by following any of the above two strategies.[40] A large variety of isovalent (Mn^{2+}, Zn^{2+}, Cd^{2+}, Mg^{2+}, Ni^{2+}, Sr^{2+} etc.) or heterovalent (Cu^{+}, Na^{+}, Ce^{3+}, Bi^{3+}, Al^{3+}, Tl^{3+}, Nd^{3+} etc.) metal ions (dopants) are doped by replacing some of the Pb^{2+} ions in perovskite lattice for various purposes ranging from improving optoelectronic properties to structural stability and for controlling light conversion efficiencies and photo-catalysis (Figure 1.8.B).[27, 28, 54, 61] Moreover doping of Pb^{2+} with an environment friendly cation reduces the toxicity of the overall system, thus making the NCs more benign for widespread applications. It is important to note that the concentration of dopants inside the perovskite crystal is highly important to sustain their intrinsic crystal structure.[60] A large dopant concentration has an adverse effect on it and may eventually lead to morphology or phase change of the NCs.

Interestingly, when the ionic radii of a dopant is smaller than that of Pb^{2+} (r = 119 pm), the tolerance factor (t) of the doped system increases.[56] Furthermore, substitution of

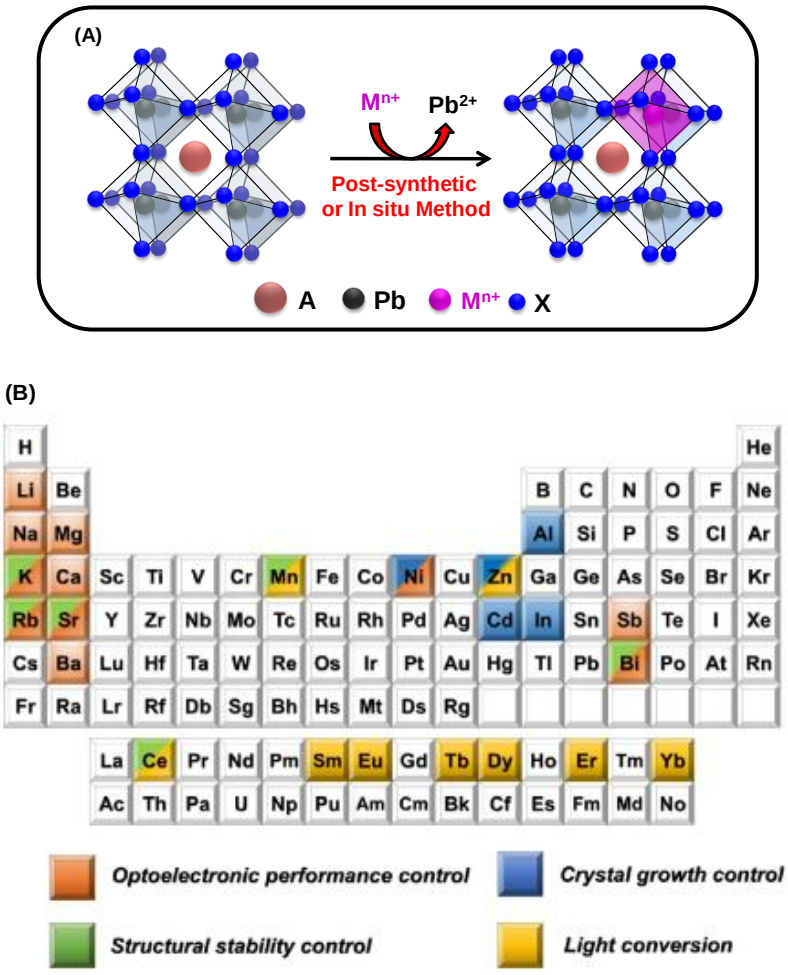

Figure 1.8. *(A) Schematic representation of partial substitution (doping) of Pb^{2+} with an arbitrary metal cation (M^{n+}) of LHP NCs. (B) Doped metal ions and their impact on different characteristics of LHP NCs. Figure (B) adopted from Reference 61.*

Pb^{2+} with smaller cations (M^{n+}) reduces size of the corresponding $[MX_6]^{n+}$ octahedral units, which in turn decreases the empty space in cuboctahedral voids (Figure 1.9.A).[54, 56] Thus crystal disorders like 'octahedral tilting' and 'local structural disorder' are lifted upon doping of a small cation at B-site which not only increases structural stability but also increase PLQY of the doped NCs (like Mn^{2+} or Ni^{2+} doping in $CsPbI_3$ and $CsPbCl_3$ NCs, respectively).[56, 57] Furthermore, in case of $CsPbI_3$ NCs, doping of some A-site Cs^+ ions with bigger cations like FA^+ and/or replacing some X-site iodide ions (I^-) with smaller anions like chlorides (Cl^-) also increase the 't' value and minimize octahedral distortion in the crystal structure.[33, 62] As the B-site cations reside at corners while the X-site anions remain in edges of the perovskite cubic unit cell,[56] a B-site cation (Pb^{2+} here) is directly associated with eight cuboctahedra through eight adjacent $[BX_6]^{4-}$ octahedral

units, while X-site anion shares only four such cuboctahedral voids. Since the size of B-site cations determines the size of $[BX_6]^{4-}$ units, which controls the cuboctahedral voids, doping at one octahedral site of Pb^{2+} with a smaller cation effectively controls the voids of eight cuboctahedral sites and thus can be more efficient over other available strategies. For example, only 12.5 mole % Mn^{2+} can be enough to completely (~100%) cure octahedral distortion in $CsPbX_3$ NCs, leading to much improved optical properties and stability of the NCs.[56]

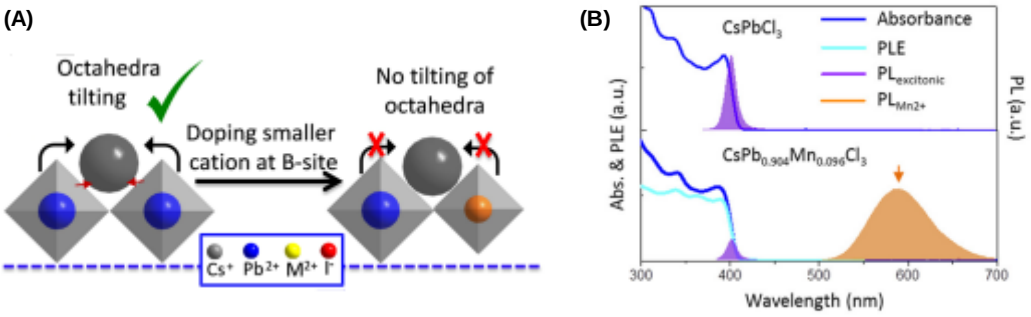

Figure 1.9. *(A) Schematic representation of octahedral tilting of $[BX_6]^{4-}$ unit towards cuboctahedral void of LHP NCs which reduces upon doping of smaller cations in place of Pb^{2+}. Adopted from reference 56. (B) Absorption and PL spectra of undoped (top) and Mn^{2+}-doped (bottom) $CsPbCl_3$ NCs. Apart from band-edge excitonic emission of the host $CsPbCl_3$ NCs, the doped sample shows distinct emission at ~586 nm corresponding to Mn^{2+} transition. Adopted from reference 63.*

In this context, some metal ions like Mn^{2+}, Cd^{2+} or Ln^{3+} (Ln = Lanthanides) show their distinct PL characteristics after sensitization through excitonic energy transfer (ET) when doped into a suitable host NCs.[63-65] Dexter type ET mechanism from host NCs to the atomic states of dopants gives rise to a new PL spectrum corresponding to the dopant ion at lower energy region of the excitonic (band-edge) PL of the host (Figure 1.9.B).[63] It is important to note that energy transfer from host NCs to dopant should be energetically feasible for achieving efficient dopant emission. High band-gap $CsPbCl_3$ NCs serve as the ideal host of these dopants with CB energy higher than their highest atomic levels (e.g. $^4T_1$ for Mn, ^3E_g for Cd) facilitating efficient ET from the $CsPbCl_3$ NCs.[63, 64] Similarly, CB energy of $CsPbI_3$ NCs is much lower than those atomic levels, resulting in no ET to the dopant ions and hence PL could not be observed. Energetically feasible back energy transfer from the atomic energy levels of the dopants to CB of the $CsPbBr_3$ NCs limits the dopant emission when the latter is employed as host.[63] Note that, usually dopant

transitions are both Laporte and spin forbidden and hence, they are characterized by long photon relaxation time, typically in ms to μs time window.[63] The Mn^{2+} and Cd^{2+} dopants show emission typically in the 590-630 nm region[63, 64] while Ln^{3+} ions exhibit emission in different regions of the Vis-NIR spectrum.[65] However, extensive non-radiative trapping in $CsPbCl_3$ NCs suppresses ET processes to the dopants, thus limiting PL efficiency of the dopant emission. It has been reported that defect free Cd-doped $CsPbCl_3$ NCs act as an ideal host for Mn^{2+} emission, resulting in near unity PLQY due to significantly suppressed non-radiative excitonic recombination of the host NCs, facilitating effective ET to Mn^{2+}.[66] Such doped systems with dual emission over a wide spectral region are of great importance from the point of view of white light-emitting applications (wLEDs).

1.3.8. Charge Transfer from Perovskite NCs

Radiative recombination of photogenerated charge carriers (electrons in CB and hole in VB) is important for optoelectronics, while their dissociation before spontaneous recombination is of paramount importance in the field of photovoltaics and photocatalysis. Thus there is a basic difference of charge carrier utilization in optoelectronics and photovoltaics. Like defect tolerant behavior and high PLQY in optoelectronics, broad and intense absorption, high carrier diffusing length and low exciton binding energy make the LHPs great contenders as solar energy harvester in photovoltaic applications.[23, 27] In general, energy selective charge transport layers are employed as electron or hole acceptor in solar cells after photo-excitation of the energy harvesting material to generate current externally (Figure 1.10.A).[67] In case of perovskite NCs, organic molecular systems are used as model carrier acceptors adsorbed at the surface of the NCs to promote such charge transfer processes.[68] The energetics of the NCs and molecular adsorbate determine whether any charge transfer is feasible for a particular pair of system. If the LUMO level of a molecular system resides below CB of the NCs, electron transfer is favorable (Figure 1.10.B).[69] Similarly, if HOMO level of the molecule has energy higher than VB of the NCs, a hole transfer is feasible.[69] Efficient charge transfer results in rapid quenching of luminescence of the NCs through suppression of band-edge excitonic recombination. The emergence of a new recombination channel in presence of carrier acceptors affects the excited state lifetime of the emitter, leading to a significantly reduced lifetime of the system.[70] However, charge transfer without any major change in lifetime is not uncommon though.[71]

In the case of semiconductor NCs (including LHP NCs), charge extraction may

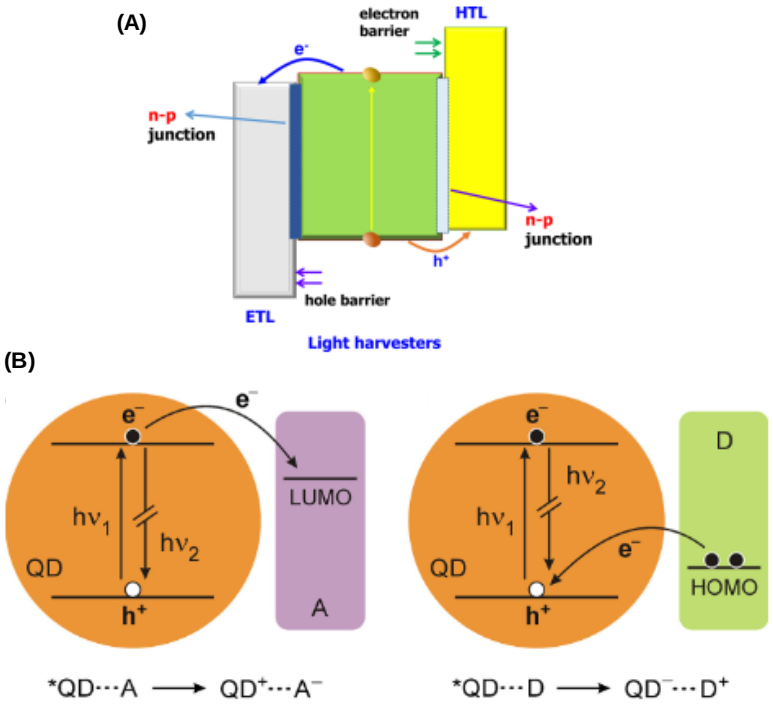

Figure 1.10. *(A) Schematic illustration of the alignment of charge transport layers in perovskite based solar cells. Adapted from reference 67. (B) Simple schematics showing photoinduced electron transfer from QDs to molecular electron acceptor A (left) and hole transfer from photoexcited QDs to molecular hole acceptor (right). In true sense, hole transfer can be visualized as electron transfer from donor molecule (D) to photoexcited QDs. Adapted from reference 68.*

take place from band-edge state (cold charge carriers) as well as from higher energy levels (hot charge carriers). Since hot carriers cool down to the band-edge states in ultrafast time scale (typically few tens of femtosecond), it is difficult to transfer hot charge carriers into molecular acceptors.[72] Hence, most of the charge transfer processes take place from band-edge states of the NCs.[68] However, if one can extract the hot charge carriers before their excess energy dissipation , a power conversion efficiency of ~66%, which is much beyond the Shockley−Queisser limit (SQ limit) of ~33% for band-edge carrier extraction of semiconductor NCs, can be achieved.[73, 74] Limited works in this direction have recently been carried out exhibiting high hot hole transfer efficiency from $CsPbBr_3$ NCs.[75-77] However, the iodide-based NCs with lowest band-gap and slowest hot carrier cooling time among all LHP NCs are expected to be the best candidates in this regard.

1.3.9. Structural Instability and How to Handle It

Structural and optical instability has been a major issue of LHP NCs despite their promising optical properties.[36] As stated earlier, deprotonation of the weakly bound OAm^+ ligands leads to their desorption from the surface making the surface ligand environment of these NCs highly fragile.[49, 52] Such ligand desorption exposes the surface to the environmental moisture and the soft ionic character of the lattice renders decomposition of the NCs into individual [PbX_6] octahedral fragments (Figure 1.11, top).[36] Thus eventually corner share geometry of the LHP NCs disintegrates, resulting in complete deterioration of their interesting optical properties. Better protection at the surface of these NCs is needed for achieving stable NCs. Therefore, ligands with more static surface coordination can be of paramount importance. Indeed, zwitterionic ligands having multiple binding sites[52] or quaternary ammonium ligands (Figure 1.11, bottom) with no possibility of deprotonation[78] or even sulfonate and phosphate ligands having better surface protection than carboxylate[79] have been shown to improve stability of the NCs. A protective shell at the surface of the NCs with inert layer like silica or compositionally matched salts like CsX or encapsulation of the NCs inside a polymer matrix can be useful technique for achieving stable NCs even in presence of polar solvents.[80] Recently covalent bonding of ligands is reported to provide much better

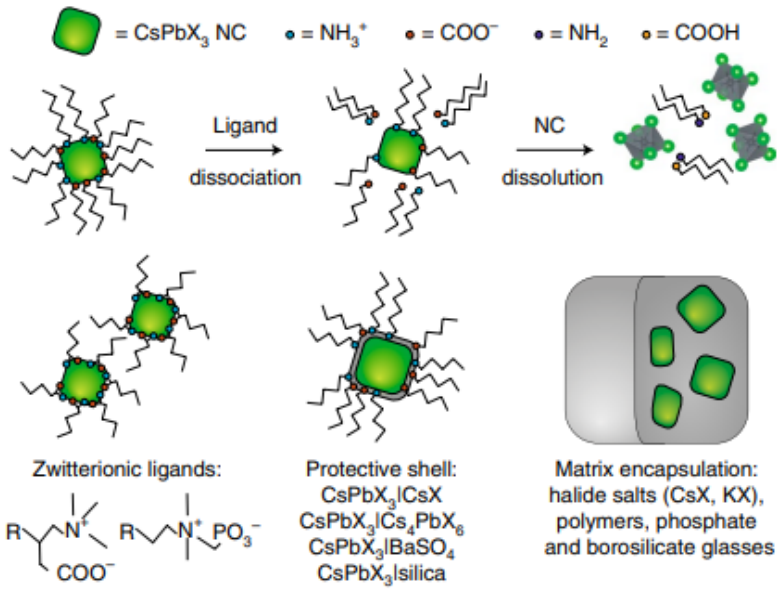

Figure 1.11. *Structural instability due to labile surface ligands of LHP NCs (top). Possible stabilization strategies focused on surface of the NCs (bottom). Adopted from reference 36.*

stability of the NCs over the conventional weakly bound cationic ligands.[50, 51] Moreover, intrinsic structural disorders like 'octahedral tilting' and 'short range disorder' are found to be additional factors contributing to the phase sensitivity of the NCs.[56, 57] Increasing 't' value of the system through efficient doping may be helpful in such scenarios.

Interestingly, unlike the previous reports, some recent works show strong binding of the OAm^+ ligands can restrict crystal distortion in iodide-based NCs and provide much higher phase stability of the NCs.[81] Therefore further studies are required in this direction. The developments toward obtaining stable LHP NCs without compromising their optical properties are still at its infancy and thus demand more attention from the point of view of real applications.

1.4. Thesis Layout

The thesis is divided into total seven chapters. ***Chapter 1*** starts with highlighting the importance of research in unconventional energy in the present scenario followed by importance of the semiconductors and their optical and electronic properties in bulk and nanocrystalline form with special emphasis on quantum confined NCs. Then we have introduced the perovskites, a new addition in semiconductor materials and discussed about their origin and evolution in the field of nanochemistry, crystal structure, salient optical and electronic properties. The surface chemistry, origin and impact of defect states, essence of metal doping, charge transfer processes and the reason of instability of the perovskite NCs are discussed. In ***Chapter 2***, we have discussed synthetic strategies and purification methods of the perovskite NCs of different compositions following different approaches. Details of different spectroscopic measurements like steady state UV-Vis absorption and emission, femtosecond pump-probe (TA), fluorescence up-conversion and time correlated single photon counting techniques are discussed with outlines of their different optical and electronic components. Information on LED fabrication and other characterization techniques like TEM, PXRD, FESEM, XPS, EDX, FTIR, NMR and ICP-OES are discussed briefly. The working chapters starts from ***Chapter 3***, in which the impact of Mg^{2+} doping on the optical properties of $CsPbX_3$ NCs (X= Cl and Br) NCs is discussed. The key factors controlling the improved optical properties are identified in ultrafast time scale employing TA measurement. In ***Chapter 4***, we have discussed a generic methodology of achieving all iodide-based LHP NCs employing a new iodide precursor with unparallel PLQY and stability. The same strategy is extended in ***Chapter 5*** for the bromide- and chloride-based NCs using a common class

of halide precursors. The carrier dynamics of the NCs are investigated and valuable insight into the key aspect of designing effective halide precursors for next generation LHP NCs is obtained. In ***Chapter 6*** the advantage of L-type coordinate bonding of surface ligands toward structural and optical stability of the $CsPbCl_3$ NCs are highlighted following a new strategy demonstrating intense violet emission of these NCs even for low density of surface ligands. Finally, all findings of this thesis are summarized in ***Chapter 7*** and possible future directions of research in the field of LHP NCs based on our results are outlined.

References:

1. NREL, https://www.nrel.gov/pv/cell-efficiency.html, (accessed on 29-08-2022).
2. P. Y. Yu and M. Cardona, *Fundamentals of Semiconductors: Physics and Materials Properties*, Springer, 2010.
3. V. I. Klimov, *Annual Review of Physical Chemistry*, 2007, **58**, 635-673.
4. A. M. Smith and S. Nie, *Acc. Chem. Res.*, 2010, **43**, 190–200.
5. M. Pope and C. E. Swenberg, *Electronic Processes in Organic Crystals and Polymers*, Oxford University Press, 1999.
6. B. Henderson and G. F. Imbusch, *Optical Spectroscopy of Inorganic Solids*, Clarendon Press, Oxford, 1989.
7. S. V. Gaponenko, *Introduction to Nanophotonics*, Cambridge University Press, 2010.
8. K. Galkowski, A. Mitioglu, A. Miyata, P. Plochocka, O. Portugall, G. E. Eperon, J. T.-W. Wang, T. Stergiopoulos, S. D. Stranks, H. J. Snaith and R. J. Nicholas, *Energy & Environmental Science*, 2016, **9**, 962--970.
9. F. Mezrag and N. Bouarissa, *Materials Research*, 2019, **22**, e20171146.
10. C. d. M. Donegá, *Chem. Soc. Rev.*, 2011, **40**, 1512-1546.
11. G. T. Einevoll, *Phys. Rev. B*, 1992, **45**, 3410-3417.
12. C. Katan, N. Mercier and J. Even, *Chem. Rev.*, 2019, **119**, 3140–3192.
13. L. E. Brus, *J. Chem. Phys.*, 1984, **80**, 4403.
14. Y. Kayanuma, *Phys. Rev. B*, 1988, **38**, 9797.
15. H. L. Wells, *Chemie*, 1893, **3**, 195−210.
16. D. Weber, *J. Chem. Sci.*, 1978, **33**, 1443−1445.
17. D. Weber, *J. Chem.Sci.*, 1978, **33**, 862−865.
18. D. Weber, *J. Chem. Sci.*, 1979, **34**, 939−941.
19. C. K. Moller, *Nature*, 1958, **182**, 1436.
20. M.Natarajan, S.Ramdas and C.N.R.Rao, *Physics Letters A*, 1969, **29**, 528.
21. D. B. Mitzi, K. Chondroudis and C. R. Kagan, *J. Res. Dev. 2001*, 2001, **45**, 29−45.
22. D. B. Mitzi, C. A. Feild, W. T. A. Harrison and A. M. Guloy, *Nature*, 1994, **369**, 467−469.
23. A. Kojima, K. Teshima, Y. Shirai and T. Miyasaka, *J. Am. Chem. Soc.*, 2009, **131**, 6050–6051.
24. L. C. Schmidt, A. Pertegás, S. González-Carrero, O. Malinkiewicz, S. Agouram, G. M. Espallargas, H. J. Bolink, R. E. Galian and J. Pérez-Prieto, *J. Am. Chem. Soc.*, 2014, **136**, 850–853.

25. L. Protesescu, S. Yakunin, M. I. Bodnarchuk, F. Krieg, R. Caputo, C. H. Hendon, R. X. Yang, A. Walsh and M. V. Kovalenko, *Nano Lett.*, 2015, **15**, 3692–3696.
26. F. Zhang, H. Zhong, C. Chen, X.-g. Wu, X. Hu, H. Huang, J. Han, B. Zou and Y. Dong, *ACS Nano*, 2015, **9**, 4533–4542.
27. A. Dey, J. Ye, A. De, E. Debroye, S. K. Ha, E. Bladt, A. S. Kshirsagar, Z. Wang, J. Yin, Y. Wang and L. N. Quan, *ACS Nano*, 2021, **15**, 10775−10981.
28. J. Shamsi, A. S. Urban, M. Imran, L. D. Trizio and L. Manna, *Chem. Rev.*, 2019, **119**, 3296−3348.
29. Q. A. Akkerman and L. Manna, *ACS Energy Lett.*, 2020, **5**, 604–610.
30. J. A. Christians, P. A. M. Herrera and P. V. Kamat, *J. Am. Chem. Soc.*, 2015, **137**, 1530–1538.
31. J. S. Manser, J. A. Christians and P. V. Kamat, *Chem. Rev.*, 2016, **116**, 12956−13008.
32. V. M. Goldschmidt, *Naturwissensenschaffen*, 1926, **14**, 477-485.
33. L. Protesescu, S. Yakunin, S. Kumar, J. Bar, F. Bertolotti, N. Masciocchi, A. Guagliardi, M. Grotevent, v. Shorubalko, M. I. Bodnarchuk, C.-J. Shih and M. V. Kovalenko, *ACS Nano*, 2017, **11**, 3119−3134.
34. M. I. Saidaminov, A. L. Abdelhady, G. Maculan and O. M. Bakr, *Chem. Commun.*, 2015, **51**, 17658-17661.
35. J. H. Oh, Y. J. Eo, H. C. Yoon, Y.-D. Huh and Y. R. Do, *J. Mater. Chem. C,*, 2016, **4**, 8326-8348.
36. Q. A. Akkerman, G. Rainò, M. V. Kovalenko and L. Manna, *Nature Materials*, 2018, **17**, 394–405.
37. M. V. Kovalenko, L. Protesescu and M. I. Bodnarchuk, *Science*, 2017, **358**, 745–750.
38. V. K. Ravi, G. B. Markad and A. Nag, *ACS Energy Lett.*, 2016, **1**, 665–671.
39. Y. Ye, X. Run, X. Hai-Tao, H. Feng, X. Fei and W. Lin-Jun, *Chin. Phys. B*, 2015, **24**, 116302.
40. Y. Dong, T. Qiao, D. Kim, D. Parobek, D. Rossi and D. H. Son, *Nano Lett.*, 2018, **18**, 3716–3722.
41. P. C. Sercel and A. L. Efros, *Nano Lett.*, 2018, **18**, 4061–4068.
42. Kenichiro Tanaka, T. Takahashi, T. Ban, T. Kondo, K. Uchida and N. Miura, *Solid State Commun*, 2003, **127**, 619−623.
43. D. Canneson, E. V. Shornikova, D. R. Yakovlev, T. Rogge, A. A. Mitioglu, M. V. Ballottin, P. C. M. Christianen, E. Lhuillier, M. Bayer and L. Biadala, *Nano Lett.*, 2017, **17**, 6177–6183.
44. D. Rossi, X. Liu, Y. Lee, M. Khurana, J. Puthenpurayil, K. Kim, A. V. Akimov, J. Cheon and D. H. Son, *Nano Lett.*, 2020, **20**, 7321–7326.
45. N. Mondal, A. De, S. Seth, T. Ahmed, S. Das, S. Paul, R. K. Gautam and A. Samanta, *ACS Energy Letters*, 2021, **6**, 588-597.
46. M. A. Becker, R. Vaxenburg, G. Nedelcu, P. C. Sercel, A. Shabaev, M. J. Mehl, J. G. Michopoulos, S. G. Lambrakos, N. Bernstein, J. L. Lyons, T. Stöferle, R. F. Mahrt, M. V. Kovalenko, D. J. Norris, G. Rainò and A. L. Efros, *Nature*, 2018, **553**, 189−193.
47. P. Tamarat, M. I. Bodnarchuk, J.-B. Trebbia, R. Erni, M. V. Kovalenko, J. Even and B. Lounis, *Nature Materials*, 2019, **18**, 717–724.
48. M. I. Bodnarchuk, S. C. Boehme, S. t. Brinck, C. Bernasconi, Y. Shynkarenko, F. Krieg, R. Widmer, B. Aeschlimann, D. Günther, M. V. Kovalenko and I. Infante, *ACS Energy Lett.*, 2019, **4**, 63–74.

49. J. D. Roo, M. Ibáñez, P. Geiregat, G. Nedelcu, W. Walravens, J. Maes, J. C. Martins, I. V. Driessche, M. V. Kovalenko and Z. Hens, *ACS Nano*, 2016, **10**, 2071–2081.
50. Q. Zhong, M. Cao, Y. Xu, P. Li, Y. Zhang, H. Hu, D. Yang, Y. Xu, L. Wang, Y. Li, X. Zhang and Q. Zhang, *Nano Lett.*, 2019, **19**, 4151–4157.
51. C. Zhang, Q. Wan, L. K. Ono, Y. Liu, W. Zheng, Q. Zhang, M. Liu, L. Kong, L. Li and Y. Qi, *ACS Energy Lett.*, 2021, **6**, 3545–3554.
52. F. Krieg, S. T. Ochsenbein, S. Yakunin, S. t. Brinck, P. Aellen, A. Süess, B. Clerc, D. Guggisberg, O. Nazarenko, Y. Shynkarenko, S. Kumar, C.-J. Shih, I. Infante and M. V. Kovalenko, *ACS Energy Lett.*, 2018, **3**, 641–646.
53. V. K. Ravi, P. K. Santra, N. Joshi, J. Chugh, S. K. Singh, H. Rensm0, P. Ghosh and A. Nag, *J. Phys. Chem. Lett.*, 2017, **8**, 4988–4994.
54. S. Seth, T. Ahmed, A. De and A. Samanta, *ACS Energy Lett.*, 2019, **4**, 1610–1618.
55. D. P. Nenon, K. Pressler, J. Kang, B. A. Koscher, J. H. Olshansky, W. T. Osowiecki, M. A. Koc, L.-W. Wang and A. P. Alivisatos, *J. Am. Chem. Soc.*, 2018, **140**, 17760–17772.
56. A. Swarnkar, W. J. Mir and A. Nag, *ACS Energy Lett.*, 2018, **3**, 286–289.
57. Z.-J. Yong, S.-Q. Guo, J.-P. Ma, J.-Y. Zhang, Z.-Y. Li, Y.-M. Chen, B.-B. Zhang, Y. Zhou, J. Shu, J.-L. Gu, L.-R. Zheng, O. M. Bakr and H.-T. Sun, *J. Am. Chem. Soc.*, 2018, **140**, 9942–9951.
58. D. Ghosh, E. Welch, A. J. Neukirch, A. Zakhidov and S. Tretiak, *J. Phys. Chem. Lett.*, 2020, **11**, 3271–3286.
59. J. Y. Woo, Y. Kim, J. Bae, T. G. Kim, J. W. Kim, D. C. Lee and S. Jeong, *Chem. Mater.*, 2017, **29**, 7088–7092.
60. W. v. d. Stam, J. J. Geuchies, T. Altantzis, K. H. W. v. d. Bos, J. D. Meeldijk, S. V. Aert, S. Bals, D. Vanmaekelbergh and C. d. M. Donega, *J. Am. Chem. Soc.*, 2017, **139**, 4087–4097.
61. Y. Zhou, J. Chen, O. M. Bakr and H.-T. Sun, *Chem. Mater.*, 2018, **30**, 6589–6613.
62. S. D. Stranks, G. E. Eperon, G. Grancini, C. Menelaou, M. J. P. Alcocer, T. Leijtens, L. M. Herz, A. Petrozza and H. J. Snaith, *Science*, 2013, **342**, 341−343.
63. W. Liu, Q. Lin, H. Li, K. Wu, I. Robel, J. M. Pietryga and V. I. Klimov, *J. Am. Chem. Soc.*, 2016, **138**, 14954–14961.
64. T. Cai, H. Yang, K. Hills-Kimball, J.-P. Song, H. Zhu, E. Hofman, W. Zheng, B. M. Rubenstein and O. Chen, *J. Phys. Chem. Lett.*, 2018, **9**, 7079–7084.
65. G. Pan, X. Bai, D. Yang, X. Chen, P. Jing, S. Qu, L. Zhang, D. Zhou, J. Zhu, W. Xu, B. Dong and H. Song, *Nano Lett.*, 2017, **17**, 8005–8011.
66. S. Ji, X. Yuan, S. Cao, W. Ji, H. Zhang, Y. Wang, H. Li, J. Zhao and B. Zou, *J. Phys. Chem. Lett.*, 2020, **11**, 2142–2149.
67. J. Seo, J. H. Noh and S. I. Seok, *Acc. Chem. Res.*, 2016, **49**, 562–572.
68. M. Palabathuni, S. Akhil, R. Singh and N. Mishra, *ACS Appl. Nano Mater.*, 2022, **5**, 10097–10117.
69. TommasoAvellini, ChristopheLincheneau, FranciscoVera, SerenSilvi and AlbertoCredi, *Coordination Chemistry Reviews*, 2014, **263-264**, 151–160.
70. K. Wu, G. Liang, Q. Shang, Y. Ren, D. Kong and T. Lian, *J. Am. Chem. Soc.*, 2015, **137**, 12792–12795.
71. A. De, N. Mondal and A. Samanta, *J. Phys. Chem. C*, 2018, **122**, 13617−13623.
72. M. Li, S. Bhaumik, T. W. Goh, M. S. Kumar, N. Yantara, M. Grätzel, S. Mhaisalkar, N. Mathews and T. C. Sum, *Nature Communications*, 2017, **8**, 14350.
73. W. Shockley and H. J. Queisser, *Journal of Applied Physics*, 1961, **32**, 510-519.

74. R. T. Ross, *Journal of Applied Physics*, 1982, **53**, 3813−3818.
75. S. Sarkar, V. K. Ravi, S. Banerjee, G. R. Yettapu, G. B. Markad, A. Nag and P. Mandal, *Nano Lett.*, 2017, **17**, 5402–5407.
76. S. S. Lim, D. Giovanni, Q. Zhang, A. Solanki, N. F. Jamaludin2, J. W. M. Lim, N. Mathews, S. Mhaisalkar, M. S. Pshenichnikov and T. C. Sum, *Sci. Adv.*, 2019, **5**, 3620.
77. Q. Shen, T. S.Ripolles, J. Even, Y. Zhang, C. Ding, F. Liu, T. Izuishi, N. Nakazawa, T. Toyoda, Y. Ogomi and S. Hayaseb, *J. Energy Chem.*, 2018, **27**, 1170−1117.
78. Y. Shynkarenko, M. I. Bodnarchuk, C. Bernasconi, Y. Berezovska, V. Verteletskyi, S. T. Ochsenbein and M. V. Kovalenko, *ACS Energy Lett.*, 2019, **4**, 2703–2711.
79. X. Zheng, Y. Deng, B. Chen, H. Wei, X. Xiao, Y. Fang, Y. Lin, Z. Yu, Y. Liu, Q. Wang and J. Huang, *Adv.Mater.*, 2018, **30**, 1803428.
80. V. K. Ravi, S. Saikia, S. Yadav, V. V. Nawale and A. Nag, *ACS Energy Lett.*, 2020, **5**, 1794–1796.
81. A. Dutta, S. K. Dutta, S. D. Adhikari and D. N. Pradhan, *Angew.Chem.Int.Ed.*, 2018, **57**, 9083–9087.

CHAPTER 2

Materials and Experimental Methods

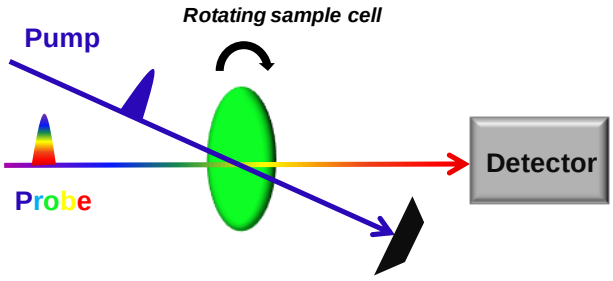

Overview

This chapter presents the strategies of synthesis of the $APbX_3$ NCs and the instruments employed for their optical and microscopic characterization. Steady state absorption, emission and different time-resolved techniques [particularly, time-correlated single photon counting (TCSPC), femtosecond transient absorption (fs-TA) and PL up-conversion] have been discussed in detail. The working principle of these techniques, different optical and electronic components and optical layout of the setups are discussed. Methodologies for the synthesis and characterization of various perovskite NCs of different compositions have also been discussed. Overall, this chapter provides a brief idea about making of these NCs and their spectroscopic and microscopic characterization following a range of basic and advanced techniques.

2.1. Materials/Chemicals

Cs_2CO_3 (99.99%, trace metal), lead oxide (PbO, 99.999%, trace metals basis), lead acetate trihydrate (99.999% trace metals basis), $PbCl_2$ (99.99%, trace metal), $PbBr_2$ (99.9%, trace metal), $MgCl_2$ (anhydrous, >98%), $MgBr_2$ (98%), MgO (97%), formamidinium acetate (99%), 1,3-dichloro-5,5-dimethylhydantoin (DCDMH, 68%), 1,3-diiodo-5,5-dimethylhydantoin (DIDMH, >96%), N-iodosuccinimide (95%), diphenyl phosphoryl chloride ($(PhO)_2POCl$, 99%), chloroform-d ($CDCl_3$, 99.8 atom% D), 1-octadecene (ODE), oleic acid (OA, 90%), oleylamine (OAm, 70%), trioctylphosphine (TOP, 97%) and methyl acetate (anhydrous, 99.5%) were purchased from Sigma-Aldrich and were used without any purification. Methylamine (2M solution in tetrahydrofuran) and 1,3-dibromo-5,5-dimethylhydantoin (DBDMH, 98%) were purchased from TCI Chemicals and Lancaster, respectively. Hexane (HPLC & Spectroscopy) and acetonitrile (ACN, dried) were bought from Finar and Merck Chemicals, respectively. All chemicals including the solvents were used without any further purification.

2.2. Synthesis of Perovskite NCs

We have employed two different strategies for the preparation of perovskite NCs of different compositions following hot injection method of synthesis. In *two-precursor* method of synthesis, PbX_2 (X= Cl, Br or I) was used as a source of both lead and halogen, while in *three-precursor* method separate lead and halide precursors were employed. The advantage of the later method of synthesis will be discussed in appropriate places of the subsequent chapters. It is to be noted in this context that in Chapter 3 the NCs were prepared following the conventional *two-precursor* method, while *three-precursor* method was adopted for the NCs in Chapter 4, Chapter 5 and Chapter 6.

2.2.1. Synthesis of $CsPbX_3$ NCs (X= Cl and Br) Following Two-precursor Method

Preparation of Cs-Oleate: Cs-Oleate was prepared by following a reported procedure by Protesescu et al. with minor modification.[1] Cs_2CO_3 (0.16 g) was taken in a 50 mL two-neck round-bottom (RB) flask containing 6 mL ODE and 0.5 mL OA. It was then degassed at room temperature for 5 min and dried under vacuum at 120^0C for 30 min. The reaction medium was then kept under N_2 atmosphere at the same temperature until all Cs_2CO_3 reacted with OA to from a clear solution of Cs-oleate. As Cs-oleate precipitates out at room temperature, it was preheated at 120^0C before use.

Preparation of $CsPbBr_3$ and $CsPbCl_3$ NCs: The NCs were synthesized by the t*wo-precursor* hot-injection method following a reported procedure.[1] In brief, 0.069 g $PbBr_2$ (or 0.052 g $PbCl_2$) was taken in a 50 mL two-neck RB containing 5 mL ODE, 0.55 mL OA and 0.55 mL OAm. The mixture was then degassed at room temperature for 5 min and vacuum dried at 120^0C for 45 min. Then the temperature was increased to 165^0C (185^0C for $CsPbCl_3$) under N_2 atmosphere and once the reaction attained the desired temperature, 0.45 mL of Cs-oleate (preheated at 120^0C) was quickly injected into the reaction medium, and after 5 s (30 s for $CsPbCl_3$) the reaction mixture was quenched in an ice-water bath. 1 mL TOP was injected at 120^0C for better solubility of $PbCl_2$ in the reaction medium. The synthesized NCs were precipitated from the crude solution through centrifugation at 7k rpm for 8 mins. The supernatant liquid was drained out and the resulting precipitate was dispersed in hexane for further studies.

2.2.2 Synthesis of Mg-doped $CsPbBr_3$ and $CsPbCl_3$ NCs

Preparation of MgX_2 stock solution: 0.30 mmol MgX_2 (0.055 g $MgBr_2$ or 0.029 g $MgCl_2$) was dissolved in 4 mL OAm by heating the mixture at 120^0C for 2h to obtain an opaque solution of MgX_2-OAm.

Post-synthetic treatment of the as-synthesized NCs: 5 µL of the above solution was diluted in 50 µL hexane. 30µL of this solution was added to 0.015 µM stirred solution (550 µL) of $CsPbX_3$ NCs in hexane taken in a 25 ml single-neck RB with a magnetic bead (as shown in scheme 3.1A). The solution was stirred under ambient condition for 1h, which was found to be the ideal time for completion of the treatment. 500 µL of the resulting solution was pipetted out, mixed with 1 mL methyl acetate and immediately centrifuged (at 13k rpm) for 5 mins. The supernatant liquid containing excess ligands and salts was discarded and the small residue of purified NCs at the bottom was dispersed in hexane. These are the high-quality Mg-doped $CsPbX_3$ NCs with bright emission and high robustness under ambient condition.

2.2.3. Synthesis of $APbX_3$ (A= Cs, MA and FA; X= Cl, Br and I or their mixtures) NCs Following *Three-precursor* Method

The first step in synthesis of the NCs by *three-precursor* hot-injection approach was preparation of the oleate salt of the corresponding ‘A’ cation which was injected into the reaction medium containing the Pb and halide precursors at desired reaction temperature.

2.2.3.1. Preparation of oleate salt of A-site cations

Preparation of Caesium-oleate (Cs-Oleate): Cs-oleate was prepared by following a reported procedure with slight modification.[1] In this method, 0.16 g of Cs_2CO_3, 6 mL of ODE and 0.55 mL of OA were taken in a 50 mL two-necked round-bottom (RB) flask, degassed for 5 min at room-temperature and heated under vacuum at 120°C for 1 h. The reaction mixture was then kept under N_2 atmosphere with constant heating until all Cs_2CO_3 reacted with OA to form a transparent solution of Cs-oleate complex. To avoid precipitation at room-temperature, it was preheated at 120°C before use.

Preparation of Formamidinium-oleate (FA-oleate): FA-oleate was also prepared by following a reported method with some modifications.[2] In brief, formamidinium acetate (0.26 g) was loaded into a 50 mL double-necked RB flask along with 6 mL of ODE and 4 mL of OA (for $FAPbI_3$) or 10 mL OA (for $FAPbBr_3$) or 4 mL OA and 6 mL ODE (for $FAPbCl_3$) and then degassed for 5 minutes at room-temperature under vacuum. It was then heated under N_2 atmosphere at 120ºC until the entire solution became clear indicating the formation of FA-oleate. The resultant solution was finally dried at 45-50ºC under vacuum for 10 min for removing moistures.

Preparation of Methylammonium-oleate (MA-oleate): Preparation of MA-oleate was quite straightforward and it did not require high temperature heating. It was obtained by thoroughly mixing 200 µL of methylamine (2M in tetrahydrofuran) with 1 mL OA (for $MAPbI_3$) or 250 µL methylamine with 2.5 mL of OA (for $MAPbBr_3$ and $MAPbCl_3$) at room-temperature.

2.2.3.2. Synthesis and Purification of $APbI_3$ (A= Cs, MA and FA) NCs

Synthesis of $CsPbI_3$ NCs: 0.072 g (0.188 mmol) lead acetate trihydrate and 0.214 g (0.564 mmol) DIDMH were taken in a double-necked RB flask along with 1 mL OA and 1 mL OAm as capping ligands and 5 mL ODE as solvent. The entire mixture was degassed at room-temperature for 5 min and then heated at 130°C under N_2 atmosphere until a clear deep brownish solution formed, indicating the formation of oleylammonium iodide.[3] The reaction temperature was then increased to 210°C sharply and quickly injected 0.5 mL preheated (at 120°C) Cs-oleate solution into the reaction mixture containing lead and halide precursors followed by rapid quenching after 5 seconds of the reaction in an ice-water bath (Figure 2.1). When the crude solution came to the room-temperature it was centrifuged at 3.5k rpm for 10 min to remove the larger particles and

possible aggregates and the supernatant solution was collected. Then anhydrous MeOAc as anti-solvent was added drop-wise into the supernatant until turbidity appeared and then quickly centrifuged at 7k rpm for 3 min. The supernatant was discarded and the precipitate was finally dispersed in hexane for further studies.

Synthesis of (FA)PbI_3 NCs: Briefly, 0.072 g (0.188 mmol) lead acetate trihydrate and 0.214 g (0.564 mmol) DIDMH were taken in a double-necked RB flask along with 1.6 mL OA and 0.8 mL OAm as capping ligands in 5 mL ODE as solvent. The precursor mixture was then dried for 5 min at room-temperature and subsequently heated at 130°C under N_2 environment until similar deep brownish solutions appeared. After complete solubilization of the precursors the reaction temperature was lowered to 85°C and then 2 mL FA-oleate solution (preheated at 100°C) was swiftly injected into the reaction mixture. After 10 seconds, the solution was quenched rapidly in an ice-water bath to stop the further reaction. The crude solution was centrifuged at 12k rpm for 5 min, the supernatant was discarded and the precipitate was dispersed in toluene. Then dried ACN (volume ratio of toluene: ACN = 3:1) was added to destabilize the colloid, followed by centrifugation at the same configurations and the precipitate was dissolved in toluene. This process was repeated one more time and the final precipitate was dissolved in hexane for further studies.

Synthesis of (MA)PbI_3 NCs: The synthetic strategy for (MA)PbI_3 NCs was quite similar to that of (FA)PbI_3 NCs stated above. The only difference was instead of FA-oleate, MA-oleate solution prepared previously was injected. Specifically, 200 µL methylamine solutions (2M in THF) was dissolved in 1 mL of OA at room-temperature and injected at 85°C for the formation of (MA)PbI_3 NCs.

2.2.3.3. Synthesis and Purification of $APbX_3$ (A= Cs, MA and FA; X= Cl, Br or mixtures) NCs

The oleate salts of the A-site cations were prepared following the methods described in section 2.2.3.1.

Preparation and purification of the $CsPbX_3$ (X= Cl and Br) NCs: In a 50 mL double-neck RB, 0.564 mmol of DBDMH (for $CsPbBr_3$ NCs) or DCDMH (for $CsPbCl_3$ NCs) and 0.188 mmol of PbO were loaded along with 2 mL each of OA and OAm as capping ligands and 5 mL ODE as solvent. The entire mixture was degassed under vacuum at RT for 5 min to remove possible moisture in the mixtures and then heated at 130°C under N_2 environment until a clear solution formed. The reaction temperature was then increased to

210°C and 0.5 mL preheated (at 120°C) Cs-oleate solution was swiftly injected into the reaction medium containing lead and halide precursors. After few seconds (~20 sec for $CsPbBr_3$ NCs and 30 sec for $CsPbCl_3$ NCs), the reaction system was rapidly cooled in an ice-water bath.

The mixed-halide $CsPb(Cl/Br)_3$ and $CsPb(Br/I)_3$ NCs were also prepared following a similar procedure employing two different halide precursors. The exact amount of halide precursors used for the synthesis of different systems is listed in Table A5.5 for convenience.

Purification: The crude reaction product was cooled down to RT, 4 mL hexane was added to it and then centrifuged at 7k rpm for 8 min. The supernatant containing possible unreacted precursors (if any) and solvent was drained out and the precipitate was then dispersed in hexane. After 15 min, the colloidal dispersion was again centrifuged at 7k rpm for 5 min to remove larger particles and possible aggregates and the supernatant solution was collected for further studies. The purification procedure is quite different only for the mixed-halide $CsPbBrI_2$ NCs. In this case, the crude reaction mixture was centrifuged at 3k rpm for 10 min and the precipitate containing larger particles and possible aggregates was removed. Then anhydrous MeOAc as anti-solvent was added drop-wise into the supernatant until turbidity appeared and then quickly centrifuged at 7k rpm for 3 min. The supernatant was discarded, and the precipitate was finally dispersed in hexane for further studies.

$MAPbX_3$ (X= Cl and Br) NCs: In brief, 0.188 mmol of PbO and 0.564/0.282 mmol of DBDMH/DCDMH for the synthesis of $MAPbBr_3$/$MAPbCl_3$ NCs were loaded into a double-neck 50 mL RB along with 1.5 mL of OA and 0.5 mL of OAm (for $MAPbBr_3$) or 2 mL of OA and 0.4 mL of OAm (for $MAPbCl_3$) in 5 mL of ODE. The reaction mixture was degassed at RT under vacuum for 5 min and after complete solubilization of the reaction mixture at 130°C, the temperature was set to 165°C (for $MAPbBr_3$) or 95°C (for $MAPbCl_3$) under N_2 atmosphere. When the reaction temperature reached the desired temperature, MA-oleate (250 μL of methylamine in 2.5 mL of OA) was swiftly injected into reaction medium, followed by rapid quenching (after 20 sec for $MAPbCl_3$) of the reaction mixture in an ice-water bath to stop the growth of the NCs.

Purification: For $MAPbBr_3$ NCs, the crude product was brought to RT, 3 mL of MeOAc was added to it and centrifuged at 7k rpm for 6 min. The supernatant containing unreacted precursors and ODE was discarded and the precipitate was dispersed in hexane. After 15 min, it was again centrifuged at 7k rpm for 5 min and the supernatant was collected for further studies. For $MAPbCl_3$ NCs, when the crude product reached RT, it

was centrifuged at 12k rpm for 7 min after addition of equal volume of MeOAc into it. The supernatant was discarded, and the precipitate was dispersed in hexane for further experiments.

$FAPbX_3$ (X= Cl and Br) NCs: The synthetic strategy and purification procedure for $FAPbX_3$ NCs was quite similar to that employed for the $MAPbX_3$ NCs described above. The ligand ratio and reaction temperature used for the preparation of these NCs are listed in Table 1. The only difference in this case was that instead of MA-oleate, 2.5 mL of FA-oleate solution preheated at 100°C was swiftly injected into the reaction medium at the desired temperature for formation of the $FAPbX_3$ NCs.

Thus our 1,3-dihalo-5,5-dimethylhydantoin (DXDMH) mediated *three-precursor* hot injection method of synthesis of $APbX_3$ NCs can schematically represented as follows.

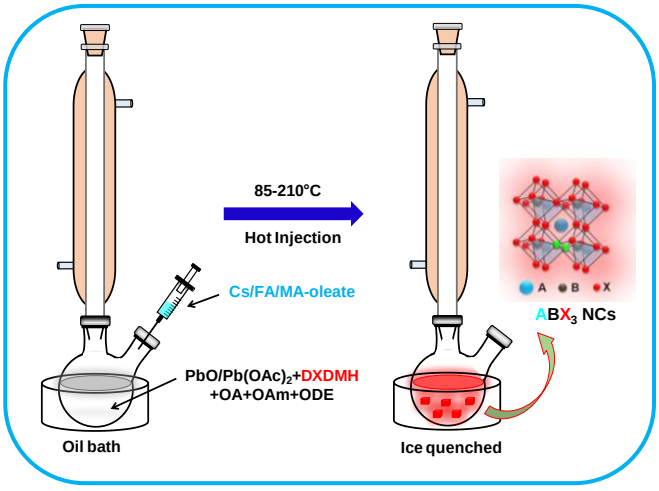

Figure 2.1. *Schematic representation of DXDMH-mediated direct synthesis of $APbX_3$ NCs.*

2.2.3.4. Synthesis of $CsPbCl_3$ NCs using $(PhO)_2POCl$ as Chloride Precursor following *Three-precursor* Approach

Synthesis of $CsPbCl_3$ NCs: In a typical synthesis, 0.2 mmol $Pb(OAc)_2 \cdot 3H_2O$ and 0.05 mmol Cs_2CO_3 were taken in a two-necked round bottom (RB) flask along with 0.3 mL OA and 1.0 mL OAm as capping ligands and 5 mL ODE as solvent. The mixture was then degassed at room-temperature for 5 min and then heated at 120°C under vacuum until a transparent clear solution was formed. The reaction temperature was then increased to 220°C sharply and 1.8 mmol (~375 µL) $(PhO)_2POCl$ was quickly injected

into the reaction mixture containing lead and cesium precursors. Immediate turbidity in the reaction mixture indicated the formation of $CsPbCl_3$ NCs, which were then rapidly quenched after 20 seconds in an ice-water bath. When the solidified crude reaction product came to RT it became liquid and then it was mixed with 2 mL hexane and 4 mL MeOAc and quickly centrifuged at 7k rpm for 6 min. The supernatant solution containing unreacted precursors and ligands was discarded and the precipitate was cleaned and then dispersed in 2 mL hexane for further studies.

Repeated washing of the NCs:

For washing with MeOAc (or hexane), the hexane dispersed solution of the NCs was mixed with MeOAc in 1:1 ratio and centrifuged at 7k rpm for 5 min. The supernatant was discarded, and the precipitate was redispersed in hexane. This process was repeated multiple times to obtain washed samples with desired number of cycles. For washing with hexane similar procedure was followed employing hexane in place of MeOAc.

2.2.3.5. RT halide exchange reaction

The halide exchange reactions were performed under ambient condition on colloidal dispersion of pre-synthesized $CsPbBr_3$ NCs. For this purpose, a saturated solution of DCDMH/DIDMH was prepared in hexane containing OAm and OA. Very small amount (few µL) of the solutions was mixed with a dilute colloidal solution of $CsPbBr_3$ NCs and shaken vigorously for the anion exchange reactions. An instant change in emission color under UV light (green-to-blue for DCDMH and green-to-red for DIDMH) indicated successful halide exchange reactions.

2.2.3.6. RT A-site cation exchange

For post-synthetic cation exchange reaction at RT, 100 µL of FA-oleate solution was diluted in 1 mL hexane and added to $CsPbBr_3$ NCs dispersion (few mM) under stirring and monitored the absorption and PL spectra at different time intervals by pipetting out small aliquots from the reaction mixture.

2.3. Instrumentation

2.3.1. Steady State Optical Measurements

Steady state UV-Vis absorption and emission of samples were measured in a dual-lamp spectrophotometer (Cary 100, Varian) and spectrofluorometer (Fuorolog-3, Horiba Jobin Yvon), respectively. A deuterium and tungsten lamp were used as UV and visible source,

respectively in the spectrophotometer and the transition from one lamp to other occurs at ~350 nm. While Xe-arc lamp (450 W) was used as the excitation source in the spectrofluorometer. In both instruments, a photomultiplier tube (PMT) was used as the detector. Baseline was corrected for each measurement in spectrophotometer to eliminate any possible absorption from impurities in solvent and the cuvette. The fluorescence was collected at right angle with respect to the excitation light to minimize possible contribution of incident beam in fluorescence. A 3 mL quartz cuvette of 1 cm path length was used for each measurement and optical density (absorbance) at the excitation wavelength was kept < 0.1 to avoid inner filter effects.

2.3.2. Time Correlated Single Photon Counting (TCSPC)

Basic Principle and Instrumental Components

TCSPC is a technique that works on statistical averaging method to give lifetime of a system in its excited state. In TCSPC, the probability of detecting a single photon at time 't' after photoexcitation of a sample by pulsed laser indicates fluorescence intensity of the sample at that instance.[4] The repetition rate of the diode laser used should be very high (~MHz) to trigger sufficient number of such photon events in a particular time so that statistical averaging could give more precise data with very low standard deviation.[5] A TCSPC instrument acts like a stopwatch which can work in two ways: START signal can either be triggered by a photon from excitation pulse (forward mode operation) or a photon from fluorescence of the sample does it (reverse mode operation). Schematic representation of different components of a TCSPC setup working in reverse mode is shown in Figure 2.2. A pulsed laser excites the sample of interest and at the same time it sends an excitation signal to constant faction discriminator (CFD1). The fluorescence photons from the sample pass through a monochromator and polarizer followed by their detection in PMT and directed to a CFD2. The CFD counts time corresponding to the incoming photons of the sample fluorescence and subsequently sends a signal to the time-to-amplitude converter (TAC) which initiates charging of a capacitor unit inside the TAC module. This charging corresponds to START of the experiment until it is terminated with another pulse. The photon of the excitation laser after passing through CFD1 is directed to TAC to stop charging of its capacitor (STOP pulse). The STOP pulses were delayed electronically so that they do not enter TAC before the START pulse. The difference of START and STOP pulse timing in TAC is then converted into voltage pulse. This voltage output of TAC is then amplified in programmable gain amplifier

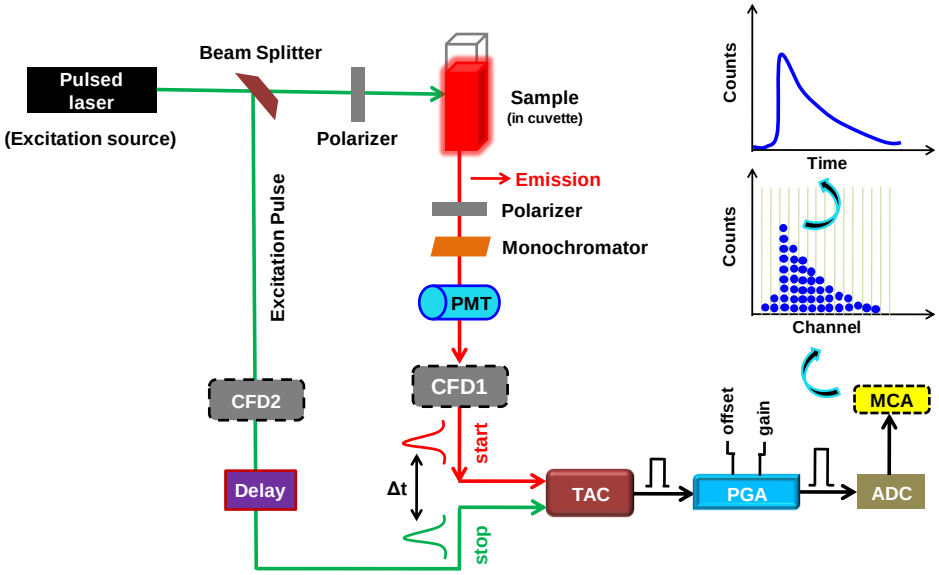

Figure 2.2. *Different electronic and optical components of TCSPC set up.*

(PGA) and eventually converted into digital signal through analog-to-digital converter (ADC). This numerical digital value is stored as a single photon counting event in a multi-channel analyzer (MCA). This process is repeated multiple times and each such numerical value of photon counting is stored in MCA which is eventually represented as histogram of fluorescence intensity as a function of delay time. One can do the measurement in forward mode also in which the START pulse comes from the laser and fluorescence photon act as the STOP pulse. However, the major issue of this measurement comes when the sample has long fluorescence lifetime. High repetition rate of laser keep generating START pulses and TAC remains active but due to slow detection rate of fluorescence photons no STOP pulses come to TAC to discharge its electronics.[4] Thus capacitor remains unnecessarily busy many times due to no STOP pulses and this decreases the signal processing efficiency.[4, 5] Further details about the TCSPC setup can be found elsewhere.[6]

Fluorescence Lifetime Measurements

In our laboratory, TCSPC spectrometer (Horiba Jobin Yvon IBH) was used for measuring PL lifetime of the LHP NCs operating at magic angle polarization (54.7º) of the PL with respect to vertical polarization of the excitation laser to ensure no contribution of fluorescence anisotropy.[4] Diode laser sources of 375 nm, 404 nm and 485 nm were used as excitation of different LHP NCs. PicoBrite lasers of 1 MHz repetition rate and pulse width of 60-85 ps were used and a micro-channel plate (MCP) photomultiplier (from Hamamatsu R3809U-50) was used as the detector. All the experiments were performed in

solution and the instrument response function (IRF) was measured using a dilute scatterer (Ludox) solution in water.

The PL decay profiles were analyzed by nonlinear least-squares iterative fitting procedure using IBH DAS6 (version 2.2) decay analysis software. The photoluminescence decay curves were fitted to the following equation and the quality of fit was judged by χ^2 value close to 1.

$$I(t) = \sum_{i=1}^{n} \alpha_i e^{-t/\tau_i}$$

where, α_i and τ_i are the amplitude and lifetime of the i^{th} component, respectively. The fractional contribution of the i^{th} component to the total steady state intensity was estimated by the following equation.

$$a_i = \frac{\alpha_i \tau_i}{\sum_{i=1}^{n} \alpha_i \tau_i}$$

The average PL lifetime was calculated by using the equation, $\tau_{av} = \sum_{i=1}^{n} a_i \tau_i$

2.3.3. Femtosecond Optical Spectroscopy

An Overview

Progress of science is directly linked with the development of techniques capable of scaling the limitations of human senses in the investigation of natural phenomena. Human eye can resolve process occurring in time scale no longer than 50×10^{-3} sec. Hence it is quite obvious that, in order to gain insight into faster dynamical processes in real time, one needs a powerful tool that uses ultra short illumination time in order to essentially 'freeze' the evolution of the object under study. Thus one can capture snapshots of different associated processes of the event of interest.

Several processes like chemical bond formation and dissociation, photoinduced dynamical processes of molecules, atoms, nano or bulk particles typically occur in a time scale of ~10^{-12} to 10^{-15} sec, which is beyond the time resolution of the TCSPC technique. Hence, to probe these processes femtosecond optical spectroscopy, a technique having time resolutions of few fs to ps is employed. Since the electronic response is not fast enough to probe these ultrafast processes, most of such slow electronic components in TCSPC are replaced by optics, more specifically, laser technology comes into forefront to interrogate these processes in these ultrashort spatial and temporal domain.[7] Thanks to a comparable pulse width of laser with the timescale of associated dynamics in these processes one can probe such phenomena. Development of ultrafast spectroscopy was

facilitated after the introduction of femtosecond laser. Femtosecond pump-probe (also known as transient absorption), fluorescence (PL) up-conversion, femtosecond Z-scan, and degenerate four-wave mixing are some widely used advanced ultrafast techniques that people use to interrogate faster dynamics of various chemical processes.[8-10] Ultrafast processes like charge carrier transport, carrier recombination and energy transfer processes can be investigated employing the ultrafast techniques. Understandings of these processes are crucial from the point of view of designing efficient devices for solar energy conversion, photo-catalysis and light-emitting applications.

Usually femtosecond laser pulses are generated through 'mode-locking' in which laser cavity allows only certain frequencies to form standing waves following constructive interference which induces phase difference among longitudinal modes inside the cavity to generate pulses of short duration. Pulse width (τ) of a laser is given by $\tau = 1/N\Delta\nu$, where $\Delta\nu$ corresponds to difference in frequency between two longitudinal modes and N is the total number of modes.[7] Short pulses can be generated by increasing the frequency spacing between two modes by decreasing the length of laser cavity and/or introducing a gain medium with large bandwidth that increases the number of lasing modes (N) inside the cavity. Ti:sapphire is widely used as main laser source in ultrafast spectroscopy owing to its large gain bandwidth of the lasing medium.

During my Ph.D., I have mostly used femtosecond pump-probe technique with occasional use of the PL up-conversion technique. In the following sections, we will discuss about these two ultrafast tools with particular emphasis on their optical components, key functions, overall optical layout and arbitrary spectral features.

2.3.2.1. Femtosecond Transient Absorption Measurement

Basic Working Principle

In fs-TA technique, typically a high power laser pulse of a selective wavelength is used to excite the system of interest and this excitation pulse is known as 'pump' pulse. The photoinduced transients generated by the action of the pump laser are interrogated after a certain time with a relatively weak broad band (white light continuum) pulse, known as 'probe' pulse (Figure 2.3).[8, 9] Thus TA study is also known as 'pump-probe' measurement where variation of pump-probe delay gives rise to spectral and temporal evolution of the photoinduced transients. A complete TA measurement is essentially a combination of such individual responses of a system as a function of probe delay and it thus provides relaxation mechanism of the transient species in ultrafast timescale. A mechanical

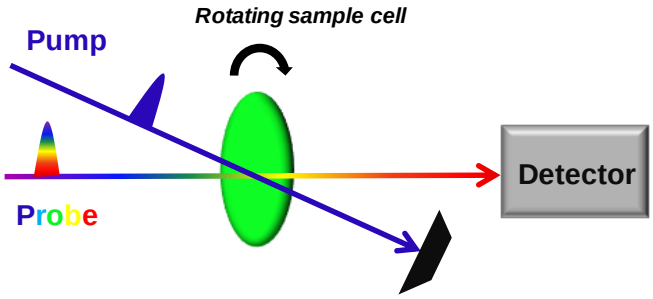

Figure 2.3. *Basic working principle of fs-TA measurement.*

chopper is used to block the pump path for such individual experiments. Difference in intensity of the transmitted probe beam when the sample is in excited state (pump on) and ground state (pump off) is then used measuring differential absorbance (ΔA) of the sample as a function of wavelength and probe delay (equation 2.1).[11]

Optical Components

The fs-TA setup (Spectra Physics, USA) used in this study consists of the following major components, A) fs Ti:sapphire oscillator (MaiTai HP), B) Nd:YLF (second harmonics) nanosecond laser (Empower 30), C) Regenerative Ti:sapphire amplifier (Spitfire ACE), D) optical paramagnetic amplifier with optical frequency mixture (TOPAS prime) and E) spectrometer (Excipro, CDP systems, Russia). The positioning and optical layout of the entire setup is schematically shown below (Figure 2.4).

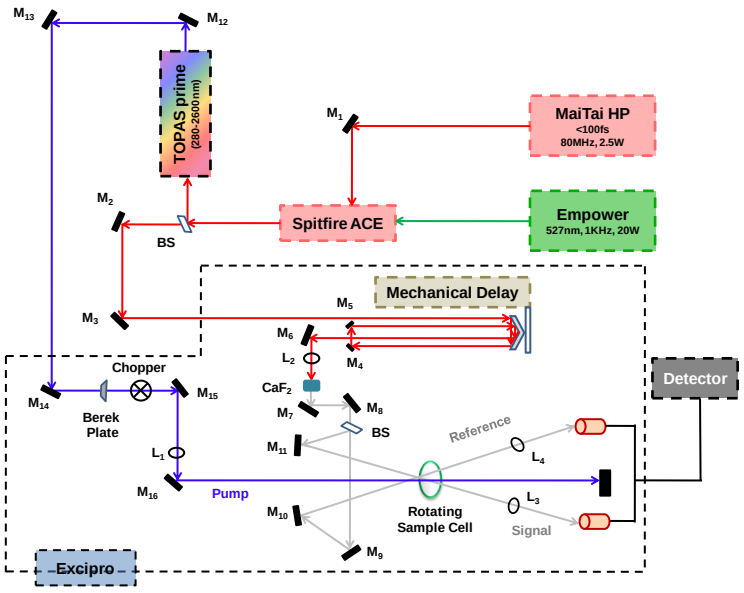

Figure 2.4. *Schematic showing overall optical layouts of the TA setup our school.*

Ti:sapphire oscillator (MaiTai HP)

This is a solid state femtosecond oscillator operated based on 'Kerr-lens mode-locking' techniques. The lasing medium in Ti:sapphire laser is Ti^{3+} doped crystalline sapphire (Al_2O_3), which is a four-level lasing medium.[12] The vibrational energy levels of Al_2O_3 strongly couples with electronic energy states of the dopant Ti^{3+} making the doped crystal as active medium with large bandwidth susceptible for generation of short femtosecond pulses.[12] A broad absorption of Ti:sapphire with peak maxima at around 500 nm further makes this active medium highly coveted for optical pumping by diode lasers. Moreover it has a wide emission in the range of 690-1040 nm peaking at 800 nm (Figure 2.5A, B).[12] A large Stokes shift makes this an efficient lasing medium through reduction of reabsorption losses.

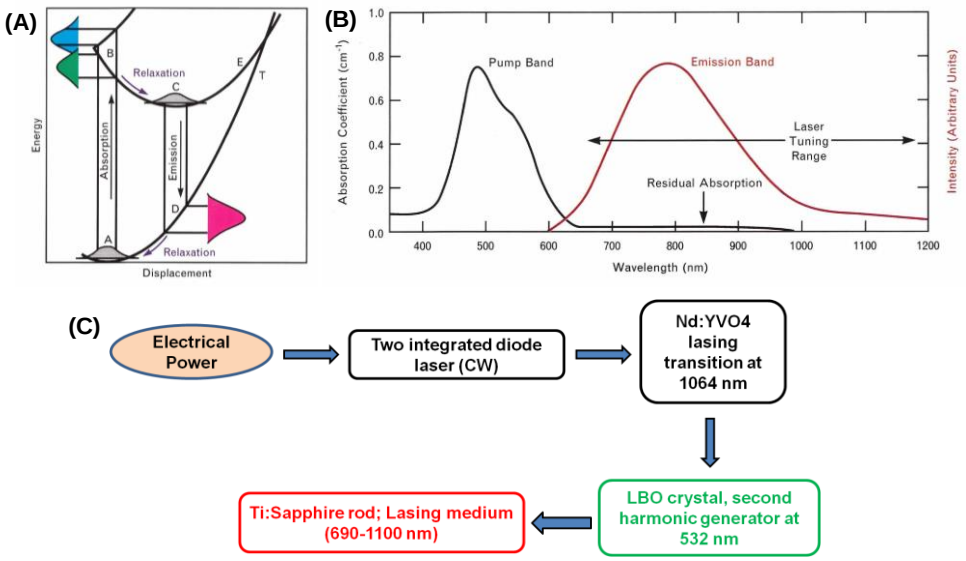

Figure 2.5. *(A) Electronic energy levels and (B) absorption and emission spectra of Ti^{3+}:sapphire lasing medium. (C) Different components inside MaiTai HP.*

The model name of our fs Ti:sapphire oscillator is MaiTai HP (from Spectra Physics, USA), which operates at a repetition rate of 80 MHz and produces pulses of <100 fs with a central wavelength of 800 nm. It is the seed laser of the TA setup with a pulse power and energy of 2.5 W and 30 nJ, respectively. The second harmonics (at 532 nm) of a Nd:YVO4 is used as pump source for MaiTai HP. Its pumping directions and integrated components are shown below (Figure 2.5C).

Ultrafast Ti:sapphire Amplifier (Spitfire ACE)

In order to achieve a range of excitation wavelengths and broad band probe beam for TA measurement, the seed laser has to undergo multiple nonlinear optical processes. However, it is not possible with a seed laser of very low power (~30 nJ). Hence amplification in energy of the seed laser is required before participating in nonlinear processes. Direct amplification of the seed laser is however difficult as peak power of this laser is sufficiently high to damage gain medium of amplifier. Two methods can be adopted in this regard either increasing the beam diameter or stretching pulse width of the laser. Increasing beam diameter of the seed laser requires bigger optical paths and larger gain medium, thus increasing the cost of the set up with additional optical losses. Therefore stretching the seed laser beam before amplification followed by compression of the amplified pulse is known to be a more advantageous technique and this is what we actually do (Figure 2.6A).

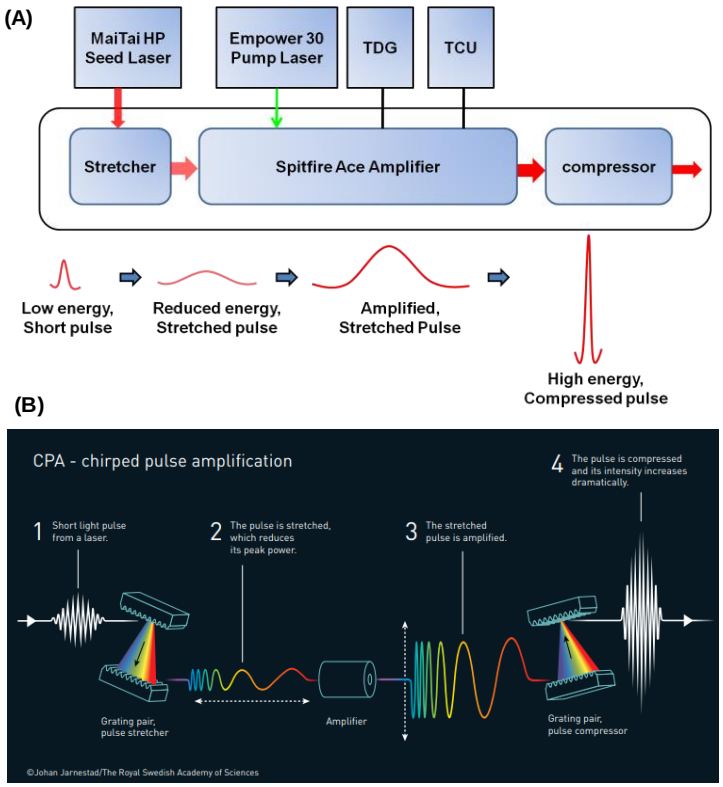

Figure 2.6. *(A) Schematic showing associated components and amplification steps inside Spitfire ACE. The timing and delay generator (TDG) synchronizes communication between optics and electronics of the amplifier while the temperature control unit (TCU) controls temperature of the active medium. (B) Processes associated with chirped pulse amplification in Spitfire ACE. Adopted from reference 14.*

The seed laser output is stretched from <100 fs to ~300-400 fs by using an optical grating pair which imparts positive dispersion on the laser (redder part of the laser moves faster). There are two ways for amplification of the stretched pulse multipass amplification and regenerative amplification (chirped pulse amplification).[13] The second one is however comparatively little easy as focusing of higher number of roundtrip beams onto a tiny spot of Ti:sapphire (inside the amplifier). In case of regenerative amplification, a laser pulse from the seed laser train is captured by a 'Pockels cell' (a birefringent material) before entering into Ti:sapphire cavity which changes polarization of the laser if a high voltage is applied. The pump beam (from Empower 30) and the stretched seed laser are tightly focused onto the Ti:sapphire crystal so that a spatial overlap is maintained between them. The seed beam passes through the amplifier cavity and once the gain medium saturates upon optical pumping, a second voltage is applied into another Pockels cell so that all the stored energy inside the Ti:sapphire cavity comes out with the amplified seed laser. It is then passed through an another grating pair having negative dispersion (bluer part of the beam moves faster) to compress the amplified pulse with higher energy (~4.2 mJ). Timing of the Pockels cells are highly important to achieve maximum energy of the amplified pulses. Our regenerative amplifier (Spitfire ACE) produces the amplified output at 800 nm with 1kHz repetition rate with a pulse width of 100-120 fs. Figure 2.6B shows different steps involved in chirp pulse amplification of the seed laser.

Empower 30

It is a Q-switched laser which produces nanosecond pulses for excitation of Ti:sapphire module in the amplifier (Spitfire ACE). Here Nd:YLF is used as the active medium for the generation of pulsed laser which is again pumped by an integrated diode laser. The output (1054 nm) of Nd:YLF is then frequency-doubled using a LBO crystal with the help of nonlinear optical processes and the final green laser peaking at 527 nm is used for excitation source of regenerative amplifier. This is a high power (~20 W) laser connected with an external chiller to always maintain temperature of the Nd-laser at ~27°C.

Optical Paramagnetic Amplifier (OPA, TOPAS Prime)

This is possibly the most complex optical component of the TA system which is associated with several nonlinear optical processes. The pump laser pulse of desired wavelength is generated here and a broadly tunable excitation wavelength of 280-2600

nm can be generated from the amplified 800 nm laser. A major portion (~80%) of the amplified beam from regenerative amplifier is directed towards TOPAS prime for generation of pump beam. A small portion (~20%) of the 800 nm laser is passed through sapphire crystal to obtain white light, which acts as seed laser inside TOPAS prime. This white light is then mixed with pump signal in a BBO (β-Barium borate) crystal to generate a weak idler (I) and amplified signal (S). By changing phase matching angle of the BBO crystal w.r.t. the white seed laser one can generate any desire signal wavelength. The 'S' is mixed with pump into another BBO crystal to generate sum frequency signal (SFS). The 'S' and 'I' is again passed through two separate external optical frequency mixtures (mixture 1 and mixture 2, typically made of BBO crystals) to obtain second and fourth harmonics signal/idler (SH-S/I and FH-S/I, respectively). The orientation of mixture 1 and mixture 2 is needed to be adjusted in generating desired excitation wavelength (pump pulse).

Spectrometer (Excipro)

After generation of pump beam in OPA unit, it was directed towards rotating sample cell inside spectrometer (Excipro, CDP Systems, Russia) where TA measurement was performed. Remaining ~20% of the amplified beam (800 nm) of regenerative amplifier was also directed towards spectrometer for the generation of white light continuum (WLC) to act as probe beam (Figure 2.7). The 800 nm laser was initially traveled through a variable optical delay line (a Au coated retro-reflector controlled by a step motor) of ~4 ns (maximum) followed by passing through a rotating CaF_2 crystal to generate board WLC in the range of ~350-900 nm. The white light was then splitted into two parts using a beam splitter and both pulses were focused on rotating sample cell to get a better signal-to-noise ratio. The white light which is spatially overlapped with the pump beam onto the sample cell is called 'signal' and the other one is 'reference'. A co-linearity (with an angle of < 5°) between the pump and signal probe beam is always maintained for better spatial overlap between the two. This overlap can be fine-tuned through adjustment of a reflecting mirror nearest to the sample cell. Moreover the diameter of the probe signal was kept slightly smaller than the pump to make sure the probe interrogate only the excited sample. The probe intensity was intestinally kept low to avoid any undesired multiphoton processes during the experiment. A mechanical external chopper is used to block the pump path to get transmitted intensity of the probe when the sample is in ground state. Thus transmitted intensity of the probe is used to measure the differential absorbance (ΔA) of the sample when it is in excited state by the action of pump pulse

minus when it is in ground state due to absence of pump. The transmitted intensity of the signal and reference probe beam were then tightly focused in two small holes of two separate optical fibers and then it was directed to polychromator and finally towards detector (photodiode array). All the measurements were performed using liquid samples which were put between two quartz glass plates of 1 mm path length. During every experiment the sample cell were kept under rotation to avoid any photoinduced bleach of the samples. In our experiment colloidal LHP NCs of different compositions have been used as samples of interest. Inbuilt Excipro software (CDP system, Russia) was used for measuring ΔA and its time dependent evolution at any required probe wavelength. The raw data were analyzes using Igor Pro software (Version 6.37).

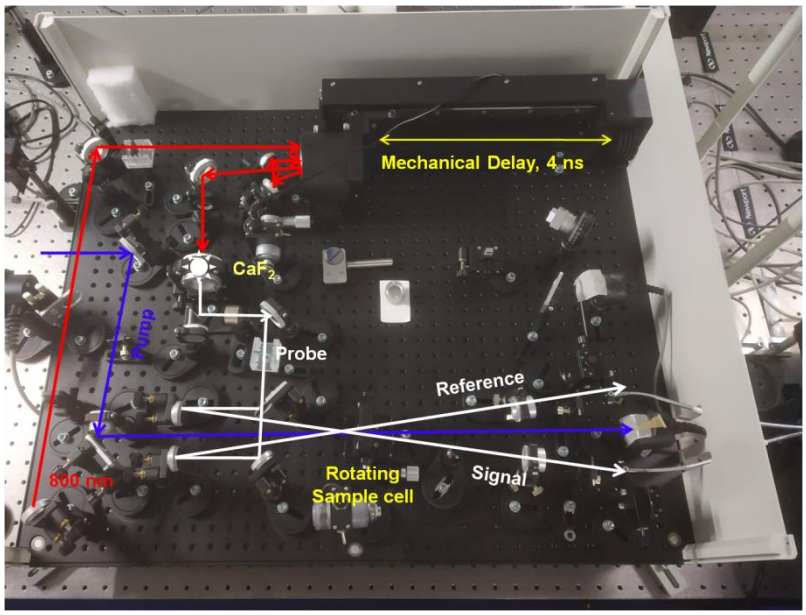

Figure 2.7. *Different components and optical layout of spectrometer (Excipro).*

The ΔA can be written as

$$\Delta A(\lambda, t) = A_{pump\ on}(\lambda, t) - A_{pump\ off}(\lambda) = A_{excited}(\lambda, t) - A_{ground}(\lambda) \quad (2.1)$$

$$\Delta A(\lambda, t) = \log\left(\frac{I_{0,excited}(\lambda)}{I_{excited}(\lambda,t)}\right) - \log\left(\frac{I_{0,ground}(\lambda)}{I_{ground}(\lambda)}\right) = \log\left(\frac{I_{ground}(\lambda)}{I_{excited}(\lambda,t)}\right) \quad (2.2)$$

Considering electronic excitation of molecular system (Figure 2.8A), three types of spectral features one can obtain from a typical TA spectra of any sample: 1) negative

(ΔA= -Ve) ground state bleach (GSB), 2) negative (ΔA= -Ve) stimulated emission (SE) and 3) positive (ΔA= +Ve) excited state absorption (ESA) or photoinduced absorption (PA). The origin of these spectral features (Figure 2.8B) is described below.

GSB: In TA spectra GSB appears as a strong negative signal at the same region where steady state absorption of the system takes place. Since pump excites some of the molecules (systems) to the excited state, the probe pulse will experience less number of molecules in the ground state. Therefore, transmitted intensity of the probe pulse will be less when the system is in excited state and the detector will experience more transmitted intensity in this scenario than what it will receive in pump-off condition. Hence denominator value in the above equation (2.2) will be more than numerator, thus GSB appears as negative signal in TA spectrum.

SE: When pump excites some of the molecules to excited state, the broadband probe pulse demotes some of the excited molecules to the ground state by emitting extra

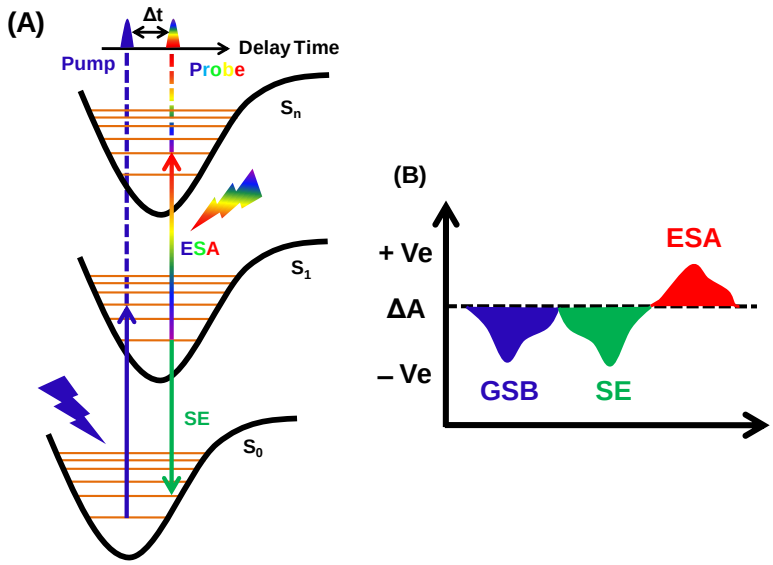

Figure 2.8. *(A) Schematic representation of molecular electronic excitation by pump followed by interrogation of the excited species by probe pulse. (B) Associated spectral features of a typical TA spectrum.*

photons in the same direction of probe photons. This phenomenon adds those photons with probe pulse and hence detector will receive more photons when the system is in excited state by the action of pump pulse. As denominator of the above equation (2.2) becomes heavier, a negative signal corresponding to SE is expected in TA spectra. Note that, both GSB and SE of a system are negative and hence it sometimes becomes difficult

to distinguish them (like in LHPs) and most often a broad bleach signal is observed unless the system has a large stokes shift.

ESA or PA: As pump pulse creates some population in the excited state, they can also absorb suitable wavelength light from the probe pulse and further promote to the higher energy states. Since probe pulse is absorbed by the excited molecules, the intensity of the transmitted probe beam decrease, resulting in lower value of the denominator in the above equation (2.2). Therefore ΔA becomes positive. Again if a new species is formed after photoexcitation, the probe transmittance will be less and a new positive signal corresponding to the newly generated species could be observed in TA spectra.

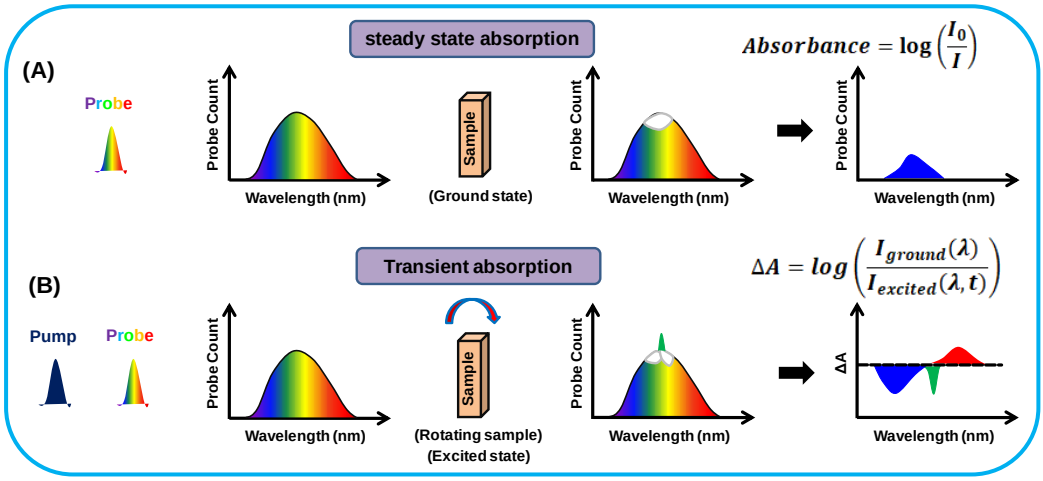

Figure 2.9. *Origin of spectral difference between steady state and transient absorption measurements.*

Thus transient species which are formed upon excitation by a short pump pulse provide some distinguished insights that are not accessible through steady state absorption technique. Figure 2.9 shows the fundamental difference between steady state absorption and TA studies of a system. In former case, a broad white light is passes through a stationary sample in its ground state and the sample absorbs a particular portion of the white light for excitation (shown as white area in Figure 2.9A, middle). As intensity of the transmitted light is less due to absorption by the system, following Lambert-Beer's law the absorbance appears as a positive signal. This is however not the case for TA measurement. Since the pump pulse generates transient species in the excited state, a number of possible transitions (discussed above) are possible when probe passes through the photo-excited sample. The probe can be absorbed by fraction of population in ground as well as excited state (shown as two white areas in Figure 2.9B, middle) and at

the same time SE from the excited state generates additional photons in the same direction to the probe pulse to hit the detector. Hence SE adds some photon in a certain wavelength region (shown as green area in Figure 2.9B, right) unlike the absorption processes. Therefore, ΔA appears as three distinct spectral signatures in TA spectra in both +Ve and –Ve directions.

2.3.2.2. Femtosecond Up-Conversion Studies:

This is possibly the best technique to probe fluorescence decay of a sample in a time resolution of few fs. This technique relies on sum frequency generation (SFG) using the advantage of nonlinear optical phenomena.[15] Fluorescence beam of a sample is mixed with a time delayed probe beam (also known as gate beam) in a sum frequency crystal maintaining a phase matching condition (Figure 2.10A) between the signals (equation 2.3) to generate up-converted PL.[16]

$$\frac{1}{\lambda_{sum}} = \frac{1}{\lambda_{gate}} + \frac{1}{\lambda_{flu}}$$

$$n_{sum}\omega_{sum} = n_{gate}\omega_{gate} + n_{flu}\omega_{flu} \qquad (2.3)$$

where λ_{sum}, λ_{gate} and λ_{flu} corresponds to sum frequency, gate and fluorescence wavelengths. The nsum, ngate and nflu are refractive indices of the three signals having frequencies of ωsum, ωgate and ωflu, respectively. The formation of up-converted PL is highly sensitive and it only generates when the fluorescence and gate beam is spatially and temporally overlapped in the sum frequency crystal (BBO crystal) and the above phase matching condition (equation 2.3) is satisfied.

In our setup, FOG 100 (CDP systems, Russia) spectrometer was used to measure fluorescence up-conversion process. A part of MaiTai HP output i.e. 800 nm laser was used for generation of excitation pulse on the experiments (Figure 2.10B). The 800 nm beam was initially frequency doubled (400 nm) by passing it through BBO crystal. A dichroic mirror is used as a beam splitter which reflects the second harmonic 400 nm signal and transmits the parent 800 nm beam towards a motor controlled optical delay line (a Au coated retroreflector) of 4 ns to act as gate pulse. The 400 nm pump was then passed through a filter (F1) to cutoff any residual gate beam followed by Berek Plate, to control polarization (at magic angle) of the pulse w.r.t. the gate beam. After collecting the fluorescence, it was collimated using a lens (L2) and subsequently passed through another filter (F2) to eliminate pump pulse (if any). Then the collimated fluorescence was focused onto the SFG BBO crystal (0.5 mm thick) and the gate beam also meets with it after travelling through the computer controlled delay line. Successful mixing of the two

beams generates up-converted signal, which was then collimated and passed through a third filter (F3) to eliminate any undesired signals except the up-converted one. Finally the signal reaches to photomultiplier tube (PMT) after passing through monochromator (MC). The BBO crystal is rotated about its crystal axis to attain a better phase matching angle between the two signals and sometimes a fine tuning provides largely improved signal-to-noise ratio for the measurement. Monochromator detector wavelength was set according to the up-converted signal and controlled through software.

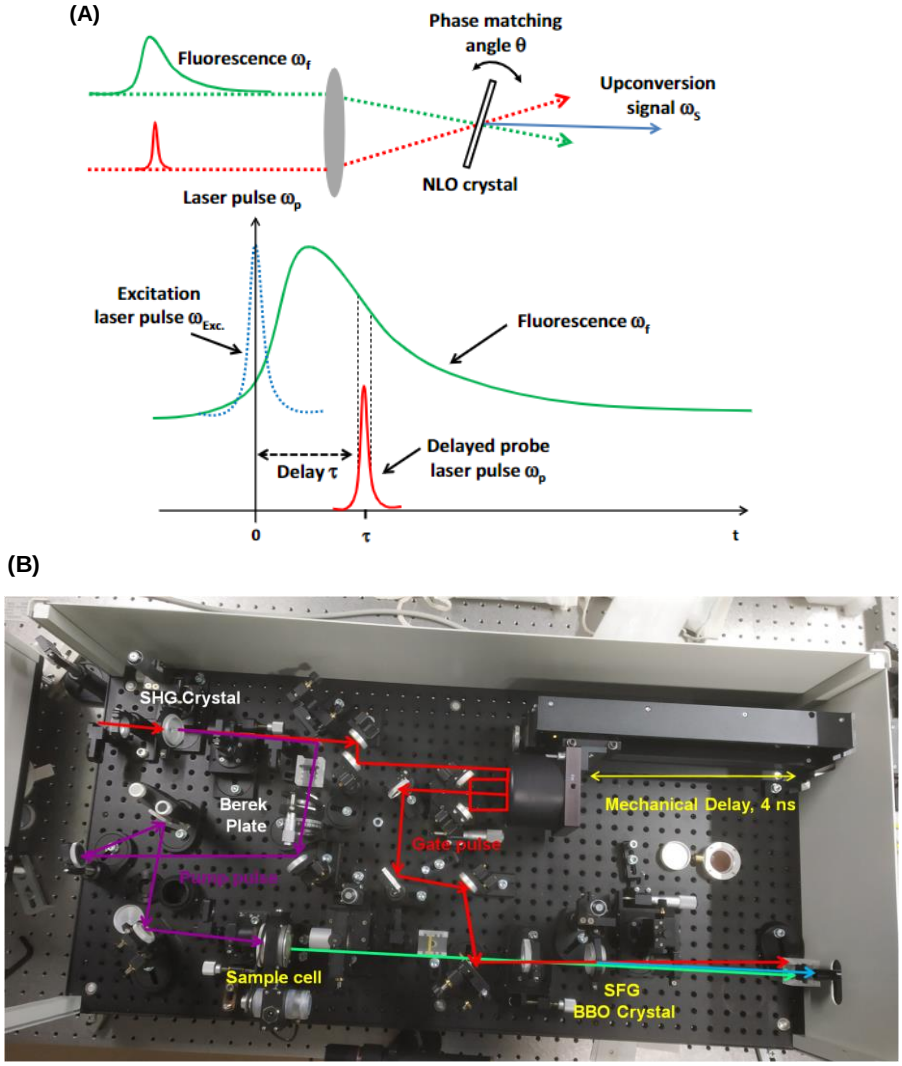

Figure 2.10. *(A) Phase matching condition and basic principles of PL up-conversion. Adopted from reference 15. (B) Optical layouts of spectrometer part (FOG 100).*

The intensity change of the up-converted beam is actually measured as a function of delay of the gate beam. It is important to note that, since the intensity of the gate beam

remains constant throughout the experiment, it is the change in fluorescence intensity that is reflected in the decay of up-converted PL signal. IRF of the instrument was measured to be in the range of 200-250 fs using the Raman signal of water. An inbuilt software 'Lumex' is used for data collection and Igor Pro (version 6.37) was used for analysis of the raw data.

2.4. Other Techniques Used for Characterization of the NCs

Transmission Electron Microscopy (TEM) Measurement: TEM measurements were carried out on JEM-F200 multi-purpose electron microscope (JEOL), which was operated at an accelerating voltage of 200 kV. For this study the samples were prepared by drop-casting a dilute colloidal solution of the NCs on a copper-grid (carbon coated) and dried overnight under vacuum.

Powder X-ray Diffraction (PXRD) Measurement: PXRD patterns of the samples (as thin films) were recorded on a X-ray diffractometer (Bruker AXS D8) using X-ray radiation of Cu-K_α (λ = 1.5406 Å). The samples were prepared by drop-casting concentrated colloidal solutions of the NCs on a clean thin quartz glass plate, which were dried under vacuum for 24-48 h before the measurements.

Energy Dispersive X-ray (EDX) Measurement: EDX spectra were recorded using Oxford Instruments X-Max^N SDD (50 mm^2) system and INCA analysis software. The samples were prepared by drop-casting concentrated colloidal solutions of the NCs on thin clean quartz plate and were dried under vacuum for 24-48h.

X-ray Photoelectron Spectroscopy (XPS) Measurement: XPS studies were performed in a Thermo Scientific K-Alpha spectrometer equipped with micro-focused monochromatic X-ray source (Al K_α, spot size ~400 µm) operating at 70 W. The energy resolution of the spectrometer was set at 0.5 eV and a pass energy and base pressure of 50 eV and 5×10^{-5} torr, respectively were maintained inside the analysis chamber. Low energy electrons from the flood gun were used for charge compensation. An optimum concentration of the NCs was drop-casted onto a clean quartz glass plate for the XPS measurements and kept under vacuum for 12h. All the XPS spectra were calibrated with respect to 'C 1s' peak at 285.0 eV.

Fourier-Transformed Infrared (FTIR) Measurement: FTIR study was performed using Bruker Tensor II spectrometer. A drop of concentrated colloidal solution of the NCs in hexane was used for this study.

Nuclear Magnetic Resonance (NMR) Measurement: ^{1}H NMR spectra were recorded on Bruker Avance NMR spectrometer operating at 400 MHz at 25ºC. For the preparation of NMR samples, the as-synthesized crude NCs solution in ODE was first centrifuged at 7k rpm for 8 min and the precipitate was dispersed in dried hexane. Then dried MeOAc/ACN was added to the NCs dispersion in 1:1 volume ratio followed by centrifugation at 7k rpm for 5 min. The supernatant was discarded and the precipitate was then dispersed in $CDCl_3$. A clear solution after centrifugation was used for measuring the ^{1}H NMR data.

Inductively Coupled Plasma-Optical Emission Spectroscopy (ICP-OES) measurements: ICP-OES measurements were performed by using Varian 720 emission spectrometer. The NCs were digested either in aqua-regia (concentrated HCl: concentrated HNO_3 (v/v) = 3:1) or in concentrated HNO_3 and kept the solution overnight for complete digestion of the NCs. The above solution was used for the measurement.

Photostability and Water Treatment Studies: Photostability of dilute colloidal dispersion of the NCs was studied under continuous illumination of 365 nm UV light (8W) at room temperature and relative-humidity of 50-60%. For this experiment, a small volume of OA and OAm (30 μL each) was mixed with the purified NCs dispersion in hexane and a small portion of it was diluted in 2.5 mL hexane in a cuvette and placed under the UV light. Then PL intensity of the sample was monitored time-to-time to determine the remnant PL of the NCs. In case of water treatment, additionally, 1 mL of distilled water was put on 2.5 mL of dilute colloidal dispersion of the NCs (in cuvette) and vigorously shaken before measuring the PL data.

Device Fabrication and Characterization: The violet-LEDs were fabricated by drop casting a solution of the $CsPbCl_3$ NCs on a commercial UV LED with λ_{em} = 365 nm. The EL spectra were measured using FlouroLog-3 (Horiba Jobin Yvon) spectrofluorimeter. The input power of the LED was provided using a regulated DC power supply and varied between 3.5 V and 4.5 V. The input and output powers were measured at the respective peak (365 nm for the UV LED and 410 nm for the fabricated violet-LED) by the Thor labs power meter (PM100D) using a photodiode (S140C). The output and input powers were considered for calculating EQE of the device.

2.5. Quantitative Estimation of Various Parameters of the NCs

Ligand density (d) at the surface of the NCs: The number of ligands per unit surface area of the NCs was calculated based on the ICP-OES, NMR and TEM data using the following formula:[17]

$$\text{Ligand density} = \frac{[\text{Oleyl}]}{6 \times [\text{NCs}] \times L^2}$$

The edge lengths of the NCs (L) after required cycles of washing (with MeOAc) were obtained from the TEM images. Molar concentration of the NCs after required washing cycles was determined from ICP-OES study. As the concentration of a chemical species is directly proportional to the corresponding integrated peak area in the ^{1}H-NMR spectrum,[17] the oleyl content (due to both OAH and OAm) at the surface of the NCs after given cycles of washing was determined from the integrated area of its characteristics peak at ~5.34 ppm. The measured values are collected in Table A4.4.

Interplanar distance (d_{100}): This was estimated from the PXRD data of the doped sample with the help of Bragg's law ($2d\sin\theta = n\lambda$) using λ = 1.5406 Å, n = 1, and 2θ value of 15.648 Å. The estimated distance (0.5658 nm) was very similar to that obtained directly from the HRTEM images of the NCs.

PLQY of the LHP NCs: PLQY of the samples was calculated using the following equation:

$$QY_S = QY_R \times \left(\frac{I_S}{I_R}\right) \times \left(\frac{OD_R}{OD_S}\right) \times \left(\frac{\eta_S}{\eta_R}\right)^2$$

where, I represents the integrated area under the PL spectrum, OD and η represent optical density at the excitation wavelength and refractive index of the medium, respectively. S and R correspond to the sample (i.e. the NCs) and reference, respectively. 9,10-diphenylanthracene (PLQY = 0.93 in ethanol), coumarin-153 (PLQY = 0.54 in ethanol), rhodamine 6G (PLQY = 0.95 in water) and cresyl violet (PLQY = 0.54 in ethanol) were used as reference for estimation of PLQY of the blue-violet-emitting $APbCl_3$ and $CsPb(Cl/Br)_3$ NCs, green-emitting $APbBr_3$ NCs, yellow-orange-red-emitting $CsPb(Br/I)_3$ and $CsPbI_3$ NCs and NIR-emitting $MAPbI_3$/$FAPbI_3$ NCs respectively.[18-21]

2.6. Standard Deviation Limits

The usual standard error limits of the numerical values obtained from different measurements are given below.

Absorption and PL maxima = ±2 nm

PLQY = ± 3%

Average PL lifetime = ±5-7%

Edge length of NCs = ±5-10%

Elemental composition = ±2-3%

Ligand density = ±5-10%

The standard deviation of other experimental quantities is mentioned at appropriate places in the working chapters.

References:

1. L. Protesescu, S. Yakunin, M. I. Bodnarchuk, F. Krieg, R. Caputo, C. H. Hendon, R. X. Yang, A. Walsh and M. V. Kovalenko, *Nano Lett.*, 2015, **15**, 3692–3696.
2. L. Protesescu, S. Yakunin, M. I. Bodnarchuk, F. Bertolotti, N. Masciocchi, A. Guagliardi and M. V. Kovalenko, *J. Am. Chem. Soc.*, 2016, **138**, 14202–14205.
3. Q. A. Akkerman, L. Martínez-Sarti, L. Goldoni, M. Imran, D. Baranov, H. J. Bolink, F. Palazon and L. Manna, *Chem. Mater.*, 2018, **30**, 6915–6921.
4. B. Valeur and M. N. Berberan-Santos, *Molecular Fluorescence: Principles and Applications, 2nd Edition*, Wiley-VCH Verlag GmbH, Weinheim, 2012.
5. *What is TCSPC?Edinburgh Instruments*, https://www.edinst.com/wp-content/uploads/2015/08/TN2-What-is-TCSPC-Red.pdf.
6. A. Dey, *Ultrafast Carrier Dynamics and Charge Transfer Processes in Photoexcited Perovskite Nanocrystals*, University of Hyderabad, India, Hyderabad, 2020.
7. M. E. Fermann, A. Galvanauskas and G. Sucha, *Ultrafast Lasers: Technology And Applications* New York, Basel, 2003.
8. A. Weiner, *Ultrafast Optics*, John Wiley and Sons, Inc, Hoboken, 2009.
9. S. C. Singh, H. B. Zeng, C. Guo and W. Cai, *Nanomaterials: Processing and Characterization with Lasers*, Wiley-VCH Verlag & Co. KGaA, Weinheim, 2012.
10. A. Cannizzo, *Phys. Chem. Chem. Phys.*, 2012, **14**, 11205-11223.
11. C. Ruckebusch, M. Sliwa, P. Pernot, A. d. Juan and R. Tauler, *Journal of Photochemistry and Photobiology C: Photochemistry Reviews*, 2012, **13**, 1-27.
12. K. F. Wall and A. Sanchez, *The Lincon Laboratory*, 1990, **3**, 447.
13. S. Witte and K. S. E. Eikema, *IEEE Journal of Selected Topics in Quantum Electronics*, 2011, **18**, 296 - 307.
14. *https://www.nobelprize.org/uploads/2018/10/press-fiq3-fy-en-cpa.pdf*.
15. H. Chosrowjan, S. Taniguchi and F. Tanaka, *FEBS Journal*, 2015, **282**, 3003–3015.
16. J. Shah, *IEEE Journal of Quantum Electronics*, 1988, **24**, 276-288.
17. J. Xue, J.-W. Lee, Z. Dai, R. Wang, S. Nuryyeva, M. E. Liao, S.-Y. Chang, L. Meng, D. Meng, P. Sun, O. Lin, M. S. Goorsky and Y. Yang, *Joule*, 2018, **2**, 1866-1878.
18. K. Rurack and M. Spieles, *Anal. Chem.*, 2011, **83**, 1232–1242.
19. J. V. Morris, M. A. Mahaney and J. R. Huber, *J. Phys. Chem.*, 1976, **80**, 969–974.
20. R. F. Kubin and A. N. Fletcher, *J. Lumin.*, 1982, **27**, 455-462.
21. O. Vybornyi, S. Yakunin and M. V. Kovalenko, *Nanoscale*, 2016, **8**, 6278-6283.

CHAPTER 3

Mg^{2+}-Doped Highly Luminescent Green and Violet Emitting Perovskite Nanocrystals with Reduced Toxicity and Enhanced Stability

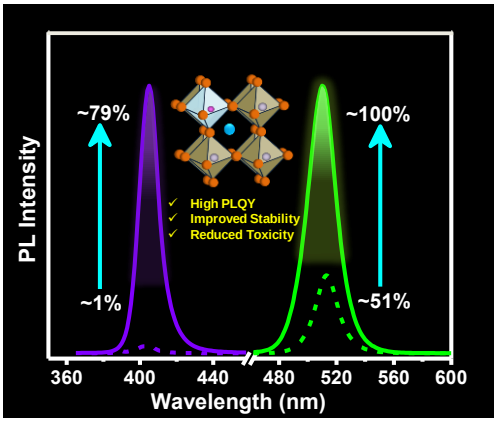

J. Phys. Chem. Lett. 2020, 11, 1178–1188

Overview

Lack of long-term stability, presence of toxic lead and low PL efficiency are the major obstacles to commercialization of the lead halide perovskites-based optoelectronic and photovoltaic devices. Herein, we report a facile ambient condition doping protocol, which addresses all three issues of the $CsPbX_3$ perovskite NCs to a substantial extent. We show that room-temperature treatment of these NCs with MgX_2 results in partial (18-23%) replacement of toxic lead, enhances PLQY of green-emitting $CsPbBr_3$ (to ~100% from ~51%) and violet-emitting $CsPbCl_3$ NCs (to ~79% from ~1%) and improves the stability under ambient condition, and in presence of light and polar solvent. Ultrafast pump-probe and temperature dependent PL studies reveal that curing of intrinsic structural disorder, introduction of some shallow energy levels close to the conduction band edge and effective passivation of the halide deficiency contribute to the improved properties of the doped system.

3.1. Introduction

The outstanding potential of the lead halide perovskites [ABX_3-type, A= Cs^+, FA^+ or MA^+), B= Pb^{2+} and X= Cl, Br or I] in various photovoltaic and optoelectronic technologies such as in solar cells,[1-4] LEDs,[5, 6] lasers[7, 8] photo-detectors and non-linear optics,[9-12] which has already been demonstrated, is owing to their unique optical and photophysical properties, namely high luminescence efficiencies,[6,13-15] high color purity,[13] large absorption coefficient,[16] defect tolerant nature,[17] ease of tunability of the bandgap throughout the entire visible region,[18, 19] and facile low-cost synthesis.[13,20-22] Unlike the conventional metal chalcogenide semiconductor NCs, the halide perovskites exhibit high PL due to their defect tolerant nature.[17,23, 24] However, in nano-dimension, large surface to volume ratio has a detrimental effect on their optical properties and stability[24-26] and the PLQY and stability of these NCs under ambient condition are often far from satisfactory.[25] For example, the violet-emitting $CsPbCl_3$ NCs are poorly luminescent with typical PLQY of <5% as deep trap centers generated by halide vacancies and distorted $[PbCl_6]^{4-}$ octahedral units facilitate non-radiative recombination of photogenerated charge carriers.[27-36] Such low PLQY is a major issue with this material in its practical utilization. In contrast, the green-emitting $CsPbBr_3$ NCs possess much higher PLQY as the defects are weakly localized and shallow in nature.[13, 14, 29, 37] However, sub-unity PLQY of the pristine $CsPbBr_3$ NCs implies non-negligible contribution of the non-radiative recombination mediated by these shallow defect states that needs to be eliminated to obtain high quality NCs with near-unity PLQY.[37]

Though several successful strategies have been developed for enhancing the PLQY of these NCs, presence of toxic lead has been a major concern for commercialization of products based on these materials. In this regard, B-cation doping is an attractive approach as it not only enhances the PLQY of the system, but also reduces the content of toxic lead in the NCs. Literature indicates that PLQY of green-emitting $CsPbBr_3$ NCs is enhanced on doping of Ce^{3+}, Zn^{2+}, Sn^{2+}, Cd^{2+} and Na^+[28, 38-42] and that of violet-emitting $CsPbCl_3$ NCs is enhanced by doping of Ni^{2+}, Y^{3+}, La^{3+}, Cd^{2+}, Cu^+ and Ca^{2+}.[27, 28, 30, 31, 43-46] Though Cd^{2+} is one metal ion, which is effective for both green and violet emitting NCs,[28] its doping does not help reducing the toxicity of the NCs as cadmium compounds are also highly toxic.[47]

In quest for a metal ion, which will enhance the PLQY and stability of both blue and green emitting $CsPbX_3$ (X = Cl and Br) NCs and at the same time will reduce the toxicity, we zeroed in on magnesium halides, MgX_2, considering their environment friendly nature, high natural abundance, strong preference for octahedral coordination[48]

and comparable Mg-X and Pb-X bond dissociation energy.[49] Another factor that influenced our choice in favor of Mg^{2+} is a recent theoretical study, which identified it as the best alternative to Pb^{2+} in the $CsPbX_3$ crystal lattice.[50] Two recent findings on the influence of Mg^{2+} on the PL of $CsPbX_3$ film and NCs were, however, not encouraging as the reported PL enhancement was rather moderate.[27, 51] Herein, we report an entirely different strategy for introducing under ambient condition significant amount of Mg^{2+} into the $CsPbX_3$ crystal, which reduces the lead-content by ~25%, dramatically improves PLQY of both green- and violet-emitting perovskite NCs (near-unity for $CsPbBr_3$, and ~79% for $CsPbCl_3$), provides superior air- and photostability and robustness towards polar solvent.

3.2. Results and Discussion

The undoped $CsPbX_3$ (X = Cl and Br) NCs were prepared following a conventional hot-injection method,[13] details of which are provided in Chapter 2 (section 2.2.1). These NCs were dispersed in hexane and used for further investigation. For doping, MgX_2 (0.30 mmol) was dissolved in 4 mL OAm by heating at 100^0C for 2 h. Addition of 30 μL of this hexane diluted solution to 0.50 mL (~0.015 μM) colloidal dispersion of $CsPbX_3$ NCs, maintained in ambient condition and stirring for 1 h (Scheme 3.1A), produced brightly luminescent solution of $CsPbX_3$ NCs. This solution was mixed with methyl acetate in 1:2 volume ratio and centrifuged at high speed (13k rpm) for 5 mins. The supernatant liquid containing excess ligands and salts was discarded and the residue at the bottom of the centrifuge tube was then collected and re-dispersed in hexane for further studies. Additional details on the method of synthesis are provided in Chapter 2 (section 2.2.2).

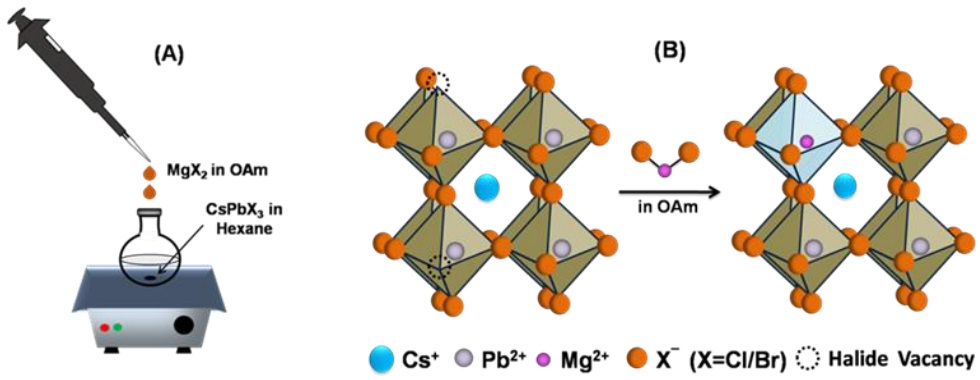

Scheme 3.1. *(A) Schematic representation of the post-synthetic doping strategy under ambient condition. (B) Illustration of substitution of Pb^{2+} by Mg^{2+} and passivation of the halide vacancy.*

The TEM images of the undoped and doped $CsPbBr_3$ NCs (Figure 3.1A, B) indicate cubic morphology of both the samples. High-resolution TEM (HRTEM) images show an inter-planar distance (100 lattice planes, d_{100}) of 0.592 nm in undoped NCs that is consistent with the literature.[14, 29] A smaller inter-planar distance of 0.573 nm in doped NCs is a reflection of lattice contraction due to smaller size of Mg^{2+} (72 pm, when hexa-coordinated) compared to Pb^{2+} (119 pm, hexa-coordinated).[52, 53] It is to be noted that the stated d_{100} lattice spacing were obtained by the inspection of ~40 NCs for both samples (Figure A1.1A, B). Although the cubic morphology of the $CsPbBr_3$ NCs was retained on doping, average edge length of the doped NCs is found noticeably smaller (11±2 nm) compared to the undoped sample (14.5±2 nm). A similar trend is observed for $CsPbCl_3$ NCs upon $MgCl_2$ treatment (Figure A1.2). The decrease in edge length of the NCs upon doping is presumably due to etching and smoothening of the doped NCs during the post-

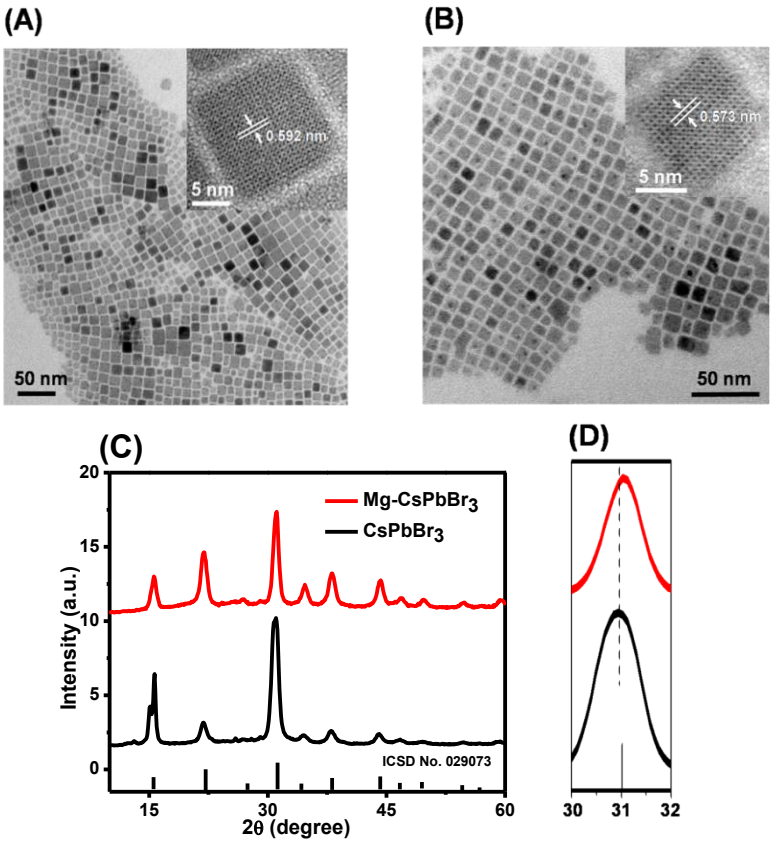

Figure 3.1. *TEM images of undoped (A) and Mg-doped (B) $CsPbBr_3$ NCs with corresponding HRTEM images (inset) showing lattice spacing of the (100) planes. (C) PXRD patterns of the undoped and doped $CsPbBr_3$ NCs of both the samples. (D) Zoomed view of the PXRD pattern shows peak shift of the (200) plane to higher angle on Mg-doping.*

synthetic treatment.[54] Doping-induced lattice contraction (*vide* later) can also contribute to this factor. A careful inspection of the individual diffraction peaks of the PXRD patterns (Figure 3.1C) of the undoped and doped $CsPbBr_3$ NCs (Figure A1.3 for $CsPbCl_3$) shows a clear shift of the peaks towards higher 2θ value further confirming the lattice contraction upon doping. For example, the peak at 31.02° for undoped $CsPbBr_3$, which corresponds to (200) plane, shifts to 31.12° for doped NCs (Figure 3.1D). Such lattice contraction induced peak shift in the PXRD patterns is well documented in literature.[39, 52, 53, 55, 56] The estimated interplanar distance (d_{100}= 0.566, see Chapter 2, section 2.5) from the PXRD data of the doped samples is very similar to that (0.573 nm) directly obtained from the HRTEM images, both confirming lattice contraction upon doping. The splitting of the (100) diffraction peak of the undoped $CsPbBr_3$ NCs is perhaps due to the existence of orthorhombic phase as well, which however, disappears upon Mg^{2+} incorporation into the lattice, indicating pure cubic phase of the doped NCs.[57, 58] Moreover, absence of any new diffraction peak in doped NCs shows that no impure crystal phase is induced by Mg^{2+} doping.

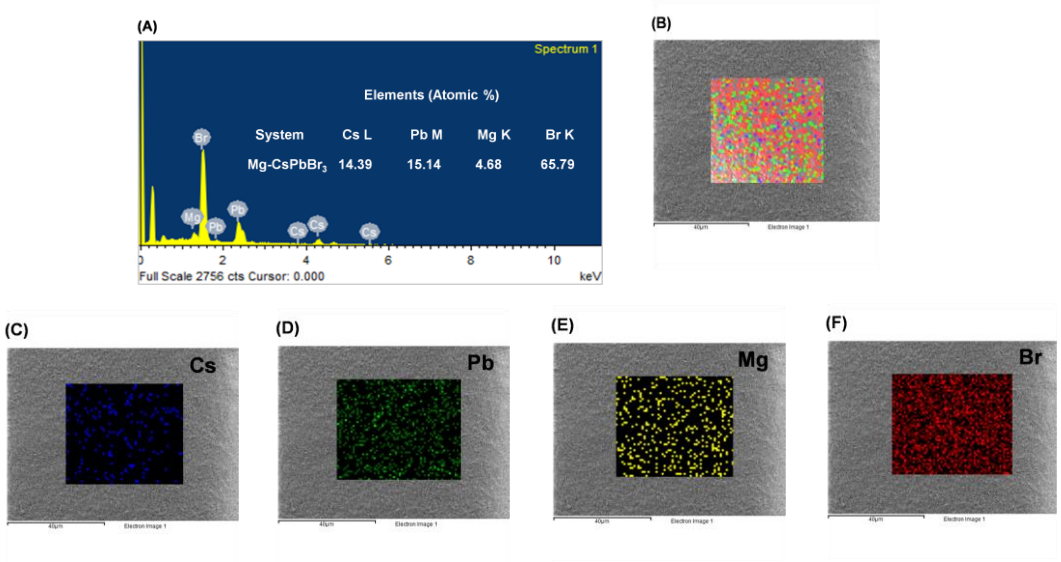

Figure 3.2. *(A) EDX spectrum of the doped $CsPbBr_3$ NCs indicating the relative content of the individual elements. (B) FESEM image of the doped NCs. The centre of the FESEM image, scanned for elemental mapping, indicates homogeneous distribution of Cs, Pb, Mg and Br throughout the scanned area of the doped NCs (C to F) respectively.*

The elemental analysis of a large area of the field emission scanning electron microscopy (FESEM) images (Figure 3.2), obtained by EDX measurement, allows quantitative estimation of the dopant content. A characteristic peak of Mg at 1.3 keV only

in the case of doped NCs (Figure 3.2A) confirms the presence of Mg^{2+}. Elemental analysis of the doped $CsPbBr_3$ NCs indicates a Cs:(Pb+Mg):Br atomic ratio of ~0.73:1.0:3.32 with overall ~4.68% Mg, suggesting replacement of ~23.4% Pb^{2+} by Mg^{2+} and significant reduction in toxicity of the pristine NCs. The Mg^{2+} content in doped NCs is also estimated through ICP-OES measurement. The Mg^{2+} content (with respect to Pb^{2+}) is estimated to be ~23.13%. This value is very close to that obtained from EDX measurement. Further, elemental mapping (Figure 3.2B-F) shows a homogeneous distribution of all four elements throughout the scanned area of doped NCs. The EDX data and elemental mapping of undoped $CsPbBr_3$, $CsPbCl_3$ and doped $CsPbCl_3$ NCs are presented in Figure A1.4-A1.6.

An XPS study of the samples provides insight into the chemical environment of the elements upon Mg^{2+} doping (Figure 3.3 and A1.7). The XPS spectrum of $CsPbBr_3$ shows that the intense peaks at ~138.1 eV and ~143 eV (Figure 3.3A) due to Pb $4f_{7/2}$ and Pb $4f_{5/2}$, respectively[59] are shifted to higher binding energy by ~0.2 eV upon doping. The Br $3d_{5/2}$ peak (Figure 3.3B) is also blue-shifted by ~0.2 eV to ~68.4 eV in doped $CsPbBr_3$ NCs.[42] The appearance of an additional peak at ~1305 eV only in doped NCs, which corresponds to Mg 1s (Figure 3.3C), re-establishes the presence of Mg^{2+}.[60] The blue-shift of the Pb 4f and Br 3d peaks on doping is due to contraction of the $[PbBr_6]^{4-}$ units (and

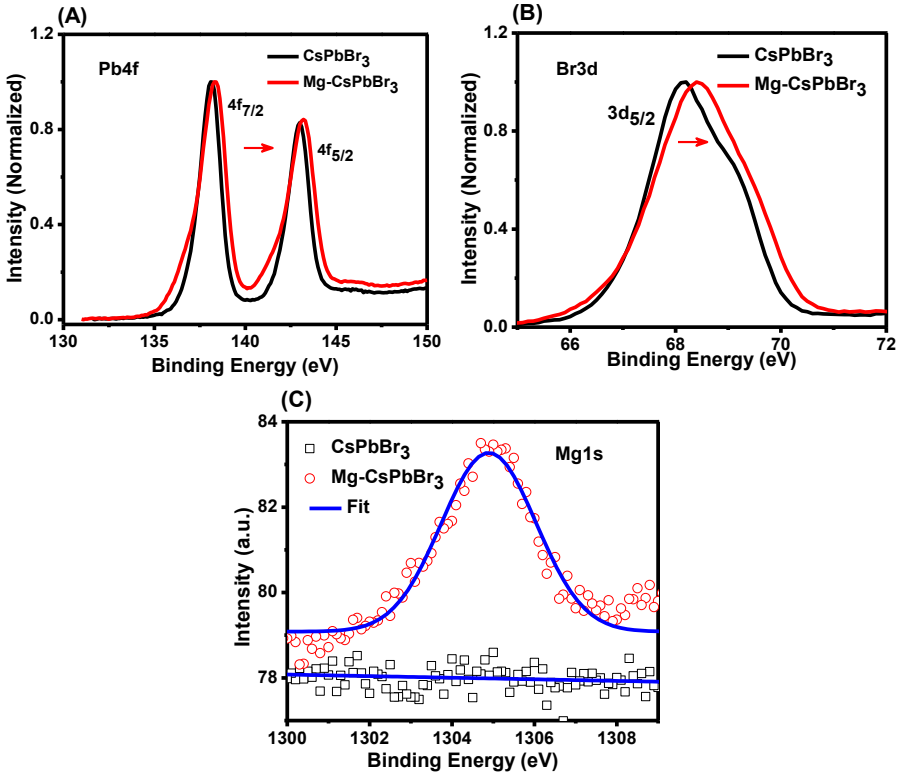

Figure 3.3. *High resolution XPS spectra of the undoped and doped $CsPbBr_3$ NCs showing signals due to (A) Pb 4f, (B) Br 3d, (C) Cs 3d and (D) Mg 1s. All spectra were calibrated with respect to the C 1s peak at 285.0 eV.*

consequent strengthening of the Pb-Br bonds) on incorporation of smaller Mg^{2+} (r_{Mg}^{2+}= 72 pm vs. r_{Pb}^{2+}= 119 pm) at B-site.[28, 53] A comparison of the FTIR spectra of the undoped and doped samples shows that except for some enhancement in oleylammonium content (Figure A1.8), the surface ligand arrangement is not changed significantly on doping. The observed change is not surprising as oleylamine solution of MgX_2 has been used for the post-synthetic treatment.

We find that the peak positions of UV-Vis absorption and emission spectra of the $CsPbX_3$ NCs are not significantly changed on doping, but the PL intensity of the systems are enhanced dramatically. For example, PLQY of the $CsPbBr_3$ NCs increases to ~100% from its initial value of ~51% and for $CsPbCl_3$ NCs, ~79% from an initial value of only ~1%. Careful inspection of the spectra reveals a small blue shift (~3 nm) of both absorption and PL maxima of $CsPbBr_3$ NCs upon doping (Figure A1.9 and 3.4A, respectively) due to lattice contraction induced by smaller Mg^{2+} ion. In this context, we take note of a very recent work by Huang et al. on Mg-doping of $CsPbBr_3$ perovskite film (not NCs) improving its morphology, crystallinity, PLQY and external quantum efficiency (EQE) of the fabricated LEDs.[51] We also note the recent observation by Sun and co-workers of increase in PLQY of violet-emitting $CsPbCl_3$ NCs from 0.8 to 36.6% on addition of $MgCl_2$ during the *hot-injection* synthesis of the NCs.[27] No doping of Mg was, however, observed like in our case. We surmise that the self-purification effect of NCs is dominant in the hot-injection synthesis and thus inhibit the doping of Mg^{2+} ions, whereas our post-synthetic doping strategy is based on the room-temperature reorganization of perovskite lattice which could feature rather weak self-purification of NCs.

PL decay behavior of undoped and Mg^{2+}-doped $CsPbBr_3$ NCs are shown in Figure 3.4B and the decay parameters are presented in Table 3.1. While $CsPbBr_3$ NCs exhibit 3-component PL decay, the decay profile of Mg-doped samples is bi-exponential in nature. The contributionof the 2.91 ns component due to the band-edge excitonic recombination[28, 29, 61] is substantially enhanced from ~28% to ~70% upon treatment and the fastest trapping component (0.64 ns), which has the largest contribution (~67%) in undoped NCs, vanishes completely in doped NCs. Another important point to note here is increase in contribution of the shallow trap-mediated radiative recombination component

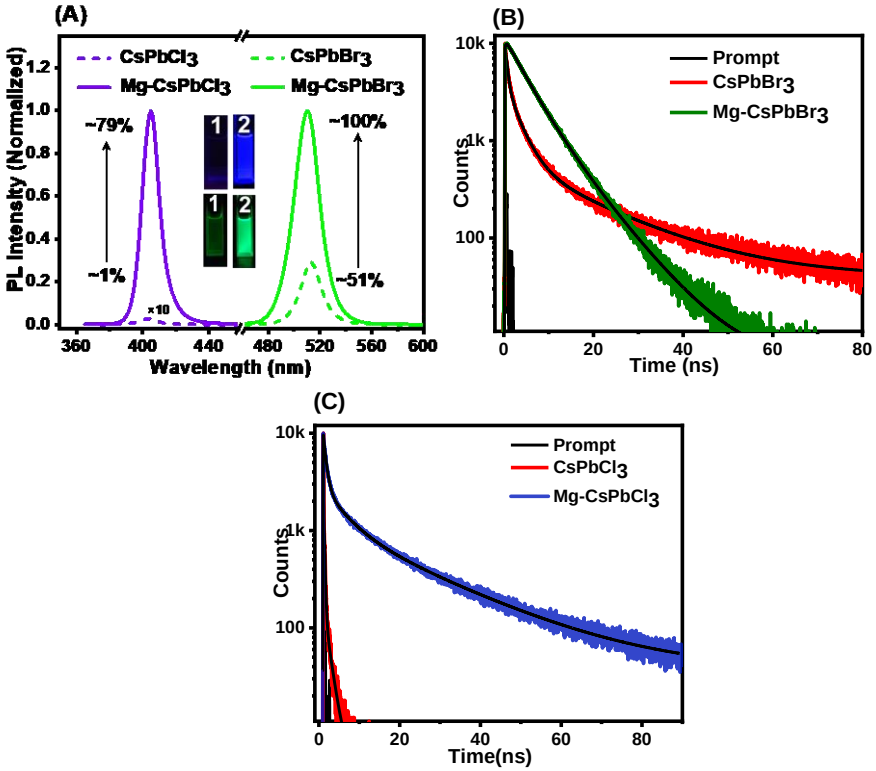

Figure 3.4. *Effect of doping on the PL spectra (A) and decay profiles (B and C) of $CsPbBr_3$ and $CsPbCl_3$ NCs. The inset in panel A shows digital images of undoped (1) and doped (2) NCs under illumination by 365 nm radiation. The PL spectra were recorded by exciting the $CsPbCl_3$ and $CsPbBr_3$NCs at 350 and 400 nm, respectively. For recording the PL decay curves, laser sources of 376 and 404 nm were used, and the PL was monitored at the respective peak wavelengths.*

Table 3.1. *PL decay parameters of undoped and doped $CsPbBr_3$ NCs.*

System	$\tau_1(a_1)^{\dagger}$/ns	$\tau_2(a_2)$/ns	$\tau_3(a_3)$/ns	$<\tau_{amp}>^{\ddagger}$/ns	k_r/ns^{-1}	k_{nr}/ns^{-1}
$CsPbBr_3$	2.91(0.28)	17.64(0.05)	0.64(0.67)	2.13	0.24	0.23
Mg-$CsPbBr_3$	4.32(0.70)	8.11(0.30)	---	5.46	0.18	0.0018

$^{\dagger}a_i$ is the amplitude associated with i-th lifetime component. $^{\ddagger}<\tau_{amp}> = \Sigma\tau_i a_i/\Sigma a_i$, k_r = PLQY/$<\tau_{amp}>$, k_{nr} = (1-PLQY)/$<\tau_{amp}>$. PL decay parameters of undoped and doped $CsPbCl_3$ NCs are summarized in Table A1.1.

from ~5% to ~30% upon doping. An estimation of the rate constant (k_{nr}) of the non-radiative deactivation process using the measured PLQY and lifetime values of the systems before and after doping shows that the k_{nr} value decreases by a factor of ~128 after the treatment (Table 3.1). Likewise, Mg-doped $CsPbCl_3$ NCs also exhibit much improved PL lifetime (Figure 3.4C), ($<\tau_{amp}>$ = 3.69 ns) compared to the undoped counterpart, which is too short to be estimated accurately in our TCSPC setup, which has a time resolution of ~61 ps.

We have also studied the carrier dynamics in undoped and doped $CsPbBr_3$ NCs by TA measurements with femtosecond time resolution. The TA spectral features (Figure 3.5A) are quite similar for both the undoped and doped systems and characterized by a sharp negative (bleach) signal due to ground state depopulation of the NCs upon excitation by the pump pulse.[62, 63] As the excitation wavelength (350 nm) corresponds to ~1.46Eg (where, E_g corresponds to the band-gap (~2.42 eV) of the undoped $CsPbBr_3$ NCs), photo-excitation of the NCs creates charge carriers much above the band-edge, which cool down to the band-edge excitonic state to initiate the bleach recovery process. The hot-carrier relaxation (hot-carrier cooling, HCC) time estimated from the bleach formation dynamics in undoped NCs is 580±21 fs, which is in good agreement with literature data.[62, 63] The hot-carriers, however, relax much faster (325±16 fs) in doped system (Figure 3.5B) presumably due to enhanced coupling of the conduction band states on introduction of the dopant states within the conduction band.[38, 64, 65] As the conduction band is formed mainly by the Pb orbitals, partial substitution of Pb with Mg is expected to change the distribution of energy levels in the conduction band. In order to validate that a faster HCC is due to the introduction of new energy levels within the conduction band on doping we have investigated the HCC dynamics of another undoped $CsPbBr_3$ NCs (λ_{ex} = 350 nm) with comparable PLQY (92±2%), synthesized following a reported three-precursor method.[21] A much slower HCC process (610±20 fs) in these NCs (Figure A1.10) compared to the doped system (325±16 fs) indeed proves the role of higher density of the states in the conduction band of the doped NCs. A stronger electron-phonon coupling upon doping may also contribute to faster HCC dynamics, but we are not sure about this aspect. As far as bleach recovery is concerned (Figure 3.5C), the undoped $CsPbBr_3$ NCs exhibit a bi-exponential dynamics comprising one major ultrafast component (~47±2.43 ps) due to carrier trapping and a much longer (>850 ps) recombination component.[38, 62] However, estimation of the exact time constant for the longer component is not possible due to the time-window limitation of our experimental set-up.[62] The presence of only >850 ps component in doped system indicates effective

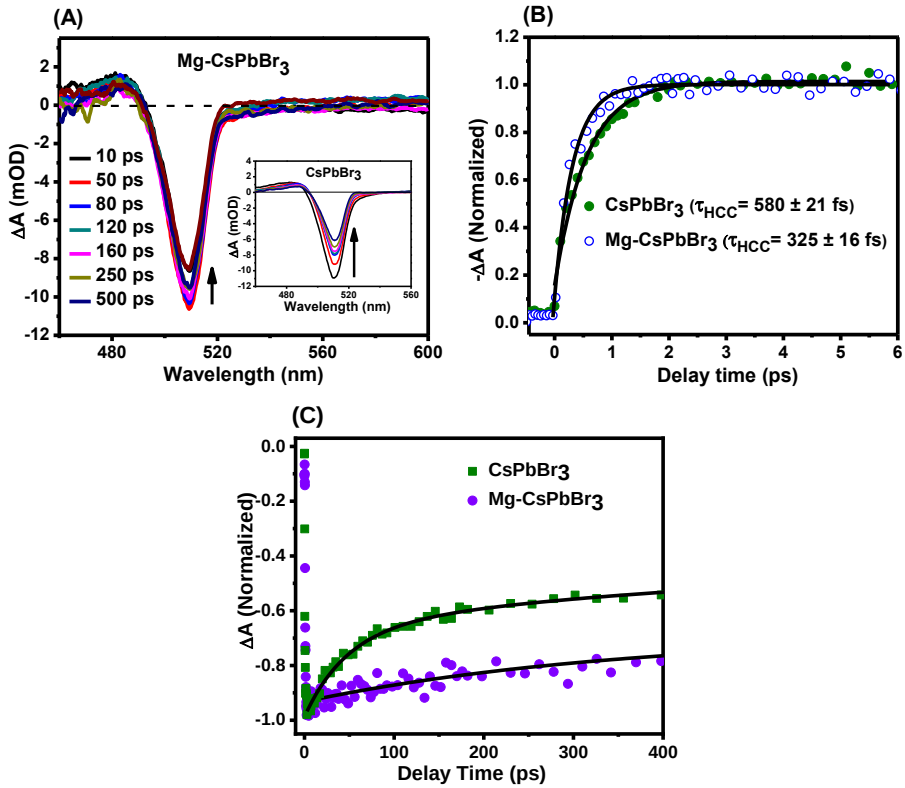

Figure 3.5. *(A) TA spectra (λ_{ex} = 350 nm) of the doped and undoped NCs (inset). (B) Comparison of the HCC dynamics of the samples. (C) Bleach recovery dynamics of the two NCs. The kinetic parameters obtained on bi-exponential fitting to the data are 47±2.43 ps (0.55) and >850 ps (0.45) for the undoped $CsPbBr_3$ NCs. For doped sample, the recovery dynamics is single exponential with a time constant of >850 ps.*

elimination of the ultrafast non-radiative recombination routes for the carriers on doping.

Further insight on carrier dynamics is obtained by examining the influence of temperature on the steady state and time-resolved PL of the undoped and doped $CsPbBr_3$ NCs decreases by a factor of ~95 on increase in temperature from 273K to 333K, but for the doped system, ~85% of its initial PL is retained even at 333K (Figure 3.6A and A1.11). This shows that carrier trapping, which is a thermally activated process, and which decreases the PL of the undoped system at higher temperature, is almost eliminated on doping. This conclusion is corroborated by the temperature dependence of the PL decay parameters (Table A1.2). With increase in temperature, the contribution of the short trapping component increases from 45% to 68% (with negligible change incontribution of the longest time component) in the case of undoped $CsPbBr_3$ NCs (Figure 3.6B); whereas, the contribution of the longest time component, which represents the trapping-detrapping process, increases from 33% to 47% for the doped system (Figure

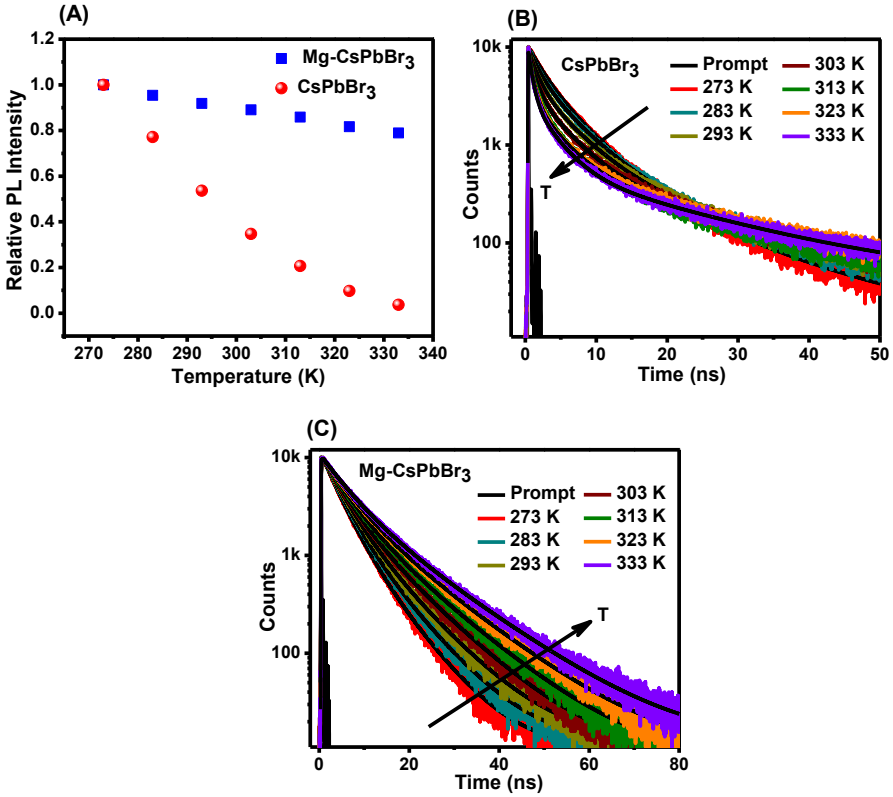

Figure 3.6. *(A) Variation of the PL intensity of undoped and doped $CsPbBr_3$ NCs with temperature. (B,C) PL decay kinetics of the two samples over the same temperature window.*

3.6C). This increase in contribution of the longest time component at higher temperature indicates involvement of new energy states, which lie very close to the excitonic state and participate in the trapping−detrapping process resulting in prolonged PL lifetime of the doped system (Figure A1.12).[61] Our ultrafast TA and these PL measurements show that the states, which facilitate non-radiative deactivation of the carriers, are largely eliminated on doping, but at the same time, doping can introduce new energy states that are distributed throughout the conduction band and little below to it (Scheme 3.2).

Halide deficiency associated point defects on the surface and distortion of the $[PbX_6]^{4-}$ octahedral units are the two main reasons for poor optical properties and low phase stability of the halide perovskite NCs.[37, 66] The halide vacancies generate inter band-gap trap states, which facilitate non-radiative recombination of the photogenerated charge carriers resulting in poor PLQY of the NCs. Better optical properties and stability of the halide rich NCs proves this point.[67] In the present case, the ratios of the atomic percentage, Br/Pb and Br/(Pb+Mg) in undoped and doped $CsPbBr_3$ NCs (~2.98 and ~3.32, respectively obtained from EDX study) indicates effective removal of the halide-

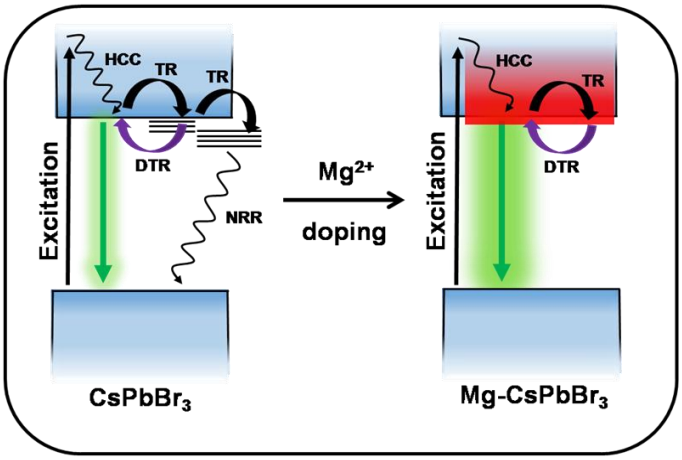

Scheme 3.2. *Schematic illustration of different photophysical processes in undoped and doped $CsPbBr_3$ NCs. The VB, CB, HCC, TR, DTR, NRR and TS are the acronyms for valence band, conduction band, hot carrier cooling, trapping, de-trapping, non-radiative recombination and trap states. The red-shaded portion in the CB of the doped NCs indicates Mg-doping induced introduction of energy states distributed throughout the CB and little below it.*

vacancy related defects on doping and concomitant increase of band-edge radiative excitonic recombination as confirmed by time-resolved PL decay (see Figure 3.4B) and TA studies (see Figure 3.5C). Apart from the halide vacancies, $[PbX_6]^{4-}$ octahedral distortion is also known to contribute to poor PLQY and stability of the $CsPbX_3$ NCs.[43, 66, 68] Well-known octahedral distortion in $CsPbX_3$ NCs arises from the size-mismatch of the cuboctahedral void and Cs^+ ion.[66] This distortion can be minimized either by replacing Cs^+ by a larger cation like formamidinium (FA^+)/methylammonium (MA^+) or by reducing the size of the octahedral unit by replacing B-site Pb^{2+} with smaller cations.[28, 66, 68-70] Some very recent reports, however, suggest that replacement of Pb^{2+} with smaller cations like Ni^{2+} (69 pm) and Cu^{2+} (73 pm) increases the defect formation energy of the resulting doped NC endowing it with much improved optical properties and stability.[43, 68,65, 70] To determine the influence of Mg^{2+} alone on the PL properties of the NCs, when similar experiments were performed using MgO, a PLQY of ~87% is achieved (as against 100% with $MgBr_2$) for $CsPbBr_3$ NCs, indicating that the doped NCs still suffer from halide vacancies, which is confirmed by the measured Br/(Pb+Mg) value of ~2.9 (Figure A1.13) in the doped sample. This is further proved by the PL decay behavior of the MgO treated NCs. These NCs exhibit a short time component (0.86 ns, 42%), which could not be observed in $MgBr_2$ treated samples (Figure A1.14). However, in the case of $CsPbCl_3$

NCs, the PLQY is enhanced only upto ~28%, indicating dominant role of the Cl^- vacancies for its low PLQY (Figure A1.12).[37] It is worth mentioning that addition of oleylamine solution alone enhances the PLQY of $CsPbBr_3$ NCs only by 8%, which is quite consistent with earlier literature.[71] Thus it is evident that both Mg^{2+} and X^- play important role in contributing to superior optical properties of the Mg-doped $CsPbX_3$ NCs compared to their undoped cousins by rectification of the octahedral distortion and suppression of the halide vacancy related defects (Scheme 3.1B). An important point to note in this context is that B-cation doping is commonly executed under high temperature reaction condition as room-temperature exchange at the B-site of perovskite NCs is considered to be quite challenging due to high energy requirement to open up the rigid $[PbX_6]^{4-}$ octahedral units.[72] In our case, the room temperature exchange is made possible, first by anchoring MgX_2 on the pre-existing halide vacancies of the NCs surface and then by elimination of the PbX_2 aided by OAm. This mechanism of incorporation of Mg^{2+} into the crystal lattice is consistent with literature.[39, 73]

Apart from reduced toxicity and high PLQY, these Mg-doped $CsPbX_3$ NCs are also characterized by remarkable stability, which is evident from Figure 3.7 (also Figure A1.15). As can be seen, under ambient condition, the PL intensity of a freshly prepared Mg-doped $CsPbBr_3$ NCs remains unchanged for almost 20 days and ~75% of its initial PL intensity is retained even after a month without any change in band position and full width at half maxima (FWHM) (Figure 3.7A, A1.15). In contrast, under similar condition, the PL of undoped NCs is quenched almost completely within 10 days. The doped NCs also exhibit excellent photostability. The initial PL intensity of doped $CsPbBr_3$ NCs remains unchanged for ~38 h (under 365 nm UV irradiation, 8 W), while for undoped NCs, the PL is lost almost completely in just 6 h (Figure 3.7B). The unchanged PXRD pattern recorded after storing the doped sample for 60 days in ambient condition (Figure 3.7C) confirms long-term stability of the sample. These measurements indicate phenomenal air- and photo-stability of the doped NCs when compared to their undoped counterparts. The doped $CsPbBr_3$ NCs are also found significantly resistant towards polar solvent like ethanol in which the bright emission can be observed for a long time (>960 min) without any change in the PL peak position and FWHM (Figure 3.7D, A1.16 and A1.17). In sharp contrast, the undoped NCs aggregate instantly in presence of ethanol, and the PL intensity drops dramatically with ~10 nm red-shift of emission maxima (Figure A1.16). The enhanced stability of the doped NCs towards polar solvent is most likely due to the protection provided by the long hydrocarbon chain of the surface

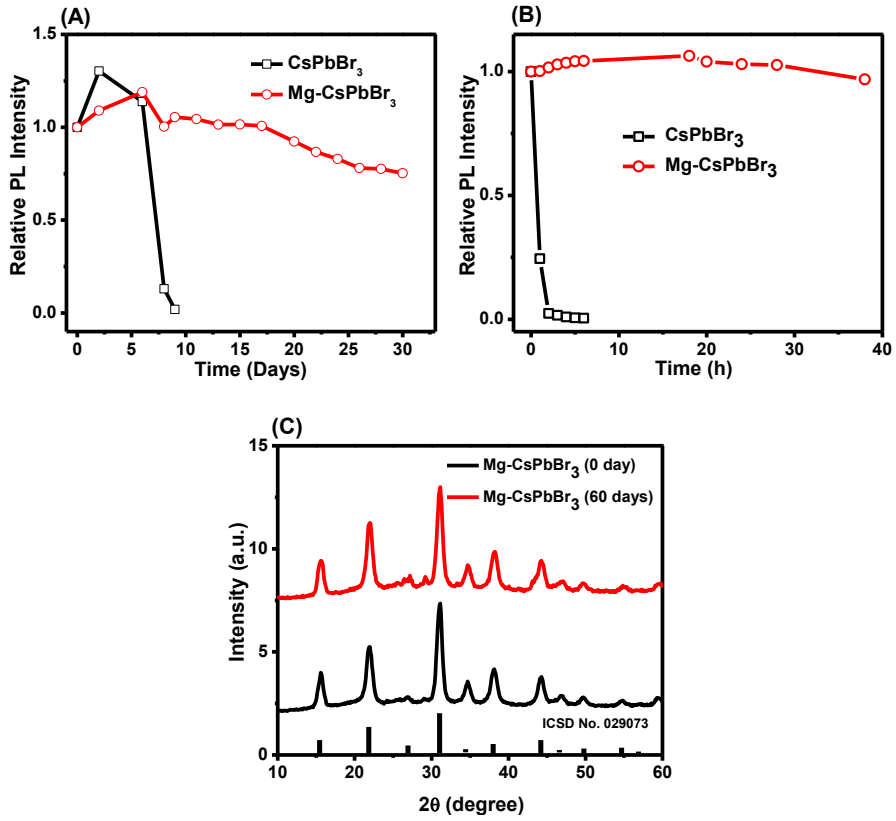

Figure 3.7. *Comparison of the stability of undoped and doped $CsPbBr_3$ NCs. (A) Air-stability under ambient condition and (B) Photo-stability under 365 nm (8W) continuous UV illumination. (C) PXRD pattern of freshly prepared and 60 days aged sample kept at ambient condition. (D) Digital images (under 365 nm UV illumination, 8W) of the doped and undoped samples in presence of 20µL ethanol at various time intervals.*

-bound oleylammonium cations, which give a more hydrophobic nature to the doped NCs.[74] The $MgBr_2$ treatment provides a bromide-rich surface for the doped $CsPbBr_3$ NCs that attracts more oleylammonium cations.[75] A drop of the ratio of Cs/Pb atomic percentage in the $CsPbBr_3$ NCs from ~0.81 to ~0.73 (as evident from the EDX data) upon doping confirms the replacement of some Cs ions from the surface by oleylammonium cations.[75-77] The presence of more oleylammonium ion at the surface is also evident from FTIR spectra of the doped $CsPbBr_3$ NCs (Figure A1.8) mentioned earlier. Thus both improved crystallinity and hydrophobicity play important roles in enhancing the stability of the doped NCs. The superior air- and photo-stability of the doped $CsPbCl_3$ NCs is evident from Figure A1.18 and A1.19. A table collecting the stability and optical properties of green- and violet-emitting perovskite NCs obtained through B-site doping is provided as supporting information (Table A1.3). It highlights the air-, photo-stability and robustness towards polar media of our doped NCs *vis-a-vis* the other samples.

3.3. Summary

It is shown that room temperature post-synthetic treatment of the $CsPbX_3$ (X = Cl and Br) NCs with MgX_2 leads to incorporation of significant quantity of Mg^{2+} into the NCs yielding systems that are brightly luminescent, highly stable, less toxic and more resistant towards polar environment. A model explaining the improved PL properties of the doped systems is proposed based on the findings of the ultrafast pump-probe and temperature dependent PL measurements. Excellent optical properties, less toxicity and high stability of these NCs under different conditions make these systems promising for optoelectronic and photovoltaic applications.

References:

1. A. Kojima, K. Teshima, Y. Shirai and T. Miyasaka, *J. Am. Chem. Soc.*, 2009, ***131***, 6050-6051.
2. M. M. Lee, J. Teuscher, T. Miyasaka, T. N. Murakami and H. J. Snaith, *Science* 2012, ***338***, 643-647.
3. N. J. Jeon, H. Na, E. H. Jung, T.-Y. Yang, Y. G. Lee, G. Kim, H.-W. Shin, S. I. Seok, J. Lee and J. Seo, *Nature Energy*, 2018, ***3***, 682–689.
4. W. S. Yang, B.-W. Park, E. H. Jung, N. J. Jeon, Y. C. Kim, D. U. Lee, S. S. Shin, J. Seo, E. K. Kim, J. H. Noh and S. I. Seok, *Science* 2017, ***356***, 1376-1379.
5. S. D. Stranks and H. J. Snaith, *Nature Nanotechnology*, 2015, ***10***, 391–402.
6. X. Du, G. Wu, J. Cheng, H. Dang, K. Ma, Y.-W. Zhang, P.-F. Tan and S. Chen, *RSC Adv.*, 2017, ***7***, 10391-10396
7. Y. Wang, X. Li, J. Song, L. Xiao, H. Zeng and H. Sun, *Adv. Mater.*, 2015, ***27***, 7101-7108.
8. F. Deschler, M. Price, S. Pathak, L. E. Klintberg, D.-D. Jarausch, R. Higler, S. Hüttner, T. Leijtens, S. D. Stranks, H. J. Snaith, M. Atatüre, R. T. Phillips and R. H. Friend, *J. Phys. Chem. Lett.*, 2014, ***5***, 1421-1426.
9. S. Yakunin, D. N. Dirin, Y. Shynkarenko, V. Morad, I. Cherniukh, O. Nazarenko, D. Kreil, T. Nauser and M. V. Kovalenko, *Nature Photonics*, 2016, ***10***, 585–589.
10. P. Ramasamy, D.-H. Lim, B. Kim, S.-H. Lee, M.-S. Lee and J.-S. Lee, *Chem. Commun.*, 2016, ***52***, 2067-2070
11. V. Caligiuri, M. Palei, M. Imran, L. Manna and R. Krahne, *ACS Photonics*, 2018, ***5***, 2287-2294.
12. R. Zhang, J. Fan, X. Zhang, H. Yu, H. Zhang, Y. Mai, T. Xu, J. Wang and H. J. Snaith, *ACS Photonics*, 2016, ***3***, 371-377.
13. L. Protesescu, S. Yakunin, M. I. Bodnarchuk, F. Krieg, R. Caputo, C. H. Hendon, R. X. Yang, A. Walsh and M. V. Kovalenko, *Nano Lett*, 2015, ***15***, 3692-3696.
14. B. A. Koscher, O. K. Swabeck, O. D. Bronstein and A. P. Alivisatos, *J. Am. Chem. Soc.*, 2017, ***139***, 6566-6569.
15. J. Pan, Y. Shang, J. Yin, M. D. Bastiani, W. Peng, I. Dursun, L. Sinatra, A. M. El-Zohry, M. N. Hedhili, A.-H. Emwas, O. F. Mohammed, Z. Ning and O. M. Bakr, *J. Am. Chem. Soc.*, 2018, ***140***, 562-565.
16. W.-J. Yin, T. Shi and Y. Yan, *Adv. Mater.*, 2014, ***26***, 4653-4658.

17. M. V. Kovalenko, L. Protesescu and M. I. Bodnarchuk, *Science*, 2017, ***358***, 745-750.
18. G. Nedelcu, L. Protesescu, S. Yakunin, M. I. Bodnarchuk, M. J. Grotevent and M. V. Kovalenko, *Nano Lett.*, 2015, ***15***, 5635-5640.
19. Q. A. Akkerman, V. D'Innocenzo, S. Accornero, A. Scarpellini, A. Petrozza, M. Prato and L. Manna, *J. Am. Chem. Soc.*, 2015, ***137***, 10276-10281.
20. F. Zhang, H. Zhong, C. Chen, X.-g. Wu, X. Hu, H. Huang, J. Han, B. Zou and Y. Dong, *ACS Nano*, 2015, ***9***, 4533-4542.
21. M. Imran, V. Caligiuri, M. Wang, L. Goldoni, M. Prato, R. Krahne, L. D. Trizio and L. Manna, *J. Am. Chem. Soc.*, 2018, ***140***, 2656−2664.
22. A. Dutta, R. K. Behera, P. Pal, P. D. S. Baitalik and D. N. Pradhan, *Angew. Chem., Int. Ed*, 2019, ***58***, 5552-5556.
23. Q. A. Akkerman, G. Rainò, M. V. Kovalenko and L. Manna, *Nature Materials*, 2018, ***17***, 394–405.
24. S. Seth, T. Ahmed, A. De and A. Samanta, *ACS Energy Lett.*, 2019, ***4***, 1610-1618.
25. T. Tachikawa, I. Karimata and Y. Kobori, *J. Phys. Chem. Lett.*, 2015, ***6***, 3195-3201.
26. S. Seth, N. Mondal, S. Patra and A. Samanta, *J. Phys. Chem. Lett.*, 2016, ***7***, 266-271.
27. J.-K. Chen, J.-P. Ma, S.-Q. Guo, Y.-M. Chen, Q. Zhao, B.-B. Zhang, Z.-Y. Li, Y. Zhou, J. Hou, Y. Kuroiwa, C. Moriyoshi, O. M. Bakr, J. Zhang and o.-T. Sun, *Chem. Mater.*, 2019, ***31***, 3974-3983.
28. N. Mondal, A. De and A. Samanta, *ACS Energy Lett.*, 2019, ***4***, 32-39.
29. T. Ahmed, S. Seth and A. Samanta, *Chem. Mater.*, 2018, ***30***, 3633-3637.
30. G. H. Ahmed, J. K. El-Demellawi, J. Yin, J. Pan, D. B. Velusamy, M. N. Hedhili, E. Alarousu, O. M. Bakr, H. N. Alshareef and O. F. Mohammed, *ACS Energy Lett.*, 2018, ***3***, 2301-2307.
31. A. De, S. Das, N. Mondal and A. Samanta, *ACS Materials Lett.*, 2019, ***1***, 116-122.
32. J.-P. Ma, Y.-M. Chen, L.-M. Zhang, S.-Q. Guo, J.-D. Liu, H. Li, B.-J. Ye, Z.-Y. Li, Y. Zhou, B.-B. Zhang, O. M. Bakr, J.-Y. Zhang and H.-T. Sun, *J. Mater. Chem. C*, 2019, ***7***, 3037-3048
33. J.-P. Ma, J. Yin, Y.-M. Chen, Q. Zhao, Y. Zhou, H. Li, Y. Kuroiwa, C. Moriyoshi, Z.-Y. Li, O. M. Bakr, O. F. Mohammed and H.-T. Sun, *ACS Materials Lett.*, 2019, ***1***, 185-191.
34. S. Mandal, D. Roy, C. K. De, S. Ghosh, M. Mandal, A. Das and P. K. Mandal, *Nanoscale Adv.*, 2019, ***1***, 3506-3513
35. A. Dutta, R. K. Behera, S. K. Dutta, S. D. Adhikari and N. Pradhan, *J. Phys. Chem. Lett.*, 2018, ***9***, 6599-6604.
36. X. Zheng, Y. Hou, H.-T. Sun, O. F. Mohammed, E. H. Sargent and O. M. Bakr, *J. Phys. Chem. Lett.*, 2019, ***10***, 2629-2640.
37. D. P. Nenon, K. Pressler, J. Kang, B. A. Koscher, J. H. Olshansky, W. T. Osowiecki, M. A. Koc, L.-W. Wang and A. P. Alivisatos, *J. Am. Chem. Soc.*, 2018, ***140***, 17760-17772.
38. J.-S. Yao, J. Ge, B.-N. Han, K.-H. Wang, H.-B. Yao, H.-L. Yu, J.-H. Li, B.-S. Zhu, J.-Z. Song, C. Chen, Q. Zhang, H.-B. Zeng, Y. Luo and S.-H. Yu, *J. Am. Chem. Soc.*, 2018, ***140***, 3626-3634.
39. W. v. d. Stam, J. J. Geuchies, T. Altantzis, K. H. W. v. d. Bos, J. D. Meeldijk, S. V. Aert, S. Bals, D. Vanmaekelbergh and O. d. M. Donega, *J. Am. Chem. Soc.*, 2017, ***139***, 4087-4097.

40. A. B. F. Vitoreti, S. Agouram, M. S. d. l. Fuente, V. Muñoz-Sanjosé, M. A. SchiavonIván and Mora-Seró, *J. Phys. Chem. C*, 2018, ***122***, 14222-14231.
41. S. Li, Z. Shi, F. Zhang, L. Wang, Z. Ma, D. Yang, Z. Yao, D. Wu, T.-T. Xu, Y. Tian, Y. Zhang, C. Shan and X. J. Li, *Chem. Mater.*, 2019, ***31***, 3917-3928.
42. J. Y. Woo, Y. Kim, J. Bae, T. G. Kim, J. W. Kim, D. C. Lee and S. Jeong, *Chem. Mater.*, 2017, ***29***, 7088-7092.
43. Z.-J. Yong, S.-Q. Guo, J.-P. Ma, J.-Y. Zhang, Z.-Y. Li, Y.-M. Chen, B.-B. Zhang, Y. Zhou, J. Shu, J.-L. Gu, L.-R. Zheng, O. M. Bakr and H.-T. Sun, *J. Am. Chem. Soc.*, 2018, **140**, 9942-9951.
44. Y. Zhai, X. Bai, G. Pan, J. Zhu, H. Shao, B. Dong, L. Xua and H. Song, *Nanoscale*, 2019, ***11***, 2484-2491.
45. R. K. Behera, S. D. Adhikari, S. K. Dutta, A. Dutta and N. Pradhan, *J. Phys. Chem. Lett.*, 2018, ***9***, 6884-6891.
46. S. D. Adhikari, R. K. Behera, S. Bera and N. Pradhan, *J. Phys. Chem. Lett.*, 2019, ***10***, 1530-1536.
47. M. R. Rahimzadeh, M. R. Rahimzadeh, S. Kazemi and A.-a. Moghadamnia, *Caspian J Intern Med.*, 2017, **8**, 135–145.
48. C. W. Bock, A. Kaufman and J. P. Glusker, *Inorg. Chem.*, 1994, **33**, 419-427.
49. D. R. Lide, CRC Press: Boca Raton, FL, USA, 2007.
50. M. R. Filip and F. Giustino, *J. Phys. Chem. C*, 2016, ***120***, 166-173.
51. Q. Huang, Y. Zou, S. A. Bourelle, T. Zhai, T. Wu, Y. Tan, Y. Li, J. Li, S. Duhm, T. Song, L. Wang, F. Deschler and B. Sun, *Nanoscale Horiz.*, 2019, ***4***, 924-932
52. R. D. Shannon, *Acta Crystallogr.*, 1976, ***32***, 751-767.
53. M. Liu, G. Zhong, Y. Yin, J. Miao, K. Li, C. Wang, X. Xu, C. Shen and H. Meng, *Adv. Sci.*, 2017, ***4***, 1700335.
54. B. A. Koscher, Z. Nett and A. P. Alivisatos, *ACS Nano*, 2019, ***13***, 11825-11833.
55. W. Liu, Q. Lin, H. Li, K. Wu, I. Robel, J. M. Pietryga and V. I. Klimov, *J. Am. Chem. Soc.*, 2016, ***138***, 14954-14961.
56. A. De, N. Mondal and A. Samanta, *Nanoscale*, 2017, ***9***, 16722-16727.
57. S. W. Eaton, M. Lai, N. A. Gibson, A. B. Wong, L. Dou, J. Ma, L.-W. Wang, S. R. Leone and P. Yang, *Proceedings of the National Academy of Sciences*, 2016, ***113***, 1993-1998.
58. M. Zhang, Z. Zheng, Q. Fu, Z. Chen, J. He, S. Zhang, L. Yan, Y. Hu and W. Luo, *CrystEngComm*, 2017, ***19***, 6797-6803
59. J. Endres, M. Kulbak, L. Zhao, B. P. Rand, D. Cahen, G. Hodes and A. Kahn, *J. Appl. Phys.*, 2017, ***121***, 035304.
60. Y.Yamada, M.Miura, K.Tajima, M.Okada and K.Yoshimura, *Sol. Energy Mater. Sol. Cells*, 2014, ***120***, 631−634.
61. V. S. Chirvony, S. González-Carrero, I. Suárez, R. E. Galian, M. Sessolo, H. J. Bolink, J. P. Martínez-Pastor and J. Pérez-Prieto, *J. Phys. Chem. C*, 2017, ***121***, 13381-13390.
62. N. Mondal and A. Samanta, *Nanoscale*, 2017, ***9***, 1878–1885.
63. N. Mondal, A. De, S. Das, S. Paul and A. Samanta, *Nanoscale*, 2019, ***11***, 9796-9818.
64. R. Begum, M. R. Parida, A. L. Abdelhady, B. Murali, O. M. Alyami, G. H. Ahmed, M. N. Hedhili, O. M. Bakr and O. F. Mohammed, *J. Am. Chem. Soc.*, 2017, ***139***, 731-737.
65. J.-S. Yao, J. Ge, K.-H. Wang, G. Zhang, B.-S. Zhu, C. Chen, Q. Zhang, Y. Luo, S.-H. Yu and H.-B. Yao, *J. Am. Chem. Soc.*, 2019, ***141***, 2069-2079.

66. A. Swarnkar, W. J. Mir and O. Nag, *ACS Energy Lett.*, 2018, ***3***, 286-289.
67. P. Liu, W. Chen, W. Wang, B. Xu, D. Wu, J. Hao, W. Cao, F. Fang, Y. Li, Y. Zeng, R. Pan, S. Chen, W. Cao, X. W. Sun and K. Wang, *Chem. Mater.*, 2017, ***29***, 5168-5173.
68. C. Bi, S. Wang, Q. Li, S. V. Kershaw, J. Tian and A. L. Rogach, *J. Phys. Chem. Lett.*, 2019, ***10***, 943-952.
69. L. Protesescu, S. Yakunin, S. Kumar, J. Bär, F. Bertolotti, N. Masciocchi, A. Guagliardi, M. Grotevent, I. Shorubalko, M. I. Bodnarchuk, C.-J. Shih and M. V. Kovalenko, *ACS Nano*, 2017, ***11***, 3119-3134.
70. J. Shamsi, A. S. Urban, M. Imran, L. D. Trizio and L. Manna, *Chem. Rev.*, 2019, ***119***, 3296-3348.
71. F. Li, Y. Liu, H. Wang, Q. Zhan, Q. Liu and Z. Xia, *Chem. Mater.*, 2018, ***30***, 8546-8554.
72. G. Huang, C. Wang, S. Xu, S. Zong, J. Lu, Z. Wang, C. Lu and Y. Cui, *Adv. Mater.*, 2017, ***29***, 1700095.
73. Z. Yang, M. Wei, O. Voznyy, P. Todorovic, M. Liu, R. Quintero-Bermudez, P. Chen, J. Z. Fan, A. H. Proppe, L. N. Quan, G. Walters, H. Tan, J.-W. Chang, U.-S. Jeng, S. O. Kelley and E. H. Sargent, *J. Am. Chem. Soc.*, 2019, ***141***, 8296-8305.
74. Q. Zhong, M. Cao, Y. Xu, P. Li, Y. Zhang, H. Hu, D. Yang, Y. Xu, L. Wang, Y. Li, X. Zhang and Q. Zhang, *Nano Lett.*, 2019, ***19***, 4151-4157.
75. Y. Cai, H. Wang, Y. Li, L. Wang, Y. Lv, X. Yang and R.-J. Xie, *Chem. Mater.*, 2019, ***31***, 881-889.
76. V. K. Ravi, P. K. Santra, N. Joshi, J. Chugh, S. K. Singh, H. Rensmo, P. Ghosh and A. Nag, *J. Phys. Chem. Lett.*, 2017, ***8***, 4988-4994.
77. S. Paul and A. Samanta, *ACS Energy Lett.*, 2020, ***5***, 64−69.

CHAPTER 4

Phase-Stable and Highly Luminescent Red/NIR-Emitting All-Inorganic and Hybrid Perovskite Nanocrystals

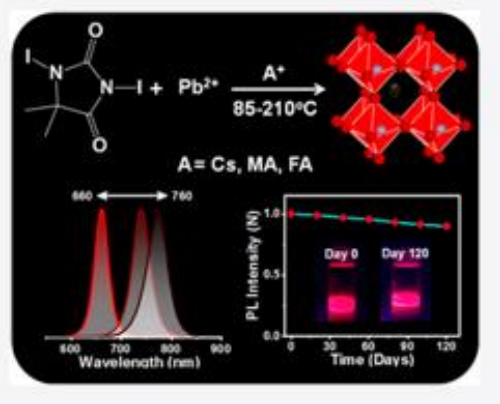

ACS Energy Lett. 2021, 6, 3780−3787

Overview

Because of their low band gap, iodide-based lead halide perovskite NCs with generic formula $APbI_3$ [A = Cs^+, MA^+, and FA^+] are most suitable for solar photovoltaic applications. However, because of their poor phase stability, obtaining these NCs with stable red/NIR emission is a challenging task and is termed the 'red wall'. We report here a generic protocol for direct synthesis of all three NCs with extraordinary characteristics employing DIDMH as iodide precursor. The as-synthesized NCs are phase-pure and monodispersed, and they exhibit phase stability for several months in ambient conditions and PLQY of near-unity for the red-emitting $CsPbI_3$ NCs and ~74 ± 2% and 67 ± 2% for NIR-emitting $MAPbI_3$ and $FAPbI_3$ NCs, respectively. The results highlight the greater efficacy of DIDMH over other iodide precursors, with which the present task could not be achieved earlier. The high-quality NCs for the red−NIR region may be useful for developing efficient perovskite-based solar photovoltaic devices.

4.1. Introduction

Among the lead-halide perovskite NCs, the iodide-based $CsPbI_3$, $MAPbI_3$ and $FAPbI_3$ are most suitable for single-junction solar cells because of their narrow bandgap.[1-10] However, unlike the widely explored bromide-based green-emitting $APbBr_3$ NCs, poor phase stability of these iodide-based NCs leads to their rapid deterioration even under ambient condition and prevents practical utility of these otherwise promising substances.[6, 11-17] The challenging task of obtaining small size and iodide-based perovskites emitting in the red and NIR region with high photoluminescence efficiency and stability, termed as 'perovskite red wall',[18] needs to accomplished for its importance.

The stability and optical property of the NCs depends to a great extent on their method of preparation.[5, 19-23] The widely used *two-precursor* method of synthesis, in which PbI_2 is used as a source of both lead and iodine, produces NCs of poor quality.[5] For example, $MAPbI_3$ and $FAPbI_3$ NCs obtained by this method exhibit a broad size distribution and low PLQY,[24-26] and even $CsPbI_3$ NCs show a PLQY of only ~30-70%.[11, 17] The *three-precursor* method, which was developed later, employs a separate halide precursor for synthesis in a halide-rich condition, produces much better quality NCs.[27, 28] However, despite great efforts in recent past in overcoming the 'perovskite red wall', the success is rather limited and no generic method of preparation of all three NCs with high phase stability and PLQY is available till date.[8, 18, 29-31] For example, Kovalenko and co-workers prepared high quality $FAPbI_3$ and mixed-cation $FA_{0.1}Cs_{0.9}PbI_3$ NCs with PLQY of ~70% that retained their phase for several months.[18] Akkerman et al succeeded in obtaining highly luminescent (PLQY ~74-79%) $CsPbI_3$ and $FAPbI_3$ NCs, which were stable for at least 2 weeks.[29] Similarly, stable $CsPbI_3$ NCs with near-unity PLQY was also prepared by Pradhan and co-workers and later by Cai et al.[8, 30, 31] Interestingly, in none of these reports, all three red-and NIR-emitting $APbI_3$ NCs could be obtained following a generic method. To the best of our knowledge, it was only Manna and co-workers, who could obtain all three iodide-based NCs using benzoyl iodide as iodide precursor with a PLQY of 58% for $CsPbI_3$, 45% for $MAPbI_3$ and 55% for $FAPbI_3$ NCs.[32] While these $CsPbI_3$ NCs were reported to be stable for ~20 days, the stability data for the two hybrid systems was not mentioned.

Recognizing the immense potential of the $CsPbI_3$, and $MAPbI_3$ and $FAPbI_3$ NCs in solar photovoltaic and optoelectronic applications, and lack of any common method of preparation of these systems in their bright and stable form, we have been working for some time towards developing a generic method for the preparation of all three all-inorganic and hybrid systems overcoming the 'perovskite red wall'. While it became

clear to us that the iodide precursor chosen for synthesis was a key factor, but we did not have much success with the iodo-analogs of the bromide precursors, which produced great quality green-emitting $APbBr_3$ NCs. For example, using N-bromosuccinamide (NBS) as bromide precursor, we obtained green-emitting $APbBr_3$ NCs with near-unity PLQY,[33] but using its iodo-analog, N-iodosuccinamide (NIS), we could obtain only $CsPbI_3$ NCs, that too with PLQY of merely 27±3%. The hybrid systems could not be prepared (Figure A2.1). Moreover, it was observed that phase transformation of the prepared $CsPbI_3$ NCs started within a day of synthesis (Figure A2.1). Our continued work in this direction and careful search of literature led us to DCDMH, which was reported to be a highly effective reagent for chloro-lactonization reaction even at -40°C.[34, 35] The N(1) halogen of DCDMH acts as an inductive activator of the N(3) halogen, which serves as the actual source of halogen. This important piece of information led us to explore the utility of its iodide analogue, DIDMH, as an iodinating agent for synthesis of the $APbI_3$ NCs.

4.2. Results and Discussion

The reaction of DIDMH with OA produces HI (Scheme A2.1)[33, 36] that reacts with OAm generating oleylammonium iodide (OAm^+I^-),[29-32] which served as the active source of iodide in the reaction (Figure 4.1a).[30, 31] The $APbI_3$ NCs were obtained using an optimum quantity of the oleate salt of the 'A' cation followed by rapid quenching of the reaction mixture (Figure 4.1a, details in Chapter 2, section 2.2.3.2).

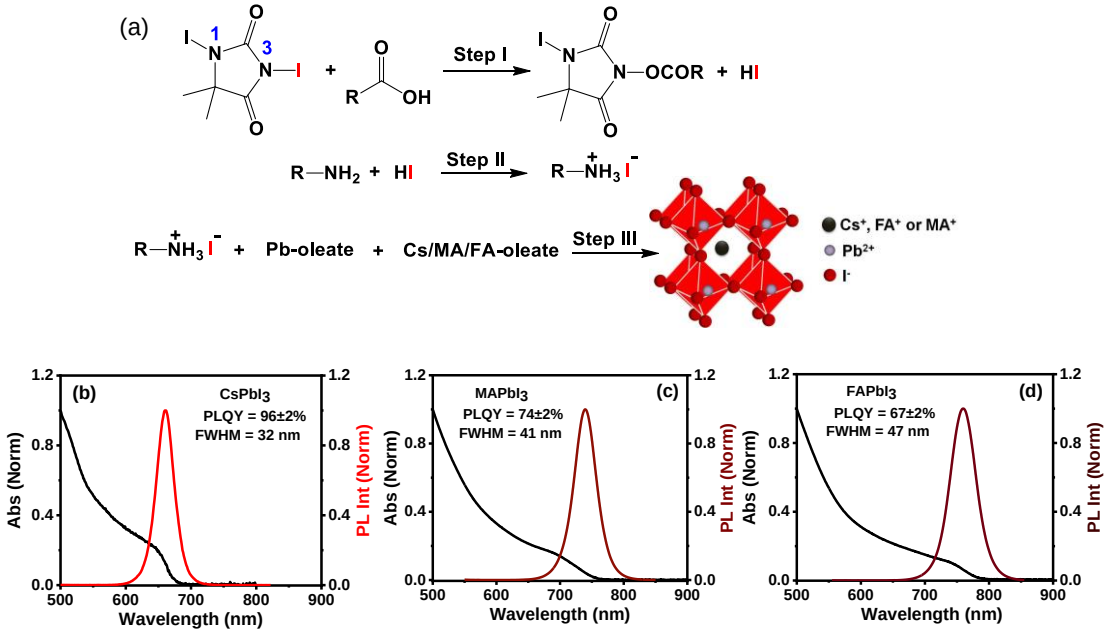

Figure 4.1. *a) Schematic representation of the steps in DIDMH-mediated synthesis of $APbI_3$ NCs. UV-Vis absorption (black) and corresponding PL spectra (colored) of b) $CsPbI_3$, c) $MAPbI_3$ and d) $FAPbI_3$ NCs. λ_{exc} = 540 nm.*

The formation of OAm^+I^- in the reaction medium was confirmed by the strong ~220 absorption in the UV spectrum and ~0.12 ppm down-shift of the ^1H NMR signal of the α-protons of OAm in the reaction mixture with respect to pure OAm (Figure A2.2 and A2.3).[29] It was also found that injection of OAm^+I^- (after preparing separately) into the reaction medium instead of its *in situ* generation produced only moderately luminescent $CsPbI_3$ NCs (PLQY of 38±2%), which exhibited poor stability under ambient condition (Figure A2.4). The phase transformation started within a day of synthesis. These results are consistent with the literature, which indicates *in situ* passivation of the perovskite NCs is much more effective in producing brightly luminescent well-passivated stable NCs.[33, 37, 38, 39]

The Pb:I molar precursor ratio and reaction temperature were found to be the two most critical factors that influenced the quality of the NCs. A 1:3 molar precursor ratio of Pb:I and a temperature of 210°C for all-inorganic $CsPbI_3$ and 85°C for both $MAPbI_3$ and $FAPbI_3$ were found as the optimum conditions for obtaining strongly luminescent, mono-dispersed, and phase-stable NCs. When the reactions were performed below or above the optimum temperature, the obtained NCs consisted of multiple phases with inhomogeneous size distribution, and they exhibited broad PL bandwidth and substantially low PLQY (Figure A2.5-A2.8 and Table A2.1).

The excellent optical properties of all $APbI_3$ NCs are evident from their high PLQY and narrow FWHM (Figure 4.1b-d, Table 4.1). The red-emitting $CsPbI_3$ NCs exhibit near-unity (96±2%) PLQY. The NIR-emitting hybrid systems, $MAPbI_3$ and $FAPbI_3$ NCs, also exhibit impressive PLQYs of 74±2 and 67±2%, respectively. These values are comparable with their best PLQY values reported till date.[18, 23] We are not aware of any literature reporting such high PLQY of both the hybrid and all-inorganic perovskite NCs prepared by a common procedure. These NCs not only exhibit excellent PL, they also display a number of other extraordinary features like high phase-purtity, monodispersity and remarkable stability under a variety of conditions. Moreover, the method is also found to be highly reproducible (Figure A2.9).

Bright field TEM images indicate cubic shape and fairly narrow size distribution of all the $APbI_3$ NCs (Figure 4.2a-c and A2.10) with mean edge length of $CsPbI_3$, $MAPbI_3$ and $FAPbI_3$ NCs are 8.8±1.2, 12.2±1.2 and 14.4±2.6 nm, respectively obtained

Table 4.1. *The parameters of synthesis and optical properties of the NCs.*

Systems	Temp (°C)	OA (mL)	OAm (mL)	λ_{em} (nm)	FWHM (nm)	PLQY (%)
$CsPbI_3$	210	1	1	660±1	32	96±2
$MAPbI_3$	85	1.6	0.8	740±1	41	74±2
$FAPbI_3$	85	1.6	0.8	761±2	47	67±2

from different batches of the NCs. The cubic and tetragonal crystal phases of $CsPbI_3$ and $MAPbI_3$ NCs, respectively are confirmed by comparing the PXRD patterns (Figure 4.2d and 4.2e) with the available ICSD codes (see insets). The diffraction peaks of the $FAPbI_3$ NCs (Figure 4.2f) suggest a cubic perovskite structure.[32, 40] Moreover, the interplanar spacings of the NCs estimated from their high-resolution TEM (HRTEM) images (Figure 4.2a, b and c insets) are consistent with the literature values.[12, 18, 41] Notwithstanding two

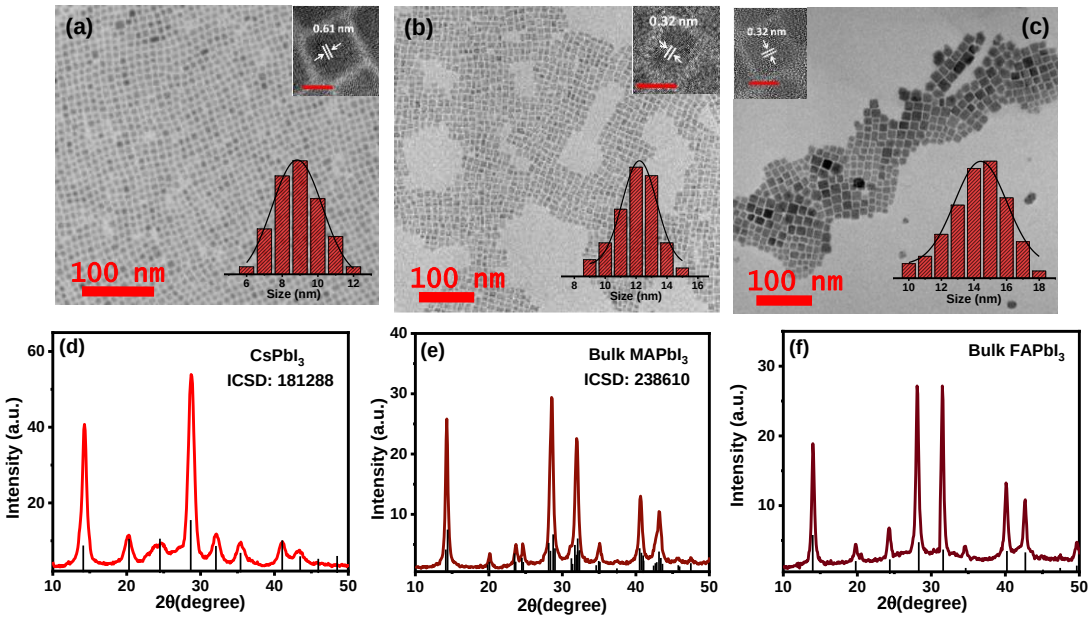

Figurer 4.2. *Bright field TEM images of a) $CsPbI_3$, b) $MAPbI_3$ and c) $FAPbI_3$ NCs. The scale bar is 100 nm for all samples. Inset shows HRTEM images of the NCs (in scale bars 5, 10 and 10 nm, respectively) with interplanar spacing corresponding to the (100), (220) and (200) planes of the $CsPbI_3$, $MAPbI_3$ and $FAPbI_3$ NCs, respectively. PXRD patterns of d) $CsPbI_3$, e) $MAPbI_3$ and f) $FAPbI_3$ NCs. Absence of any additional diffraction peaks suggests that the $APbI_3$ NCs are highly phase pure in nature.*

unidentified peaks in Figure 4.2d and one in Figure 4.2f, which is not uncommon,[9, 10, 29, 42] absence of any additional diffraction peak corresponding to other phases (as per ICSD data) eliminates the possibility of formation of any secondary undesired phase of the NCs indicating high phase purity.

We have examined the PL decay characteristics of the $APbI_3$ NCs to understand the photophysical processes in these systems. The PL of the $CsPbI_3$ NCs decays bi-exponentially with time constants of 9.17 (68%) and 17.12 (32%) ns (Figure 4.3a and Table A2.2). The first component, which has a major contribution, is assigned to direct excitonic recombination and the slower component to shallow trap-mediated band-edge recombination.[43-45] It is important to note here that the shallow trap states even in defect-tolerant $CsPbI_3$ NCs with near-unity PLQY arise from intrinsic point defects, which usually do not participate in the nonradiative recombination of the photogenerated charge carriers.[46] For $CsPbI_3$ NCs, a range of lifetimes including some large and short values are reported.[11, 12, 42, 47, 48] A short PL lifetime for good quality $CsPbI_3$ NCs is not uncommon[17, 44] as iodide-rich nature of the surface[49] and/or small size of the NCs (smaller than effective Bohr-diameter of ~12 nm) can contribute to it.[50, 51] Absence of any sub-

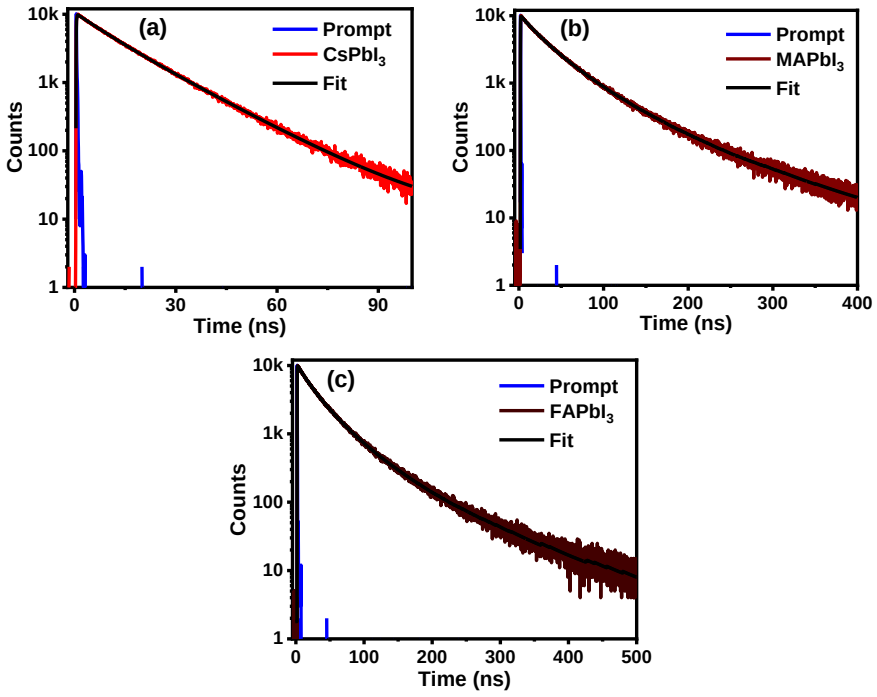

Figure 4.3. *PL decay profile of a) $CsPbI_3$, b) $MAPbI_3$ and c) $FAPbI_3$ NCs and bi/tri-exponential fits to the data. The samples were excited at 481 nm using a diode laser and the decay was monitored at their respective PL maxima. The decay parameters are presented in Table A2.2.*

nanosecond component suggests that the $CsPbI_3$ NCs are largely free from surface defect related nonradiative recombination channels. A much higher value of the radiative rate constant (k_r) compared to the nonradiative one (k_{nr}) is consistent with high PLQY of the system (Table A2.2). The PL decay profiles of both $MAPbI_3$ (Figure 3b) and $FAPbI_3$ NCs (Figure 4.3c) are found to be tri-exponential and the third (shortest) lifetime-component is attributed to trapping (Table A2.2).[32]

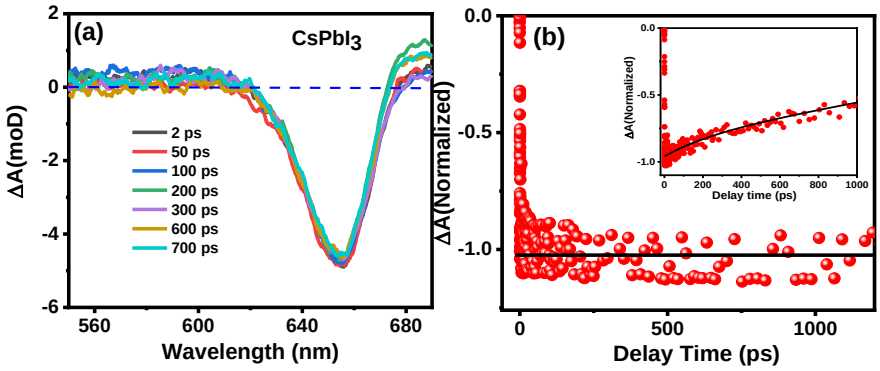

Figure 4.4. *a) TA spectra of $CsPbI_3$ NCs at different time intervals after excitation by a fs-laser (λ_{ex} = 530 nm, ~100 fs). b) Bleach recovery kinetics of the NCs (λ_{ex} = 530 nm), monitored at the bleach maxima ~656 nm. The inset shows bleach recovery kinetics of the $CsPbI_3$ NCs prepared using Pb:I molar ratio of 1:2.*

We have studied the carrier dynamics of the NCs in the early time-scale using ultrafast (femtosecond resolution) TA technique. The strong bleach signal (ΔA = -ve), which arises from ground state depopulation of the system,[52, 53] exhibits very sluggish recovery even after ~700 ps (Figure 4.4a), which is more clearly observable from the nearly flat bleach recovery kinetic trace (Figure 4.4b, Table A2.3) indicating a long (>1000 ps) recombination component and negligible nonradiative carrier trapping in these NCs.[10, 42] In contrast, the bleach recovery dynamics of samples of $CsPbI_3$ NCs, which are prepared using a lower Pb:I ratio of 1:2, exhibit clearly an ultrafast trapping component (243±15 ps) (Figure 4.4b inset and Table A2.3).

As mentioned earlier, the biggest issue with the red/NIR-emitting perovskite NCs is their phase sensitivity under ambient condition. For instance, large ionic radius of iodine (~220 pm) induces octahedral distortion in $CsPbI_3$ NCs and triggers phase transformation from luminescent cubic (α) phase to non-luminescent orthorhombic (δ) phase within few days.[11, 12] The hybrid $MAPbI_3$ NCs, on the other hand, are thermally less stable due to volatile MA^+ and the $FAPbI_3$ NCs, which are best suited for single-absorber

solar cell, transform into non-perovskite photo-inactive hexagonal (δ) phase, due to hygroscopic nature of large FA^+.[13-16] Therefore, stability of these important substances is a major issue that needs to be urgently addressed. Interestingly, all three $APbI_3$ NCs prepared following our protocol are exceptionally stable under ambient atmospheric condition. For example, the $CsPbI_3$ NCs stored in a sealed bottle in air retains almost its original PL for several months (Figure A2.11 and Table A2.4). Excellent stability of the $CsPbI_3$ NCs is also evident from retention of >80% PLQY even after exposure in ambient condition for 20 days with relative humidity of ~55-70 % (Figure 4.5a). The unchanged PXRD pattern of a film of the sample kept on bench-top for the same period also suggests superb phase stability of these NCs (Figure 4.5b). Excellent photostability and water resistivity of these NCs is also evident from their robustness towards continuous UV light exposure and in presence of water (Figure A2.12 and A2.13). The hybrid $MAPbI_3$ and $FAPbI_3$ NCs are also found to be highly stable and resistant to the environmental stresses. The unchanged PXRD pattern even after 2 months of storage in ambient conditions is a reflection of their phenomenal phase (black, α) stability in air (Figure 4.5d and A2.14b).

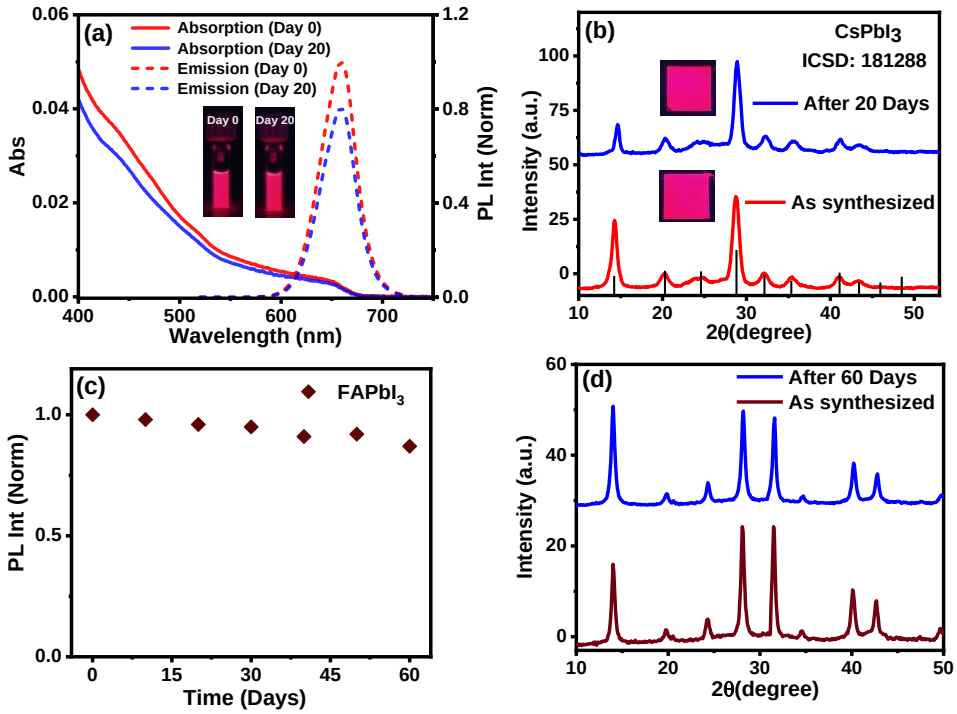

Figure 4.5. *a) UV-Vis absorption and PL spectra of as-synthesized and 20 days old $CsPbI_3$ NCs kept under ambient condition on bench-top. b) PXRD patterns of the same samples. c) Air stability of (FA)PbI_3 NCs colloidal dispersion stored in ambient conditions and d) PXRD patterns of the corresponding as-synthesized and aged samples stored in air.*

Retention of ~87-90% of the original PL during the same period further confirms the stability of these systems (Figure 4.5c and A2.14a). Retention of the cubic morphology of all three samples stored for 2 months under ambient condition is also evident from the TEM images (Figure A2.15). The exceptional phase and optical stability of all three $APbI_3$ NCs under different external conditions is quite remarkable, considering that these are red/NIR-emitting promising candidates for both photovoltaic and optoelectronic applications. The outstanding characteristics of the NCs obtained by our method are clearly evident when they are compared with samples obtained by other methods (Table A2.5).

To determine the factors that impart exceptional qualities to these $APbI_3$ NCs, we closely inspect the analytical data using $CsPbI_3$ NCs as the model system. Elemental analysis of a large scanned area of the FESEM images of the $CsPbI_3$ NCs (EDX measurements) shows a Cs:Pb:I ratio of 0.88:1.00:3.26, suggesting an iodide-rich surface of these NCs (Figure A2.16a, A2.16c) and hence, the absence of iodide vacancy related surface defects, which facilitate nonradiative deactivation of the photogenerated carriers. Indeed, the iodide deficient $CsPbI_3$ NCs prepared using 1:2 Pb:I molar ratio are poorly luminescent (Figure A2.16b) and exhibit an ultrafast bleach recovery component due to nonradiative transition through the iodide vacancy mediated surface trap states (Figure 4.4b inset). XPS measurements were performed to examine the chemical environment of the constituting elements of the $CsPbI_3$ NCs (Figure 4.6, A2.17 and A2.18). The Pb 4f core level XPS spectrum exhibits $4f_{7/2}$ (138.1 eV) and $4f_{5/2}$ (143.0 eV) peaks, which are assigned to the Pb-I bond in the NCs (Figure 4.6a).[31, 37] For the $CsPbI_3$ NCs, which are prepared using a Pb:I molar ratio of 1:2, each band exhibits a hump towards the lower binding energy region (~136.69 and~141.67 eV), which is attributed to Pb-oleate species in these NCs (Figure 4.6b).[38, 54-56] Appearance of the Pb-oleate signal for these NCs indicate iodide vacancy related surface defect[38] and the absence of this signal for the $CsPbI_3$ NCs prepared using 1:3 molar ratio of Pb:I implies that use of a stoichiometric amount of DIDMH produces an iodide-rich surface. The latter is also evident from the calculated atomic % ratio of the NCs (insets of Figure 4.6 and Table A2.6). It is to be noted that the atomic % ratio estimated from the XPS measurements (Table A2.6) is in good agreemnt with that obtained from EDX studies (Figure A2.16c). This iodide-rich environment is a key element in providing better stability and bringing a desirable near-perfect surface structure of the $CsPbI_3$ NCs.[28, 31, 42, 57] The surface ligand environment, which also influences the stability and PL properties of the perovskite NCs,[8, 58-63] is assessed by ^{1}H NMR and FTIR studies. The ^{1}H NMR spectra (Figure A2.19) show two

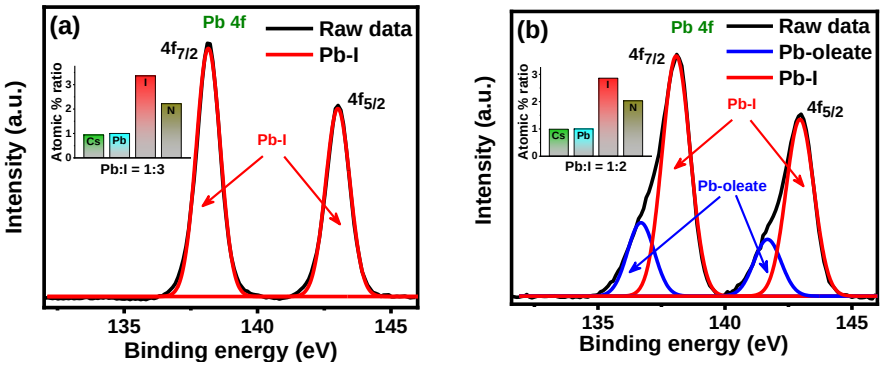

Figure 4.6. *High resolution XPS spectra of Pb 4f for $CsPbI_3$ NCs prepared using a Pb:I molar ratio of a) 1:3 and b) 1:2. Inset shows the estimated atomic percentage ratio (with respect to Pb) of the samples from the data.*

broad peaks (at ~6.9 and ~3.6 ppm), which are signatures of the α-protons (NH_3^+) and β-protons ($-CH_2-N$), respectively, of OAm^+.[58, 60] This not only indicates the presence of OAm^+ on the surface of the $CsPbI_3$ NCs, but broadness of the two peaks suggests that OAm^+ is firmly anchored on the surface.[8, 60] Interestingly, the ~2.4 ppm peak (marked a) characteristic of the oleate ion, is quite sharp indicating that unlike OAm^+ it is not bound to the NCs. Lack of surface-bound oleate indicates the absence of under-coordinated Pb^{2+} on the surface and reconfirms an iodide rich surface of the NCs.[60] This observation is consistent with the XPS data, which did not show any signal due to Pb-oleate for the $CsPbI_3$ NCs obtained with a Pb:I ratio of 1:3 (Figure 4.6a). The asymmetric and symmetric bending absorption of N^+-H at ~1641 and 1554 cm^{-1}, respectively in the FTIR spectrum further confirms surface-bound nature of the OAm^+ (Figure A2.20).[8, 58] A point to note here is that due to overlapping spectral signatures of OA, OAm and ODE (both in ^{1}H NMR and FTIR), it is not possible to specify from these data whether DIDMH also acts as a protective surface ligand for the synthesized NCs (Figure A2.21). However, high solubility of DIDMH in polar solvents like MeOAc and ACN, which were used for purification of the NCs, indicates this possibility to be very low. An iodide rich surface attracts greater number of OAm^+ giving it access to the surface sites occupied originally by Cs^+. Low Cs^+ content in the EDX and XPS data and a higher N/Pb ratio for $CsPbI_3$ NCs in XPS measurement support this point (Figure 4.6 inset, A2.18c, and Table A2.6). Substitution of some of these surface Cs^+ with alkylammonium ligand provides high stability to the perovskite NCs as the surface-bound ligand (OAm^+ in the present case) prevents crystal deformation through octahedral tilting (i.e., in maintaining the sensitive α phase of the NCs).[8, 64, 65] The tightly bound hydrophobic envelope of OAm^+ also provides

protection from moisture and polar media, thus preventing the decomposition of the sensitive cubic phase of the NCs.[61, 66] Although OA does not bind to the surface of the NCs, it helps maintaining a ratio of OAm^+ and oleate (or OAm and OA) that is crucial for the stability of the final product.[60] It is therefore evident that oleylammonium iodide produced *in situ* during the reaction helps to maintain an iodide rich environment, which leads to the oleylammonium-lead iodide terminated surface by replacing some Cs^+ that provides exceptional stability and optical properties to the NCs obtained by this method.

4.3. Summary

In summary, monodispersed, phase-pure, highly stable, and luminescent red-NIR-emitting $CsPbI_3$, $MAPbI_3$, and $FAPbI_3$ NCs have been obtained by a generic method employing DIDMH as iodide precursor. DIDMH-assisted formation of the oleylammonium-lead iodide-terminated surface is shown to impart the exceptional characteristics of these NCs. The outstanding phase durability and excellent PLQY of all three all-inorganic and hybrid systems obtained by a common procedure by breaching the so-called perovskite red wall significantly brightens the prospect of utilization of these narrow band gap materials for optoelectronic and photovoltaic applications, particularly in single-absorber solar cells.

References:

1. C. C. Stoumpos and M. G. Kanatzidis, *Acc. Chem. Res.*, 2015, **48**, 2791–2802.
2. J. S. Manser, J. A. Christians and P. V. Kamat, *Chem. Rev.*, 2016, **116**, 12956–13008.
3. M. V. Kovalenko, L. Protesescu and M. I. Bodnarchuk, *Science*, 2017, **358**, 745-750.
4. H. Huang, M. I. Bodnarchuk, S. V. Kershaw, M. V. Kovalenko and A. L. Rogach, *ACS Energy Lett.*, 2017, **2**, 2071–2083.
5. J. Shamsi, A. S. Urban, M. Imran, L. D. Trizio and L. Manna, *Chem. Rev.*, 2019, **119**, 3296–3348.
6. A. Dutta and N. Pradhan, *ACS Energy Lett.*, 2019, **4**, 709–719.
7. G. E. Eperon, G. M. Paternò, R. J. Sutton, A. Zampetti, A. A. Haghighirad, F. Cacialli and H. J. Snaith, *J. Mater. Chem. A*, 2015, **3**, 19688-19695
8. A. Dutta, S. K. Dutta, S. D. Adhikari and N. Pradhan, *Angew. Chem. Int. Ed.*, 2018, **57**, 9083–9087.
9. C. Wang, A. S. R. Chesman and J. J. Jasieniak, *Chem. Commun.*, 2017, **53**, 232-235
10. F. Liu, Y. Zhang, C. Ding, S. Kobayashi, T. Izuishi, N. Nakazawa, T. Toyoda, T. Ohta, S. Hayase, T. Minemoto, K. Yoshino, S. Dai and Q. Shen, *ACS Nano*, 2017, **11**, 10373–10383.

11. L. Protesescu, S. Yakunin, M. I. Bodnarchuk, F. Krieg, R. Caputo, C. H. Hendon, R. X. Yang, A. Walsh and M. V. Kovalenko, *Nano Lett.*, 2015, **15**, 3692–3696.
12. A. Swarnkar, A. R. Marshall, E. M. Sanehira, B. D. Chernomordik, D. T. Moore, J. A. Christians, T. Chakrabarti and J. M. Luther, *Science*, 2016, **354**, 92-95.
13. E. J. Juarez-Perez, Z. Hawash, S. R. Raga, L. K. Ono and Y. Qi, *Energy Environ. Sci.*, 2016, **9**, 3406-3410.
14. J. Yang, B. D. Siempelkamp, D. Liu and T. L. Kelly, *ACS Nano*, 2015, **9**, 1955–1963.
15. D. H. Fabini, D. C. C. Stoumpos, D. G. Laurita, D. A. Kaltzoglou, D. A. G. Kontos, D. P. Falaras, P. D. M. G. Kanatzidis and P. D. R. Seshadri, *Angew.Chem. Int. Ed.*, 2016, **55**, 15392–15396.
16. S. Masi, A. s. F. Gualdrón-Reyes and I. n. Mora-Seró, *ACS Energy Lett.*, 2020, **5**, 1974−1985.
17. J. Pan, Y. Shang, J. Yin, M. D. Bastiani, W. Peng, I. Dursun, L. Sinatra, A. M. El-Zohry, M. N. Hedhili, A.-H. Emwas, O. F. Mohammed, Z. Ning and O. M. Bakr, *J. Am. Chem. Soc.*, 2018, **140**, 562–565.
18. L. Protesescu, S. Yakunin, S. Kumar, J. Bär, F. Bertolotti, N. Masciocchi, A. Guagliardi, M. Grotevent, I. Shorubalko, M. I. Bodnarchuk, C.-J. Shih and M. V. Kovalenko, *ACS Nano*, 2017, **11**, 3119–3134.
19. Q. A. Akkerman, G. Rainò, M. V. Kovalenko and L. Manna, *Nature Materials*, 2018, **17**, 394–405.
20. H. Huang, L. Polavarapu, J. A. Sichert, A. S. Susha, A. S. Urban and A. L. Rogach, *NPG Asia Materials*, 2016, **8**, 328.
21. X. Zheng, Y. Hou, H.-T. Sun, O. F. Mohammed, E. H. Sargent and O. M. Bakr, *J. Phys. Chem. Lett.*, 2019, **10**, 2629−2640.
22. N. Pradhan, *ACS Energy Lett.*, 2019, **4**, 1634−1638.
23. J.-F. Liao, Y.-X. Chen, J.-H. Wei, Y.-T. Cai, X.-D. Wang, Y.-F. Xu and D.-B. Kuang, *Nano Research*, 2019, **12**, 2640–2645.
24. O. Vybornyi, S. Yakunin and M. V. Kovalenko, *Nanoscale*, 2016, **8**, 6278-6283.
25. I. Levchuk, A. Osvet, X. Tang, M. Brandl, J. D. Perea, F. Hoegl, G. J. Matt, R. Hock, M. Batentschuk and C. J. Brabec, *Nano Lett.*, 2017, **17**, 2765–2770.
26. F. Zhang, H. Zhong, C. Chen, X.-g. Wu, X. Hu, H. Huang, J. Han, B. Zou and Y. Dong, *ACS Nano*, 2015, **9**, 4533–4542.
27. S. Wei, Y. Yang, X. Kang, L. Wang, L. Huang and D. Pan, *Chem. Commun.*, 2016, **52**, 7265-7268.
28. P. Liu, W. Chen, W. Wang, B. Xu, D. Wu, J. Hao, W. Cao, F. Fang, Y. Li, Y. Zeng, R. Pan, S. Chen, W. Cao, X. W. Sun and K. Wang, *Chem. Mater.*, 2017, **29**, 5168−5173.
29. Q. A. Akkerman, L. Martínez-Sarti, L. Goldoni, M. Imran, D. Baranov, H. J. Bolink, F. Palazon and L. Manna, *Chem. Mater.*, 2018, **30**, 6915–6921.
30. A. Dutta, R. K. Behera, P. Pal, S. Baitalik and N. Pradhan, *Angew. Chem. Int. Ed.*, 2019, **58**, 5552–5556.
31. Y. Cai, H. Wang, Y. Li, L. Wang, Y. Lv, X. Yang and R.-J. Xie, *Chem. Mater.*, 2019, **31**, 881–889.
32. M. Imran, V. Caligiuri, M. Wang, L. Goldoni, M. Prato, R. Krahne, L. D. Trizio and L. Manna, *J. Am. Chem. Soc.*, 2018, **140**, 2656–2664.
33. S. Paul and A. Samanta, *ACS Energy Lett.*, 2020, ***5***, 64–69.
34. D. C. Whitehead, R. Yousefi, A. Jaganathan and B. Borhan, *J. Am. Chem. Soc.*, 2010, **132**, 3298–3300.

35. R. Yousefi, D. C. Whitehead, J. M. Mueller, R. J. Staples and B. Borhan, *Org. Lett.*, 2011, **13**, 608–611.
36. H. Xue, H. Tan, D. Wei, Y. Wei, S. Lin, F. Liang and B. Zhao, *RSC Adv.*, 2013, **3**, 5382-5385.
37. Y. Wu, C. Wei, X. Li, Y. Li, S. Qiu, W. Shen, B. Cai, Z. Sun, D. Yang, Z. Deng and H. Zeng, *ACS Energy Lett.*, 2018, **3**, 2030–2037.
38. J. Y. Woo, Y. Kim, J. Bae, T. G. Kim, J. W. Kim, D. C. Lee and S. Jeong, *Chem. Mater.*, 2017, **29**, 7088–7092.
39. F. Zhang, S. Huang, P. Wang, X. Chen, S. Zhao, Y. Dong and H. Zhong, *Chem. Mater.*, 2017, **29**, 3793–3799.
40. A. A. Zhumekenov, M. I. Saidaminov, M. A. Haque, E. Alarousu, S. P. Sarmah, B. Murali, I. Dursun, X.-H. Miao, A. L. Abdelhady, T. Wu, O. F. Mohammed and O. M. Bakr, *ACS Energy Lett.*, 2016, **1**, 32–37.
41. X. Liang, R. W. Baker, K. Wu, W. Deng, D. Ferdani, P. S. Kubiak, F. Marken, L. Torrente-Murciano and P. J. Cameron, *React. Chem. Eng.*, 2018, **3**, 640-644.
42. F. Liu, C. Ding, Y. Zhang, T. Kamisaka, Q. Zhao, J. M. Luther, T. Toyoda, S. Hayase, T. Minemoto, K. Yoshino, B. Zhang, S. Dai, J. Jiang, S. Tao and Q. Shen, *Chem. Mater.*, 2019, **31**, 798–807.
43. V. S. Chirvony, S. González-Carrero, I. Suárez, R. E. Galian, M. Sessolo, H. J. Bolink, J. P. Martínez-Pastor and J. Pérez-Prieto, *J. Phys. Chem. C*, 2017, **121**, 13381–13390.
44. J.-S. Yao, J. Ge, K.-H. Wang, G. Zhang, B.-S. Zhu, C. Chen, Q. Zhang, Y. Luo, S.-H. Yu and H.-B. Yao, *J. Am. Chem. Soc.*, 2019, **141**, 2069–2079.
45. X. Zhang, M. Lu, Y. Zhang, H. Wu, X. Shen, W. Zhang, W. Zheng, V. L. Colvin and W. W. Yu, *ACS Central Science*, 2018, **4**, 1352-1359.
46. J. Kang and L.-W. Wang, *J. Phys. Chem. Lett.*, 2017, ***8***, 489–493.
47. W. J. Mir, A. Swarnkar and A. Nag, *Nanoscale*, 2019, **11**, 4278-4286.
48. N. Mondal, A. De, S. Das, S. Paul and A. Samanta, *Nanoscale*, 2019, **11**, 9796-9818.
49. W. Kong, T. Ding, G. Bi and H. Wu, *Phys. Chem. Chem. Phys.*, 2016, **18**, 12626-12632.
50. V. Malgras, S. Tominaka, J. W. Ryan, J. Henzie, T. Takei, K. Ohara and Y. Yamauchi, *J. Am. Chem. Soc.*, 2016, **138**, 13874–13881.
51. D. X. Zhang, P. X. Bai, H. Wu, X. Zhang, C. Sun, P. Y. Zhang, P. W. Zhang, P. W. Zheng, P. W. W. Yu and P. A. L. Rogach, *Angew.Chem. Int.Ed.*, 2018, **57**, 3337 – 3342.
52. N. Mondal and A. Samanta, *Nanoscale*, 2017, **9**, 1878-1885.
53. I. Dursun, P. Maity, J. Yin, B. Turedi, A. A. Zhumekenov, K. J. Lee, O. F. Mohammed and O. M. Bakr, *Adv. Energy Mater.*, 2019, **9**, 1900084.
54. M. Li, X. Zhang, K. Matras-Postolek, H.-S. Chen and P. Yang, *J. Mater. Chem. C,*, 2018, **6**, 5506-5513.
55. L.R.Pederson, *J. Electron Spectrosc. Relat. Phenom.*, 1982, **28**, 203–209.
56. W. E. Morgan and J. R. V. Wazer, *J. Phys. Chem.*, 1973, **77**, 964–969.
57. Y. Huang, W. Luan, M. Liu and L. Turyanska, *J. Mater. Chem. C*, 2020, ***8***, 2381-2387.
58. J. D. Roo, M. Ibáñez, P. Geiregat, G. Nedelcu, W. Walravens, J. Maes, J. C. Martins, I. V. Driessche, M. V. Kovalenko and Z. Hens, *ACS Nano*, 2016, **10**, 2071–2081.

59. A. Pan, B. He, X. Fan, Z. Liu, J. J. Urban, A. P. Alivisatos, L. He and Y. Liu, *ACS Nano*, 2016, **10**, 7943–7954.
60. V. K. Ravi, P. K. Santra, N. Joshi, J. Chugh, S. K. Singh, H. Rensmo, P. Ghosh and A. Nag, *J. Phys. Chem. Lett.*, 2017, **8**, 4988–4994.
61. S. Das, A. De and A. Samanta, *J. Phys. Chem. Lett.*, 2020, ***11***, 1178–1188.
62. D. W.-k. Koh, D. S. Park and Y. Ham, *ChemistrySelect*, 2016, ***1***, 3479-3482.
63. L. Wu, Q. Zhong, D. Yang, M. Chen, H. Hu, Q. Pan, H. Liu, M. Cao, Y. Xu, B. Sun and Q. Zhang, *Langmuir*, 2017, ***33***, 12689–12696.
64. Y. Chen, S. R. Smock, A. H. Flintgruber, F. A. Perras, R. L. Brutchey and A. J. Rossini, *J. Am. Chem. Soc.*, 2020, ***142***, 6117–6127.
65. L. Pan, L. Zhang, Y. Qi, K. Conkle, F. Han, X. Zhu, D. Box, T. V. Shahbazyan and Q. Dai, *ACS Appl. Nano Mater.*, 2020, ***3***, 9260−9267.
66. Q. Zhong, M. Cao, Y. Xu, P. Li, Y. Zhang, H. Hu, D. Yang, Y. Xu, L. Wang, Y. Li, X. Zhang and Q. Zhang, *Nano Lett.*, 2019, **19**, 4151–4157.

CHAPTER 5

Direct Synthesis of High Quality $APbX_3$ ($A= Cs^+$, MA^+ and FA^+; $X= Cl^-$, Br^- and I^-) Nanocrystals Following a Generic Approach

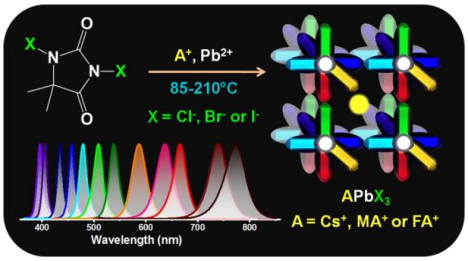

Nanoscale, 2022, 14, 9349-9358

Overview

Direct synthesis of the $APbX_3$ [A= Cs^+, MA^+ or FA^+ and X= Cl^-, Br^- or I^-] perovskite NCs following a generic approach is a challenging task even today. Motivated by our recent success (Chapter 4) in obtaining directly high-quality red/NIR-emitting $APbI_3$ NCs employing DIDMH as iodide precursor, we explore here whether violet/green-emitting $APbCl_3$ and $APbBr_3$ NCs can also be obtained using the bromo- and chloro-analog of DIDMH keeping in mind that a positive outcome will provide the generic protocol for direct synthesis of all $APbX_3$ NCs using similar halide precursors. It is shown that green-emitting $APbBr_3$ NCs with near-unity PLQY and violet-emitting $CsPbCl_3$ NCs with an impressive PLQY of ~70%, mixed-halide NCs, $CsPb(Cl/Br)_3$ and $CsPb(Br/I)_3$, emitting in the blue and yellow-orange region with PLQY of 87-95% and 68-98%, respectively can indeed be obtained employing the bromo- and chloro-analog of DIDMH. These NCs exhibit remarkable stability in different conditions including polar environment. Femtosecond pump-probe studies show no ultrafast carrier trapping in these systems. The key elements of the halide precursors that facilitated the synthesis and the factors contributing to the excellent characteristics of the NCs are determined by careful analysis of the data. The results are of great significance because a direct method of obtaining highly luminescent and stable $APbX_3$ NCs (excepting violet-emitting hybrid NCs) is eventually identified and the work provides valuable insight on selection of appropriate halide precursors for development of superior systems.

5.1. Introduction

Owing to their fascinating optical properties,[1-8] the popularity of the lead-halide based perovskite NCs with general chemical formula of $APbX_3$ in optoelectronic applications as LEDs, lasing medium and photodetectors has skyrocketed in recent years.[9-14] Increasing demand for various lighting and display technologies has generated huge interest in developing methodologies for preparation of high quality perovskite NCs.[8, 12, 15, 16] While these studies helped targeted synthesis of violet-, green- or red-emitting all-inorganic and/or hybrid NCs,[6, 17-31] no generic method of obtaining all these systems with good optical properties and stability is reported till date despite intense efforts. For example, Pradhan and co-workers obtained $CsPbX_3$ (X= Cl, Br and I) NCs with near-unity PLQY, but not the hybrid systems.[6] Manna and co-workers succeeded in obtaining all $APbX_3$ NCs with highest PLQY of 65, 92 and 58% for the violet-, green- and red-emitting NCs, respectively using benzoyl halide as halide precursor, but stability of these systems (except for $CsPbI_3$) was not examined.[32]

The halide precursor chosen for synthesis of the NCs is an important parameter that determines the yield, quality and even the stability. The halide precursor reacts with a nucleophile and generate HX.[32] The latter combines with OAm forming oleylammonium halides (OAm^+X^-), which serves not only as an active source of halogen, but also passivates the halide vacancies and protects the surface from its surrounding.[6] An understanding of the chemistry of formation of HX from the halide precursor is key to identifying the right halide precursor for synthesis of quality NCs. Our recent success in obtaining high quality red/NIR-emitting iodide-based $APbI_3$ (with A= Cs, MA and FA) NCs with unmatched optical properties and stability using DIDMH as iodide precursor[33] substantiates this statement. As the goal is to develop a generic strategy for the preparation of not only the iodides, but the other halides as well, the next step naturally is to examine whether green-emitting $APbBr_3$ and violet-emitting $APbCl_3$ NCs can also be obtained using the bromo- and chloro-analog of DIDMH as halide precursor. Herein we undertake this study, and the results show that the bromo- and chloro-analogs of DIDMH, namely, DBDMH and DCDMH, are equally effective in producing highly luminescent and stable $APbBr_3$ and $APbCl_3$ NCs. This implies that we have eventually found a generic protocol for direct synthesis of phase pure, highly mono-dispersed, stable and luminescent $APbX_3$ NCs (A= Cs, MA, FA and X= Cl, Br, I or mixtures) emitting over the entire visible range using 1,3-dihalo-5,5-dimethylhydantoin (DXDMH) as halide precursor.

5.2. Results and Discussion

Scheme 5.1 depicts preparation of the $APbX_3$ NCs by hot-injection method using DXDMH (Figure A3.1) in presence of OA and OAm in ODE. The mechanism of *in situ* generation of OAm^+X^- as intermediate and subsequent formation of the NCs is shown in Scheme A3.1 and additional details can be found in Chapter 4.[33] The quality of the as-synthesized NCs, as indicated by PLQY and size-uniformity, is found to depend on the Pb:X molar precursor ratio and reaction temperature. 1:3 (Pb:X) molar precursor ratio was found optimum for all systems except for $MAPbCl_3$ NCs (discussed later). A lower content of the halide precursor yields NCs with a mixture of phases, broad size distribution and low PLQY (Figure A3.2, Table A3.1). The optimum reaction temperatures for the synthesis of most luminescent, phase pure, homogeneous, and stable all-inorganic $CsPbX_3$ and mixed-halide NCs, green-emitting hybrid $APbBr_3$ and violet-emitting hybrid $APbCl_3$ NCs are found to be 210, 165 and 95°C, respectively (Table 5.1). Reactions when carried out below the optimum temperature, the obtained NCs were of inhomogeneous size distribution displaying higher PL bandwidth and rapidly decreasing PLQY (Figure A3.3, A3.4 and Table A3.1). The reproducibility of the present method is examined and found to be very good (Figure A3.5).

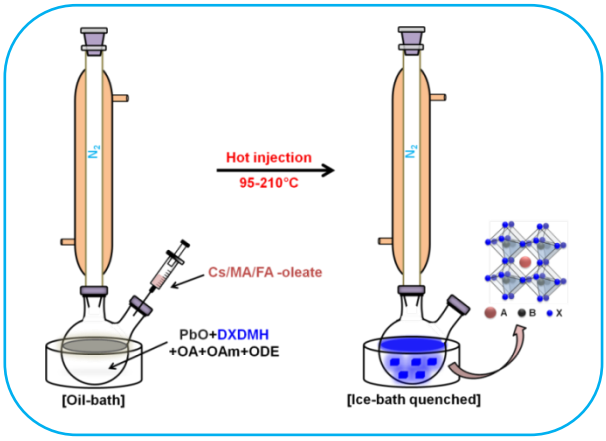

Scheme 5.1. *DXDMH-mediated direct synthesis of the $APbX_3$ (X= Cl and Br) NCs.*

Bright-field TEM images show cubic morphology and narrow size distribution of all $APbX_3$ NCs (Figure 5.1A-C and A3.6A-C), with average edge length of 8.03±0.5, 10.06±0.6 and 14.6±1.3 nm for the $CsPbBr_3$, $MAPbBr_3$ and $FAPbBr_3$ NCs, respectively and 7.08±0.05, 12.5±1.15 and 10.4±1.28 nm for the $CsPbCl_3$, $MAPbCl_3$ and $FAPbCl_3$ NCs, respectively (Figure A3.6 and A3.7). Additional TEM images of different resolutions are made available in Figure A3.7 and A3.8. High crystallinity of the NCs

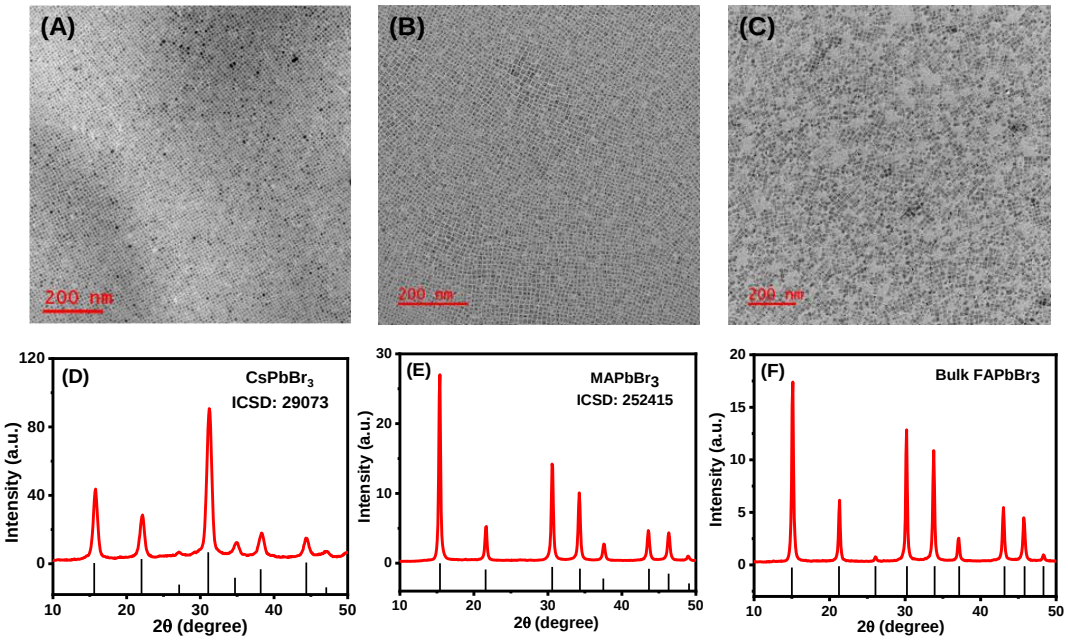

Figure 5.1. *Bright-field TEM images of (A) $CsPbBr_3$, (B) $MAPbBr_3$ and (C) $FAPbBr_3$ NCs. The scale is bar is 200 nm for all the samples. PXRD patterns of (D) $CsPbBr_3$, (E) $MAPbBr_3$ and (F) $FAPbBr_3$ NCs with reference patterns obtained from their bulk cubic phases.*

allows clear observation of the lattice fringes in high-resolution TEM images (Figure A3.9 and A3.10). The PXRD patterns are also consistent with cubic crystal structure of all $APbX_3$ NCs (Figure 5.1D-F and A3.6D-F). Comparison of the measured PXRD patterns with available ICSD codes confirms the cubic perovskite structures for $CsPbBr_3$ (ICSD Code: 29073), $MAPbBr_3$ (ICSD Code: 252415) and $CsPbCl_3$ (ICSD Code: 23108) NCs. The cubic crystal structure of the $FAPbBr_3$, $MAPbCl_3$ and $FAPbCl_3$ NCs is confirmed by comparing the diffraction peaks with the literature data.[32, 34, 35] The absence of any additional diffraction peak in the PXRD spectra eliminates the possibility of formation of any secondary (undesired) phases in the prepared NCs and suggests high phase purity of the samples.

The excellent optical properties of the NCs obtained by the present method are evident from high PLQY and narrow FWHM of all three green-emitting $APbBr_3$ NCs emitting between 513±1 and 533±2 nm (Figure 5.2). All $APbBr_3$ NCs exhibit near-unity (99±1%) PLQY with narrow FWHM of 19, 21 and 20 nm for $CsPbBr_3$, $MAPbBr_3$ and $FAPbBr_3$ NCs, respectively (Figure 5.2A-C and Table 5.1). These values are comparable or better than the best PLQY reported for these systems by any method till date.[22, 32] Similarly, the violet-emitting $APbCl_3$ NCs, especially all-inorganic $CsPbCl_3$ NCs display

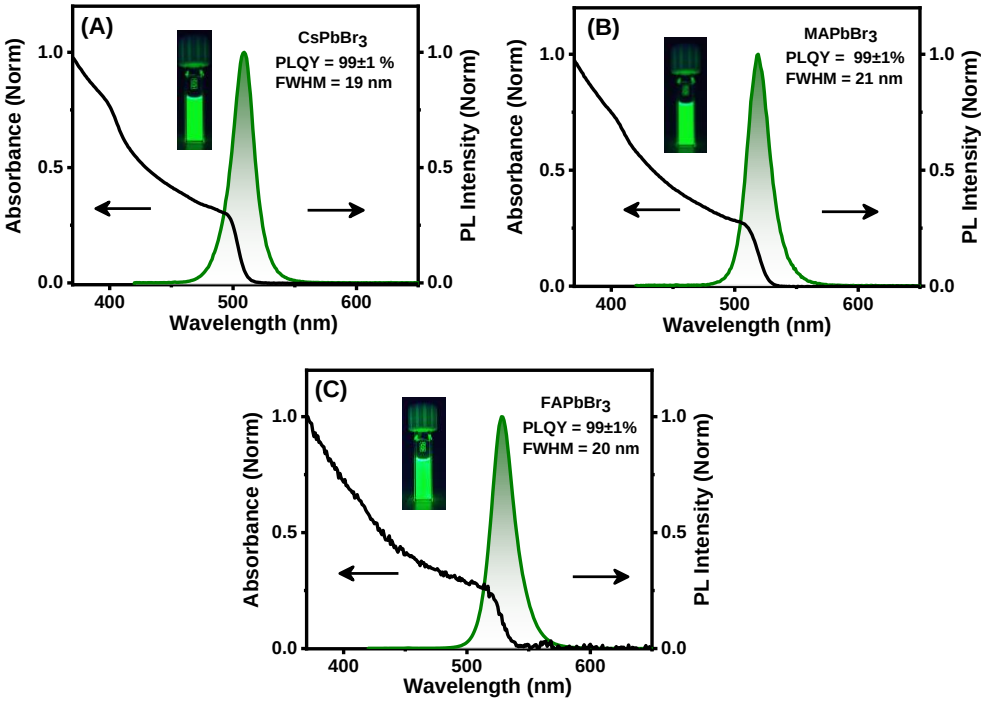

Figure 5.2. *UV-Vis absorption and PL spectra of (A) $CsPbBr_3$, (B) $MAPbBr_3$ and (C) $FAPbBr_3$ NCs. The excitation wavelength (λ_{ex}) was 400 nm in each case. Digital images of the respective NCs under 365 nm UV illuminations are also shown in the insets.*

impressive optical properties (Figure A3.6). A PLQY of 70±2% for violet-emitting $CsPbCl_3$ NCs (λ_{em} = 406 nm, Figure A3.6G) is quite remarkable as it represents one of the highest reported values for this system obtained by any direct method of synthesis (Table A3.2).[6, 24, 25, 32] An important point to note here is that a stoichiometric amount of DCDMH produces these brightly luminescent $CsPbCl_3$ NCs (Table A3.2), unlike earlier cases, where much higher amount of chloride precursor was necessary.[6, 24, 25, 32] We found that an excess amount of DCDMH did not have much influence on the PLQY of the system initially, but the PLQY dropped for Pb:Cl precursor ratio exceeding 1:7 (Figure A3.11). The hybrid $MAPbCl_3$ and $FAPbCl_3$ NCs, which emit in the 396 - 400 nm region, are however, found to be poorly luminescent with PLQY of 3.3±0.2% and 1.2±0.1%, respectively (Figure A3.6H-I, Table 5.1). The violet-emitting $CsPbCl_3$, $MAPbCl_3$ and $FAPbCl_3$ NCs show narrow FWHM of 10, 11 and 13 nm, respectively. Another point to note in this context is that, in case of $MAPbCl_3$ NCs, 1:3 Pb:Cl molar precursor ratio results in formation of undesired $PbCl_2$ (Figure A3.12), which is, however, not surprising as $PbCl_2$ formation during the preparation of $MAPbCl_3$ NCs is reported earlier.[32] To avoid this problem, a lower Pb:Cl ratio (1:1.5) is used for synthesis of this system (Figure

A3.12B). The reaction parameters and optical properties of all $APbX_3$ NCs (including the iodides obtained in Chapter 4)[33] are collected in Table 5.1.

Table 5.1. *Reaction conditions and PL characteristics of the $APbX_3$ NCs.*

Samples	Temp. (°C)	Pb:X	OA (mL)	OAm (mL)	PLQY (%)	FWHM (nm)	λ_{em} (nm)	Ref.
$CsPbBr_3$	210	1:3	2.0	2.0	99±1	19	513±1	This work
$MAPbBr_3$	165	1:3	1.5	0.5	99±1	21	520±2	
$FAPbBr_3$	165	1:3	1.5	0.5	99±1	20	533±2	
$CsPbCl_3$	210	1:3	2.0	2.0	70±2	10	406±1	
$MAPbCl_3$	95	1:1.5	2.0	0.4	3.3±0.2	11	397±1	
$FAPbCl_3$	95	1:3	2.0	0.8	1.2±0.1	13	400±1	
$CsPbI_3$	210	1:3	1	1	96±2	32	660±1	33
$MAPbI_3$	85	1:3	1.6	0.8	74±2	41	740±1	
$FAPbI_3$	85	1:3	1.6	0.8	67±2	47	761±2	

We examined the PL decay characteristics of the NCs to understand the associated photophysical processes. All three green-emitting ($APbBr_3$) NCs exhibit bi-exponential decay kinetics, but the violet-emitting ($APbCl_3$) NCs display a 3-component decay profile (Figure 5.3, A3.13). Specifically, PL decay of the $CsPbBr_3$ NCs (Figure 5.3A) consists of 4.97 (73%) and 12.50 (27%) ns lifetime components (Table A3.3). While the major (4.97 ns) component arises from excitonic recombination, the longer component is assigned to shallow trap-mediated excitonic recombination.[6, 22, 36] Absence of any sub-nanosecond component indicates that these NCs are free from surface defect related non-radiative recombination channels.[22] Indeed, $CsPbBr_3$(II) NCs, which are

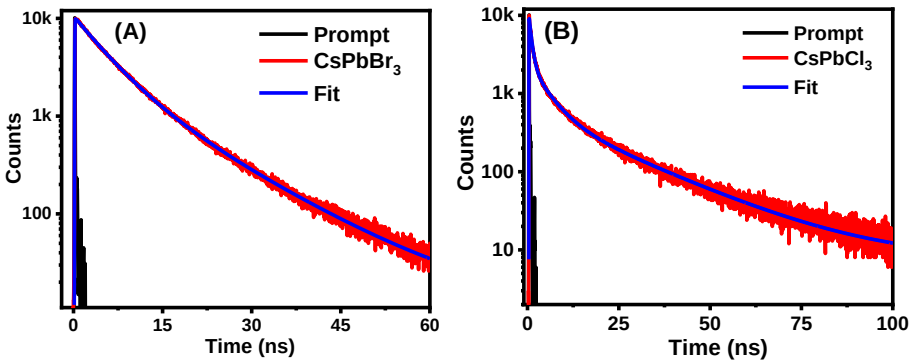

Figure 5.3. *PL decay profiles of (A) $CsPbBr_3$ and (B) $CsPbCl_3$ NCs. For recording the PL decay curves laser sources of 404 and 376 nm were used, and the PL was monitored at 513 and 406 nm for the $CsPbBr_3$ and $CsPbCl_3$ NCs, respectively.*

prepared using a lower bromide concentration (Pb:Br = 1:2), possess a sub-nanosecond component (0.61 ns, 12%) indicating the presence of surface defect states (Figure A3.14 and Table A3.3). The PL decay of the $CsPbCl_3$ NCs consists of 4.63 (19%), 20.72 (5%) and 0.47 (76%) ns lifetime components (Figure 5.3B). The shortest and major component (0.47 ns, 76%) is due to rapid nonradiative relaxation of the carriers through the trap states.[25, 37] The absence of this trapping component for the $CsPbBr_3$ NCs explains its higher PLQY compared to the $CsPbCl_3$ NCs. The calculated radiative (k_r) and non-radiative (k_{nr}) rate constants of the systems give further insight into the charge carrier recombination processes. A much higher k_r/k_{nr} value for $CsPbBr_3$ NCs compared to $CsPbCl_3$ NCs (140 vs. 2.33) is in line with the PLQY values of the systems. The PL decay profiles and associated decay parameters of other $APbX_3$ NCs are presented in Figure A3.13 and A3.14 and in Table A3.3.

The early-time photophysical processes in these systems have been studied by femtosecond TA measurements (details in Chapter 2, section 2.3.3) and for a clear understanding of these events, we have compared the ultrafast carrier dynamics of the $CsPbBr_3$ NCs and $CsPbBr_3$(II) NCs. As can be seen (Figure 5.4), the TA spectra comprising excitonic bleach (ΔA= -ve) at ~509 nm and transient absorption (ΔA= +ve) in the lower wavelength region (470 - 490 nm), are quite similar for both samples.[38, 39] However, the recovery of bleach in $CsPbBr_3$ NCs is substantially smaller than that in $CsPbBr_3$(II) NCs (~20% vs. ~46% in initial ~600 ps, Figure 5.4A and 5.4B) due to slower bleach recovery kinetics in the former system and this is clearly seen in Figure 5.4C. Moreover, while the bleach recovery is bi-exponential for the $CsPbBr_3$(II) NCs comprising a 53.2±5 ps component due to carrier trapping and a >1000 ps due to direct recombination (Table A3.4),[39-41] the dynamics is single exponential comprising only the long component in the case of $CsPbBr_3$ NCs (Figure 5.4C). Similarly, though the TA spectra of $CsPbCl_3$ and $CsPbCl_3$(II) NCs are similar (Figure 5.4D and 5.4E), the bleach recovery kinetics of the $CsPbCl_3$ NCs (Figure 5.4F) is found to be bi-exponential comprising a trapping component of 5.9±1.6 ps (27%, Table A3.4) unlike a 3-component decay of the $CsPbCl_3$(II) NCs consisting of two dominant (total 85%) ultrafast trapping components (5.8±0.3 and 74.8±5 ps) and a long direct recombination component (>1000 ps).[42] We have also performed an fs-TA experiment on the violet-emitting hybrid NCs (Figure A3.15) for the first time. The bleach recovery kinetics of these NCs are tri-exponential with large contribution (~86-89%) of ultrafast trapping component (Table A3.4) consistent with poor PLQY of these samples.

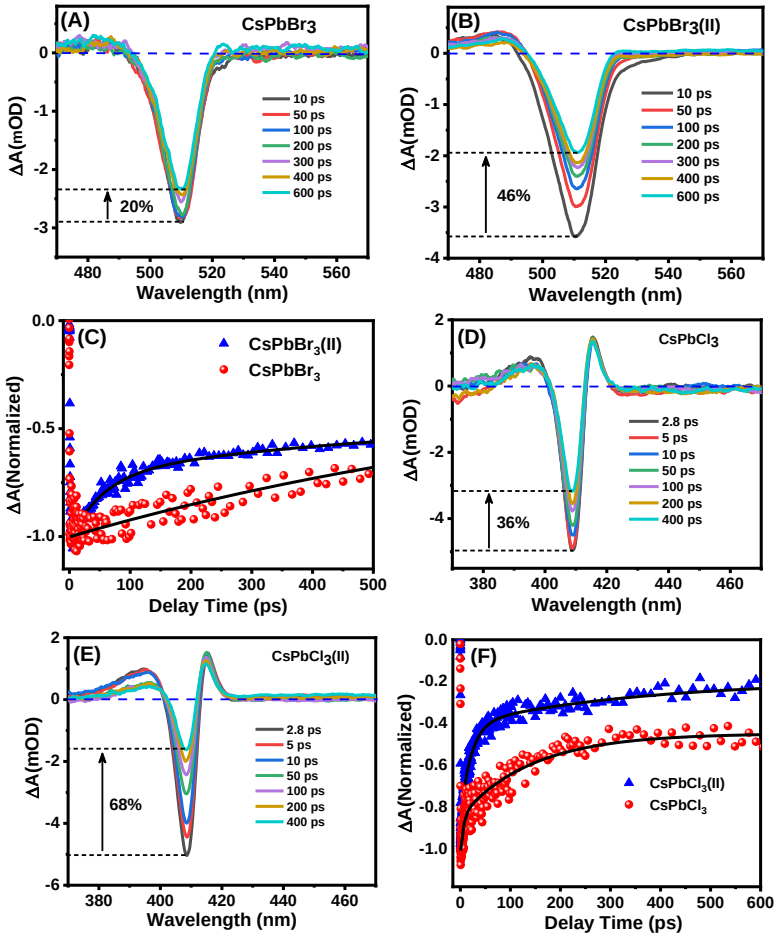

Figure 5.4. *TA spectra of (A) $CsPbBr_3$ and (B) $CsPbBr_3$(II) NCs. (C) A comparison of the bleach recovery dynamics of the two samples. TA spectra of (D) $CsPbCl_3$, (E) $CsPbCl_3$(II) and (F) bleach recovery dynamics of the two NCs. The NCs were excited at 350 nm by fs-laser pulses and the bleach recovery dynamics were monitored at respective bleach maxima.*

The universality of the present method is examined by extending the synthesis to mixed-halide $CsPb(Cl/Br)_3$ and $CsPb(Br/I)_3$ NCs as well. The mixed-halide NCs were obtained readily using appropriate quantities of two halide precursors during the reaction (Table A3.5). The blue-emitting $CsPbCl_2Br$, $CsPbCl_{1.5}Br_{1.5}$ and $CsPbClBr_2$ NCs exhibit outstanding PLQY of 87±1%, 95±1%, 96±1% with PL peak between 431 and 478 nm and narrow FWHM (Figure 5.5A, Table A3.6), as compared to commonly observed PLQY of <40% of these systems.[43-45] These values are impressive as they are comparable or better than the PLQY of previously reported blue-emitting NCs obtained by other direct methods (Table A3.7).[25, 46] The yellow-orange-emitting $CsPb(Br/I)_3$ NCs also display excellent PL properties as exemplified by narrow FWHM and PLQY of 68±2 to

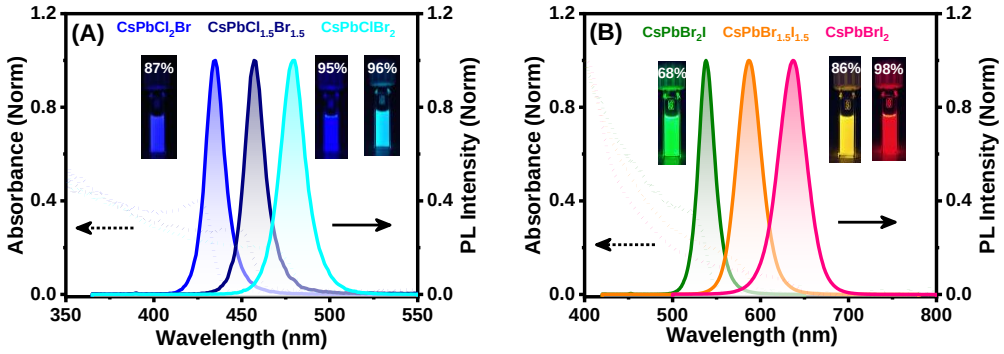

Figure 5.5. *UV-Vis absorption and PL spectra of (A) blue-emitting $CsPb(Cl/Br)_3$ and (B) yellow-orange-emitting $CsPb(Br/I)_3$ NCs obtained by using mixture of different DXDMH. The insets show digital photographs of the respective NCs under 365 nm UV light with their PLQY values.*

98±1% (Figure 5.5B, Table A3.6). We are not aware of any literature reporting this high PLQY of these mixed-halide NCs emitting in the 531 - 635 nm region by any direct synthetic method. PL decay profiles of the mixed-halide NCs are mostly tri-exponential with major contribution from the band-edge radiative recombination process (Figure A3.16 and Table A3.8). Thus, a wide 430 - 635 nm range is covered by these directly synthesized mixed-halide NCs (Figure A3.17). This wavelength range extends much wider (395 - 760 nm, Figure 5.6) when the results of our recent work (in Chapter 4) following this generic strategy is taken into consideration.[33]

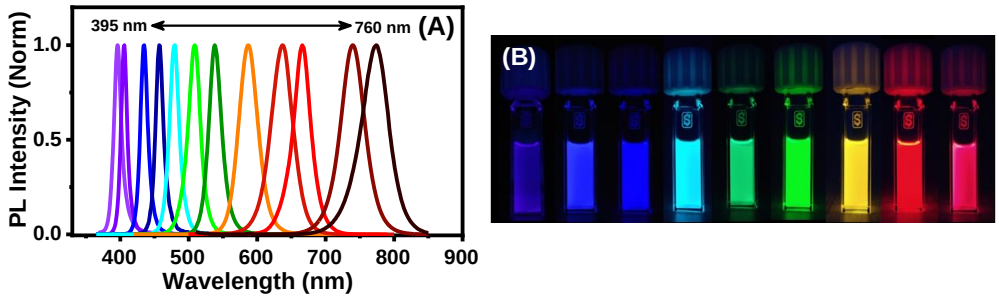

Figure 5.6. *(A) PL spectra of all $APbX_3$ (X = Cl, Br and I) and mixed-halide NCs prepared by our method (including data from Chapter 4 on $APbI_3$ NCs) showing the wide window of PL. (B) Digital photographs of the colloidal solutions of the $CsPbX_3$ NCs under UV illumination.*

Bright-field TEM images indicate cubic morphology of these mixed-halide NCs with an average size of ~6.9 - 10 nm depending on the halide compositions (Figure A3.18). Furthermore, a linear shift of the PXRD diffraction peak toward lower angle,

while moving from chloride- to iodide-based NCs (via the bromide ones), also indicates uniform cubic crystal structure of all these mixed-halide NCs (Figure A3.19).

The great effectiveness of DXDMH as halide precursor even at room-temperature (RT) is evident from instantaneous post-synthetichalide exchange reactions on the as-synthesized NCs. For example, a green colloidal dispersion of pre-synthesized $CsPbBr_3$ NCs turns violet (or red) instantly on addition of a small amount of hexane solution of DCDMH (or DIDMH) in OA and OAm due to rapid anion exchange reactions at ambient condition (Figure A3.20). This allows tuning of the PL peak position of the NCs post-synthetically over a wide range (~410 to 660 nm) using appropriate DXDMH. High reactivity of these halide precursors even at RT is quite impressive considering that commonly used metal halide solutions for halide-exchange are not very effective in non-polar media or they induce phase transformation of the system.[47] We have also examined post-synthetic A-site cation (Cs^+ here) exchange at RT by treating the $CsPbBr_3$ NCs with dilute FA–oleate solution in hexane. A gradual red-shift of the PL maximum from ~513 to ~530 nm in 15 min suggests partial replacement for Cs^+ with FA^+. The PLQY of the system is however not affected by this exchange (Figure A3.21).

Lack of long-term stability of the perovskite NCs is a major issue and a variety of methods, which include protective coating of the surface with an inert layer,[48-50] ligand engineering,[20, 24, 51] *in situ* modification,[52, 53] doping,[40, 42] etc. have been attempted for enhancing their stability. The NCs obtained by our method are found to be exceptionally stable under atmospheric conditions and in presence of polar solvent like water. For example, PLQY of the $CsPbBr_3$ NCs decreases only ~16% after 70 days in ambient condition (Figure 5.7A) with no change in PL peak position (Figure A3.22A). Unchanged PXRD patterns and TEM images recorded after storing the sample for 60 days under ambient condition suggest excellent phase stability of these NCs (Figure 5.7B and 5.7C). Excellent photostability of these NCs is evident from only 15% reduction of PLQY after ~38 h of continuous UV illumination (Figure A3.22B). The perovskite NCs readily degrade in polar environment due to their ionic nature. However, the $CsPbBr_3$ NCs obtained by this method display significant resistance to water retaining ~75% PLQY in presence of water even after a day of storage under ambient condition (Figure 5.7D). The hybrid $MAPbBr_3$ and $FAPbBr_3$ NCs too are highly stable under atmospheric condition. The impressive air stability of these systems is evident from 80-82% PLQY and cubic morphology even after 80 days of storage under ambient conditions (Figure A3.23-25). The hybrid systems are generally not very stable; they undergo rapid photo-degradation with concomitant shift of the PL peak wavelength.[54] A PLQY of 82-87% of the hybrid

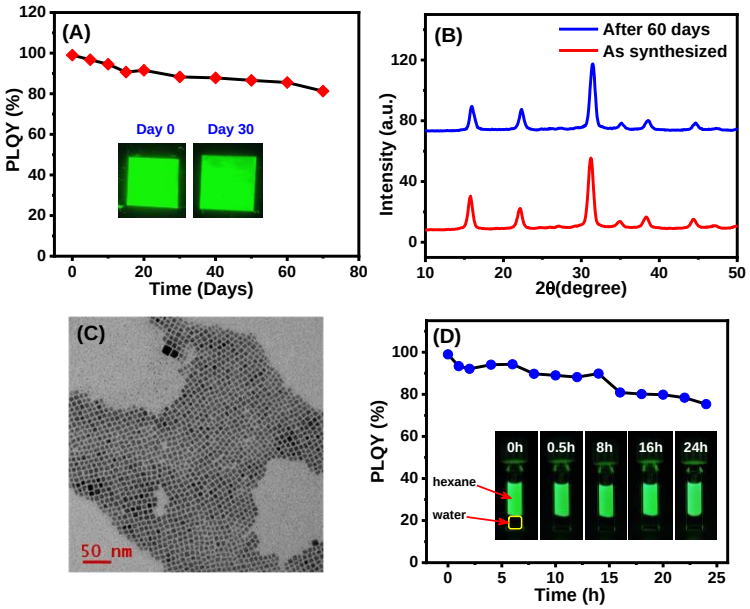

Figure 5.7. *(A) Stability of colloidal $CsPbBr_3$ NCs stored under ambient condition. Inset shows digital image of a films of the NCs under UV light stored in ambient condition for one month. (B) PXRD patterns of the NCs after 60 days. (C) TEM images of the NCs after the same period of time. Scale bar is 50 nm. (D) Time-dependent change of PLQY of the $CsPbBr_3$ NCs in presence of polar solvent (water). Digital images at different time intervals under UV light are shown in the inset.*

systems after a long time under continuous illumination of UV light without any shift of PL peak and change of FWHM indicates much better photostability of these NCs (Figure A3.23 and A3.24). The stability of the violet-emitting $CsPbCl_3$ NCs is also quite impressive. A PLQY of 55% and 58% is still maintained after ~45 days of storage under ambient condition and 24 h under continuous illumination at 365 nm by a UV lamp, respectively (Figure A3.26). A major problem with the mixed-halide systems is halide migration, which causes continuous drifting of the PL peak.[55] However, our mixed-halide systems show distinctive stability with a PLQY of 85-90% without any change in PL peak position and FWHM even after 25 days of storage in ambient condition (Figure A3.27). However, the violet-emitting $MAPbCl_3$ and $FAPbCl_3$ NCs show poor stability under ambient condition with a PLQY of only 1.6% and 0.2%, respectively after ~7 days of storage (Figure A3.28). The exceptional characteristics of the NCs obtained by the present method becomes clear when these are compared for different green- and violet-emitting samples obtained by other direct synthetic methods (Table A3.9).

A separate halide precursor is used in three-precursor method of synthesis of the lead-halide perovskite NCs. Under the reaction condition, the halide precursor generates

HX that reacts with oleylamine to form OAm^+X^-, which serves as the active source of halide in reaction medium (Scheme A3.1). Benzoyl halides are good choice as halide precursor[32] as they readily produce HX upon nucleophilic attack by OA and OAm at the electron-deficient carbonyl carbon.[56] On the other hand, the N-haloimides (NXI_m, Scheme 5.2) like N-halosuccinimide or N-halophthalimide, produce HX by protonation of one of the carbonyl oxygens followed by nucleophilic (oleate ion) attack at the halogen center.[22, 57] A key point to note here is that in NXI_m, X is electrophilic due to the presence of two electron withdrawing carbonyl groups linked to the nitrogen with which X is attached. Protonation of the carbonyl oxygen further enhances the electrophilicity of X making its release as HX easier upon nucleophilic attack by oleate.[57] This explains the effectiveness of NXI_m as a halogenating agent for all green and selective violet-emitting NCs. However, the chloro/iodo-based hybrid systems are not formed or of poor quality (like

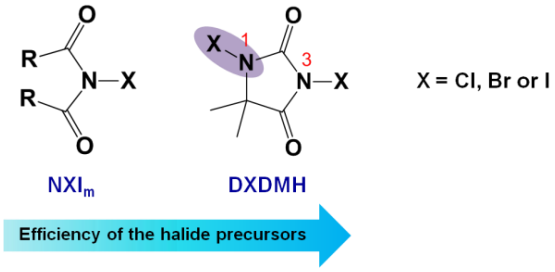

Scheme 5.2. *Increased effectiveness of DXDMH over NXI_m towards nucleophilic attack leading to the formation of HX. The N(1) halogen in DXDMH is marked for convenience.*

$CsPbI_3$) using NXI_m. In the case of DXDMH, HX formation is much more facile because of the presence of an additional halogen at N(1), which acts as an inductive activator of the N(3) halogen (the actual source of halogen) and makes it much more electrophilic than that in NXI_m (Scheme 5.2).[58, 59] Facile formation of HX in the reaction medium generates *in situ* OAm^+X^-, which acts as a source of active halide and also, a surface passivating ligand for the $APbX_3$ NCs. Instantaneous post-synthetic halide excange reactions at RT (Figure A3.20) shows the ease of formation of HX (and OAm^+X^-) from DXDMH. Therefore, when the halogen atom of the halide precursor is electron deficient (like in DXDMH) or directly attached to an electron withdrawing group (EWG) (like C=O in benzoyl halides[32] or P=O in $PhPOCl_2$[24]), nucleophilic attack at the halogen center or electrophilic center of the EWG, leads to facile generation of HX and subsequent formation of OAm^+X^- and high quality perovskite NCs. Table A3.10 summarizes the advantages and disadvantages of popular halide precursors used in hot-injection method of synthesis.

The factors responsible for the exceptional characteristics of the present NCs are identified as follows using the $CsPbBr_3$ NCs as model system. The EDX measurements, which show a Cs:Pb:Br ratio of 0.80:1.00:3.15 in these NCs (Figure 5.8A), indicate a bromide-rich surface of these NCs as compared to the bromide deficient $CsPbBr_3$(II) NCs (Figure 5.8A and A3.29), which exhibit poor stability under ambient condition (Figure A3.30). The XPS measurements provide additional insight on the chemical environment of the elements. The XPS survey spectra confirm the presence of all constituent elements of $CsPbBr_3$ NCs (Figure A3.31). The Pb 4f XPS core-level spectrum shows characteristics Pb $4f_{5/2}$ and Pb $4f_{7/2}$ peaks at 143.17 and 138.27 eV, respectively (Figure 5.8B),[52] but, for $CsPbBr_3$(II) NCs, each signal consists of two clearly resolvable peaks representing two different chemical environments of Pb (Figure 5.8C); the signals with higher and lower binding energy are assigned to Pb-Br (138.23 and 143.09 eV) and Pb-oleate (136.14 and 141.02 eV), respectively.[60, 61] The latter is a reflection of bromide vacancy related surface defect in $CsPbBr_3$(II) NCs, which is absent in $CsPbBr_3$ NCs. The atomic percentage ratio calculated from the XPS data (insets of Figure 5.8B, 5.8C and Table A3.11) matches that obtained from EDX measurements (Figure 5.8A) and further confirm bromide rich surface of the $CsPbBr_3$ NCs.[52] The core-level Br 3d XPS spectrum (Figure A3.32) shows Br $3d_{3/2}$ and Br $3d_{5/2}$ signal, representing the bromide ions at the surface and core, respectively.[62] The much intense and blue-shifted (~0.12 eV) Br $3d_{3/2}$ peak of the $CsPbBr_3$ NCs compared to $CsPbBr_3$(II) NCs corroborates the bromide rich surface of the $CsPbBr_3$ NCs (Figure A3.32A).[52, 62] Similarly, a chloride rich surface of the $CsPbCl_3$ NCs compared to the $CsPbCl_3$(II) NCs is also observed (Figure A3.33). A point to note in this context is that atomic % of chloride in $CsPbCl_3$ NCs is very similar for Pb:Cl precursor molar ratio between 1:3 and 1:7 (Table A3.12). However, for ratios >1:7, the formation of $PbCl_2$ as a byproduct (Figure A3.34) decreases the effective amount of chloride in the reaction medium and the $CsPbCl_3$ NCs formed under this condition contain a lower atomic % of chloride and are weakly luminescent (Figure A3.11A).

The surface ligand environment, which influences the optical properties and stability of the perovskite NCs,[63, 64] is determined by ^{1}H NMR and FTIR studies. The ^{1}H NMR spectrum of purified $CsPbBr_3$ NCs (Figure A3.35) shows two broad signature peaks of the α-protons ($-NH_3^+$) and β-protons ($-CH_2-NH_3^+$) of OAm^+ at ~7 and ~3.6 ppm,[64] respectively, indicating the presence of OAm^+ at the surface of the NCs and the broadness of these two peaks (denoted as a and b) suggests firm anchoring of OAm^+ on the surface.[33, 64] In this context, it may be noted that the NMR signal for the three α-protons of OAm^+ in the present case appears as a broad singlet,[63, 64] not as a multiplet.[27] In

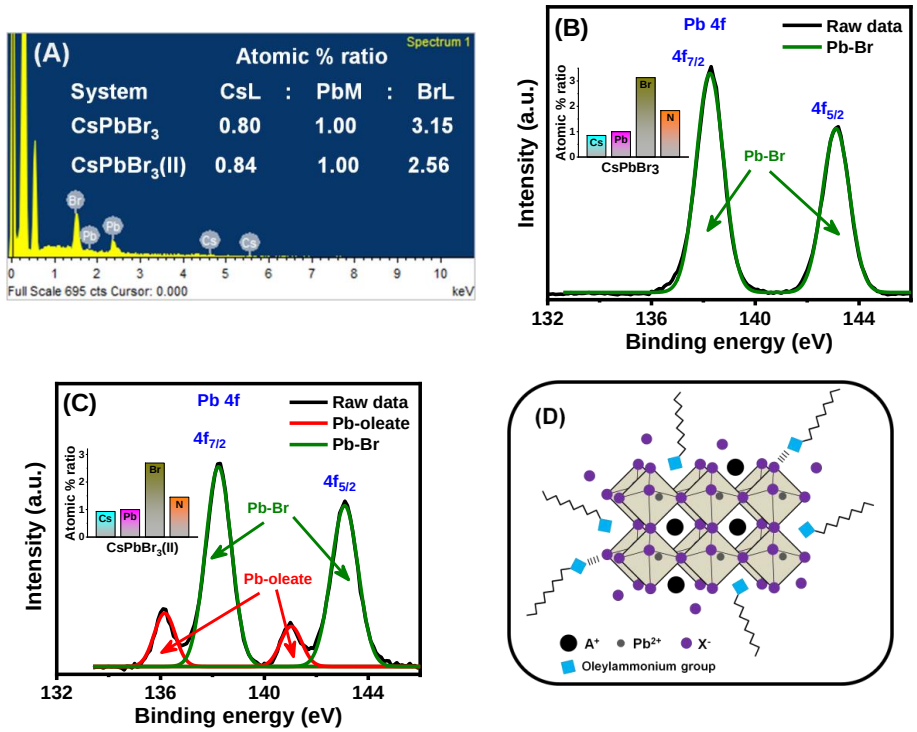

Figure 5.8. *(A) EDX spectra of $CsPbBr_3$ NCs. The claculated atomic % ratio of the $CsPbBr_3$ and $CsPbBr_3$(II) NCs obtained from the EDX measurements are provided in the inset. High-resolution Pb 4f XPS signal of the (B) $CsPbBr_3$ and (C) $CsPbBr_3$(II) NCs. Inset shows the atomic % ratio (with respect to lead) of the respective samples calculated based on the XPS results. (D) Schematic representation of halide rich surface of the synthesized $APbX_3$ NCs, showing direct binding of oleylammonium on the surface.*

contrast, sharp nature of the characteristic peak of the oleate ion at ~2.4 ppm (labeled as c) indicates that oleate ion is not bound to the surface, but present in solution,[33, 64] suggesting a bromide rich surface and absence of uncoordinated surface Pb^{2+} of the NCs. This finding is consistent with the XPS data presented earlier, where no signature of Pb-oleate was observed for $CsPbBr_3$ NCs (Figure 5.8B). The asymmetric and symmetric bending absorption of the N^+-H bond at ~1641 and 1548 cm^{-1} in the FTIR spectrum further establishes anchoring of OAm^+ on the surface (Figure A3.36).[27] A halide-rich surface attracts a greater number of OAm^+ and provide them access to some of the surface exposed A-sites and allow replacement of some Cs^+ ions.[26] A higher N/Pb ratio and low Cs^+ content in $CsPbBr_3$ NCs (Figure 5.8B inset and Table A3.11) support this picture. It is thus evident that strongly bound OAm^+ provides a robust ligand environment at the surface that contributes to the exceptional stability of the NCs.[27, 33] Moreover, the hydrophobic environment of OAm^+ protects the NCs from moisture and polar solvents

preventing or slowing down the decomposition of optically active inorganic framework.[33] Although OA is not bound to the surface, it maintains an optimum concentration of oleate and OAm^+ ligands and provides colloidal stability.[64] Therefore, OAm^+X^- produced *in situ* creates a halide-rich surface of the NCs that eventually turns into an oleylammonium-lead halide terminated surface by replacing some of the surface Cs^+ that endows exceptional characteristics to the NCs (Figure 5.8D).

5.3. Conclusions

It is shown that high quality all-inorganic and hybrid lead halide perovskite $APbX_3$ NCs (where A= Cs^+, MA^+ or FA^+ and X= Cl^-, Br^- or I^-) emitting in the 395 - 760 nm region can be obtained in direct synthesis by a generic method using DXDMH as halide precursors. The high phase purity, narrow size distribution, high PLQY and excellent stability (except for $MAPbCl_3$ and $FAPbCl_3$ NCs) of such large collection of NCs obtained by a common method are attributed to the efficacy of this class of halide precursors facilitating formation of oleylammonium-lead halide terminated surface, which passivates the defect states and provides necessary protection to the NCs. The present work not only provides a generic methodology for direct synthesis of good quality $APbX_3$ NCs, but also provides useful insight for design and development of even better $APbX_3$ NCs.

References:

1. L. Protesescu, S. Yakunin, M. I. Bodnarchuk, F. Krieg, R. Caputo, C. H. Hendon, R. X. Yang, A. Walsh and M. V. Kovalenko, *Nano Lett.*, 2015, ***15***, 3692–3696.
2. F. Zhang, H. Zhong, C. Chen, X.-g. Wu, X. Hu, H. Huang, J. Han, B. Zou and Y. Dong, *ACS Nano*, 2015, ***9***, 4533–4542.
3. Q. A. Akkerman, V. D'Innocenzo, S. Accornero, A. Scarpellini, A. Petrozza, M. Prato and L. Manna, *J. Am. Chem. Soc.*, 2015, ***137***, 10276–10281.
4. G. Nedelcu, L. Protesescu, S. Yakunin, M. I. Bodnarchuk, M. J. Grotevent and M. V. Kovalenko, *Nano Lett.*, 2015, ***15***, 5635–5640.
5. V. G. V. Dutt, S. Akhil and N. Mishra, *CrystEngComm*, 2020, ***22***, 5022-5030.
6. A. Dutta, R. K. Behera, P. Pal, P. D. S. Baitalik and D. N. Pradhan, *Angew. Chem., Int. Ed.*, 2019, ***58***, 5552−5556.
7. G. H. Ahmed, J. Yin, O. M. Bakr and O. F. Mohammed, *J. Chem. Phys.*, 2020, ***152***, 020902.
8. J. Shamsi, A. S. Urban, M. Imran, L. D. Trizio and L. Manna, *Chem. Rev.*, 2019, ***119***, 3296–3348.
9. J. Song, J. Li, X. Li, L. Xu, Y. Dong and H. Zeng, *Adv. Mater.*, 2015, ***27***, 7162−7167.
10. S. Yakunin, L. Protesescu, F. Krieg, M. I. Bodnarchuk, G. Nedelcu, M. Humer, G. D. Luca, M. Fiebig, W. Heiss and M. V. Kovalenko, *Nat. Commun.*, 2015, ***6***, 8056.

11. J. Pan, S. P. Sarmah, B. Murali, I. Dursun, W. Peng, M. R. Parida, J. Liu, L. Sinatra, N. Alyami, C. Zhao, E. Alarousu, T. K. Ng, B. S. Ooi, O. M. Bakr and O. F. Mohammed, *J. Phys. Chem. Lett.*, 2015, ***6***, 5027–5033.
12. A. Dey, J. Ye, A. De, E. Debroye, S. K. Ha, E. Bladt, A. S. Kshirsagar, Z. Wang, J. Yin and Y. Wang, *ACS Nano*, 2021, ***15***, 10775–10981.
13. Y. Wei, Z. Cheng and J. Lin, *Chem. Soc. Rev.*, 2019, ***48***, 310-350.
14. H. Huang, L. Polavarapu, J. A. Sichert, A. S. Susha, A. S. Urban and A. L. Rogach, *NPG Asia Materials*, 2016, ***8***, e328-e328.
15. J. Ye, D. M. M. Byranvand, C. O. Martínez, D. R. L. Z. Hoye, D. M. Saliba and D. L. Polavarapu, *Angew.Chem.Int. Ed.*, 2021, ***60***, 21636–21660.
16. N. Pradhan, *ACS Energy Lett.*, 2019, ***4***, 1634−1638.
17. L. Protesescu, S. Yakunin, M. I. Bodnarchuk, F. Bertolotti, N. Masciocchi, A. Guagliardi and M. V. Kovalenko, *J. Am. Chem. Soc.*, 2016, ***138***, 14202–14205.
18. P. Liu, W. Chen, W. Wang, B. Xu, D. Wu, J. Hao, W. Cao, F. Fang, Y. Li, Y. Zeng, R. Pan, S. Chen, W. Cao, X. W. Sun and K. Wang, *Chem. Mater.*, 2017, ***29***, 5168–5173.
19. E. Yassitepe, Z. Yang, O. Voznyy, Y. Kim, G. Walters, J. A. Castañeda, P. Kanjanaboos, M. Yuan, X. Gong, F. Fan, J. Pan, S. Hoogland, R. Comin, O. M. Bakr, L. A. Padilha, A. F. Nogueira and E. H. Sargent, *Adv. Funct. Mater.*, 2016, ***26***, 8757–8763.
20. F. Krieg, S. T. Ochsenbein, S. Yakunin, S. t. Brinck, P. Aellen, A. Süess, B. Clerc, D. Guggisberg, O. Nazarenko, Y. Shynkarenko, S. Kumar, C.-J. Shih, I. Infante and M. V. Kovalenko, *ACS Energy Lett.*, 2018, ***3***, 641–646.
21. M. Imran, P. Ijaz, D. Baranov, L. Goldoni, U. Petralanda, Q. Akkerman, A. L. Abdelhady, M. Prato, P. Bianchini, I. Infante and L. Manna, *Nano Lett.*, 2018, ***18***, 7822–7831.
22. S. Paul and A. Samanta, *ACS Energy Lett.*, 2020, ***5***, 64–69.
23. S. Akhil, V. G. V. Dutt and N. Mishra, *Nanoscale*, 2021, ***13***, 13142-13151.
24. C. Zhang, Q. Wan, L. K. Ono, Y. Liu, W. Zheng, Q. Zhang, M. Liu, L. Kong, L. Li and Y. Qi, *ACS Energy Lett.*, 2021, ***6***, 3545−3554.
25. S. Paul, T. Ahmed, S. Das and A. Samanta, *J. Phys. Chem. C*, 2021, ***125***, 23539−23547.
26. Y. Cai, H. Wang, Y. Li, L. Wang, Y. Lv, X. Yang and R.-J. Xie, *Chem. Mater.*, 2019, ***31***, 881–889.
27. A. Dutta, S. K. Dutta, S. D. Adhikari and D. N. Pradhan, *Angew.Chem. Int.Ed.*, 2018, ***57***, 9083 –9087.
28. L. Protesescu, S. Yakunin, S. Kumar, J. Bär, F. Bertolotti, N. Masciocchi, A. Guagliardi, M. Grotevent, I. Shorubalko, M. I. Bodnarchuk, C.-J. Shih and M. V. Kovalenko, *ACS Nano*, 2017, ***11***, 3119–3134.
29. Q. A. Akkerman, L. Martínez-Sarti, L. Goldoni, M. Imran, D. Baranov, H. J. Bolink, F. Palazon and L. Manna, *Chem. Mater.*, 2018, ***30***, 6915–6921.
30. S. K. Mahankudo, A. Das, K. Mishra, M. Barai, P. Mal and S. Ghosh, *ACS Appl. Nano Mater.*, 2022, ***5***, 4360–4366.
31. I. Levchuk, A. Osvet, X. Tang, M. Brandl, J. D. Perea, F. Hoegl, G. J. Matt, R. Hock, M. Batentschuk and C. J. Brabec, *Nano Lett.*, 2017, ***17***, 2765–2770.
32. M. Imran, V. Caligiuri, M. Wang, L. Goldoni, M. Prato, R. Krahne, L. D. Trizio and L. Manna, *J. Am. Chem. Soc.*, 2018, ***140***, 2656–2664.
33. S. Das and A. Samanta, *ACS Energy Lett.*, 2021, ***6***, 3780−3787.

34. G. Maculan, A. D. Sheikh, A. L. Abdelhady, M. I. Saidaminov, M. A. Haque, B. Murali, E. Alarousu, O. F. Mohammed, T. Wu and O. M. Bakr, *J. Phys. Chem. Lett.*, 2015, ***6***, 3781–3786.
35. A. A. Zhumekenov, M. I. Saidaminov, M. A. Haque, E. Alarousu, S. P. Sarmah, B. Murali, I. Dursun, X.-H. Miao, A. L. Abdelhady, T. Wu, O. F. Mohammed and O. M. Bakr, *ACS Energy Lett.*, 2016, ***1***, 32–37.
36. V. G. V. Dutt, S. Akhil and N. Mishra, *Nanoscale*, 2021, ***13***, 14442-14449.
37. A. De, S. Das, N. Mondal and A. Samanta, *ACS Materials Lett.*, 2019, ***1***, 116–122.
38. N. Mondal and A. Samanta, *Nanoscale*, 2017, ***9***, 1878-1885.
39. R. K. Gautam, S. Das and A. Samanta, *J. Phys. Chem. C*, 2021, **125**, 24170–24179.
40. S. Das, A. De and A. Samanta, *J. Phys. Chem. Lett.*, 2020, ***11***, 1178–1188.
41. A. De, S. Das and A. Samanta, *ACS Energy Lett.*, 2020, ***5***, 2246–2252.
42. N. Mondal, A. De and A. Samanta, *ACS Energy Lett.*, 2019, ***4***, 32–39.
43. D. P. Nenon, K. Pressler, J. Kang, B. A. Koscher, J. H. Olshansky, W. T. Osowiecki, M. A. Koc, L.-W. Wang and A. P. Alivisatos, *J. Am. Chem. Soc.*, 2018, ***140***, 17760–17772.
44. X. Zheng, S. Yuan, J. Liu, J. Yin, F. Yuan, W.-S. Shen, K. Yao, M. Wei, C. Zhou, K. Song, B.-B. Zhang, Y. Lin, M. N. Hedhili, N. Wehbe, Y. Han, H.-T. Sun, Z.-H. Lu, T. D. Anthopoulos, O. F. Mohammed, E. H. Sargent, L.-S. Liao and O. M. Bakr, *ACS Energy Lett.*, 2020, ***5***, 793–798.
45. R. K. Gautam, S. Das and A. Samanta, *ChemNanoMat*, 2022, ***8***, e20220002.
46. Y. Shynkarenko, M. I. Bodnarchuk, C. Bernasconi, Y. Berezovska, V. Verteletskyi, S. T. Ochsenbein and M. V. Kovalenko, *ACS Energy Lett.*, 2019, ***4***, 2703–2711.
47. S. E. Creutz, E. N. Crites, M. C. D. Siena and D. R. Gamelin, *Chem. Mater.*, 2018, ***30***, 4887–4891.
48. H. Huang, B. Chen, Z. Wang, T. F. Hung, A. S. Susha, H. Zhong and A. L. Rogach, *Chem. Sci.*, 2016, ***7***, 5699-5703.
49. S. Wang, C. Bi, J. Yuan, L. Zhang and J. Tian, *ACS Energy Lett.*, 2018, ***3***, 245–251.
50. V. K. Ravi, S. Saikia, S. Yadav, V. V. Nawale and A. Nag, *ACS Energy Lett.*, 2020, ***5***, 1794–1796.
51. Q. Zhong, M. Cao, Y. Xu, P. Li, Y. Zhang, H. Hu, D. Yang, Y. Xu, L. Wang, Y. Li, X. Zhang and Q. Zhang, *Nano Lett.*, 2019, ***19***, 4151–4157.
52. J. Y. Woo, Y. Kim, J. Bae, T. G. Kim, J. W. Kim, D. C. Lee and S. Jeong, *Chem. Mater.*, 2017, ***29***, 7088–7092.
53. Y. Wu, C. Wei, X. Li, Y. Li, S. Qiu, W. Shen, B. Cai, Z. Sun, D. Yang, Z. Deng and H. Zeng, *ACS Energy Lett.*, 2018, ***3***, 2030–2037.
54. L. Liu, L. Deng, S. Huang, P. Zhang, J. Linnros, H. Zhong and I. Sychugov, *J. Phys. Chem. Lett.*, 2019, ***10***, 864–869.
55. P. V. Kamat and M. Kuno, *Acc. Chem. Res.*, 2021, ***54***, 520–531.
56. M. F. Ansell, ed., *Preparation of acyl halides*, John Wiley & Sons Ltd. UK, London, **1972**.
57. H. Xue, H. Tan, D. Wei, Y. Wei, S. Lin, F. Liang and B. Zhao, *RSC Adv.*, 2013, ***3***, 5382-5385.
58. D. C. Whitehead, R. Yousefi, A. Jaganathan and B. Borhan, *J. Am. Chem. Soc.*, 2010, ***132***, 3298–3300.
59. R. Yousefi, D. C. Whitehead, J. M. Mueller, R. J. Staples and B. Borhan, *Org. Lett.*, 2011, ***13***, 608–611.
60. M. Li, X. Zhang, K. Matras-Postolek, H.-S. Chen and P. Yang, *J. Mater. Chem. C*, 2018, ***6***, 5506-5513. .

61. W. E. Morgan and J. R. V. Wazer, *J. Phys. Chem.*, 1973, ***77***, 964–969.
62. T. Cai, F. Li, Y. Jiang, X. Liu, X. Xia, X. Wang, J. Peng, L. Wang and W. A. Daoud, *Nanoscale*, 2019, ***11***, 1319-1325.
63. J. D. Roo, M. Ibáñez, P. Geiregat, G. Nedelcu, W. Walravens, J. Maes, J. C. Martins, I. V. Driessche, M. V. Kovalenko and Z. Hens, *ACS Nano*, 2016, ***10***, 2071–2081.
64. V. K. Ravi, P. K. Santra, N. Joshi, J. Chugh, S. K. Singh, H. Rensmo, P. Ghosh and A. Nag, *J. Phys. Chem. Lett.*, 2017, ***8***, 4988–4994.

CHAPTER 6

Direct Synthesis of Exceptionally Stable and Intense Violet Emitting $CsPbCl_3$ Nanocrystals: A Paradigm of L-type Surface Passivation

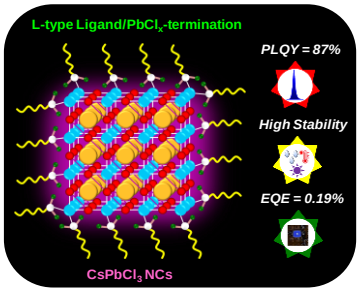

(Manuscript Submitted)

Overview

Poor PLQY and stability of the violet-emitting $CsPbCl_3$ NCs is responsible for very low efficiency of the violet-LEDs (<435 nm) based on these substances. Herein, we report a direct method of obtaining $CsPbCl_3$ NCs with exceptional characteristics employing diphenlyphosphoryl chloride, which serves not only as an efficient chloride precursor, but also prevents protonation of the amine ligand. High PLQY (~87%) and remarkable stability of these NCs in polar environment, at high temperature and with low density capping ligands are attributed to strong L-type coordination of the unprotonated amine ligand with Pb^{2+} of a $PbCl_x$-terminated surface. A high-performance violet-LED with ultrapure electroluminescence at 410 nm, narrow bandwidth of 12 nm and external quantum efficiency of ~0.16-0.19 % is achieved using these NCs as emitting material. The results not only provide a new approach to obtaining quality $CsPbCl_3$ NCs, but also highlight their potential in optoelectronic devices in this challenging high-energy spectral region.

6.1. Introduction

Growing demand for low-cost luminescent devices has drawn worldwide attention towards the $CsPbX_3$ (X= Cl, Br or I) perovskite NCs because of their high PLQY, narrow PL bandwidth, halide composition dependent PL tunability and easy solution processability.[1-3] While the luminous efficiency of the blue- and green-/red-emitting perovskite LEDs has reached over 12.3 and 20%, respectively,[4-6] that of the violet-LEDs (<435 nm) is still way behind (0.25%)[7-9] because unlike the green- and red-emitting counterparts, the large band-gap $CsPbCl_3$ NCs are weakly luminescent (PLQY typically <5%) due to high density of the deep trap states arising from chloride vacancies and less stable due to the distorted $[PbCl_6]^{4-}$ octahedra.[3, 10-14]

Following the first synthesis of the $CsPbCl_3$ NCs,[15] a number of methods have been developed later employing independent source of chloride for obtaining more luminescent systems.[16-20] However, these moderately stable NCs[17, 18] are not good enough for applications like LEDs due to the insulating nature of high density long-chain capping ligands.[21, 22] Except for a very recent work by Qi and co-workers, who succeeded in obtaining strongly luminescent (PLQY ~71%) and stable $CsPbCl_3$ NCs with low density surface capping ligands, and fabricated LED with an efficiency of ~0.18% using these systems,[19] we are not aware of any other work reporting such desired qualities of these NCs.

In this work, for synthesis of the $CsPbCl_3$ NCs, we have used diphenlyphosphoryl chloride [$(PhO)_2POCl$, Figure 6.1A] as chloride precursor as it is expected to be more efficient than Ph_2POCl, a chloride precursor reported to be superior to widely popular benzoyl chloride and $PhPOCl_2$,[23] due to stronger inductive (–I) effect of the phenoxy groups compared to the phenyl moieties.[24, 25] The results show that the NCs obtained by our method not only exhibit intense violet emission, but they also maintain bright emission and phase even for low density of surface ligands, which allow fabrication of down-converted violet-LED employing these NCs with ultra-narrow electroluminescence (EL) peaking at 410 nm and luminous efficiency of ~0.16-0.19%.

6.2. Results and Discussion

An excess amount of $(PhO)_2POCl$ was swiftly injected into a solution of the Cs- and Pb-precursors containing oleic acid (OAH) and OAm in ODE maintained at 220°C. Immediate appearance of white precipitate indicated formation of the $CsPbCl_3$ NCs, which were washed using a mixture of hexane and MeOAc and collected through

centrifugation followed by re-dispersion in hexane (details in Chapter 2, section 2.2.3.4). The reaction temperature and chloride concentration were found to be crucial for overall quality of these NCs. A Pb:Cl precursor molar ratio of 1:9 and a temperature of 220°C yielded the best quality NCs (Figure A4.1). A lower concentration of the Cl precursor or a lower reaction temperature yielded inhomogeneous NCs with low PLQY (Figure A4.2).

Bright field TEM images show cubic morphology and a tight size distribution of the NCs with average edge-length of ~8.7±1.2 nm (Figure 6.1B, A4.3 and A4.4). Clearly observable lattice fringes in the high-resolution image indicate high crystallinity of the $CsPbCl_3$ NCs (Figure 6.1B, inset) and a lattice spacing of ~0.56 nm corresponding to the (100) planes, which is in agreement with literature.[20] The PXRD pattern matches with the cubic crystal structure (ICSD Code: 23108) of the NCs[16] (Figure 6.1C) and suggests high phase purity of the sample.

The steady state UV-Vis absorption and PL spectra of the NCs (Figure 6.1D) show excitonic absorption at ~402 nm and PL maximum at ~405 nm with narrow bandwidth (fwhm ~10 nm). The PLQY of the NCs, measured to be ~87%, is the second

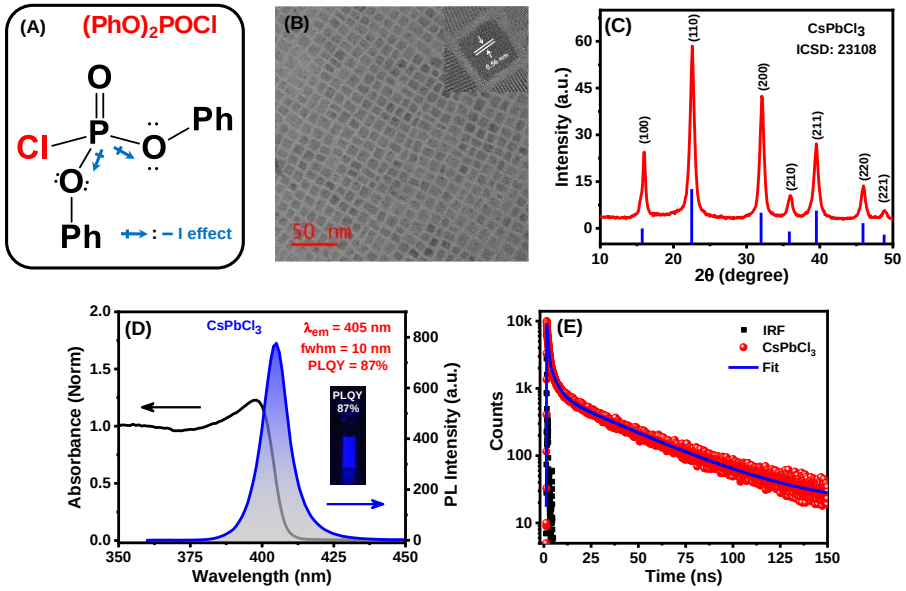

Figure 6.1. *(A) Chemical structure of tetrahedral $(PhO)_2POCl$. (B) Bright-field TEM images of the $CsPbCl_3$ NCs (scale bar 50 nm). Inset shows HRTEM image of the NCs with a lattice spacing of 0.56 nm. (C) PXRD patterns of the NCs. (D) UV-Vis absorption and PL spectra of the NCs. Inset shows digital image of a colloidal solution of the NCs under UV exposure (365 nm, 8W/cm^2). (E) PL decay kinetics of the NCs monitored at 405 nm (λ_{ex} = 375 nm).*

best reported value of the $CsPbCl_3$ NCs till date (Table A4.1).[16-20] The average PL lifetime (<τ>) of 2.30 ns for these NCs is comparable to the brightly luminescent $CsPbCl_3$ NCs (Figure 6.1E).[17, 19, 26]

While surface ligands are essential for the stability and PL of the $CsPbCl_3$ NCs, high density of the most commonly used surface capping ligands like OAH and OAm hinders charge flow across the surface due to insulating nature of the long chains.[21, 27, 28] Replacement of the long chain ligands with smaller ones improves charge transportation,[21, 27] but it sometimes trigger unwanted growth of the NCs resulting in a change of morphology and emission characteristics.[19, 29, 30] Lowering the density of the capping ligands by washing of the NCs can improve the charge flow across the surface. However, in the case of $CsPbCl_3$ NCs, this is reported to form non-emissive $CsPb_2Cl_5$ NCs.[31] Interestingly, unlike earlier reports,[31, 32] our NCs exhibit fairly strong emission even after multiple cycles of washing by polar (MeOAc) and non-polar (hexane) solvents (details in Chapter 2, section 2.2.3.4), monitored by periodic removal of the ligand by FTIR measurements (Figure A4.5). For example, these NCs exhibit a PLQY of >67 and >71%, respectively after five cycles of washing with MeOAc (Figure 6.2A) and hexane (Figure 6.2B) without any shift in the absorption or PL maximum (Figure A4.6). The unchanged PXRD patterns (Figure 6.2C and A4.7) and TEM images (Figure 6.2D and A4.7) indicate intact crystal phase and morphology of the NCs even after multiple washing. The stability of the NCs is quite remarkable even beyond five cycles of washing. After 10 cycles of washing with MeOAc and hexane, the NCs exhibit PLQY of ~43% and ~52%, respectively (Figure 6.2A and 6.2B) with very little change in crystal

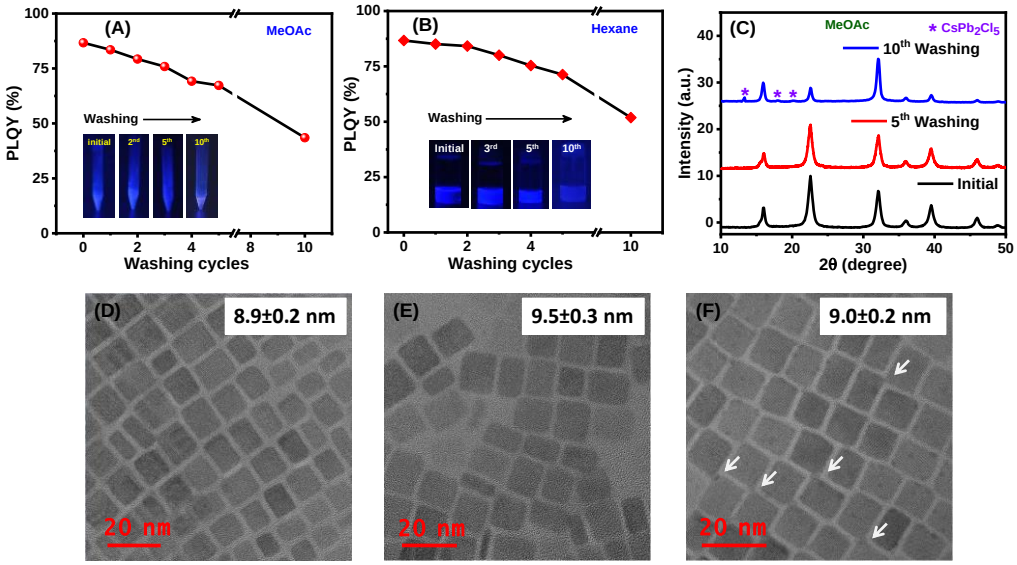

Figure 6.2. *Variation of PLQY of the NCs on repeated washing with (A) MeOAc and (B) Hexane. (C) PXRD patterns of the NCs before and after multiple cycles of washing with MeOAc. Bright-field TEM images of the NCs after (D) five and (E) ten washing cycles with MeOAc. (F) Bright-field TEM images of the NCs after ten cycles of washing with hexane. Insets in Figures (A) and (B) show digital images of the NCs solution before and after different cycles of washing with respective solvents. The arrows in Figure (F) point to the attached corners of the NCs after washing with hexane.*

structure and morphology (Figure 6.2C, 6.2E, 6.2F and A4.7). A few low intensity diffraction peaks observed between 10-20 degrees after ten cycles of washing with MeOAc indicate formation of small amount of non-emitting $CsPb_2Cl_5$ in the sample (Figure 6.2C).[31, 32] This becomes more clear from the TEM and PXRD data (Figure A4.8) of the samples recorded after 14 cycles of washing. The size of the NCs increases slightly due to removal of the surface ligands[21, 33] beyond ten cycles of washing. This leads to small (~ 2 nm) red-shift of the absorption and PL spectra of the NCs (Figure A4.6). Very low ligand density after ten cycles of washing with hexane exposes the surface of the NCs and facilitates fusion of the adjacent nanocubes through their corners (Figure 6.2F, white arrows).[34] A comparison of the structural and optical stability data of the $CsPbCl_3$ NCs obtained by different methods reveals superior resistivity of the present NCs towards repeated washing (Table A4.2).

Distinctive stability of these NCs under different external stress condition is evident from the fact that even after two days of contact with water the NCs exhibit a PLQY of ~64% (Figure 6.3A) with unchanged FWHM and PL peak position (Figure A4.9A). Bright emission can also be seen in presence of ethanol (Figure A4.10). A PLQY of ~80% (Figure 6.3B) with unchanged PL peak position (Figure A4.9B) even after 10 h of continuous exposure to 365 nm UV radiation demonstrates excellent photostability of these NCs. Unchanged PXRD patterns with bright emission after continuous heating for over 10 h reflects remarkable thermal stability of these NCs (Figure 6.3C). Exceptional stability of these NCs under atmospheric conditions is evident from unchanged PXRD pattern (Figure 6.3D), TEM images (Figure 6.3E) and a PLQY of ~79% (Figure 6.3F) after 48 days of storage under ambient condition. A *vis-a-vis* comparison of the $CsPbCl_3$ NCs prepared by different *three-precursor* methods (Table A4.3) clearly places the present NCs atop as far as their optical properties and stability are concerned.

To determine the factors that contribute to the remarkable characteristics of these NCs, we first examine the surface ligand environment. We note that $(PhO)_2POCl$ is not

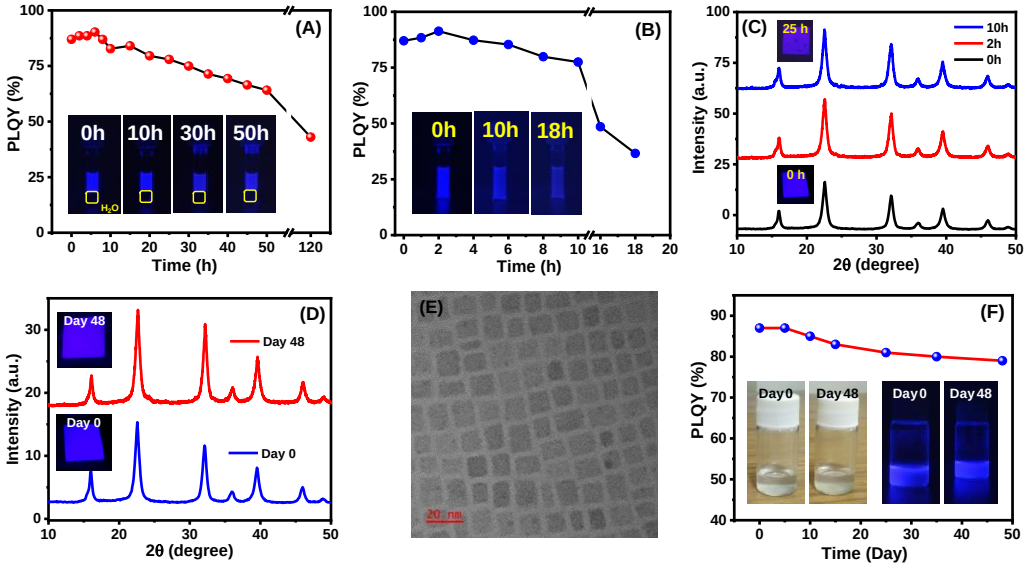

Figure 6.3. *(A) Change in PLQY of the $CsPbCl_3$ NCs in presence of water as a function of time. (B) Photoinduced change in PLQY of the NCs under continuous illumination of UV light (365 nm, 8W/cm^2). (C) PXRD patterns of the NCs before and after heating at 85°C for 10h. (D) PXRD patterns, (E) TEM images and (F) change in PLQY of the NCs after 48 days of storage under ambient condition. The inset in Figure (A and B) and (C-D) shows digital images of the NCs solution and films, respectively, under UV light. Digital images of the as-synthesized and aged NCs under sunlight (left) and UV light (right) are shown in the inset of Figure (F).*

merely a chlorinating agent, but can also passivate the surface of the NCs through the lone pair of electrons (O of the P=O moiety and Cl).[23] However, the absence of characteristic P=O stretching absorption (at ~1298 cm^{-1})[35] in the FTIR spectrum (Figure A4.11) and lack of any signal due to 'P' both in the ^{31}P-NMR and core-level XPS spectrum (Figure A4.12) rule out the possibility of $(PhO)_2POCl$ acting as a surface capping agent.

The ^{1}H-NMR spectrum of oleylammonium ($OAmH^+$)-capped perovskite NCs commonly shows two broad singlet at ~3.5 and ~7.0 ppm, respectively, due to the β-protons (-CH_2-NH_3^+) and α-protons (-NH_3^+) of the surface-bound long-chain ammonium ligand.[36, 37] The 7.0 ppm α-proton signal sometimes appears as a multiplet.[38] However, for our $CsPbCl_3$ NCs, only a sharp singlet at ~2.9 ppm due to the β-protons (Figure 6.4A) is observed. Absence of the signature peak of the α-protons and consequent up-field shift of the β-protons signal (by ~0.6 ppm) indicate that these NCs are capped by unprotonated (L-type) OAm ligand instead of conventional protonated $OAmH^+$.[19, 39] The ~42.28 ppm

peak in the ^{13}C-NMR spectrum of the NCs (Figure A4.13), which is due to the α-carbon of neutral OAm, further confirms unprotonated nature of the ligand (signal due to the α-carbon of $OAmH^+$ capped NCs was expected at ~39.6 ppm[39]).[40] Therefore, it becomes clear that the $CsPbCl_3$ NCs are capped with L-type unprotonated OAm ligand.

The surface ligand coverage of the NCs is assessed by monitoring the intensity of the signature peak of the oleyl protons (at ~5.34 ppm) in the ^{1}H-NMR spectra after successive washing with MeOAc (Figure A4.14).[21, 33] The number of ligands per unit surface area (often termed as ligand density, details in Chapter 2, section 2.5) in as-synthesized, five- and ten-times MeOAc-washed samples is estimated to be ~5.34, 3.92 and 0.43 nm^{-2}, respectively (Table A4.4), indicating effective removal of excessive insulating ligands upon repeated washing.

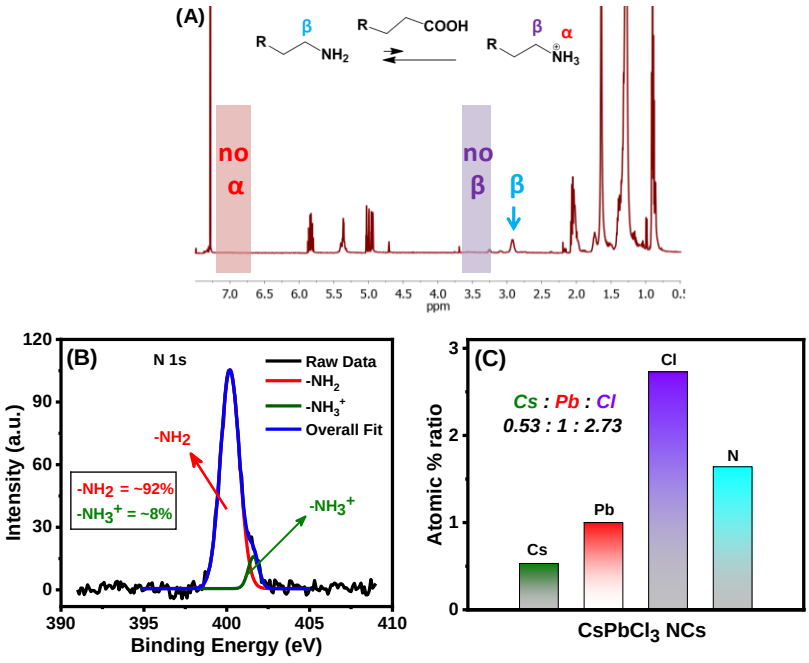

Figure 6.4. *(A) ^{1}H-NMR spectrum of the as-synthesized NCs in $CDCl_3$ and an illustration of the plausible acid-base equilibrium between OAH and OAm (R= alkene part) in the current method of synthesis. (B) Core level 'N 1s' spectrum of the NCs and its deconvolution indicating the contribution due to the protonated and unprotonated amines. (C) Atomic % ratio of the $CsPbCl_3$ NCs estimated from the XPS results. The presented XPS data is calibrated with respect to 'C 1s' signal at 285.0 eV.*

Valuable information on the surface ligand chemistry is obtained from the core-level 'N 1s' XPS spectrum. Close inspection of the 'N 1s' high-resolution signal shows a hump towards the higher binding energy region (Figure 6.4B), deconvolution of which

yields two peaks at ~400.1 and ~401.9 eV, characteristics of unprotonated amine (-NH_2) and protonated ammonium (-NH_3^+), respectively, of the surface ligand.[39, 41] The estimated weightages of free and protonated species (~92% and ~8%, respectively) clearly show that these NCs are indeed largely passivated by the L-type (unprotonated) OAm ligand. This uncommon surface passivation with free amine can be explained considering strong affinity of the 'P=O' moiety towards the acidic proton of OAH,[42] which protonates the former and reduces the concentration of protonated OAm in the reaction medium (Figure 6.4A, Inset),[19] thus facilitating such L-type passivation of the NCs.

A chloride rich surface usually enhances the PL of the $CsPbCl_3$ NCs.[16, 17, 43] However, the XPS data of the present NCs (Figure 6.4C and Table A4.5), shows sub-stoichiometric chloride content (Cs:Pb:Cl ratio of 0.53:1.0:2.73), suggesting a $PbCl_x$-rich surface (*vide later*).[19, 30] As the EDX data is also in agreement with the XPS data (Figure A4.15), it is clear that the present $CsPbCl_3$ NCs are passivated by L-type neutral OAm ligand through coordinate bonding with Pb^{2+} on a $PbCl_x$-rich/terminated surface.

The organic-inorganic interface of the perovskite NCs passivated by $OAmH^+$ is highly dynamic in nature due to its loose association with the surface.[44, 45] Deprotonation of $OAmH^+$, bound to the surface chlorides through weak H-bonds,[36, 44] by processes like $OAmH^+ + OA^- = OAm + OAH$ or $OAmH^+ + Cl^- = OAm + HCl$ leads to its desorption and sometimes results in concomitant removal of Cl^- from the surface, introducing Cl^- vacancy related surface defects.[44, 45] However, in the present case, much stronger binding of the OAm ligand to Pb^{2+} of a $PbCl_x$-terminated surface using the nitrogen lone-pair of

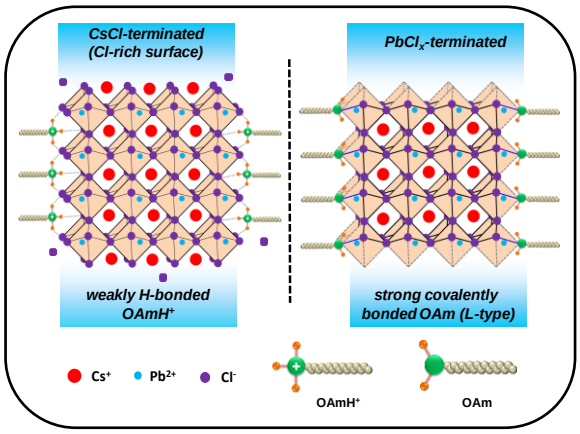

Scheme 6.1. *Schematic representation of (left) conventional CsCl-terminated (Cl-rich) $CsPbCl_3$ NCs passivated by weakly H-bonded $OAmH^+$ ligand and (right) $PbCl_x$-terminated NCs passivated by strong coordination of unprotonated OAm ligand (L-type) at the surface.*

electrons (similar to that reported for the $CsPbBr_3$ NCs[39]) compared to traditional weak H-bonding interaction of $OAmH^+$ with Cl^- (Scheme 6.1) provides greater stability to the NCs under different external stresses and towards multiple washing. Strong binding of OAm with surface Pb^{2+} effectively eliminates surface defects arising from under-coordinated Pb^{2+} explaining a high PLQY of ~87%, the second-best reported value till date for directly prepared samples of $CsPbCl_3$ NCs (Table A4.1). Conventional $OAmH^+$ capped high-quality $CsPbCl_3$ NCs on the other hand, show a PLQY of ~70%, which converts into poorly luminescent NCs (PLQY ~6%) after 10 cycles of washing with MeOAc (Figure A4.16). It is to be noted that repeated washing of the NCs removes not only the unbound ligands, but also some bound ligands (Scheme A4.1). Which results in a decrease of PLQY (Figure A4.17). However, the OAm protected NCs exhibit far better optical and phase stability for low density of surface ligands compared to the common $OAmH^+$ capped NCs. Therefore, L-type association of the OAm ligand is key to providing greater protection and surface passivation of these high-quality $CsPbCl_3$ NCs.

To explore how removal of excess ligands influences the charge transport across the interface of $CsPbCl_3$ NCs we have studied the current (*I*) – voltage (*V*) responses of the as-synthesized and ten times washed NCs deposited on FTO plates. A higher current density of the washed NCs compared to the as-synthesized NCs for any given voltage (Figure A4.18) indicates better charge transport properties of the washed samples. From an application point of view, as a proof-of-concept, we have fabricated down-converted LED using the washed NCs as emitting material on a commercial ultraviolet LED chip emitting at 365 nm. The fabricated LED exhibits ultrapure EL spectrum peaking at ~410 nm with a narrow fwhm (~12 nm) under bias voltage of 3.5V (Figure 6.5A). The fwhm of the emission is narrower than that for the best performing perovskite-based violet-LED (Table A4.6).[7-9, 19] Figure 6.5A (inset) shows digital image of the working violet-LED in dark. A comparison of the EL and PL spectra of the washed NCs shows that the EL arises only from the $CsPbCl_3$ NCs (Figure 6.5A). A small red-shift (~3-4 nm) of the EL spectrum (in film) with respect to the PL spectrum (in solution) of the washed NCs (Figure 6.5A) is not uncommon.[7, 28] The EL intensity (Figure A4.20) and output power (Figure 6.5B) of the LED increase monotonically with bias voltage without any change in shape and spectral position (Figure A4.19). A linear increase in output power (measured at the EL maximum) suggests negligible loss of the applied voltage under the operating condition. The estimated EQE of the device (~0.16 –0.19 %) is comparable to the highest value (~0.25%) achieved so far in the violet region for any lead-based or lead-free perovskite LEDs till date (Table A4.6).[8, 9, 19] The calculated Commission Internationale

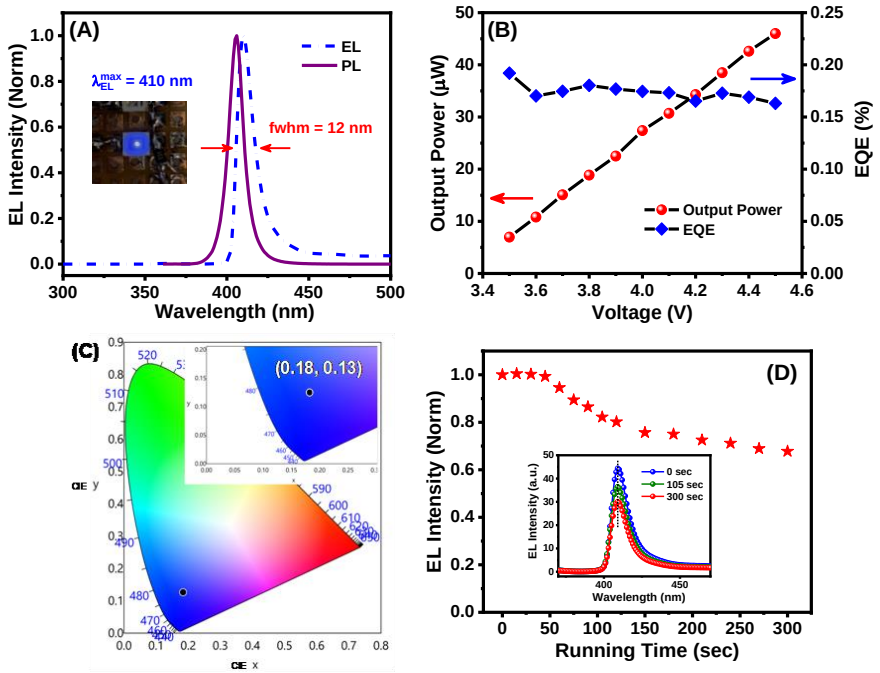

Figure 6.5. *(A) Normalized EL spectra (dotted line) of the violet-LED under bias voltage of 3.5V. The PL spectrum (solid line) of the NCs is also shown for comparison. Inset shows a digital image of the working LED. (B) Output power and EQE at different bias voltage. (C) CIE coordinates of the fabricated LED. Inset provides zoomed in view of the coordinates. (D) Variation of EL intensity with running time at a fixed applied bias voltage of 3.5V. The EL spectra of the device before and after running for 3 h are shown in the inset.*

de l'Eclairage coordinate (CIE chromaticity), (0.18, 0.13), is located at the violet region of the chromaticity diagram (Figure 6.5C). The present fabricated LED works continuously for over 3h at a fixed applied voltage of 3.5 V (Figure 6.5D) retaining ~70% of its initial EL intensity under ambient condition (RH of ~50%) with unchanged spectral feature (Figure 6.5D inset) suggesting high colour purity of the device even in long run, highlighting great working stability of a device based on present $CsPbCl_3$ NCs.

6.3. Summary

In short, phase pure, monodispersed and exceptionally stable $CsPbCl_3$ NCs with a PLQY of ~87% is obtained in direct synthesis using a new chloride precursor that also suppresses protonation of the capping ligand. Strong L-type coordination of the unprotonated ligand with Pb^{2+} on a $PbCl_x$-terminated surface contributes to the extraordinary features of these NCs. Possible utility of these strongly photoluminescent,

highly crystalline and stable NCs even for low density capping ligands in light-emitting applications is explored by fabricating a high-performance down-converted violet-LED with an ultra-narrow EL spectrum and high EQE of ~0.16-0.19%. The results provide a new route for obtaining efficient short wavelength perovskite-based optoelectronic devices.

References:

1. A. Dey, J. Ye, A. De, E. Debroye, S. K. Ha, E. Bladt, A. S. Kshirsagar, Z. Wang, J. Yin and Y. Wang, *ACS Nano*, 2021, ***15***, 10775–10981.
2. J. Shamsi, A. S. Urban, M. Imran, L. D. Trizio and L. Manna, *Chem. Rev.*, 2019, ***119***, 3296–3348.
3. X. Zheng, Y. Hou, H.-T. Sun, O. F. Mohammed, E. H. Sargent and O. M. Bakr, *J. Phys. Chem. Lett.*, 2019, ***10***, 2629–2640.
4. Y. Dong, Y.-K. Wang, F. Yuan, A. Johnston, Y. Liu, D. Ma, M.-J. Choi, B. Chen, M. Chekini, S.-W. Baek, L. K. Sagar, J. Fan, Y. Hou, M. Wu, S. Lee, B. Sun, S. Hoogland, R. Quintero-Bermudez, H. Ebe, P. Todorovic, F. Dinic, P. Li, H. T. Kung, M. I. Saidaminov, E. Kumacheva, E. Spiecker, L.-S. Liao, O. Voznyy, Z.-H. Lu and E. H. Sargent, *Nature Nanotechnology*, 2020, ***15***, 668–674.
5. K. Lin, J. Xing, L. N. Quan, F. P. G. d. Arquer, X. Gong, J. Lu, L. Xie, W. Zhao, D. Zhang, C. Yan, W. Li, X. Liu, Y. Lu, J. Kirman, E. H. Sargent, Q. Xiong and Z. Wei, *Nature*, 2018, ***562***, 245–248.
6. Y. Cao, N. Wang, H. Tian, J. Guo, Y. Wei, H. Chen, Y. Miao, W. Zou, K. Pan, Y. He, H. Cao, Y. Ke, M. Xu, Y. Wang, M. Yang, K. Du, Z. Fu, D. Kong, D. Dai, Y. Jin, G. Li, H. Li, Q. Peng, J. Wang and W. Huang, *Nature*, 2018, ***562***, 249–253.
7. D. Liang, Y. Peng, Y. Fu, M. J. Shearer, J. Zhang, J. Zhai, Y. Zhang, R. J. Hamers, T. L. Andrew and S. Jin, *ACS Nano*, 2016, ***10***, 6897–6904.
8. Z. Ma, Z. Shi, D. Yang, F. Zhang, S. Li, L. Wang, D. Wu, Y. Zhang, G. Na, L. Zhang, X. Li, Y. Zhang and C. Shan, *ACS Energy Letters*, 2020, ***5***, 385-394.
9. W. Deng, X. Jin, Y. Lv, X. Zhang, X. Zhang and J. Jie, *Adv. Funct. Mater.*, 2019, ***29***, 1903861.
10. Z.-J. Yong, S.-Q. Guo, J.-P. Ma, J.-Y. Zhang, Z.-Y. Li, Y.-M. Chen, B.-B. Zhang, Y. Zhou, J. Shu, J.-L. Gu, L.-R. Zheng, O. M. Bakr and H.-T. Sun, *J. Am. Chem. Soc.*, 2018, ***140***, 9942−9951.
11. S. Seth, T. Ahmed, A. De and A. Samanta, *ACS Energy Lett.*, 2019, ***4***, 1610−1618.
12. A. De, S. Das, N. Mondal and A. Samanta, *ACS Materials Lett.*, 2019, ***1***, 116−122.
13. D. P. Nenon, K. Pressler, J. Kang, B. A. Koscher, J. H. Olshansky, W. T. Osowiecki, M. A. Koc, L.-W. Wang and A. P. Alivisatos, *J. Am. Chem. Soc.*, 2018, ***140***, 17760−17772.
14. S. Das, A. De and A. Samanta, *J. Phys. Chem. Lett.*, 2020, ***11***, 1178–1188.
15. L. Protesescu, S. Yakunin, M. I. Bodnarchuk, F. Krieg, R. Caputo, C. H. Hendon, R. X. Yang, A. Walsh and M. V. Kovalenko, *Nano Lett.*, 2015, ***15***, 3692−3696.
16. M. Imran, V. Caligiuri, M. Wang, L. Goldoni, M. Prato, R. Krahne, L. D. Trizio and L. Manna, *J. Am. Chem. Soc.*, 2018, ***140***, 2656−2664.
17. A. Dutta, R. K. Behera, P. Pal, S. Baitalik and N. Pradhan, *Angew. Chem. Int. Ed.*, 2019, ***58***, 5552 –5556.

18. S. Paul, T. Ahmed, S. Das and A. Samanta, *J. Phys. Chem. C*, 2021, ***125***, 23539–23547.
19. C. Zhang, Q. Wan, L. K. Ono, Y. Liu, W. Zheng, Q. Zhang, M. Liu, L. Kong, L. Li and Y. Qi, *ACS Energy Lett.*, 2021, ***6***, 3545−3554.
20. S. Das and A. Samanta, *Nanoscale*, 2022, ***14***, 9349-9358.
21. J. Li, L. Xu, T. Wang, J. Song, J. Chen, J. Xue, Y. Dong, B. Cai, Q. Shan, B. Han and H. Zeng, *Adv. Mater*, 2017, ***29***, 1603885.
22. T. Chiba, K. Hoshi, Y.-J. Pu, Y. Takeda, Y. Hayashi, S. Ohisa, S. Kawata and J. Kido, *ACS Appl. Mater. Interfaces*, 2017, ***9***, 18054–18060.
23. D. Ma, P. Todorović, S. Meshkat, M. I. Saidaminov, Y.-K. Wang, B. Chen, P. Li, B. Scheffel, R. Quintero-Bermudez, J. Z. Fan, Y. Dong, B. Sun, C. Xu, C. Zhou, Y. Hou, X. Li, Y. Kang, O. Voznyy, Z.-H. Lu, D. Ban and E. H. Sargent, *J. Am. Chem. Soc.*, 2020, ***142***, 5126–5134.
24. N. K. Dey, I.-S. Han and H. W. Lee, *Bull. Korean Chem. Soc.*, 2007, ***28***, 2003-2008.
25. A. K. Guha, H. W. Lee and I. Lee, *J. Chem. Soc.,*, 1999, ***2***, 765–769.
26. D. Chakraborty, N. Preeyanka, A. Akhuli and M. Sarkar, *J. Phys. Chem. C*, 2021, ***125***, 26652–26660.
27. J. Pan, L. N. Quan, Y. Zhao, W. Peng, B. Murali, S. P. Sarmah, M. Yuan, L. Sinatra, N. M. Alyami, J. Liu, E. Yassitepe, Z. Yang, O. Voznyy, R. Comin, M. N. Hedhili, O. F. Mohammed, Z. H. Lu, D. H. Kim, E. H. Sargent and O. M. Bakr, *Adv.Mater.*, 2016, ***28***, 8718–8725.
28. B.-B. Zhang, S. Yuan, J.-P. Ma, Y. Zhou, J. Hou, X. Chen, W. Zheng, H. Shen, X.-C. Wang, B. Sun, O. M. Bakr, L.-S. Liao and H.-T. Sun, *J. Am. Chem. Soc.*, 2019, ***141***, 15423–15432.
29. Y.-H. Suh, T. Kim, J. W. Choi, C.-L. Lee and J. Park, *ACS Appl. Nano Mater.*, 2018, ***1***, 488–496.
30. M. I. Bodnarchuk, S. C. Boehme, S. t. Brinck, C. Bernasconi, Y. Shynkarenko, F. Krieg, R. Widmer, B. Aeschlimann, D. Günther, M. V. Kovalenko and I. Infante, *ACS Energy Lett.*, 2019, ***4***, 63−74.
31. R. K. Behera, S. D. Adhikari, S. K. Dutta, A. Dutta and N. Pradhan, *J. Phys. Chem. Lett.*, 2018, ***9***, 6884–6891.
32. Y. Ji, M. Wang, Z. Yang, H. Wang, M. A. Padhiar, H. Qiu, J. Dang, Y. Miao, Y. Zhoua and A. S. Bhatti, *Nanoscale*, 2022, ***14***, 2359-2366.
33. J. Xue, J.-W. Lee, Z. Dai, R. Wang, S. Nuryyeva, M. E. Liao, S.-Y. Chang, L. Meng, D. Meng, P. Sun, O. Lin, M. S. Goorsky and Y. Yang, *Joule*, 2018, ***2***, 1866–1878.
34. S. Wang, Y. Wang, Y. Zhang, X. Zhang, X. Shen, X. Zhuang, P. Lu, W. W. Yu, S. V. Kershaw and A. L. Rogach, *J. Phys. Chem. Lett.*, 2019, ***10***, 90–96.
35. T.-S. Leu and C.-S. Wang, *J. Appl. Polym. Sci.*, 2004, ***92***, 410−417.
36. V. K. Ravi, P. K. Santra, N. Joshi, J. Chugh, S. K. Singh, H. Rensmo, P. Ghosh and A. Nag, *J. Phys. Chem. Lett.*, 2017, ***8***, 4988–4994.
37. S. Das and A. Samanta, *ACS Energy Lett.*, 2021, ***6***, 3780−3787.
38. A. Dutta, S. K. Dutta, S. D. Adhikari and D. N. Pradhan, *Angew.Chem.Int.Ed.*, 2018, ***57***, 9083–9087.
39. Q. Zhong, M. Cao, Y. Xu, P. Li, Y. Zhang, H. Hu, D. Yang, Y. Xu, L. Wang, Y. Li, X. Zhang and Q. Zhang, *Nano Lett.*, 2019, ***19***, 4151–4157.
40. G. Almeida, L. Goldoni, Q. Akkerman, Z. Dang, A. H. Khan, S. Marras, I. Moreels and L. Manna, *ACS Nano*, 2018, ***12***, 1704–1711.
41. V. G. V. Dutt, S. Akhil and N. Mishra, *Nanoscale*, 2021, ***13***, 14442-14449.

42. G. Almeida, O. J. Ashton, L. Goldoni, D. Maggioni, U. Petralanda, N. Mishra, Q. A. Akkerman, I. Infante, H. J. Snaith and L. Manna, *J. Am. Chem. Soc.*, 2018, ***140***, 14878–14886.
43. G. H. Ahmed, J. K. El-Demellawi, J. Yin, J. Pan, D. B. Velusamy, M. N. Hedhili, E. Alarousu, O. M. Bakr, H. N. Alshareef and O. F. Mohammed, *ACS Energy Lett.*, 2018, ***3***, 2301−2307.
44. J. D. Roo, M. Ibáñez, P. Geiregat, G. Nedelcu, W. Walravens, J. Maes, J. C. Martins, I. V. Driessche, M. V. Kovalenko and Z. Hens, *ACS Nano*, 2016, ***10***, 2071–2081.
45. F. Krieg, S. T. Ochsenbein, S. Yakunin, S. t. Brinck, P. Aellen, A. Süess, B. Clerc, D. Guggisberg, O. Nazarenko, Y. Shynkarenko, S. Kumar, C.-J. Shih, I. Infante and M. V. Kovalenko, *ACS Energy Lett.*, 2018, ***3***, 641−646.

CHAPTER 7

Summary and Concluding Remarks

Overview

This chapter briefly summarizes the background and results obtained. Also, based on the current findings, future direction of studies and possible challenges are discussed.

7.1. Conspectus

The thesis revolves around photophysical studies of lead-halide perovskite NCs, a newly emerged semiconductor of this century with great potential in light-emitting and absorbing applications. However, apart from the presence of toxic lead, these NCs suffer from poor PL efficiency and ambient stability which back-foot their promising utility in real applications. In this thesis, we have attempted to identify the factors responsible for these detrimental properties of the NCs and develop new strategies to partially overcome those challenges in achieving stable and brightly luminescent NCs. Since relaxation dynamics of the photoinduced transients is the key in achieving efficient devices of any materials, an in-depth understanding of the nonradiative and radiative charge carrier recombination processes in the photoexcited NCs was acquired using ultrafast pump-probe and TCSPC techniques. Besides, the steady state UV-Vis spectrophotometer and spectrofluorimeter were used as preliminary studies of every optical measurement. The surface ligand environment, which has a profound role in stabilization of the NCs, was investigated employing NMR (^{1}H and ^{13}C) and FTIR studies. Any change in morphology and crystal phase of the NCs was determined from TEM and PDRD data, respectively. EDX and XPS provide useful insight into the elemental composition and surface stoichiometry, which were needed for elucidation of the structure-property relationship of the NCs. A summary of the experimental findings of this study is presented below.

Though perovskite NCs are known to be defect tolerant, they are however not completely free from surface and/or intrinsic defects resulting in a sub-unity PLQY of the NCs. Impurity doping is reported to be an effective strategy in modulating optical properties of the conventional metal chalcogenide QDs that was later extended to the perovskite NCs. Here we have shown that a simple room temperature post-synthetic treatment of $CsPbX_3$ (X = Cl and Br) NCs with MgX_2 leads to incorporation of significant amount of Mg^{2+} into the NCs (in place of Pb^{2+}) yielding systems that are brightly luminescent (PLQY of ~51% to ~100% for $CsPbBr_3$ and from ~1% to ~79% for $CsPbCl_3$ NCs), highly stable, less toxic (~23% less lead content) and more resistant towards polar environment like water and ethanol. We have proposed a model explaining the improved PL properties of the doped systems based on the findings of the ultrafast pump-probe and temperature dependent PL measurement. Effective suppression of the halide vacancy related surface defects and curing of octahedral distortion are found to be the key factors for such improved PLQY and stability of the doped NCs. Moreover, Mg-doping introduces some energy states in the conduction band resulting in faster HCC in these systems. Excellent optical properties, less toxicity and high stability of these NCs

under different conditions are expected to make them promising materials for optoelectronic and photovoltaic applications.

Although 'three-precursor' method of synthesis of the perovskite NCs using an independent source of halide produces much better quality NCs compared to the conventional 'two-precursor' method, PLQY and stability of the NCs again largely depend on efficiency of the employed halide precursors. Iodide-based NCs are the most demanding due to their low band-gap. However, high phase sensitivity and abundant iodide vacancy related surface defects are impediments to their utilization particularly in solar photovoltaic applications. Therefore, achieving highly luminescent and stable $APbI_3$ NCs emitting in the red-to-NIR region is a challenging task, termed as 'perovskite red-wall'. Here we have developed a generic method of preparation of mono-dispersed, phase-pure, exceptionally stable and highly luminescent red/NIR-emitting all three iodide-based systems, $CsPbI_3$, $(MA)PbI_3$ and $(FA)PbI_3$ NCs, employing 1,3-diiodo-5,5-dimethylhydantoin (DIDMH) as iodide precursor. The $CsPbI_3$ NCs exhibit a near-unity PLQY, while $(MA)PbI_3$ and $(FA)PbI_3$ NCs display PLQY of 74±2 and 67±2%, respectively. These values are comparable with their best PLQY values reported till date. Moreover, the NCs retain their crystal phase for several months under ambient conditions. DIDMH-assisted formation of oleylammonium-lead iodide terminated surface contributes to such exceptional characteristics to these NCs. Outstanding phase durability and excellent PLQY of all three all-inorganic and hybrid systems obtained by a common procedure is an important advancement that significantly brightens the prospect of utilization of these narrow bandgap materials in optoelectronic and photovoltaic applications, particularly in single-absorber solar cells.

Direct syntheis of all possible lead-halide perovskite NCs of $APbX_3$ type [A= Cs^+, methylammonium (MA^+) or formamidinium (FA^+) and X= Cl^-, Br^- or I^-] following a common method is found to be a challenging job even after seven years of their invention. Motivated by our earlier success in achieving high quality iodide-based NCs with unmatched optical properties and stability using DIDMH as iodide precursor, we have extended this approach even for the violet-emitting $APbCl_3$ and green-emitting $APbBr_3$ NCs using the chloro- and bromo-analogs of DIDMH. Our experimental findings show that, indeed one can directly obtain all-inorganic and hybrid lead halide perovskite $APbX_3$ NCs (where A= Cs^+, MA^+ or FA^+ and X= Cl^-, Br^- or I^-) of high-quality emitting in the 395 - 760 nm region using the respective halo-analog of the hydantoin derivative as halide precursors. The excellent characteristics of these NCs, e.g. great phase purity, narrow size distribution, high PLQY (near-unity for $APbBr_3$ and ~70% for $CsPbCl_3$ NCs)

and superb stability (except for $MAPbCl_3$ and $FAPbCl_3$ NCs), make our $APbX_3$ NCs by far the best systems obtained by a common procedure. Thanks to highly effective halide precursors, which facilitate *in situ* generation of OAm^+X^- resulting in oleylammonium-lead halide terminated surface, such exceptional characteristics of the NCs are observed. This methodology that works for all three 'A^+' and 'X^-' components clearly stands out for its versatility and impressive outcomes.

The violet-emitting $CsPbCl_3$ NCs are the least emitting systems among the perovskite NCs, and this feature impedes their utilization in violet-LEDs. Moreover, large density of insulating surface ligands hinders the charge injection processes into the perovskite NCs further diminishing the efficiency of LEDs based on $CsPbCl_3$ NCs. Therefore brightly luminescent stable $CsPbCl_3$ NCs with low density of passivating ligands are required for obtaining highly efficient violet-emitting optoelectronic devices. We have shown that phase pure and monodispersed $CsPbCl_3$ NCs with very high PLQY of ~87% can indeed be obtained directly employing DPPC as a chlorinating agent. Moreover, unlike weakly H-bonded protonated amines, the NCs prepared by our method are found to be strongly coordinated by neutral amine ligands with surface Pb^{2+}, which effectively passivates the uncoordinated Pb ions in achieving such high PL efficiency of the NCs. More interestingly, the NCs retain their bright emission even after 10 times washing with polar and nonpolar solvents making them ideal for real applications by removing excessive insulating surface capping ligands. We have also demonstrated ultrapure down-converted violet-LEDs based on these NCs with emission peak at 410 nm, EQE of up to 0.19% and FWHM of 12 nm. Thus we have eventually opened up a new avenue for achieving a broad range of efficient perovskite-based light-emitting devices in this high-energy spectral region.

7.2. Future Scope and Challenges

Although Mg doping boosts PLQY of the Mg-$CsPbBr_3$ NCs to near-unity, for the Mg-$CsPbCl_3$ NCs, this value is limited to 79%. Again, post-synthetic Mg-doping is not that effective for the iodide–based $CsPbI_3$ NCs. A common post-synthetic metal ion doping to attain near-unity PLQY of all $CsPbX_3$ (X= Cl, Br and I) NCs covering the entire visible region is not reported yet. As doping not only improves the PLQY and stability of the NCs but also reduces the toxicity of the overall system, we need to find a suitable benign metal salt that is equally effective for all systems. Although we have succeeded in obtaining all $APbX_3$ NCs through a common procedure, the chloride-based hybrid NCs are poorly luminescent (PLQY of ~1-3%) compared to the other NCs. The same is true

for the hybrid $MAPbI_3$ and $FAPbI_3$ NCs, which exhibit PLQY in the range of 67-74%. This indicates that, DXDMH is clearly not equally effective for all lead-halide NCs and this invites more attention in designing new halide precursors for all the NCs with equal effectivity. Near-unity PLQY of the $APbX_3$ NCs will be a huge breakthrough from the point of view of light-emitting applications. Again, we have to look into methodologies for even better stabilization of the iodide-based NCs keeping in mind of their great promise towards solar photovoltaics. As L-type coordination of capping ligands provides better structural and optical stability of the $CsPbCl_3$ NCs, we can use this methodology even for the $CsPbBr_3$ and $CsPbI_3$ NCs, possibly using the respective halo derivatives of DPPC or any other halogen sources. Also, $CsPbCl_3$ NCs with near-unity PLQY are rare and any success in this direction will definitely boost the efficiency of perovskite based violet-LEDs.

Finally, perovskites are sometimes termed as ‘miracle material’ as the mechanism by which they interact with metal halide salts are frequently not predictable. Hence, identifying a metal salt or designing a halide precursor for achieving great quality $APbX_3$ NCs is indeed a challenging task. Different electronic band structure of the NCs for different halide compositions is possibly the reason behind such highly specific behaviour. Again a popular paradigm about the stability of perovskite NCs is that they are as easy as to make, it is just as easy to break. Although a great progress has been made in terms of optical and structural stability of these NCs since their introduction, a long way still needs to be covered for practical utility of these highly coveted materials for the mankind.

Appendices

Appendix 1

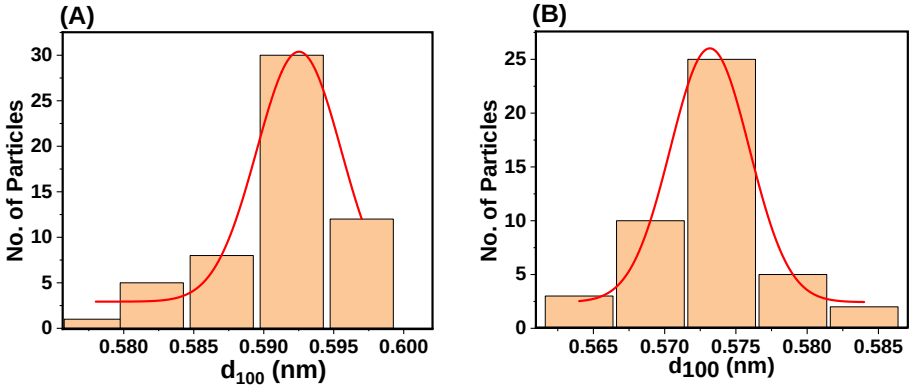

Figure A1.1. *Lattice distances of the 100 planes as obtained from the TEM images of (A) undoped and (B) doped NCs.*

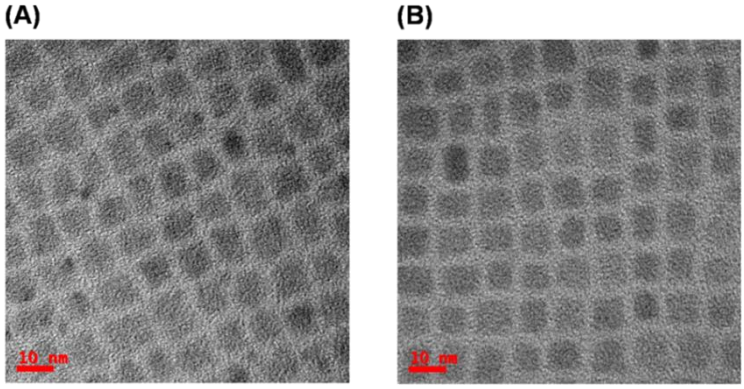

Figure A1.2. *TEM images of (A) undoped and (B) Mg-doped $CsPbCl_3$ NCs. The edge-length of the undoped and doped NCs are found to be 8.6±1.5 and 7.5±1.5 nm respectively.*

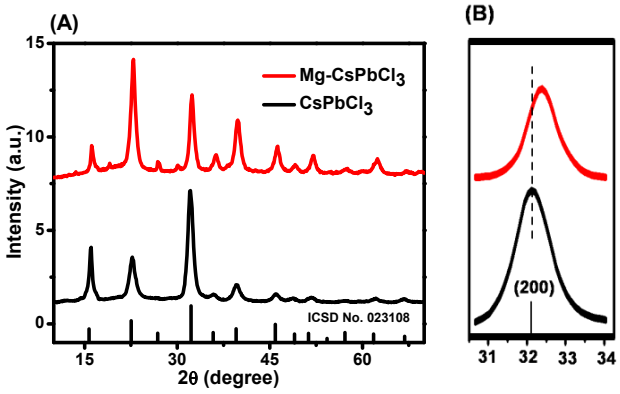

Figure A1.3. *(A) PXRD patterns of undoped and Mg-doped $CsPbCl_3$ NCs. (B) Shift of PXRD peak position at higher angle corresponding to the (200) plane indicates lattice contraction in the doped NCs.*

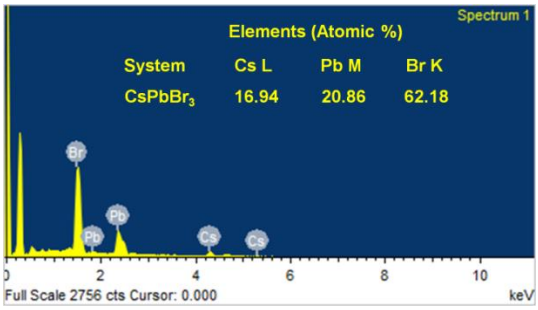

Figure A1.4. *EDX spectrum of undoped $CsPbBr_3$ NCs.*

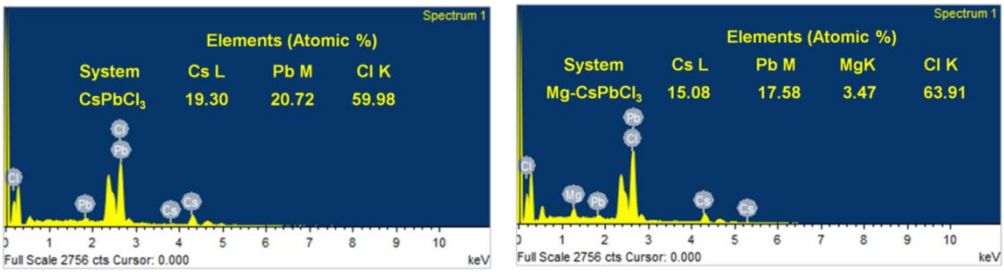

Figure A1.5. *EDX spectrum of undoped and Mg-doped $CsPbCl_3$ NCs.*

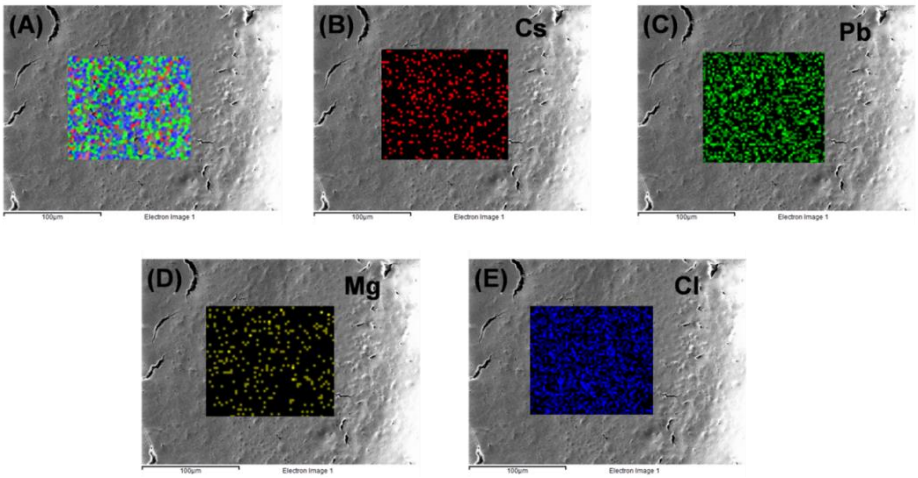

Figure A1.6. *(A) FESEM images of doped $CsPbCl_3$ NCs. The central portion is scanned for elemental mapping. (B to E) Elemental mapping indicates homogeneous distribution of all the corresponding elements throughout the scanned area.*

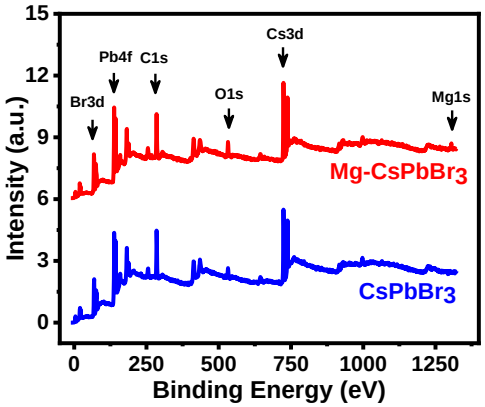

Figure A1.7. *XPS survey spectra of undoped and Mg-doped $CsPbBr_3$ NCs. The spectra were calibrated with respect to 'C1s' peak at 285.0 eV.*

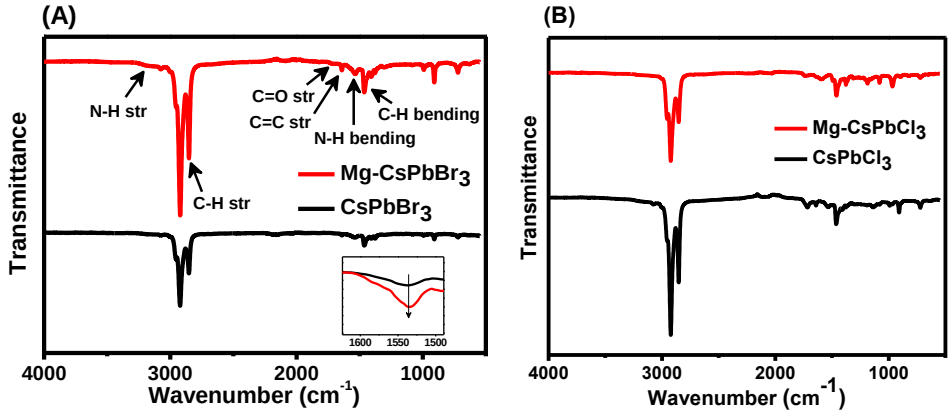

Figure A1.8. *FTIR spectra of undoped and doped (A) $CsPbBr_3$ and (B) $CsPbCl_3$ NCs.The inset in (A) shows enhanced intensity of N-H bending (scissoring) of the surface oleylammonium cations.*[1, 2]

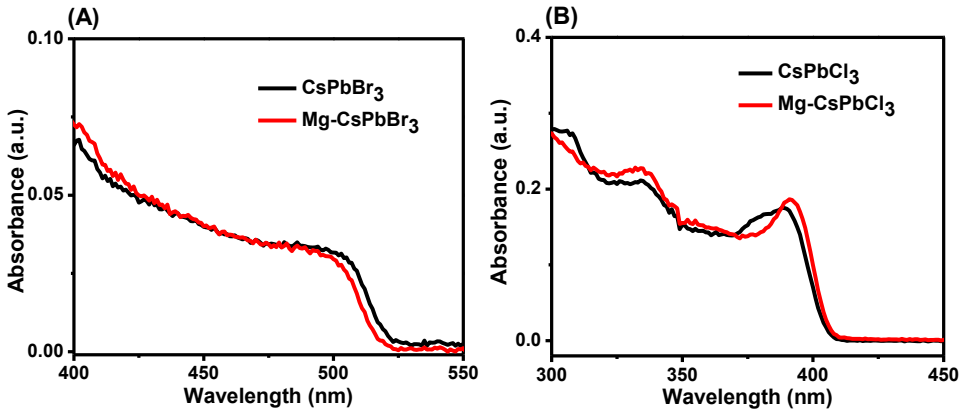

Figure A1.9. *Absorption spectra of undoped and doped (A) $CsPbBr_3$ and (B) $CsPbCl_3$ NCs.*

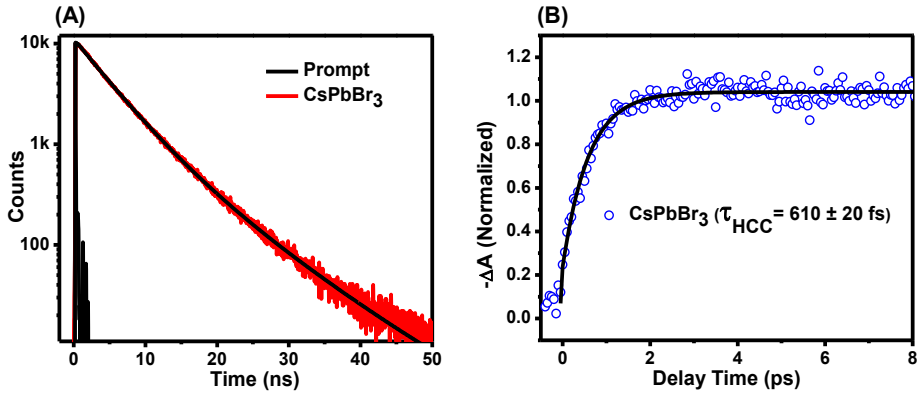

Figure A1.10. *(A) PL decay profile (λ_{ex} = 404 nm) of $CsPbBr_3$ NCs synthesized by following ref. 3 (PLQY of 92±2%). The decay parameters obtained on bi-exponential fitting of the data are: τ_1 = 4.49 ns (0.83) and τ_2 = 9.06 ns (0.17) with $<\tau_{amp}>$ of 5.27 ns. (B) HCC dynamics of the same NCs showing a cooling time of (610±20 fs) (λ_{ex} = 350 nm).*

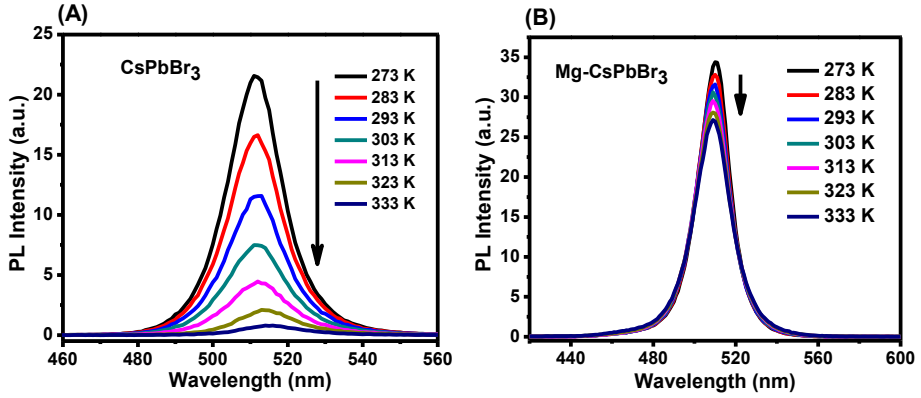

Figure A1.11. *Temperature dependence of the PL spectra of undoped (A) and doped (B) $CsPbBr_3$ NCs. A red-shift (~5 nm) of the PL maximums observed for undoped sample, while it remains unchanged for the doped one over the same temperature window.*

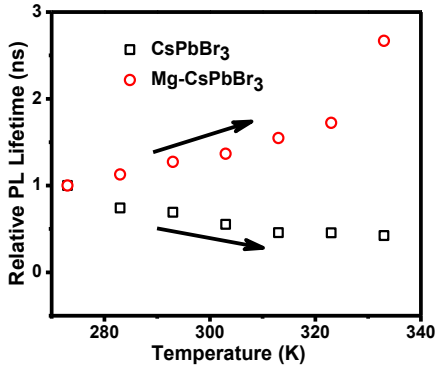

Figure A1.12. *Comparison of the average PL lifetime of undoped and doped $CsPbBr_3$ NCs with temperature.*

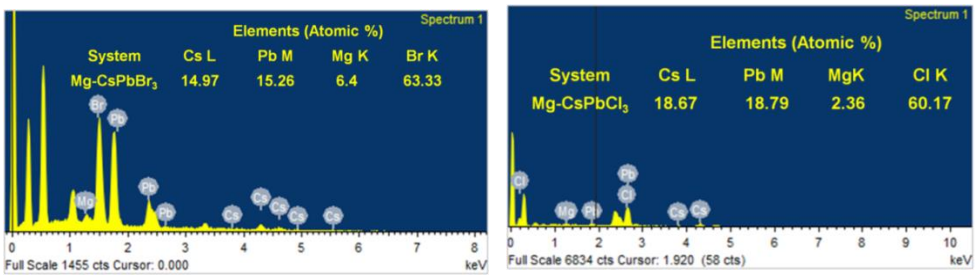

Figure A1.13. *EDX spectrum of MgO-treated $CsPbBr_3$ and $CsPbCl_3$ NCs, respectively.*

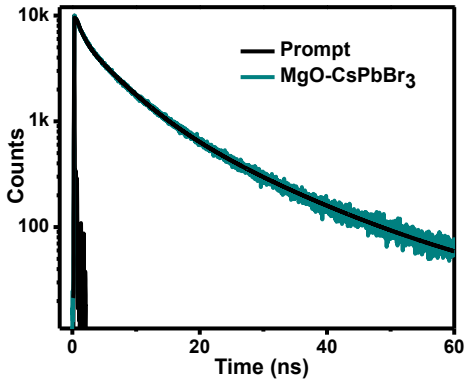

Figure A1.14. *PL decay profile of MgO treated $CsPbBr_3$ NCs. PL decay was recorded by exciting the sample with 405 nm laser, and monitored at the corresponding emission maxima. The decay parameters obtained on tri-exponential fitting of the data are: τ_1 =5.41 ns (0.44), τ_2 = 15.69 ns (0.14) and τ_3 = 0.86 ns (0.42), which correspond to $<\tau_{amp}>$ of 4.94 ns. Presence of faster trapping component i.e τ_3 indicates the existence of bromide vacancy related trap states, resulting in sub-unity (~87%) PLQY of the doped NCs.*

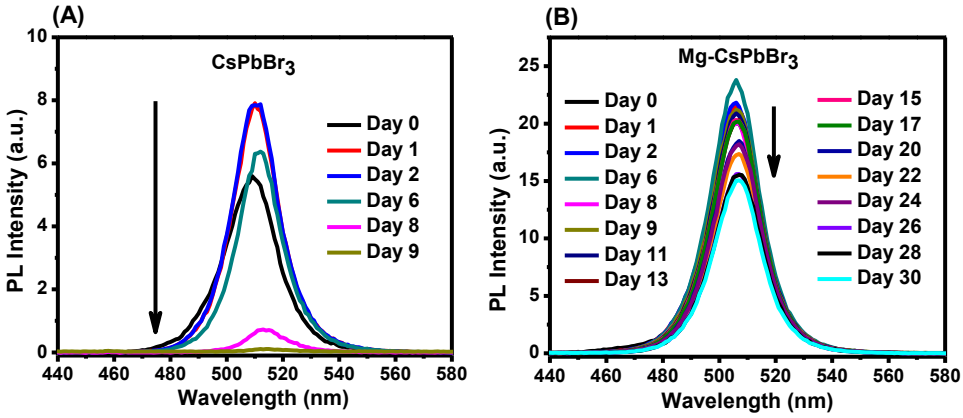

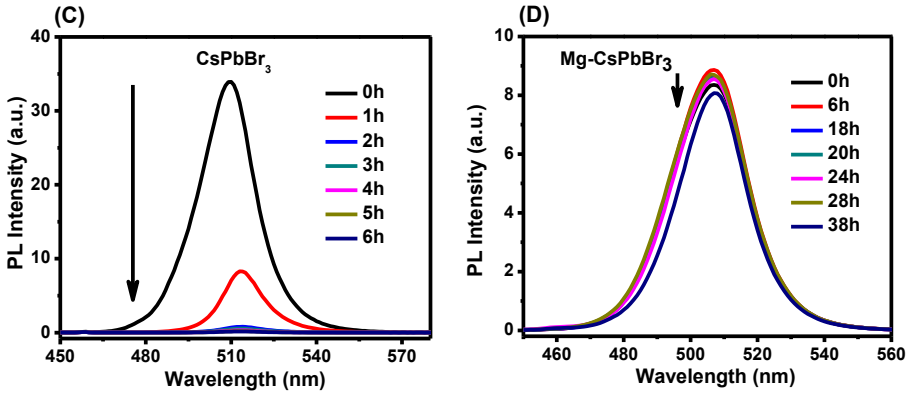

Figure A1.15. *Time-dependence of the PL spectra of undoped and doped $CsPbBr_3$ NCs in air (A and B respectively) and under 365 nm (8W) continuous UV light exposure (C and D respectively).*

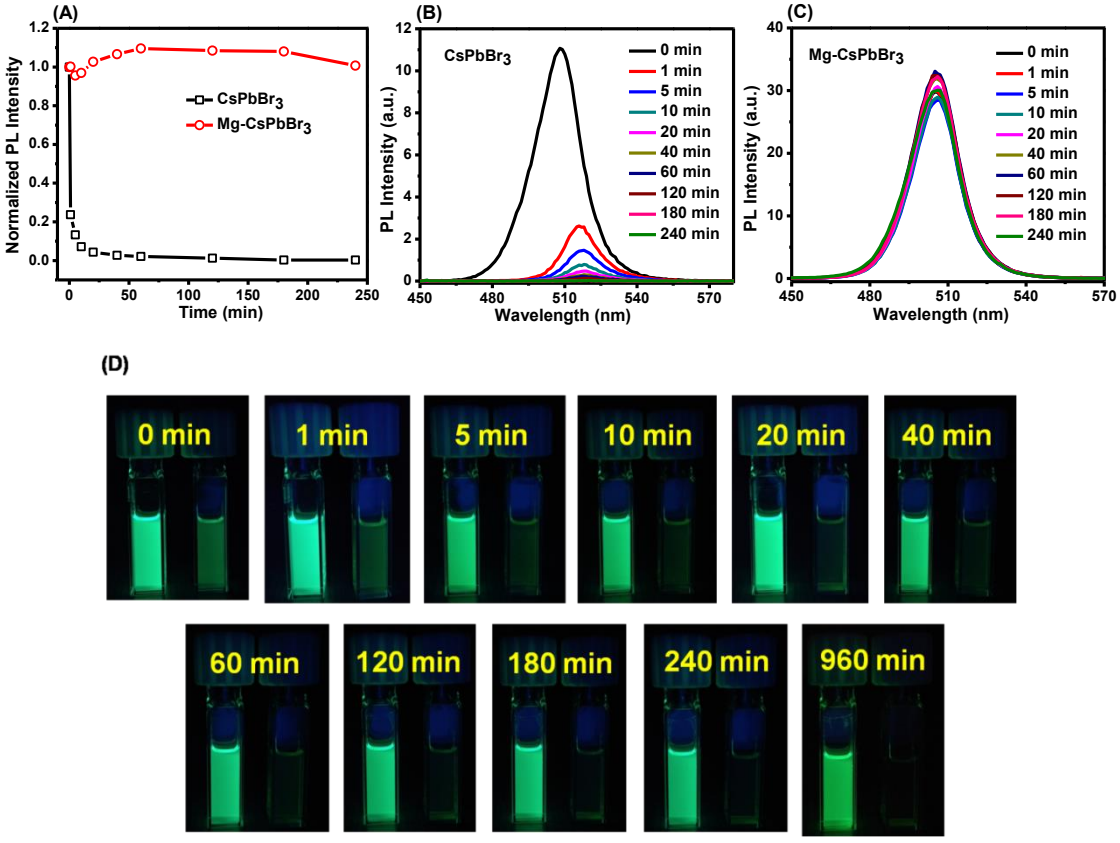

Figure A1.16. *Resistance of undoped and doped $CsPbBr_3$ NCs towards ethanol. Here 20 µl ethanol was mixed with a colloidal dispersion of the doped/undoped NCs in hexane (0.01 µM) and PL intensity was monitored with time. (A) PL is quenched almost completely in just 20 mins for the undoped NCs while for the doped one PL is hardly affected after 240 min under similar environment. (B,C) Change in PL spectra with time for the two samples. In addition to drastic drop in PL intensity, the undoped sample*

shows a red shift of ~8-10 nm of the PL peak position immediately after addition of ethanol indicating rapid degradation of the NCs, whereas the PL peak position remains unchanged for the doped system. (D) Corresponding digital photographs (under 365 nm UV light) of the two samples showing the greater resistance of the doped NCs towards ethanol.

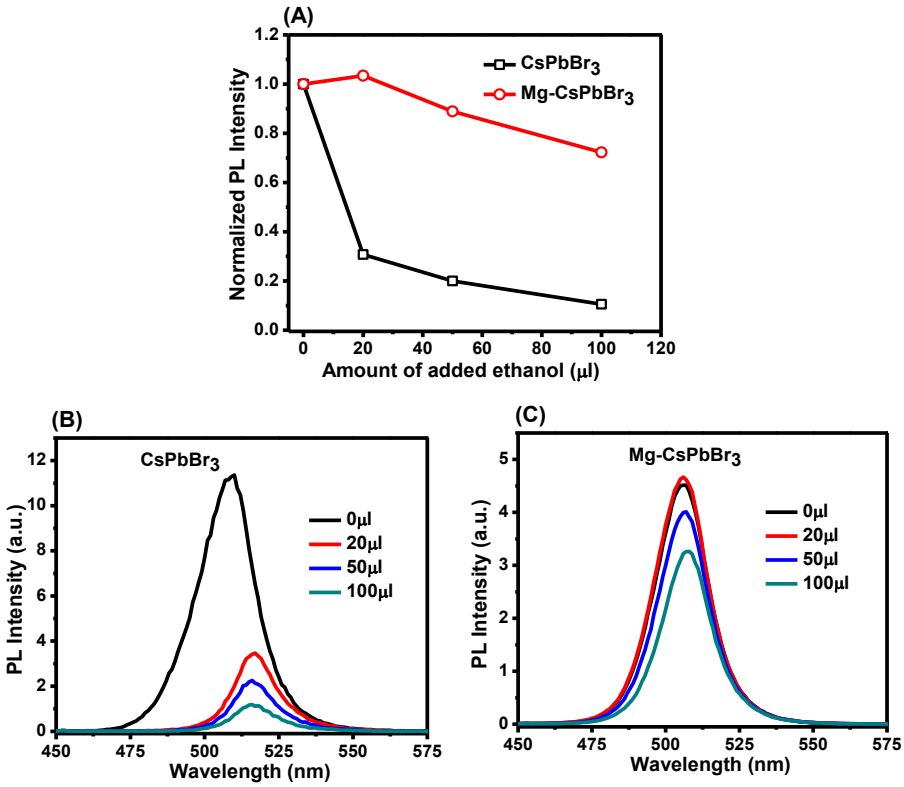

Figure A1.17. *(A) Comparison of the relative PL intensity of undoped and doped $CsPbBr_3$ NCs with progressive addition of ethanol. For undoped NCs ~80% of the initial PL intensity reduces upon addition of maximum volume (100 µl) of ethanol, while for the doped sample ~75% PL intensity is retained after adding same volume of ethanol. (B,C) Apart from the drop in PL intensity, ~10 nm red-shift of the PL maximum is observable for undoped NCs. The Mg-doped $CsPbBr_3$ system, however, shows only ~2 nm red-shift.*

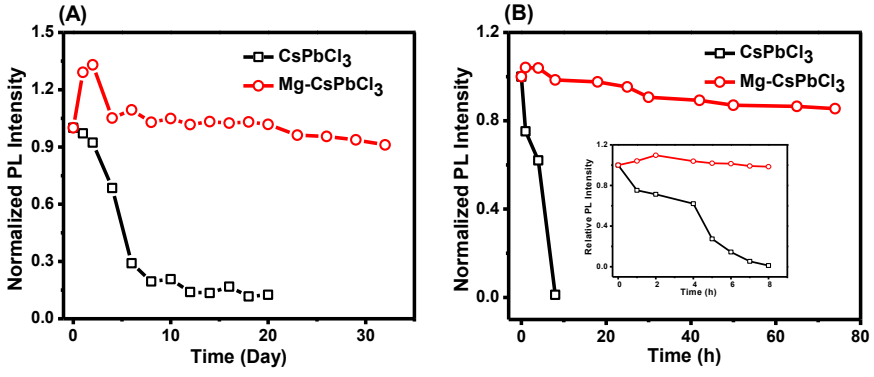

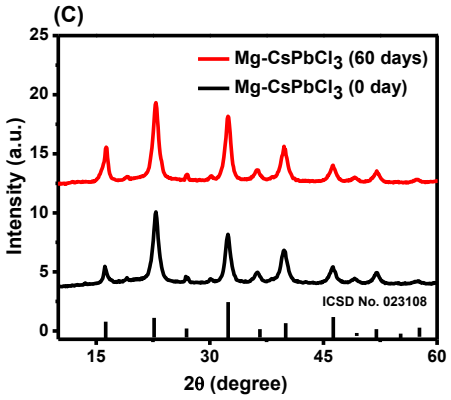

Figure A1.18. *Comparison of (A) air-stability under ambient condition and (B) photo-stability under 365 nm (8W) continuous UV illumination of undoped and doped $CsPbCl_3$ NCs. (C) unchanged PXRD patterns of freshly prepared and 60 days old doped sample indicates superior phase stability of the doped NCs compared to the undoped sample.*

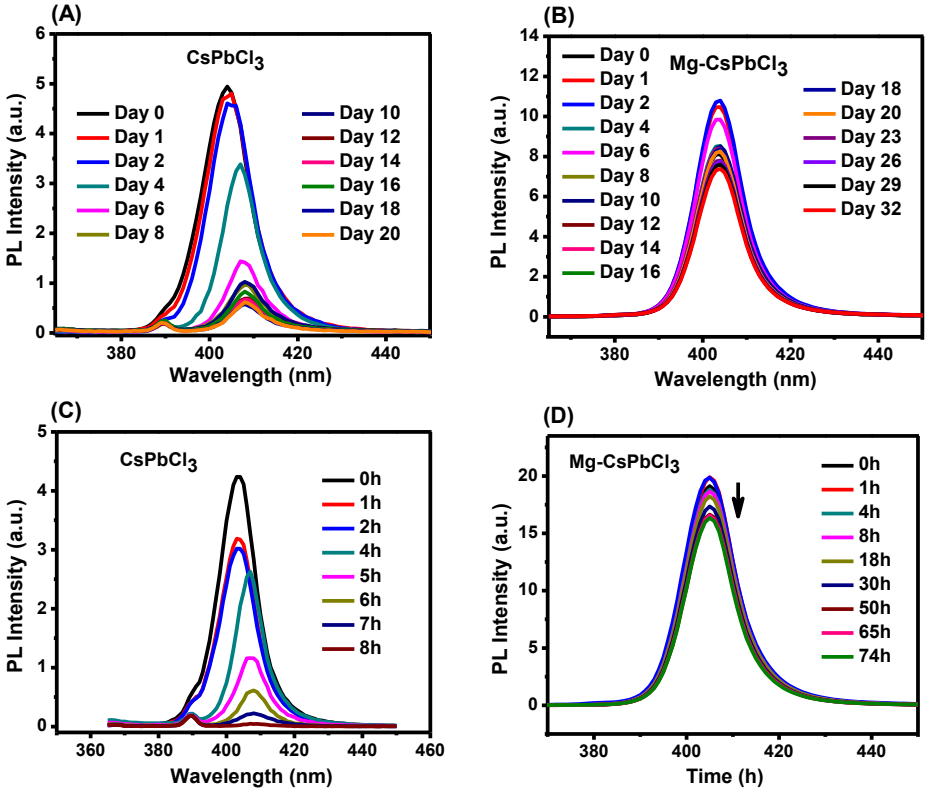

Figure A1.19. *Change of PL spectra of undoped and doped $CsPbCl_3$ NCs in air (A and B respectively) and under 365 nm (8W) continuous UV light exposure (C and D respectively) with time.*

Table A1.1. *PL decay parameters of undoped and doped $CsPbCl_3$ NCs.*

System	Time(h)	$\tau_1(a_1)$/ns	$\tau_2(a_2)$/ns	$\tau_3(a_3)$/ns	$<\tau_{amp}>$/ns
$CsPbCl_3$	---	---	---	---	---
Mg-$CsPbCl_3$	1h	5.04(0.16)	21.35(0.11)	0.74(0.73)	3.69

Table A1.2. *Temperature dependencies of the PL decay parameters of undoped and doped $CsPbBr_3$ NCs.*

System	Temperature/K	$\tau_1(a_1)$/ns	$\tau_2(a_2)$/ns	$\tau_3(a_3)$/ns	$<\tau_{amp}>$/ns
$CsPbBr_3$	273	3.39(0.45)	6.79(0.50)	13.59(0.05)	5.60
	283	1.53(0.47)	5.11(0.47)	17.24(0.06)	4.15
	293	1.22(0.53)	4.87(0.40)	18.31(0.07)	3.88
	303	0.90(0.59)	4.20(0.35)	18.20(0.06)	3.09
	313	0.76(0.66)	3.81(0.29)	19.10(0.05)	2.56
	323	0.65(0.67)	3.49(0.27)	19.60(0.06)	2.55
	333	0.59(0.68)	3.14(0.26)	19.30(0.06)	2.37
System	**Temperature/K**	**$\tau_1(a_1)$/ns**	**$\tau_2(a_2)$/ns**		**$<\tau_{amp}>$/ns**
Mg-$CsPbBr_3$	273	3.30(0.67)	6.70(0.33)		4.42
	283	3.52(0.65)	7.70(0.35)		4.98
	293	3.87(0.63)	8.62(0.37)		5.63
	303	3.85(0.60)	9.33(0.40)		6.04
	313	4.20(0.58)	10.48(0.42)		6.84
	323	4.59(0.56)	11.46(0.44)		7.61
	333	4.89(0.53)	19.57(0.47)		11.79

Table A1.3. *Comparison of the stability and optical properties of green- and violet-emitting perovskite NCs obtained through B-site doping. PS, HI and RT represents post-synthetic treatment, hot-injection method and room-temperature respectively. The % values in bracket under stability column indicate the retained PLQY values.*

system	method	PLQY (%)	λ_{em} (nm)	air-stability	photo-stability	polar solvent stability	ref.
$Zn^{2+}/Cd^{2+}/Sn^{2+}$:$CsPbBr_3$	PS	>50	512-462	several months	---	---	11
Sn^{2+}:$CsPbBr_3$	HI	73.4	503	months (~100%)	---	---	12
Na^{+}:$CsPbBr_3$	RT	85	~509	6 days (~90%)	35 h (>80%)	20 min (>85%)	13
Zn^{2+}:$CsPbBr_3$	HI	78	518	5 days (~50%)	---	---	14
Cu^{2+}:$CsPbBr_3$	HI	95	~500	30 days (>90%)	---	---	15
Mg^{2+}:$CsPbBr_3$	PS	~100	513	30 days (>75%)	38 h (~100%)	>960 min (~100%)	**this work**
Ni^{2+}:$CsPbCl_3$	HI	96.5	~408	6 days (>90%)	---	---	16
Cd^{2+}:$CsPbCl_3$	PS	96	406	60 days (95%)	260 h (60%)	---	17
Y^{3+}:$CsPbCl_3$	PS	60	404	14 days (100%)	---	---	18
Cu^{+}:$CsPbCl_3$	HI	60	403	6 days (60%)	---	---	19
La^{3+}/F^{-}:$CsPbCl_3$	HI	36.5	410	---	48 h (40%)	---	20
Mg^{2+}:$CsPbCl_3$	PS	~79	403	30 days (>90%)	78 h (>90%)	---	**this work**

References:

1. A. Pan, B. He, X. Fan, Z. Liu, J. J. Urban, A. P. Alivisatos, L. He and Y. Liu, *ACS Nano*, 2016, ***10***, 7943-7954.
2. I. O. P. D. Berti, M. V. Cagnoli, G. Pecchi, J. L. Alessandrini, S. J. Stewart, J. F. Bengoa and S. G. Marchetti, *Nanotechnology*, 2013, ***24***, 175601-175612.
3. M. Imran, V. Caligiuri, M. Wang, L. Goldoni, M. Prato, R. Krahne, L. D. Trizio and L. Manna, *J. Am. Chem. Soc.*, 2018, ***140***, 2656-2664.

4. W. v. d. Stam, J. J. Geuchies, T. Altantzis, K. H. W. v. d. Bos, J. D. Meeldijk, S. V. Aert, S. Bals, D. Vanmaekelbergh and C. d. M. Donega, *J. Am. Chem. Soc.*, 2017, ***139***, 4087-4097.
5. A. B. F. Vitoreti, S. Agouram, M. S. d. l. Fuente, V. Muñoz-Sanjosé, M. A. Schiavon and I. Mora-Seró, *J. Phys. Chem. C*, 2018, ***122***, 14222-14231.
6. S. Li, Z. Shi, F. Zhang, L. Wang, Z. Ma, D. Yang, Z. Yao, D. Wu, T.-T. Xu, Y. Tian, Y. Zhang, C. Shan and X. J. Li, *Chem. Mater.*, 2019, ***31***, 3917-3928.
7. J. Y. Woo, Y. Kim, J. Bae, T. G. Kim, J. W. Kim, D. C. Lee and S. Jeong, *Chem. Mater.*, 2017, ***29***, 7088-7092.
8. C. Bi, S. Wang, Q. Li, S. V. Kershaw, J. Tian and A. L. Rogach, *J. Phys. Chem. Lett.*, 2019, ***10***, 943-952.
9. Z.-J. Yong, S.-Q. Guo, J.-P. Ma, J.-Y. Zhang, Z.-Y. Li, Y.-M. Chen, B.-B. Zhang, Y. Zhou, J. Shu, J.-L. Gu, L.-R. Zheng, O. M. Bakr and H.-T. Sun, *J. Am. Chem. Soc.*, 2018, ***140***, 9942-9951.
10. N. Mondal, A. De and A. Samanta, *ACS Energy Lett.*, 2019, ***4***, 32-39.
11. G. H. Ahmed, J. K. El-Demellawi, J. Y. Pan, D. B. Velusamy, M. N. Hedhili, E. Alarousu, O. M. Bakr, H. N. Alshareef and O. F. Mohammed, *ACS Energy Lett.*, 2018, ***3***, 2301-2307.
12. A. De, S. Das, N. Mondal and A. Samanta, *ACS Materials Lett.*, 2019, ***1***, 116-122.
13. Y. Zhai, X. Bai, G. Pan, J. Zhu, H. Shao, B. Dong, L. Xu and H. Song, *Nanoscale*, 2019, ***11***, 2484-2491.

Appendix 2

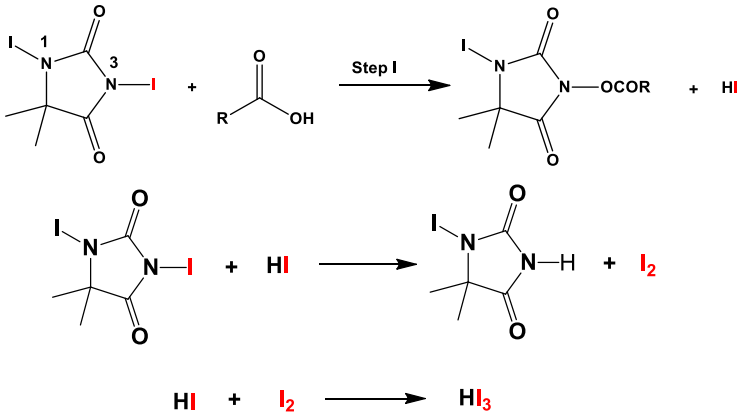

Mechanism of Step 1:

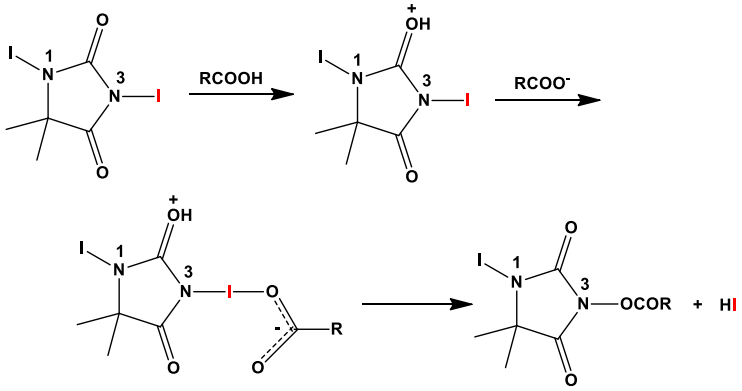

Scheme A2.1. *Reaction intermediates and mechanism of formation of HI in the reaction between DIDMH and OA (represented as RCOOH).*

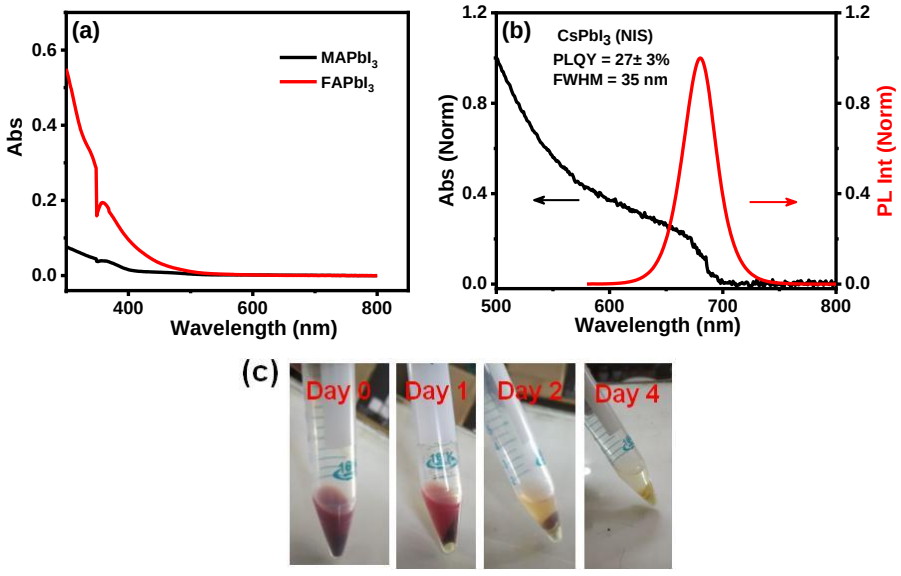

Figure A2.1. *a) UV-Vis absorption spectra of $(MA)PbI_3$ and $(FA)PbI_3$ NCs obtained using NIS as iodinating agent. b) UV-Vis absorption and PL spectra of $CsPbI_3$ NCs prepared using NIS as iodide source. c) Digital photographs of the NCs under ambient conditions at different time intervals.*

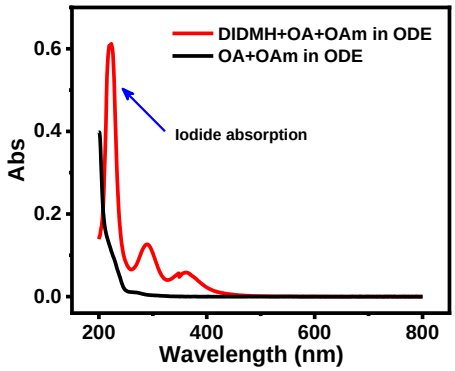

Figure A2.2. *Comparison of the UV-Vis absorption spectra of two solutions of OA and OAm in ODE with (red) and without (black) DIDMH (heated at 130°C). Presence of a sharp absorption peak at ~220 nm for the former suggests the formation of iodide in the medium.*

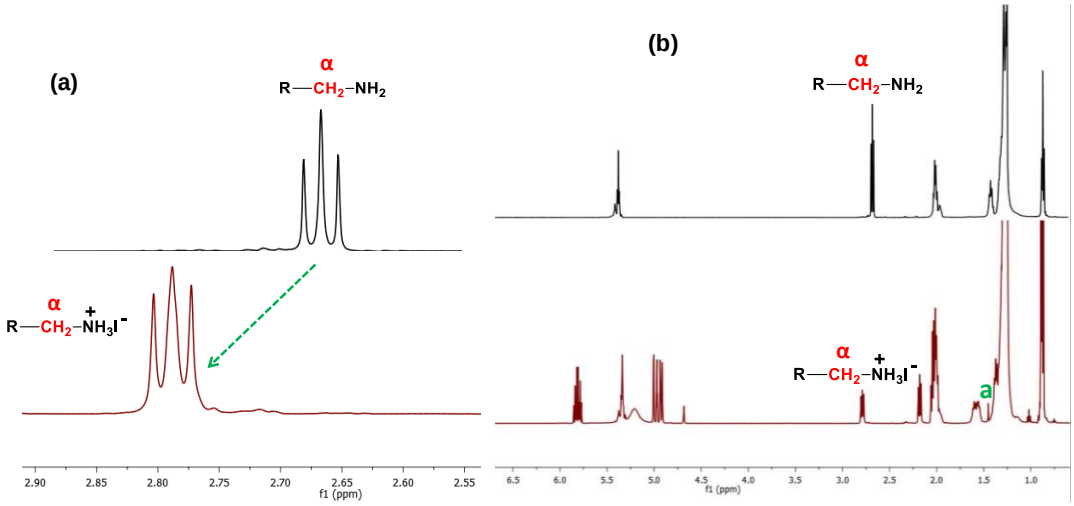

Figure A2.3. *A comparison of the ^1H NMR spectra of pure OAm (black) and a mixture of DIDMH, OA and OAm in ODE (brown) (heated at 130°C). a) Selected portion of the ^1H NMR spectrum and b) corresponding full range ^1H NMR spectrum. The measurements were performed in $CDCl_3$. All the peaks are consistent with the reported literatures.[1, 2] The singlet resonance marked 'a' corresponds to methyl protons of the complex formed in 'step 1' of our reaction (Scheme 4.1 and A2.1).*

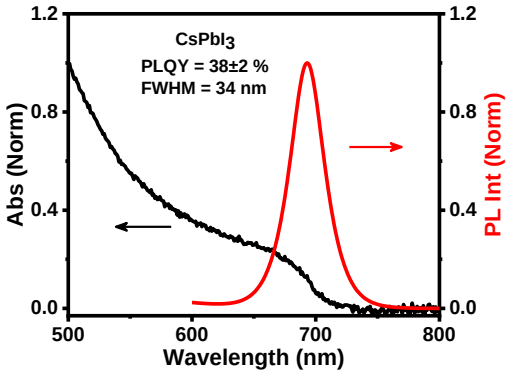

Figure A2.4. *UV-Vis absorption and PL spectra of the $CsPbI_3$ NCs obtained by injecting OAm^+I^- at 210°C in a solution containing Cs-oleate and Pb-oleate. The OAm^+I^- was prepared by reacting DIDMH with OA and OAm in ODE at 130°C.*

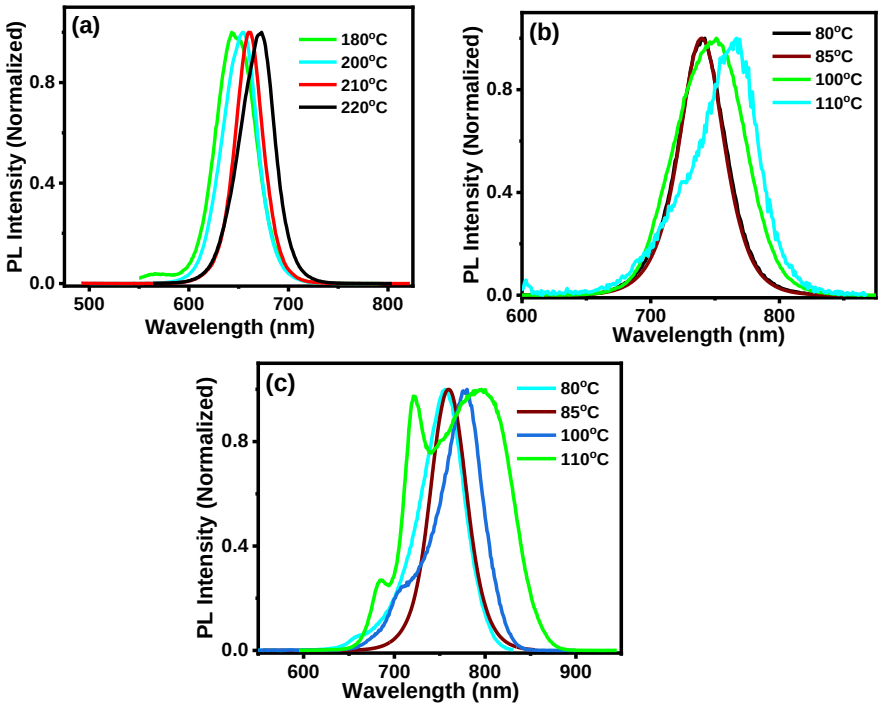

Figure A2.5. *PL spectra of a) $CsPbI_3$, b) $(MA)PbI_3$ and c) $(FA)PbI_3$ NCs obtained at different reaction temperature.*

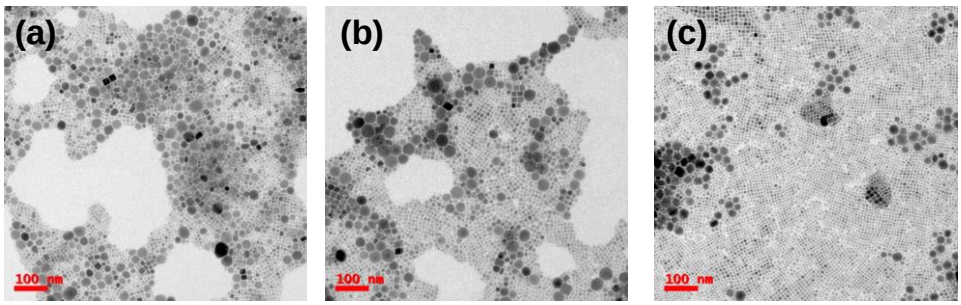

Figure A2.6. *Bright-field TEM images of $CsPbI_3$ NCs obtained at a) 130°C, b) 160°C and c) 180°C. The scale bar is 100 nm in each case.*

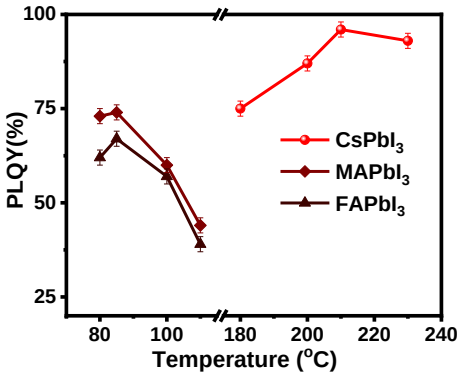

Figure A2.7. *Dependence of the PLQY of $APbI_3$ NCs on the reaction temperature.*

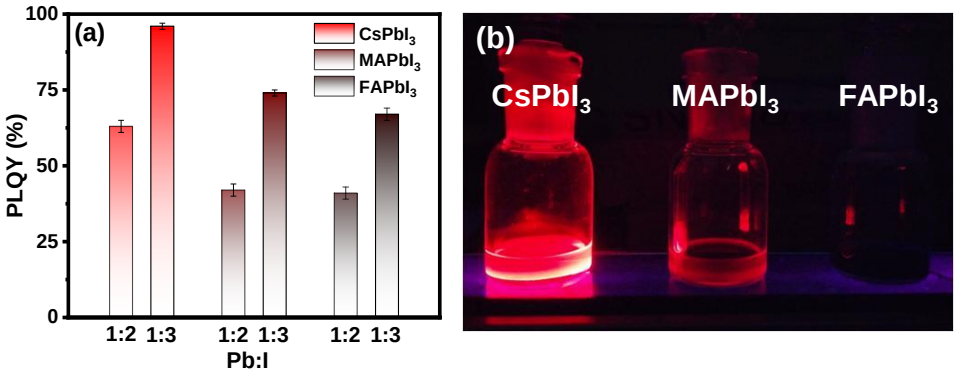

Figure A2.8. *a) Dependence of PLQY of the NCs on the Pb:I precursor molar ratio (at respective optimum temperature). b) Digital images of the $APbI_3$ NCs (Pb:I = 1:3) under 365 nm UV light.*

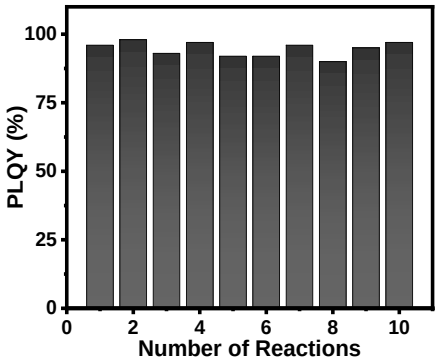

Figure A2.9. *Batch-to-batch variation of the PLQY of the $CsPbI_3$ NCs obtained using a molar Pb to I ratio of 1:3 at 210°C.*

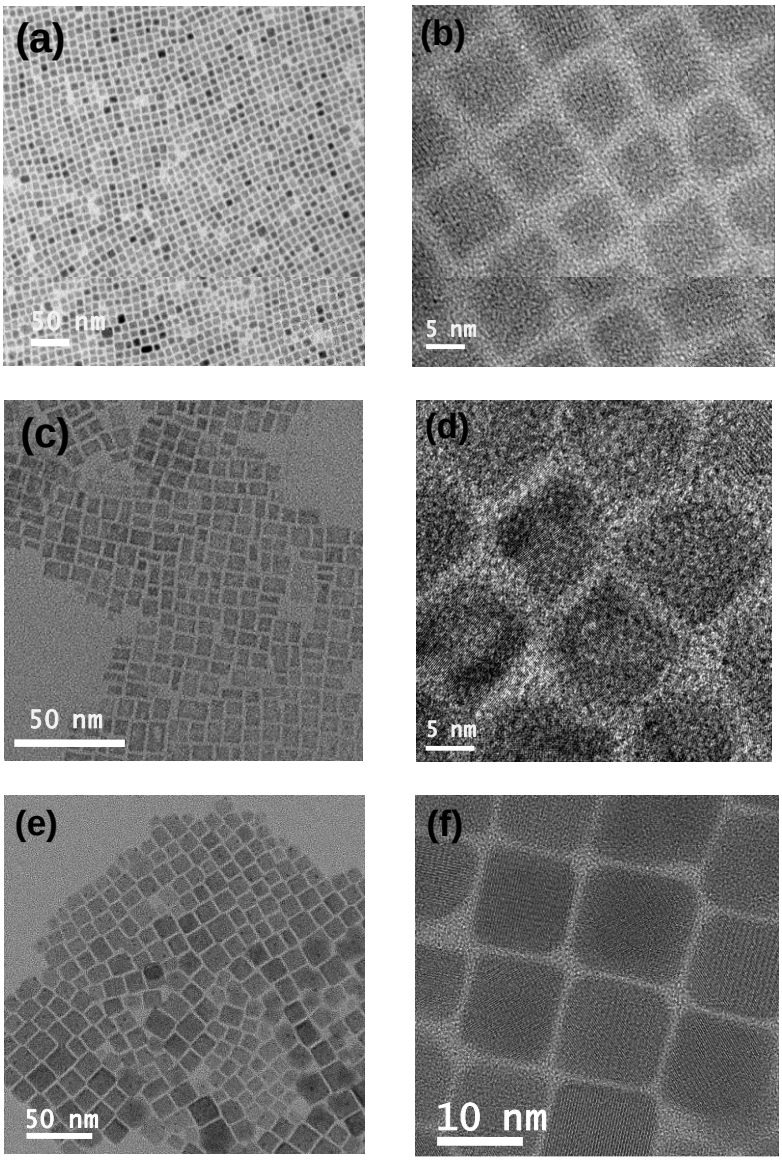

Figure A2.10. *Bright-field TEM images of a,b) $CsPbI_3$, c,d) $(MA)PbI_3$ and e,f) $(FA)PbI_3$ NCs highlighting the homogeneous size distribution of the NCs. The b), d) and f) are high resolution TEM images of the corresponding NCs. The scale bars (in white) are indicated in the bottom left corner of each image.*

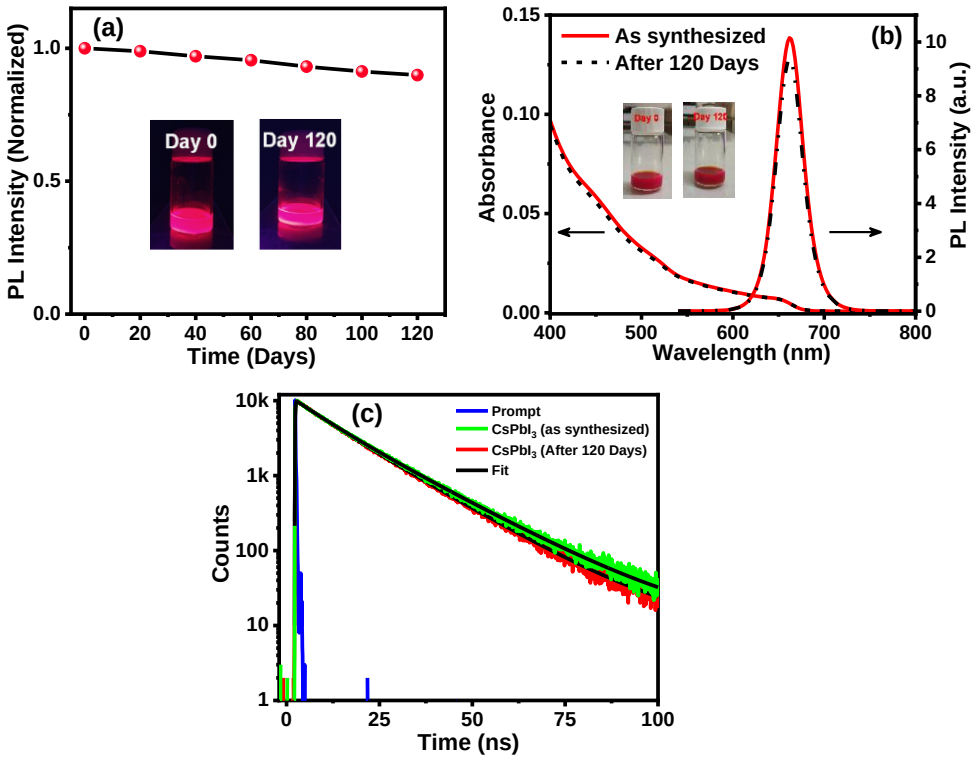

Figure A2.11. *Long term air stability of the $CsPbI_3$ NCs. a) Variation of PL intensity at emission maxima of the NCs with time when stored under ambient conditions. b) UV-Vis absorption and PL spectra of the as-synthesized and 4 months old sample of $CsPbI_3$ NCs stored in a sealed bottle in ambient conditions and c) PL decay profiles of the corresponding as-synthesized and aged samples. The excitation wavelength was 481 nm and the decay was monitored at their respective PL maxima. The digital photographs of the NCs under 365 nm lamp and sunlight are shown as insets in the (a) and (b) panels.*

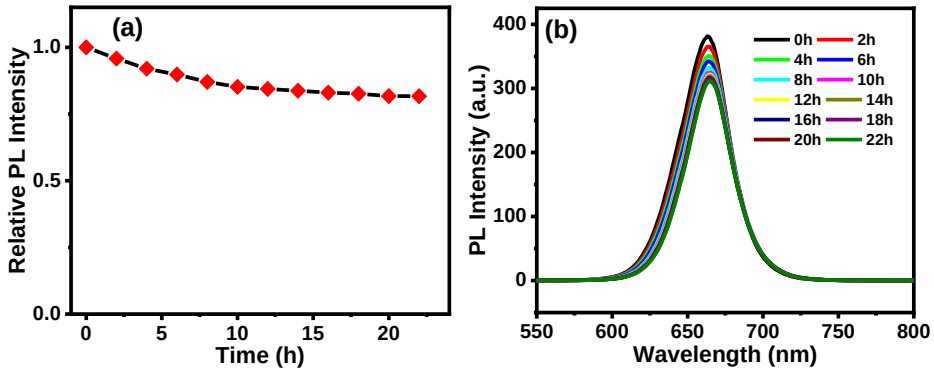

Figure A2.12. *a) Time-dependence of the PL intensity (λ_{em} = 661 nm) and b) corresponding PL spectra of the $CsPbI_3$ NCs under continuous irradiation of UV light (365 nm, 8W) at room-temperature under ambient condition.*

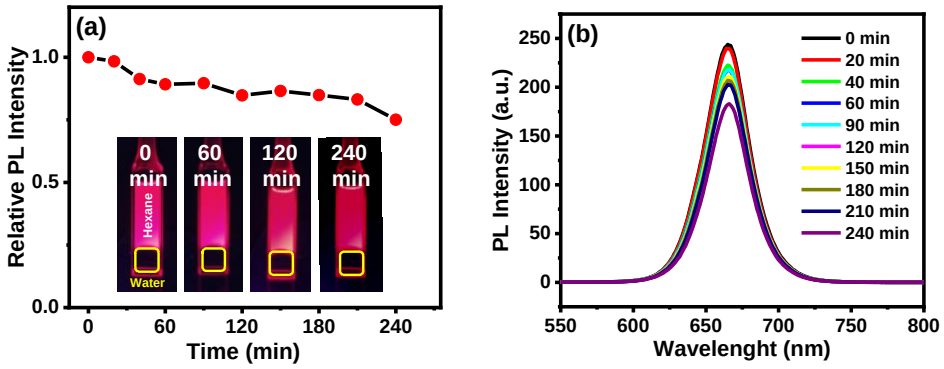

Figure A2.13. *a) Evolution of the PL intensity (at 661 nm) and b) PL spectra of the $CsPbI_3$ NCs in presence of water under ambient condition. The digital images of the NCs dispersion under UV light are also shown.*

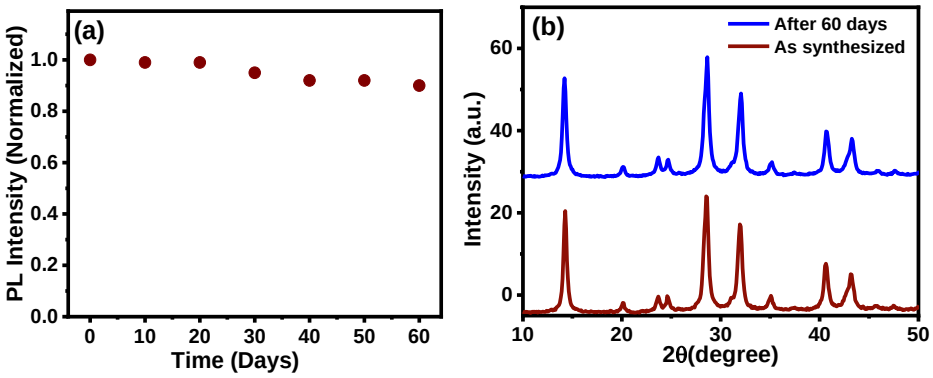

Figure A2.14. *a) Change in PL intensity (λ_{em} = 740 nm) of $(MA)PbI_3$ NCs stored under ambient condition for 2 months. b) Unchanged PXRD patterns of the NCs over the same course of time.*

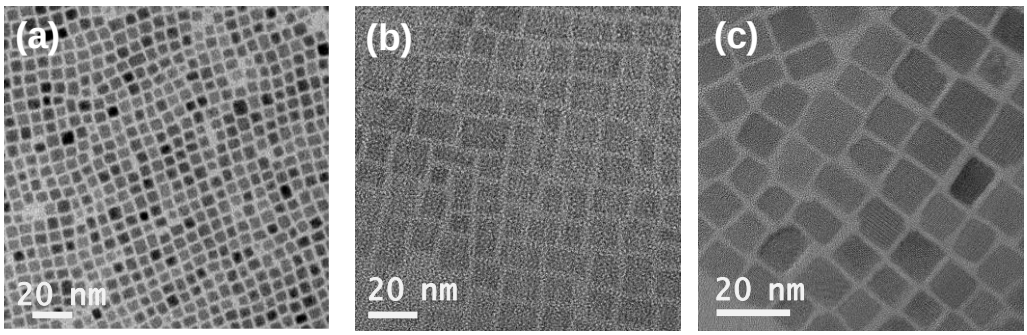

Figure A2.15. *Bright field TEM images of the a) $CsPbI_3$, b) $(MA)PbI_3$ and c) $(FA)PbI_3$ NCs, stored under ambient condition in sealed bottle for 2 months. The scale bar is 20 nm in each image.*

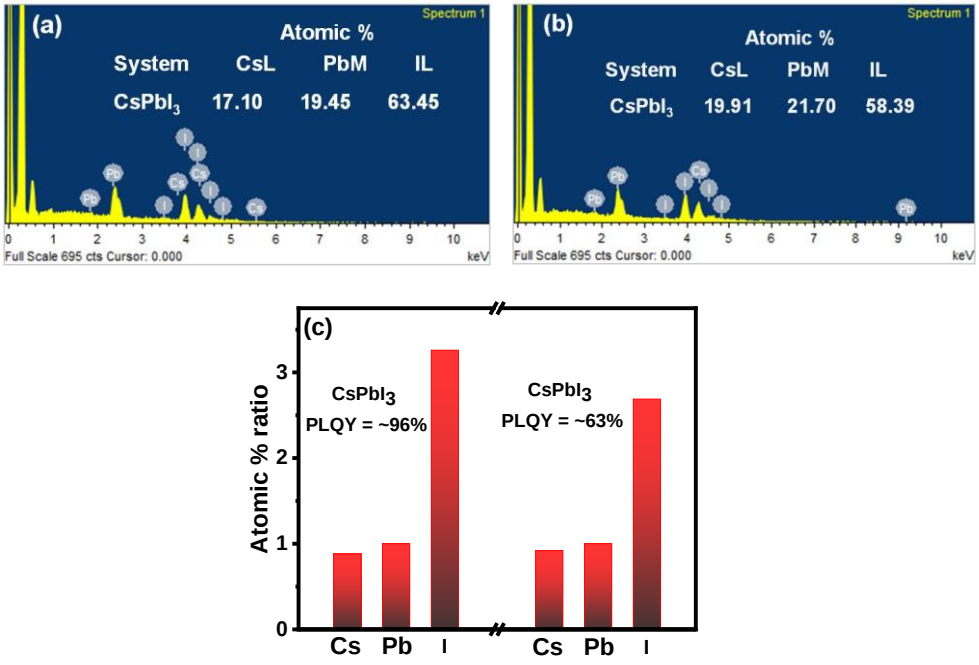

Figure A2.16. *EDX spectra of the $CsPbI_3$ NCs prepared at 210°C using Pb:I precursor molar ratio of a) 1:3 and b) 1:2. c) Ratio of the atomic percentage of the constituting elements, as obtained from the EDX measurements, showing a halide rich environment for the NCs synthesized with Pb:I of 1:3.*

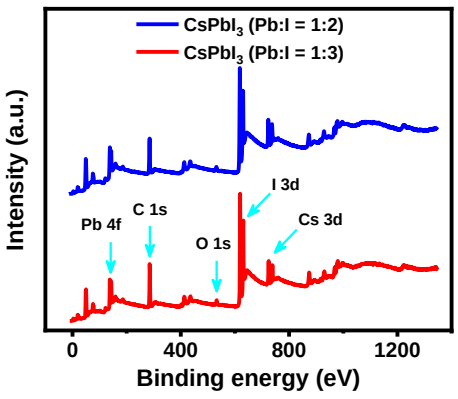

Figure A2.17. *Survey XPS spectra of the $CsPbI_3$ NCs prepared using a Pb:I molar ratio of 1:3 (red) and 1:2 (blue). Similar energy bands of Cs, Pb, I and N indicate the same elemental composition of both the $CsPbI_3$ NCs.*

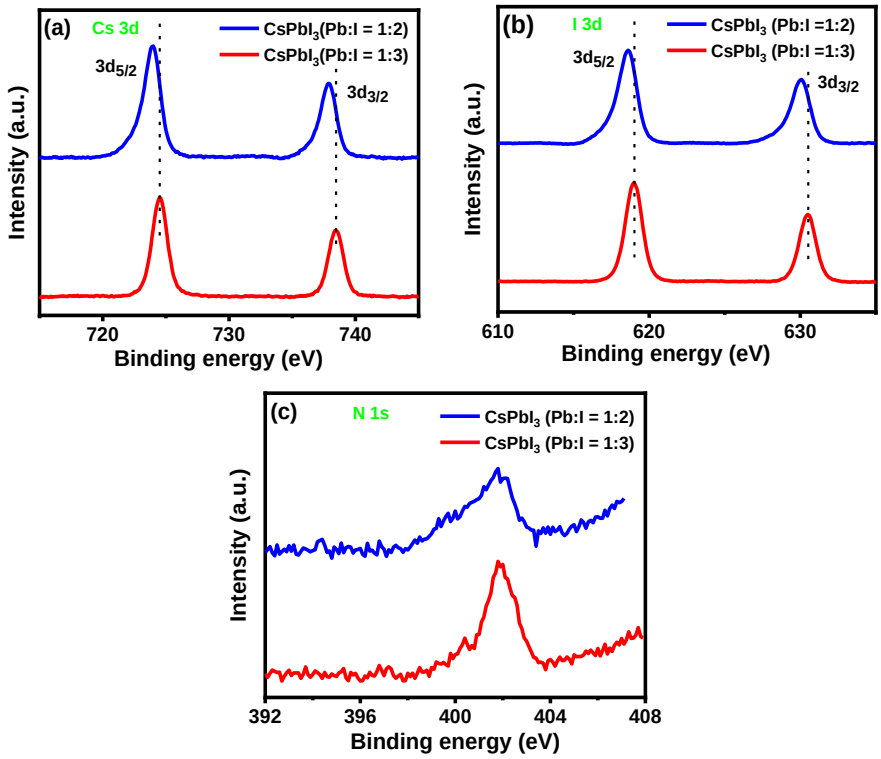

Figure A2.18. *Core level XPS spectra of a) Cs 3d, b) I 3d and c) N 1s for the $CsPbI_3$ NCs obtained using a Pb:I molar precursor ratio of 1:3 (red) and 1:2 (blue).*

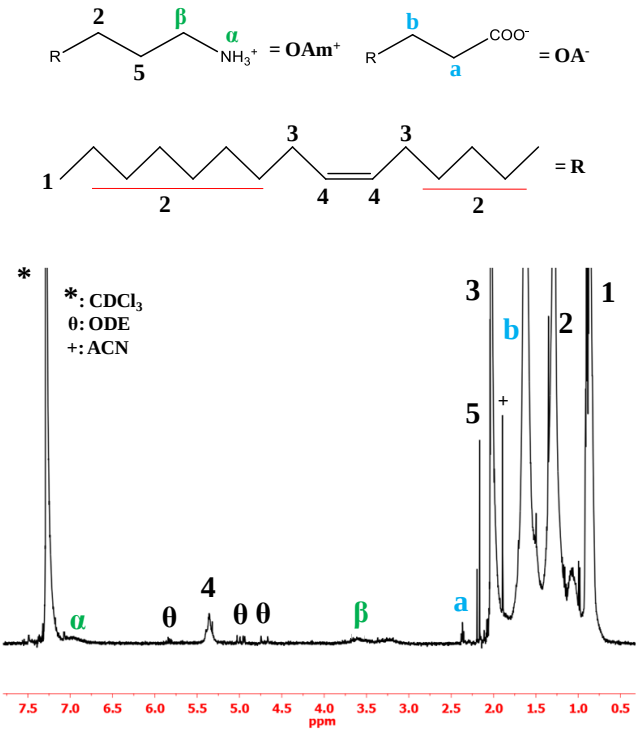

Figure A2.19. *^1H NMR spectrum of purified $CsPbI_3$ NCs in $CDCl_3$.*

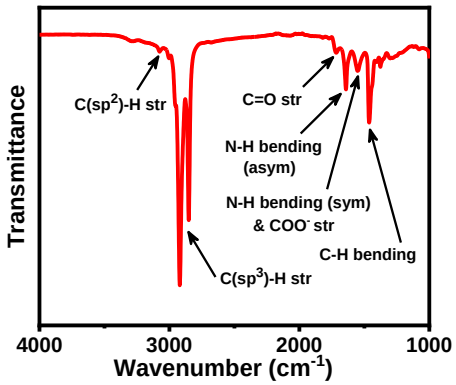

Figure A2.20. *FTIR spectrum of purified $CsPbI_3$ NCs in hexane.*

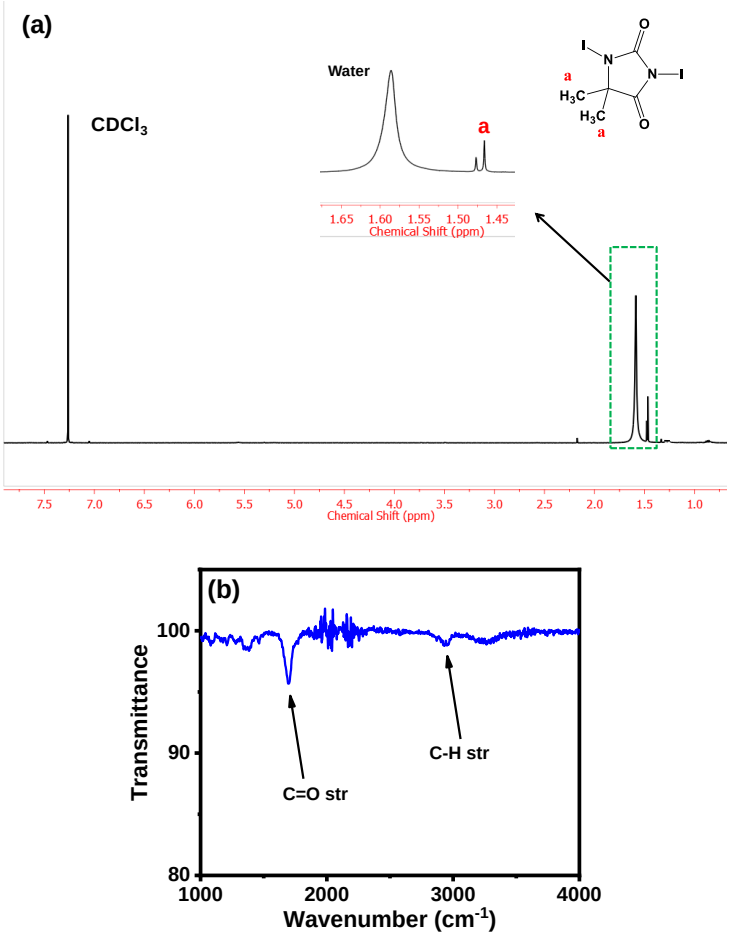

Figure A2.21. *a) ^1H NMR and b) FTIR spectra of DIDMH in $CDCl_3$.*

Table A2.1. *Variation of the optical properties of the $APbI_3$ NCs with reaction temperature and Pb:I precursor molar ratio.*

Systems	Reaction temp (°C)	Pb:I	λ_{em} (nm)	PLQY(%)
$CsPbI_3$	180	1:3	657	75
	200	1:3	654	87
	210	1:3	660	96
	220	1:3	661	93
	210	1:2	659	63
$(MA)PbI_3$	80	1:3	740	73
	85	1:3	740	74
	100	1:3	746	60
	110	1:3	765	44
	85	1:2	739	42
$(FA)PbI_3$	80	1:3	759	62
	85	1:3	760	67
	100	1:3	775, 705	57
	110	1:3	794, 721, 684	39
	85	1:2	760	41

Table A2.2. *PL decay parameters of the $APbI_3$ NCs. The radiative (k_r) and non-radiative (k_{nr}) rate constants, calculated using the measured PLQY and $<\tau_{amp}>$ values, are also shown.*

Systems	$\tau_1(a_1)$/ns	$\tau_2(a_2)$/ns	$\tau_3(a_3)$/ns	$<\tau_{amp}>$/ns	k_r/ns^{-1}	k_{nr}/ns^{-1}
$CsPbI_3$	9.17 (0.68)	17.12 (0.32)	----	11.71	0.08	0.003
$(MA)PbI_3$	41.7(0.51)	108.65(0.05)	17.56(0.44)	34.43	0.02	0.008
$(FA)PbI_3$	42.10(0.59)	103.33(0.08)	17.94(0.33)	39.30	0.02	0.009

Table A2.3. *Kinetic parameters of the bleach recovery dynamics of $CsPbI_3$ NCs obtained from fs-TA study.*

Systems	Pb:I	λ_{ex}(nm)	$\tau_1(a_1)$/ps	$\tau_2(a_2)$/ps
$CsPbI_3$	1:3	530	----	>1000
$CsPbI_3$	1:2	530	243±15 (0.11)	>1000 (0.89)

Table A2.4. *PL decay parameters, radiative (k_r) and non-radiative (k_{nr}) rate constants of the as-synthesized and 4-month aged samples preserved in ambient conditions.*

Samples	$\tau_1(a_1)$/ns	$\tau_2(a_2)$/ns	$\tau_3(a_3)$/ns	$<\tau_{amp}>$/ns	k_r/ns^{-1}	k_{nr}/ns^{-1}
$CsPbI_3$ (as-synthesized)	9.17 (0.68)	17.12 (0.32)	----	11.71	0.08	0.003
$CsPbI_3$ (aged)	9.11 (0.65)	15.35 (0.35)	----	11.29	0.08	0.009

Table A2.5. *A comparison of the optical property and phase stability of red/NIR-emitting perovskite NCs obtained by different groups through direct synthesis method with our samples.*

System/s	Synthetic strategy	Approach	PLQY	Stability	Reference
$CsPbI_3$	PbI_2 used as iodide source, hot-injection	HI	50-90%	few hours to days	3
$CsPbI_3$	Alkyl phosphinic acid as anionic ligand	HI	NA	20 days	4
$CsPbI_3$	Tri-octylphosphine (TOP) used as additional capping ligand	HI	100%	retain ~85% PLQY after 1 month of storage	5
$CsPbI_3$	TOP mediated ligand replacement	PST	30%	1 month	6
$CsPbI_3$	Used zwitterionic capping ligand	HI	~80%	NA	7
$CsPbI_3$	PbI_2 and oleylammonium iodide used as halide source	HI	80-95%	1 month in ambient condition and 6h under heating at 100°C	8
$CsPbI_3$	Benzoyl iodide taken as iodide precursor	HI	58%	20 days	9

$(MA)PbI_3$			45%	NA	
$(FA)PbI_3$			55%	NA	
$CsPbI_3$	Trimethylsilyl iodide as halide source	HI	96%	86% PLQY retained after 105 days; photostability: 30% after 3h	10
$CsPbI_3$	Excess OAm^+I^- as sole halide source	HI	90-100%	NA	11
$CsPbI_3$	Molecular I_2 as halide source	HI	79%	2 weeks	1
$(FA)PbI_3$			74%	2 weeks	
$(FA)PbI_3$	PbI_2 or oleylammonium iodide used as iodide source	HI	70%	6 months	12
$(FA)PbI_3$	PbI_2used as iodide source	LARP	55%	150 days	13
$(MA)PbI_3$	PbI_2 used as iodide precursor	LARP	~50-70%	NA	14
$(MA)PbI_3$	PbI_2 used as iodide precursor	RT	27%	39 days	15
$(MA)PbI_3$	$(MA)PbI_3$ single crystal powder	LARP	79%	Photostability: 30% after 15h	16
$(MA)PbI_3$	PbI_2 serves as iodide source	HI	20-30%	Non-purified samples stable for weeks but purified samples decomposes quickly	17
$CsPbI_3$	1,3-diiodo-5,5-dimethylhydantion (DIDMH) as iodide	HI	96±1%	20 days when exposed to ambient	

	precursor	condition and >4 months when stored in a sealed bottle in similar conditions; Photostability: 82% after 22h	**This work**
$(MA)PbI_3$	74±1%	Water resistivity: 75% after 240 min	
$(FA)PbI_3$	67±2%	retains 90% PLQY after 2 months of storage at room-temperature	
		retains 87% PLQY after 2 months of storage under ambient condition	

HI= Hot-injection, RT= Room-temperature, PST= Post-synthetic treatment and LARP= Ligand assisted re-precipitation.

Table A2.6. *Atomic % ratio of the constituting elements (with respect to Pb) of the $CsPbI_3$ NCs calculated based on the XPS data and using atomic sensitivity factor of the elements.*[18, 19]

Samples	**Atomic % ratio (with respect to Pb)**				
	Pb:I	**Cs**	**Pb**	**I**	**N**
$CsPbI_3$	1:3	0.94	1.00	3.36	2.22
$CsPbI_3$	1:2	0.99	1.00	2.86	2.03

References:

1. Q. A. Akkerman, L. Martínez-Sarti, L. Goldoni, M. Imran, D. Baranov, H. J. Bolink, F. Palazon and L. Manna, *Chem. Mater.*, 2018, **30**, 6915–6921.
2. V. K. Ravi, P. K. Santra, N. Joshi, J. Chugh, S. K. Singh, H. Rensmo, P. Ghosh and A. Nag, *J. Phys. Chem. Lett.*, 2017, **8**, 4988–4994.
3. L. Protesescu, S. Yakunin, M. I. Bodnarchuk, F. Krieg, R. Caputo, C. H. Hendon, R. X. Yang, A. Walsh and M. V. Kovalenko, *Nano Lett.*, 2015, **15**, 3692–3696.
4. C. Wang, A. S. R. Chesman and J. J. Jasieniak, *Chem. Commun.*, 2017, **53**, 232-235
5. F. Liu, Y. Zhang, C. Ding, S. Kobayashi, T. Izuishi, N. Nakazawa, T. Toyoda, T. Ohta, S. Hayase, T. Minemoto, K. Yoshino, S. Dai and Q. Shen, *ACS Nano*, 2017, **11**, 10373-10383.
6. C. Lu, H. Li, K. Kolodziejski, C. Dun, W. Huang, D. Carroll and S. M. Geyer, *Nano Research*, 2018, **11**, 762–768.
7. F. Krieg, S. T. Ochsenbein, S. Yakunin, S. t. Brinck, P. Aellen, A. Süess, B. Clerc, D. Guggisberg, O. Nazarenko, Y. Shynkarenko, S. Kumar, C.-J. Shih, I. Infante and M. V. Kovalenko, *ACS Energy Lett.*, 2018, **3**, 641−646.
8. A. Dutta, S. K. Dutta, S. D. Adhikari and D. N. Pradhan, *Angew.Chem. Int.Ed.*, 2018, **57**, 9083 –9087.
9. M. Imran, V. Caligiuri, M. Wang, L. Goldoni, M. Prato, R. Krahne, L. D. Trizio and L. Manna, *J. Am. Chem. Soc.*, 2018, **140**, 2656–2664.
10. Y. Cai, H. Wang, Y. Li, L. Wang, Y. Lv, X. Yang and R.-J. Xie, *Chem. Mater.*, 2019, **31**, 881–889.
11. A. Dutta, R. K. Behera, P. Pal, P. D. S. Baitalik and D. N. Pradhan, *Angew. Chem. Int. Ed.*, 2019, **58**, 5552 –5556.
12. L. Protesescu, S. Yakunin, S. Kumar, J. Bär, F. Bertolotti, N. Masciocchi, A. Guagliardi, M. Grotevent, I. Shorubalko, M. I. Bodnarchuk, C.-J. Shih and M. V. Kovalenko, *ACS Nano*, 2017, **11**, 3119–3134.
13. I. Levchuk, A. Osvet, X. Tang, M. Brandl, J. D. Perea, F. Hoegl, G. J. Matt, R. Hock, M. Batentschuk and C. J. Brabec, *Nano Lett.*, 2017, **17**, 2765–2770.
14. F. Zhang, H. Zhong, C. Chen, X.-g. Wu, X. Hu, H. Huang, J. Han, B. Zou and Y. Dong, *ACS Nano*, 2015, **9**, 4533–4542.
15. X. Liang, R. W. Baker, K. Wu, W. Deng, D. Ferdani, P. S. Kubiak, F. Marken, L. Torrente-Murciano and P. J. Cameron, *React. Chem. Eng.*, 2018, **3**, 640-644.
16. J.-F. Liao, Y.-X. Chen, J.-H. Wei, Y.-T. Cai, X.-D. Wang, Y.-F. Xu and D.-B. Kuang, *Nano Research*, 2019, **12**, 2640–2645.
17. O. Vybornyi, S. Yakunin and M. V. Kovalenko, *Nanoscale*, 2016, **8**, 6278-6283.
18. S. K. Balakrishnan and P. V. Kamat, *Chem. Mater.*, 2018, **30**, 74–78.
19. C. D. Wanger, W. M. Riggs, L. E. Davis, J. F. Moulder and G. E.Muilenberg, *Perkin-Elmer Corp., Physical Electronics Division, Eden Prairie, Minnesota, USA*, 1979.

Appendix 3

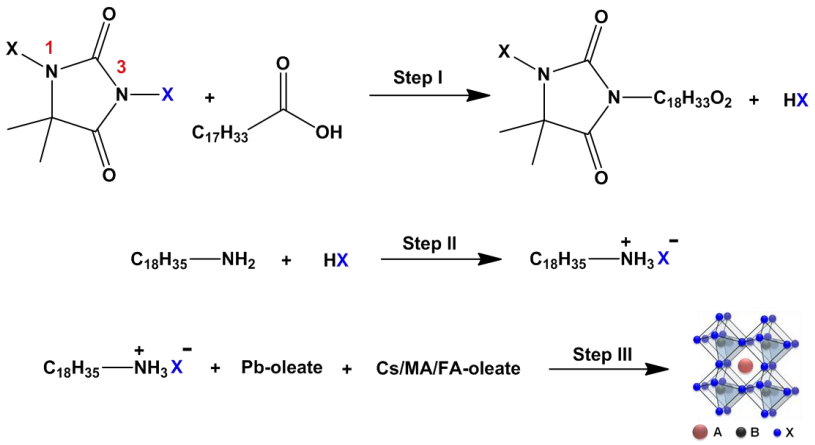

Scheme A3.1. *Schematic representation of the steps involved in DXDMH-mediated hot injection synthesis of the $APbX_3$ NCs.*

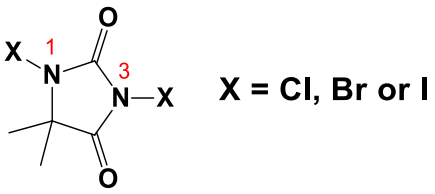

1,3-dihalo-5,5-dimethylhydantoin (DXDMH)

Figure A3.1. *Chemical structure of 1,3-dihalo-5,5-dimethylhydantoin (DXDMH). 'X' represents the halogen atom.*

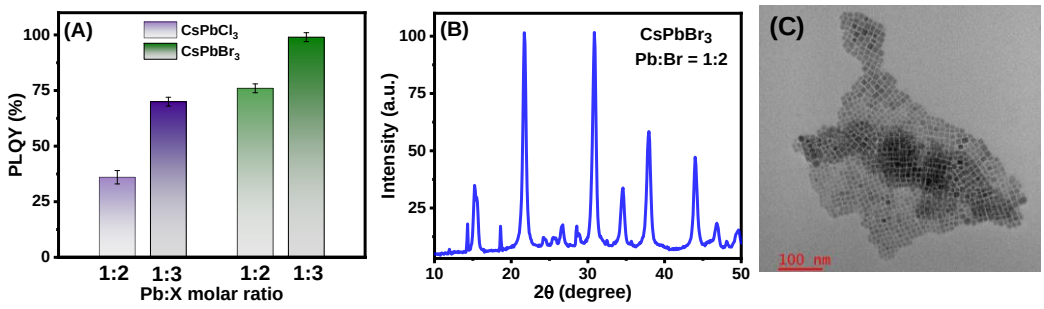

Figure A3.2. *(A) Dependence of PLQY of the $CsPbCl_3$ and $CsPbBr_3$ NCs (obtained at 210°C) on the Pb:X precursor molar ratio. (B) PXRD pattern and (C) TEM image of the samples of $CsPbBr_3$(II) NCs (prepared using a Pb:Br molar ratio of 1:2). The scale bar is 100 nm.*

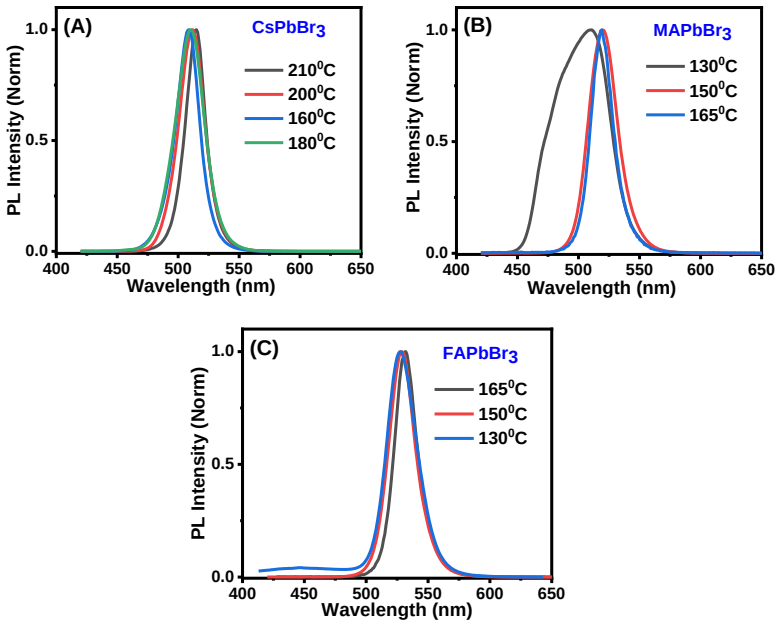

Figure A3.3. *PL spectra (normalized) of the (A) $CsPbBr_3$, (B) $MAPbBr_3$ and (C) $FAPbBr_3$ NCs obtained at different reaction temperature.*

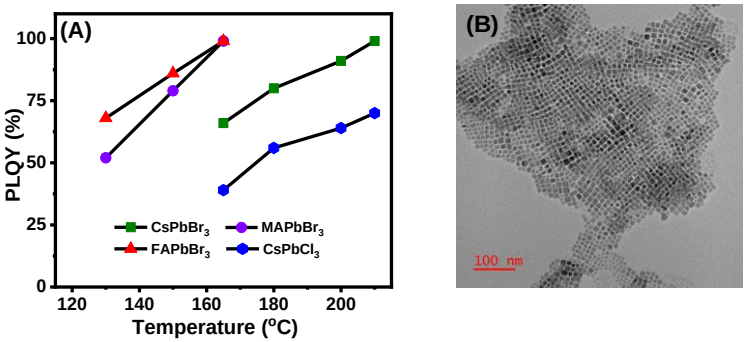

Figure A3.4. *(A) PLQY of the NCs as a function of reaction temperature. (B) TEM image of the $CsPbBr_3$ NCs prepared at 180°C. The scale bar is 100 nm.*

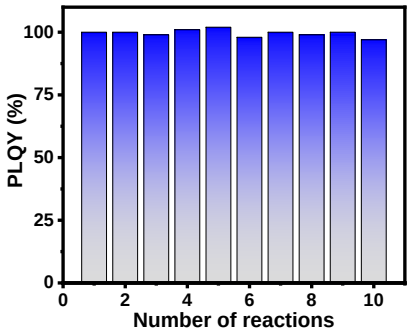

Figure A3.5. *PLQY of the $CsPbBr_3$ NCs of different batches highlighting reproducibility of our method.*

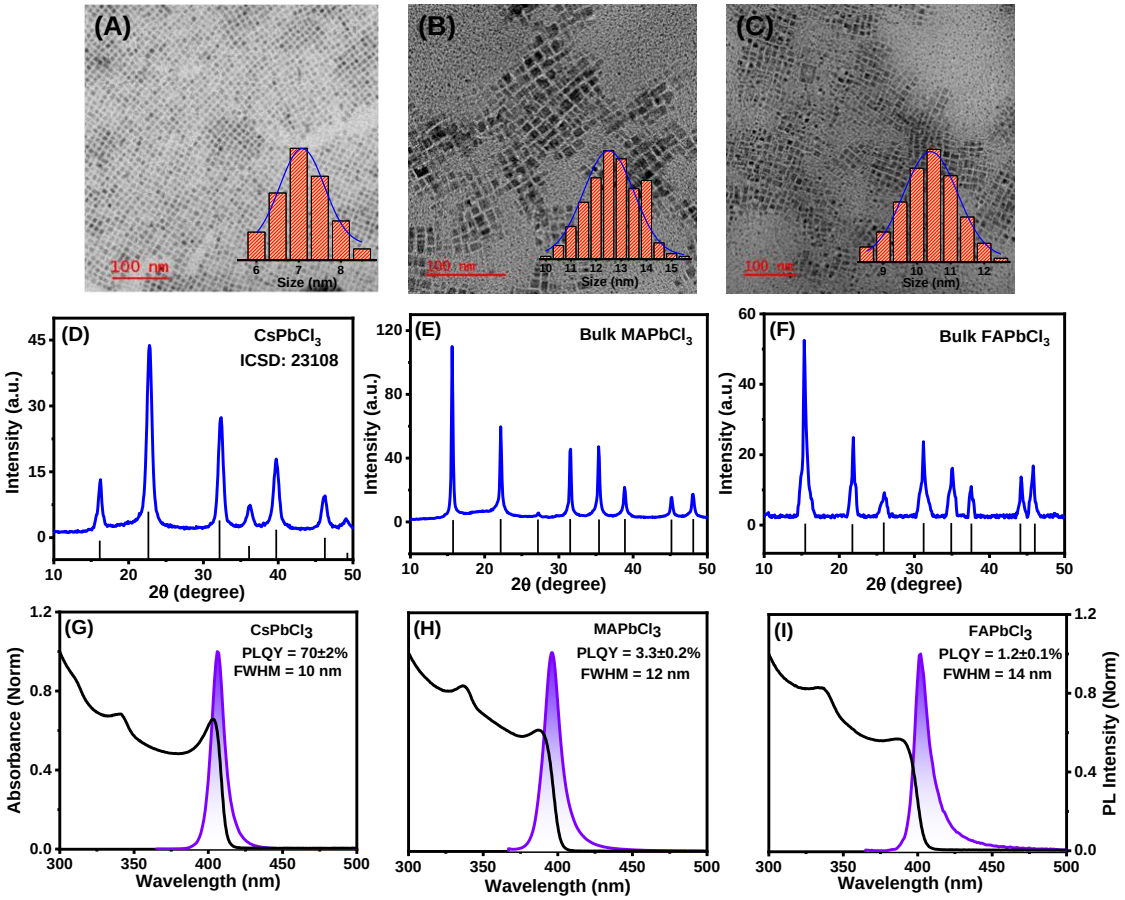

Figure A3.6. *Bright-field TEM images of (A) $CsPbCl_3$, (B) $MAPbCl_3$ and (C) $FAPbCl_3$ NCs. Inset shows size distribution histogram of the respective NCs. The scale bar is 100 nm for all samples. PXRD patterns of (D) $CsPbCl_3$, (E) $MAPbCl_3$ and (F) $FAPbCl_3$ NCs with reference patterns obtained from their cubic bulk counterparts. UV-Vis absorption and PL spectra of (G) $CsPbCl_3$, (H) $MAPbCl_3$ and (I) $FAPbCl_3$ NCs. The samples were excited at 400 nm.*

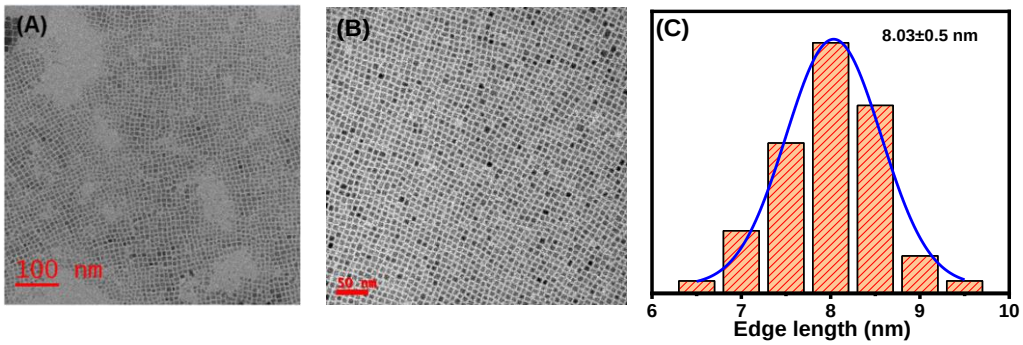

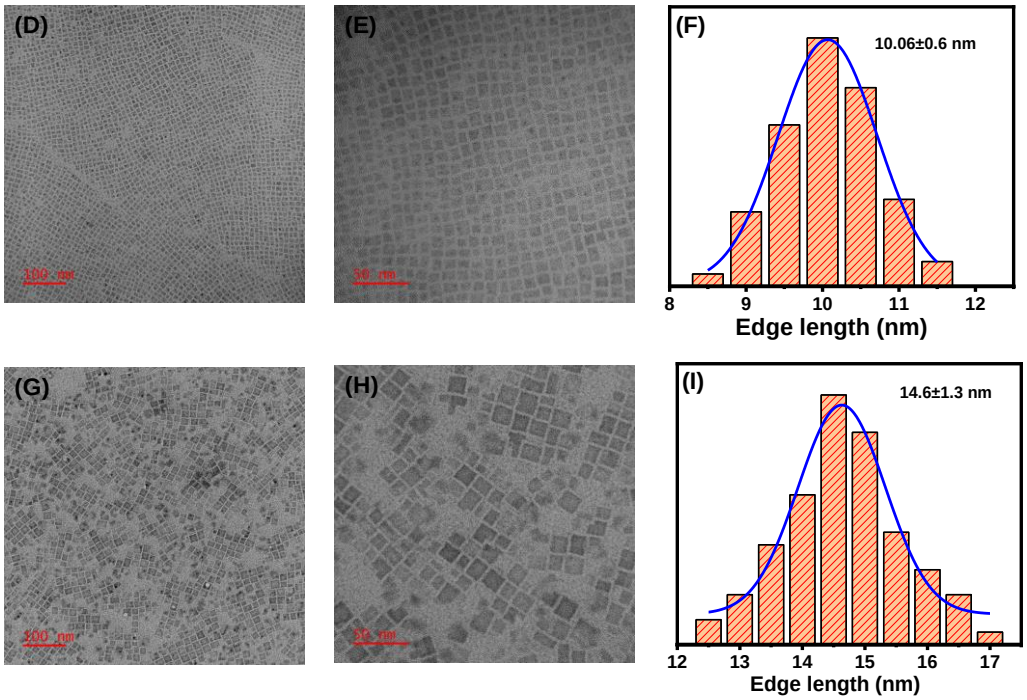

Figure A3.7. *Additional bright-field TEM images and size distribution histogram of (A-C) $CsPbBr_3$, (D-F) $MAPbBr_3$ and (G-I) $FAPbBr_3$ NCs. The scale bar is indicated at the bottom left corner of each image.*

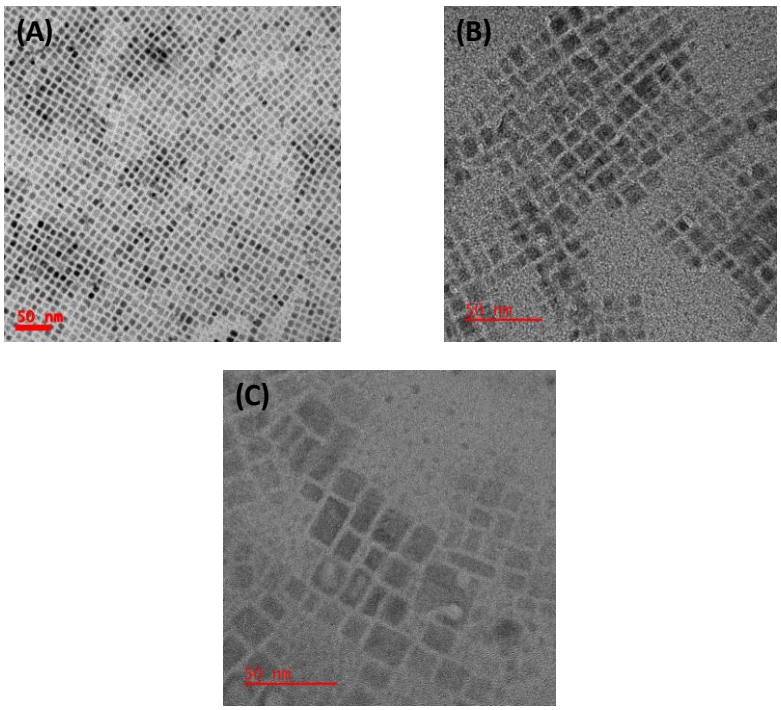

Figure A3.8. *Additional bright-field TEM images of (A) $CsPbCl_3$, (B) $MAPbCl_3$ and (C) $FAPbCl_3$ NCs. The scale bar is 50 nm in all cases.*

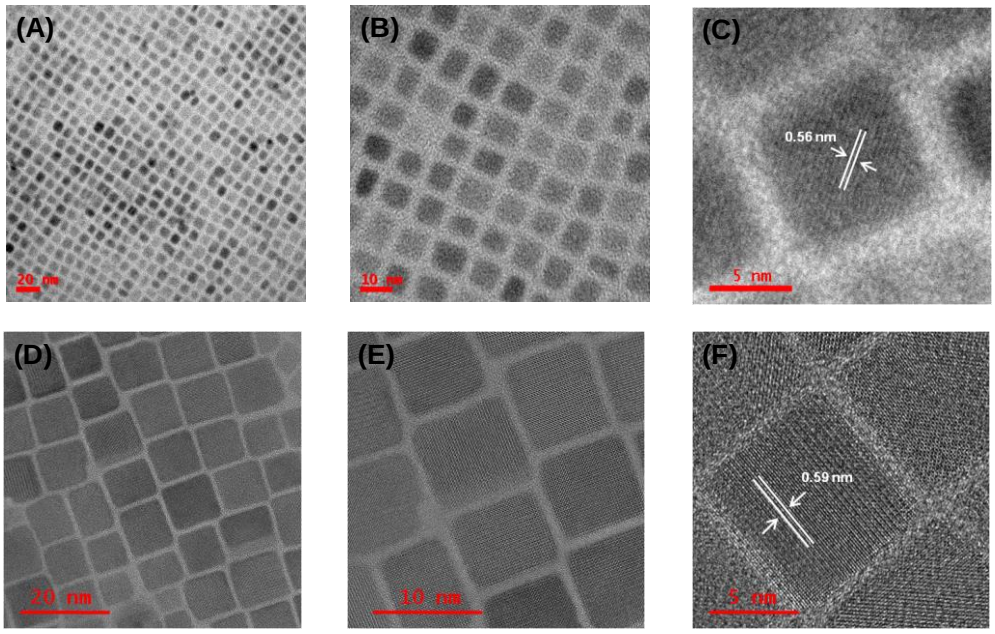

Figure A3.9. *High-resolution TEM images of (A-C) $CsPbCl_3$ and (D-F) $CsPbBr_3$ NCs. The inter-planar spacing (d_{100}) corresponding to the (100) planes of the NCs is also measured and shown in Figure C and F. The scale bar is shown in the bottom-left corner of each image.*

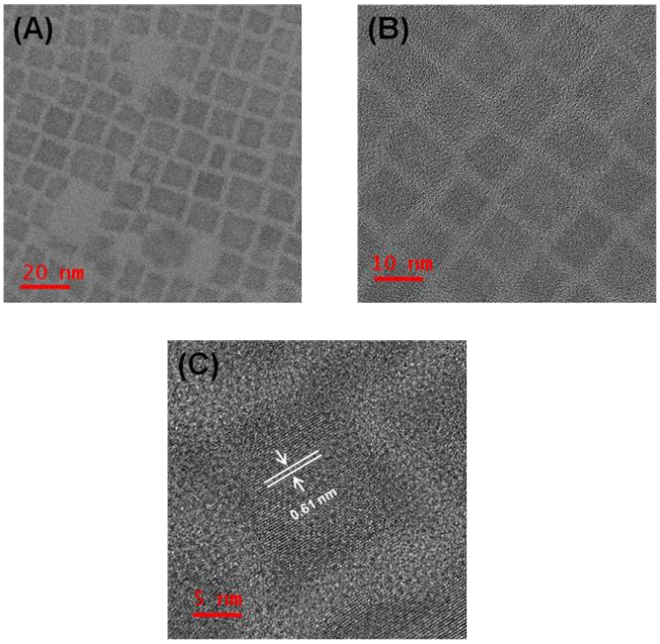

Figure A3.10. *(A-C) High-resolution TEM images of $FAPbBr_3$ NCs. The inter-planar spacing (d_{100}) corresponding to the (100) planes of the NCs is also measured and shown in Figure C. The scale bar is shown in the bottom-left corner of each image.*

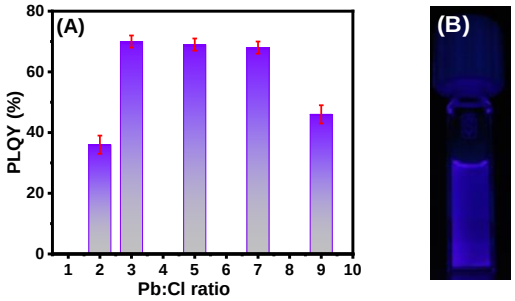

Figure A3.11. *(A) Dependence of PLQY of the $CsPbCl_3$ NCs on the Pb:Cl molar precursor ratio. An excess amount of DCDMH is seen to have a detrimental effect on the optical properties of the NCs. (B) Digital image showing the PL of the $CsPbCl_3$ NCs obtained using Pb:Cl precursor molar ratio of 1:3.*

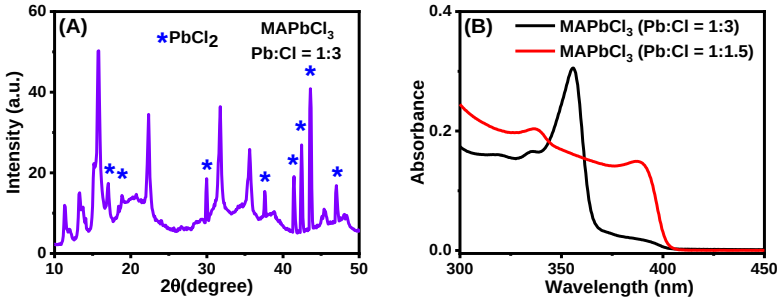

Figure A3.12. *(A) PXRD pattern of the $MAPbCl_3$ NCs prepared using 1:3 ratio of Pb:Cl showing the additional diffraction peaks arising from undesired $PbCl_2$ by-product. (B) Absorption spectra of the $MAPbCl_3$ NCs prepared using Pb:Cl precursor ratio of 1:3 and 1:1.5.*

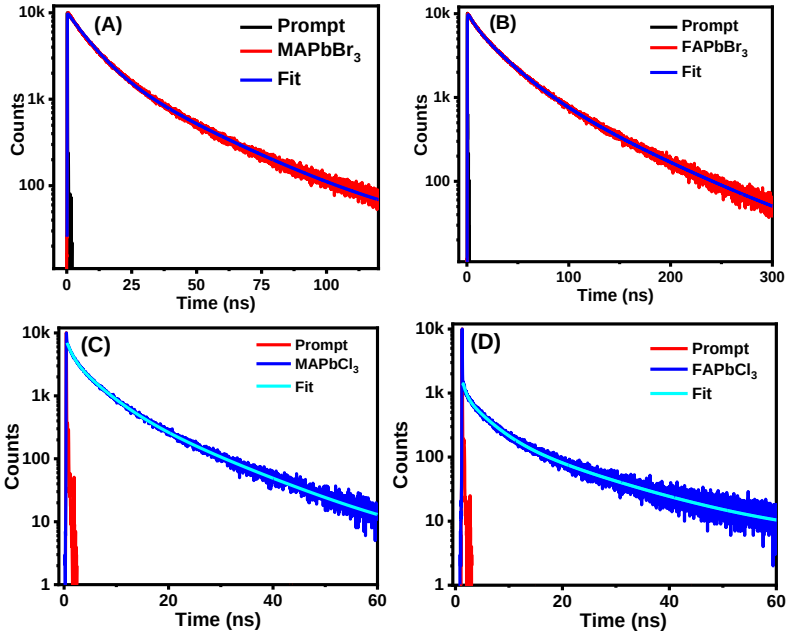

Figure A3.13. *PL decay characteristics of the (A) $MAPbBr_3$, (B) $FAPbBr_3$, (C) $MAPbCl_3$ and (D) $FAPbCl_3$ NCs. The excitation wavelengths are 405 and 376 nm for the bromide- and chloride-based NCs, respectively and the PL was monitored at their respective PL peak maxima. The early (short) component of the PL decay of $FAPbCl_3$ NCs could not be measured accurately as this component is shorter than the time-resolution of our TCSPC setup (~63 ps).*

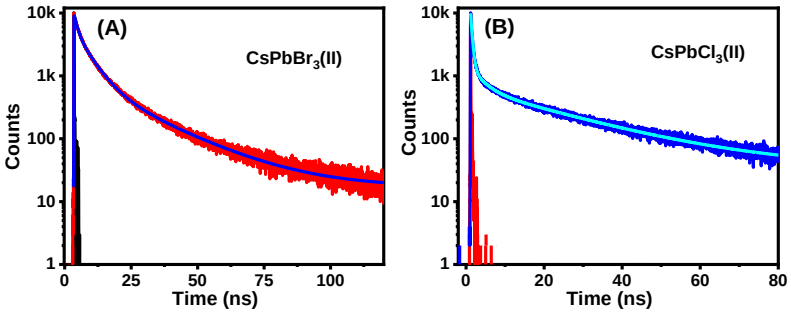

Figure A3.14. *PL decay of (A) $CsPbBr_3$(II) and (B) $CsPbCl_3$(II) NCs (prepared using Pb:X precursor molar ratio of 1:2). These samples were excited at 405 and 376 nm, respectively and the decay was monitored at the corresponding PL maxima.*

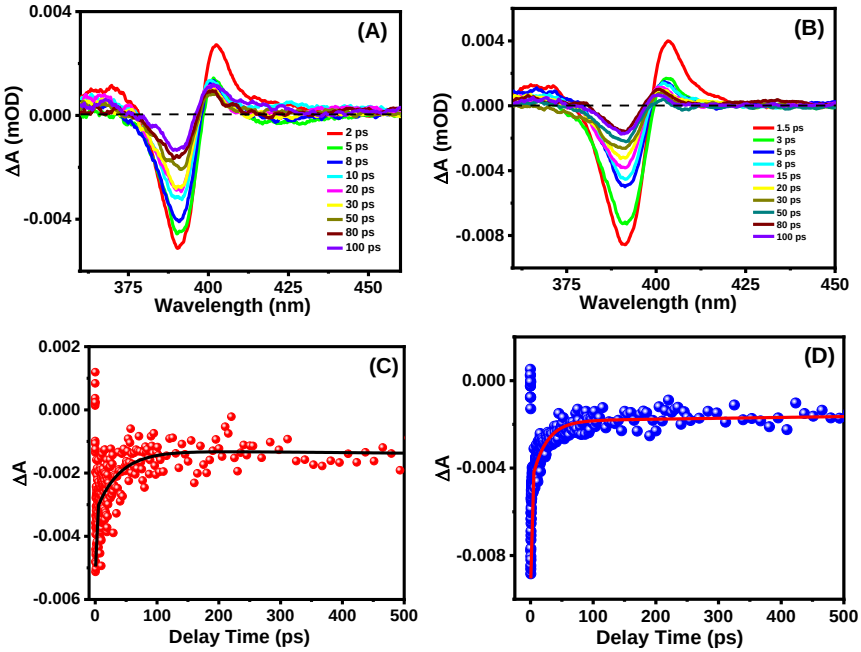

Figure A3.15. TA spectra of (A) $MAPbCl_3$ and (B) $FAPbCl_3$ NCs obtained upon excitation at 350 nm by a fs-pulsed laser. Bleach recovery dynamics of (C) $MAPbCl_3$ and (D) $FAPbCl_3$ NCs monitored at their respective bleach maxima.

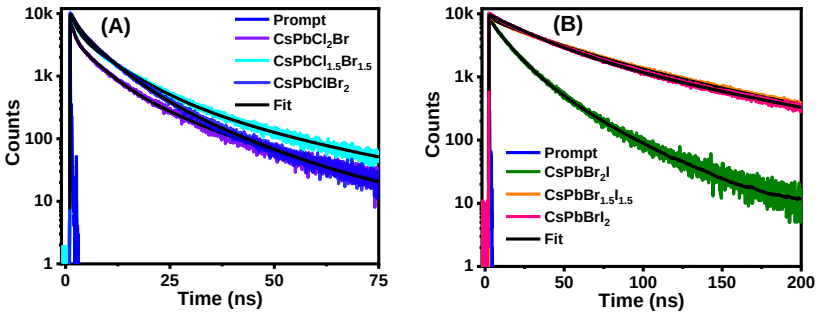

Figure A3.16. *PL decay behavior of the (A) blue-emitting $CsPb(Cl/Br)_3$ and (B) yellow-orange-emitting $CsPb(Br/I)_3$ NCs. The samples were excited at 375 and 405 nm, respectively and the decay curves were monitored at their respective peak maxima.*

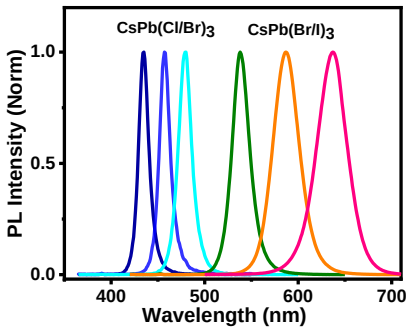

Figure A3.17. *(A) PL spectra (normalized) of our samples of mixed-halide NCs covering a wide (431 to 635 nm) range of the visible region.*

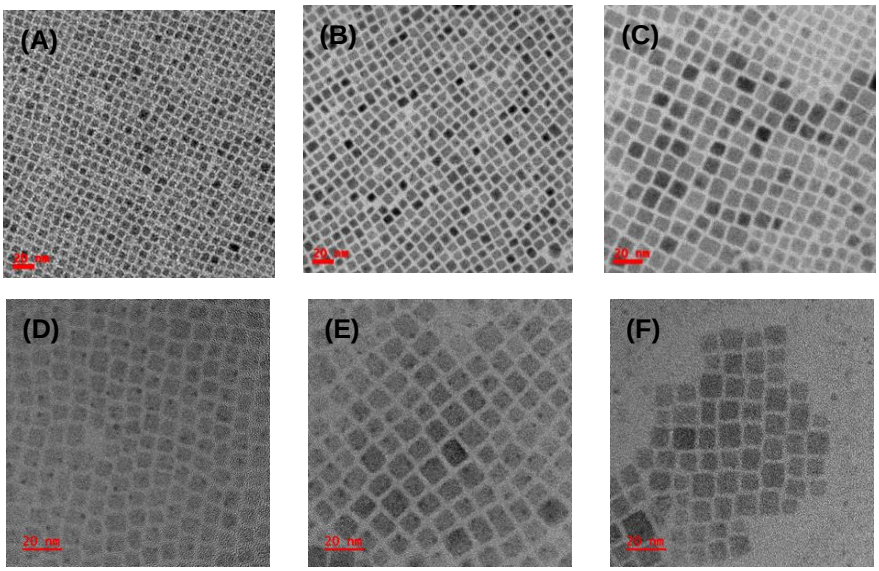

Figure A3.18. *Bright field TEM images (A) $CsPbCl_2Br$, (B) $CsPbCl_{1.5}Br_{1.5}$, (C) $CsPbClBr_2$, (D) $CsPbBr_2I$, (E) $CsPbBr_{1.5}I_{1.5}$ and (F) $CsPbBrI_2$ NCs. The average edge*

lengths of the NCs are 6.9±1.4, 7.8±1.2, 9.3±2.2, 8.5±1.7, 9.4±2.5 and 10±2 nm, respectively.

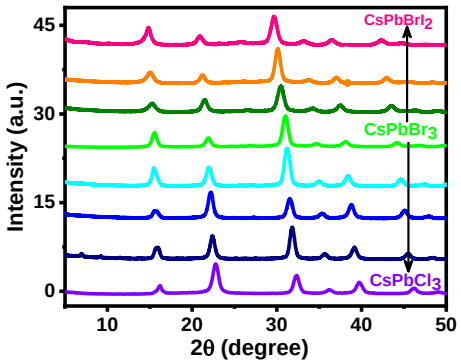

Figure A3.19. *PXRD patterns of pristine $CsPbCl_3$, $CsPbBr_3$ and the mixed-halide $CsPb(Cl/Br)_3$ and $CsPb(Br/I)_3$ NCs.*

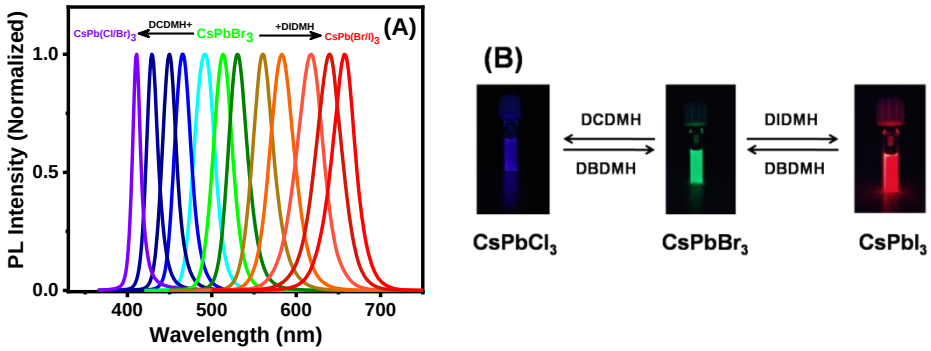

Figure A3.20. *(A) Addition of a small quantity of DCDMH/DIDMH solution (in OAm and OA) to a colloidal dispersion of $CsPbBr_3$ NCs results in an instantaneous blue/red shift of the PL maximum in the range of ~410 to 660 nm due to room-temperature post-synthetic reversible halide exchange on the NCs. (B) Digital images of the $CsPbBr_3$ NCs before and after halide exchange reactions.*

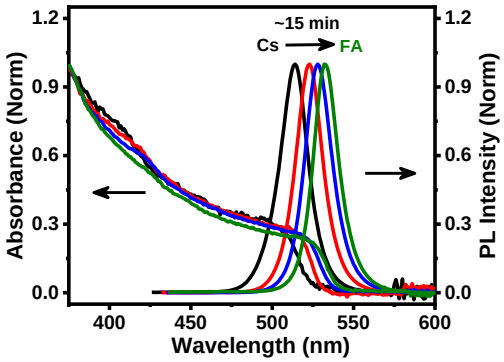

Figure A3.21. *Post-synthetic cation exchange (A-site) on $CsPbBr_3$ NCs using FA-oleate solution at RT.*

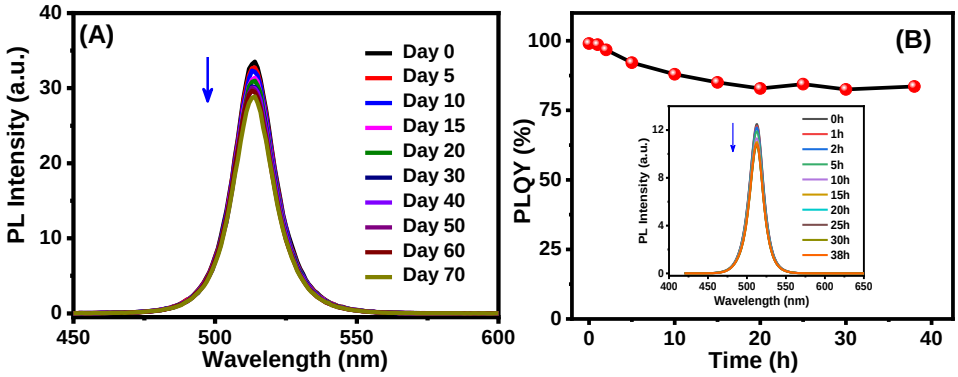

Figure A3.22. *(A) Change in PL spectrum of the $CsPbBr_3$ NCs with time (stored under ambient conditions). (B) Photoinduced change in the PLQY of the $CsPbBr_3$ NCs under continuous illumination of 365 nm UV light (8W). Inset shows the PL spectra of the sample during the testing period.*

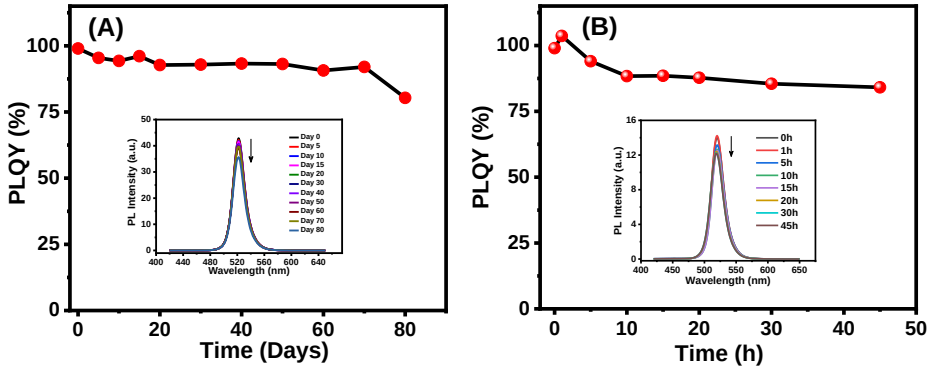

Figure A3.23. *Change in PL spectrum of the $MAPbBr_3$ NCs with time (stored under ambient conditions). (B) Photoinduced change in the PLQY of the $MAPbBr_3$ NCs under continuous illumination of 365 nm UV light (8W). Inset shows the PL spectra of the sample during the testing period.*

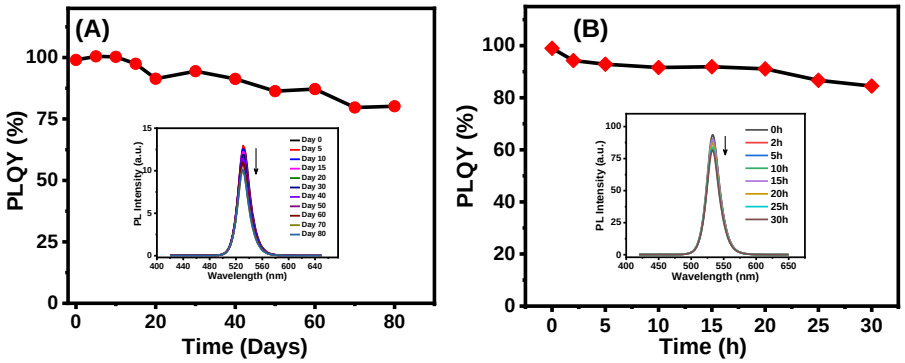

Figure A3.24. *Change in PL spectrum of the $FAPbBr_3$ NCs with time (stored under ambient conditions). (B) Photoinduced change in the PLQY of the $FAPbBr_3$ NCs under*

continuous illumination of 365 nm UV light (8W). Inset shows the PL spectra of the sample during the testing period.

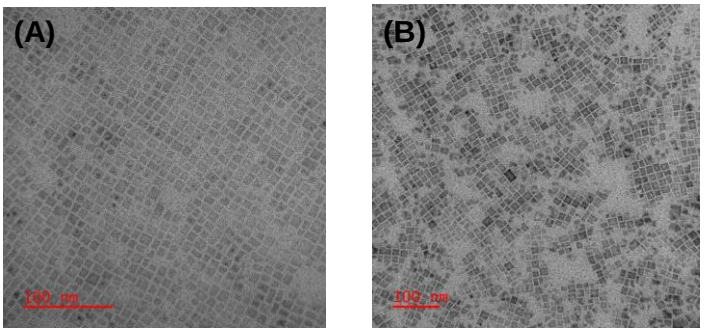

Figure A3.25. *Bright-field TEM images of the (A) $MAPbBr_3$, (B) $FAPbBr_3$ NCs taken after 80 days of storage under ambient condition. The scale bar is 100 nm in each image.*

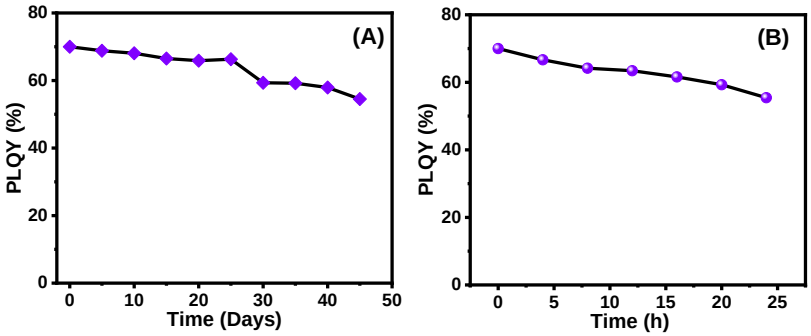

Figure A3.26. *Time-dependent change in PLQY of the $CsPbCl_3$ NCs under (A) ambient condition and (B) UV light (365 nm, 8W) illumination highlighting the air-stability and photo-stability of the samples.*

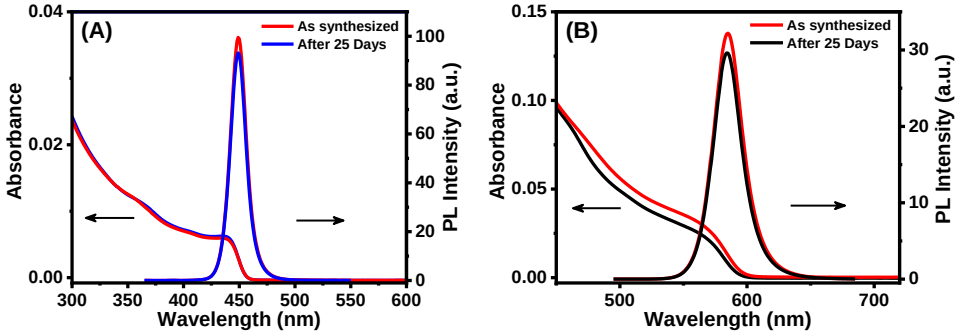

Figure A3.27. *Absorption and PL spectra of (A) $CsPbCl_{1.5}Br_{1.5}$ and (B) $CsPbBr_{1.5}I_{1.5}$ NCs recorded after storing under ambient conditions for 25 days.*

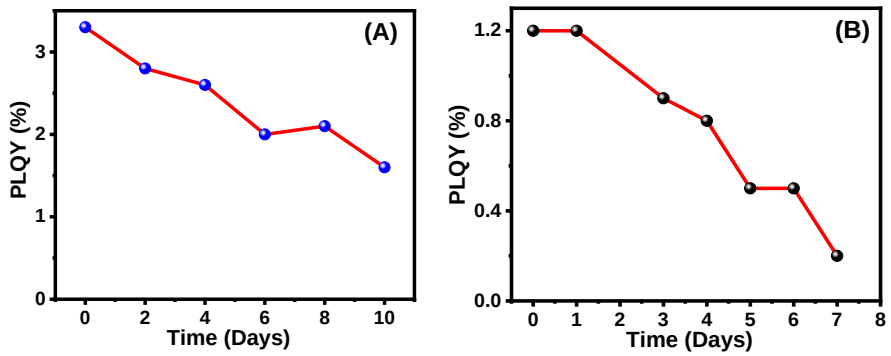

Figure A3.28. *Time dependent evolution of PLQY of (A) $MAPbCl_3$ and (B) $FAPbCl_3$ NCs under ambient condition.*

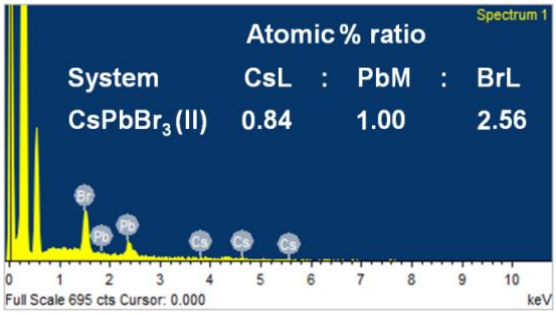

Figure A3.29. *EDX spectrum of the $CsPbBr_3$(II) NCs. The atomic % ratio of the constituting elements is indicated in the panel.*

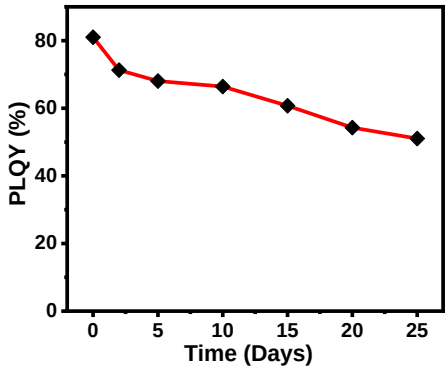

Figure A3.30. *Time-dependent change in PLQY of the $CsPbBr_3$(II) NCs stored under ambient condition.*

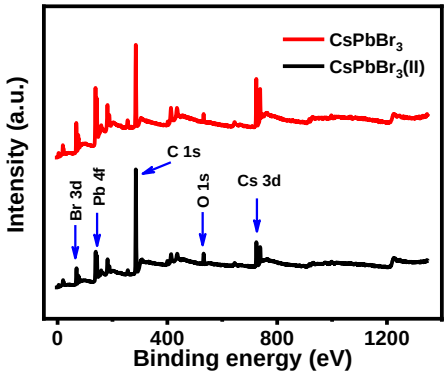

Figure A3.31. *XPS general survey scans of the $CsPbBr_3$ and $CsPbBr_3$(II) NCs indicating the presence of all constituent elements in both samples. Both spectra were corrected with respect to 'C 1s' peak at 285.0 eV.*

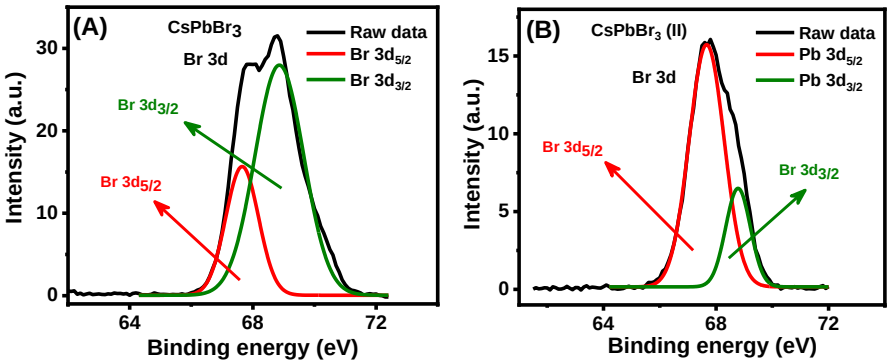

Figure A3.32. *Core-level XPS spectra of Br 3d of (A) $CsPbBr_3$ and (B) $CsPbBr_3$(II) NCs.*

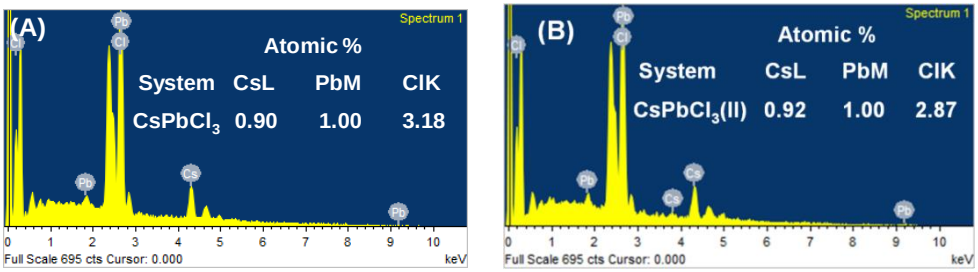

Figure A3.33. *EDX spectra of (A) $CsPbCl_3$ and (B) $CsPbCl_3$(II) NCs. Atomic % ratios of the NCs are shown in the panels.*

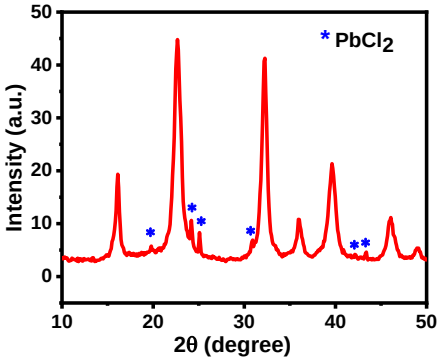

Figure A3.34. *PXRD spectra of $CsPbCl_3$ NCs prepared with Pb:Cl molar ratio of 1:9. (*) represent $PbCl_2$ diffraction peaks.*

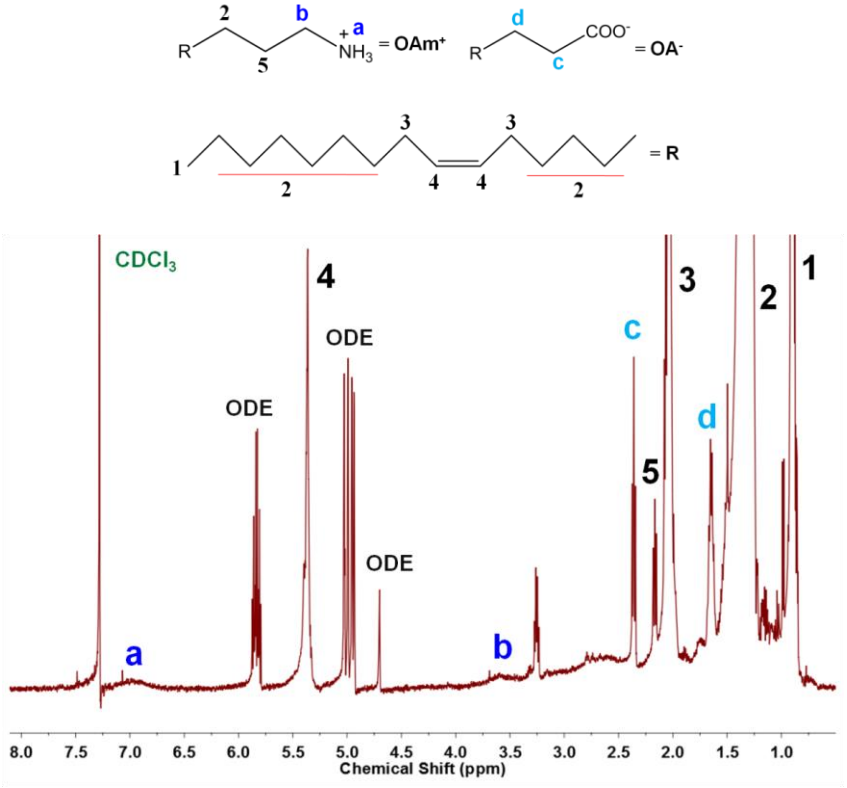

Figure A3.35. *^1H NMR spectrum of purified $CsPbBr_3$ NCs in $CDCl_3$.*

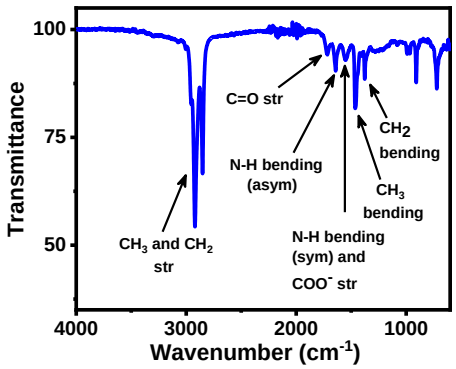

Figure A3.36. *FTIR spectrum of purified $CsPbBr_3$ NCs in hexane.*

Table A3.1. *Dependence of the optical properties of the $APbX_3$ NCs on reaction temperature and Pb:X precursor molar ratio.*

Systems	Pb:X	Temperature (^{0}C)	PLQY (±2 %)	FWHM (nm)
$CsPbBr_3$	1:3	165, 180, 200 and 210	66, 80, 91 and 99	26, 23, 20 and 19
$MAPbBr_3$	1:3	130, 150 and 165	52, 79 and 99	55, 26 and 21
$FAPbBr_3$	1:3	130, 150 and 165	68, 86, 99	29,24 and 19
$CsPbCl_3$	1:3	165, 180, 200 and 210	39, 56, 64 and 70	14-10
$CsPbBr_3$(II)	1:2	210	81	20
$CsPbCl_3$(II)	1:2	210	36	11

Table A3.2. *Comparison of the PLQY of violet-emitting $CsPbCl_3$ NCs obtained by different methods of direct synthesis.*

System	Pb:Cl ratio	PLQY (%)	λ_{em}(nm)	References
$CsPbCl_3$	1:(5.5-6.6)	97	411	1
	1:9	65	408	2
	1:4.5	71	404	3
	1:9	80	404	4
	1.3	70±2	406	**This work**

Table A3.3. *PL decay parameters, radiative (k_r) and non-radiative (k_{nr}) rate constants of the $APbX_3$ NCs. The decay was monitored at the respective PL maximum after excitation at 375 nm (for violet-blue-emitting), 404 nm (for green-emitting) and 485 nm (for yellow-orange-emitting) samples. The k_r and k_{nr} values were calculated using $k_r=PLQY/<\tau_{amp}>$ and $k_{nr}=(1-PLQY)/<\tau_{amp}>$.*

Systems	Pb:X ratio	$\tau_1(a_1)$[ns]	$\tau_2(a_2)$[ns]	$\tau_2(a_2)$[ns]	$<\tau_{amp}>$ [ns]	k_r [ns^{-1}]	k_{nr} [ns^{-1}]
$CsPbBr_3$	1:3	4.97 (0.73)	12.50 (0.27)	---	7.0	0.14	0.001
$CsPbBr_3$(II)	1:2	5.31 (0.42)	20.65 (0.08)	0.61 (0.50)	4.18	0.18	0.057
$MAPbBr_3$	1:3	8.50 (0.74)	29.20 (0.26)	---	13.88	0.07	0.0007
$FAPbBr_3$	1:3	21.02 (0.68)	65.80 (0.32)	---	35.35	0.03	0.0003
$CsPbCl_3$	1:3	4.63 (0.19)	20.72 (0.05)	0.47 (0.76)	2.48	0.28	0.120
$CsPbCl_3$(II)	1:2	3.67 (0.07)	18.05 (0.07)	0.40 (0.86)	1.86	0.19	0.344
$MAPbCl_3$	1:1.5	4.52 (0.43)	12.79 (0.13)	1.05 (0.44)	4.10	0.008	0.240
$FAPbCl_3$	1:3	3.90 (0.45)	15.39 (0.15)	0.59 (0.40)	4.30	0.003	0.229

Table A3.4. *Kinetic parameters of the bleach recovery dynamics of different samples of $CsPbBr_3$ and $CsPbCl_3$ NCs.*

Samples	Pb:X	τ_1 (a_1)/ps	τ_2 (a_2)/ps	τ_3 (a_3)/ps
$CsPbBr_3$	1:3		>1000	
$CsPbBr_3$ (II)	1:2	53.2 (0.43)	>1000 (0.57)	
$CsPbCl_3$	1:3	5.9±1.6 (0.31)		>1000 (0.69)
$CsPbCl_3$ (II)	1:2	5.8±0.3 (0.29)	74.8±5 (0.56)	>1000 (0.15)
$MAPbCl_3$	1:1.5	2.9±1.0 (0.60)	36.3±3.5 (0.26)	>1000 (0.14)
$FAPbCl_3$	1:3	2.1±0.4 (0.56)	20±2.2 (0.33)	>1000 (0.11)

Table A3.5. *Amount of DCDMH, DBDMH or DIDMH taken for the synthesis of mixed-halide NCs at 210°C.*

Systems	Pb:X ratio	X:X' ratio	DCDMH/mg	DBDMH/mg	DIDMH/mg
$CsPbCl_2Br$	1:3	2:1	74.08	53.75	---
$CsPbCl_{1.5}Br_{1.5}$	1:3	1.5:1.5	55.56	80.63	---
$CsPbClBr_2$	1:3	1:2	37.04	107.51	---
$CsPbBr_2I$	1:3	2:1	---	107.51	71.42
$CsPbBr_{1.5}I_{1.5}$	1:3	1.5:1.5	---	80.63	107.14
$CsPbBrI_2$	1:3	2:1	---	53.75	142.85

Table A3.6. *Optical properties of various mixed-halide $CsPb(Cl/Br)_3$ and $CsPb(Br/I)_3$ NCs.*

Systems	λ_{em}(nm)	PLQY (%)	FWHM (nm)
$CsPbCl_2Br$	431±2	87±1	12
$CsPbCl_{1.5}Br_{1.5}$	458±2	95±1	13
$CsPbClBr_2$	478±2	96±1	15
$CsPbBr_2I$	531±2	68±2	21
$CsPbBr_{1.5}I_{1.5}$	584±2	86±2	32
$CsPbBrI_2$	635±2	98±1	37

Table A3.7. *Comparison of the optical properties of different mixed-halide systems obtained directly by different methods.*

Systems	Synthetic strategy	Method	PLQY (%)	PL peak/ FWHM (nm)	Ref.
$CsPbCl_3$	PbX_2 as lead and halide source		10	10/12	
$CsPbCl_{1.5}Br_{1.5}$			37	455/16	
$CsPbClBr_2$			70	478/18	

$CsPbBr_2I$ $CsPbBr_{1.5}I_{1.5}$ $CsPbBr_{1.2}I_{1.8}$ $CsPbBrI_2$		LARP	78 72 80 70	548/26 600/38 628/35 640/35	5
$CsPb(Br_{1-x}Cl_x)_3$ Where x= 0-0.39	Quaternary alkyl ammonium halides as additional halide source with PbX_2	HI	25 (x = 0.39) 32 (x = 0.24) 48 (x = 0.19) 62 (x = 0.11) 80 (x = 0)	462 476 487 499 510 FWHM= 18-20	6
$CsPbCl_3$ $CsPbCl_2Br$ $CsPbCl_{1.5}Br_{1.5}$ $CsPbClBr_2$ $CsPbBr_3$	N-chloro- and N-bromophthalimides as halide precursors	HI	80 85 92 97 99	404/9 428/14 447/15 475/17 51020	4
$CsPbCl_2Br$ $CsPbCl_{1.5}Br_{1.5}$ $CsPbClBr_2$ $CsPbBr_2I$ $CsPbBr_{1.5}I_{1.5}$ $CsPbBrI_2$	DHDMH as halide precursor	HI	87±1 95±1 96±1 68±2 86±2 98±1	431±2/12 458±2/13 478±2/15 531±2/21 584±2/32 635±2/37	**This work**

Table A3.8. *PL decay components of different mixed-halide samples of $CsPb(Cl/Br)_3$ and $CsPb(Br/I)_3$ NCs.*

Systems	**$\tau_1(a_1)$/ns**	**$\tau_2(a_2)$/ns**	**$\tau_3(a_3)$/ns**	**$<\tau_{amp}>$/ns**	**k_r/ns^{-1}**	**k_{nr}/ns^{-1}**
$CsPbCl_2Br$	5.37(0.34)	17.32(0.09)	0.71(0.57)	3.79	0.23	0.03
$CsPbCl_{1.5}Br_{1.5}$	7.78(0.43)	24.20(0.08)	1.53(0.49)	6.03	0.16	0.008
$CsPbClBr_2$	6.14(0.54)	16.60(0.10)	1.5(0.36)	5.52	0.17	0.007
$CsPbBr_2I$	11.30(0.53)	30.90(0.17)	0.94(0.30)	11.52	0.06	0.03
$CsPbBr_{1.5}I_{1.5}$	34.20(0.50)	88.60(0.30)	2.44(0.20)	44.17	0.02	0.003
$CsPbBrI_2$	27.30(0.69)	84.60(0.31)	---	45.06	0.02	0.0004

Table A3.9. *Comparison of the optical properties and stability of the green- and violet-emitting perovskite NCs obtained by different three-precursor method of synthesis.*

Systems	Halide precursor	PLQY (%)/ FWHM (nm)	Stability parameters	Ref.
$FAPbBr_3$	Oleylammonium bromide	85/22	Stable up to 2-3 round of purification with ACN	7
$CsPbBr_3$	Tetraoctyl ammonium bromide	78	~20% PLQY retained after 35 days in air and ~24% PLQY reduced after 3 heating-cooling circle at 100°C	8
$CsPbBr_3$	Tetraoctyl ammonium bromide	70	Stable towards purification with polar solvents up to 2 times	9
$CsPbBr_3$	NH_4Br	75/19	Stable towards purification	10
$FAPbBr_3$	Octadecylamine bromide	88/21	~75% retention of PLQY after 50 days of storage in air	11
$CsPbBr_3$ $MAPbBr_3$ $FAPbBr_3$ $CsPbCl_3$	Benzoyl halide	92/18 92/19 92/20	NA	2
$CsPbBr_3$	Trioctylphosphene-Br_2 adduct	90/17	PLQY retained in the range of 70-90% for 28-50 days	12
$CsPbBr_3$	Benzoyl halide	48-80/16-17	NA	13
$CsPbCl_3$	Oleylammonium halide	97	80% PLQY retained after 7 days	1
$CsPbBr_3$		97	NA	
$CsPbBr_3$ $MAPbBr_3$ $FAPbBr_3$	N-bromosuccinamide	99/18 98/21 95/20	*Air-stability:*$CsPbBr_3$ retains 90% while $MAPbBr_3$ and $FAPbBr_3$ retains 85% of initial PLQY after 3 and 2 months in air, respectively	14

			Photo-stability:$CsPbBr_3$, $MAPbBr_3$ and $FAPbBr_3$ retains 81, 75 and 80% of their initial PL intensity after 24h of UV illumination *Polar solvent stability:*$CsPbBr_3$ NCs retains 70% of its initial PL intensity after 24h in presence of water	
$CsPbBr_3$	Bromopropane	78.5/18.2	Initial PLQY reduced by 17%in air after 120 days and retained 67.85%under UV light for 96 h	15
$CsPbCl_3$	Phenylphosphonicdichloride	71/12	80% and 50% of initial PLQY retained after 5h under UV light and 10 rounds of purification	3
$CsPbCl_3$ $CsPbBr_3$	N-halophthalimide as halide source	80/9 99/20	*Air-stability:*Retention of 85% PLQY after 2 weeks in ambient condition NA	4
$CsPbBr_3$ $MAPbBr_3$ $FAPbBr_3$	1,3-dihalo-5,5-dimethylhydantoin	99/19 99/21 99/20	*Air-stability:* ~80-85% of initial PL intensity retained after 70-80 days of storage under ambient condition *Photo-stability:* ~85% of initial PLQY restored after >30h of continuous UV irradiation *Polar solvent stability:* ~80% of initial PL intensity retained even after 24h in presence of water	**This work**

$CsPbCl_3$		70/10	*Air/Photo-stability:* ~80% of initial PLQY retained after 45 days in ambient condition and under 24h UV irradiation, respectively.

Table A3.10. *Advantages and disadvantages of different halide precursor used in hot-injection method of synthesis.*

Halide Precursor	Advantage	Disadvantage/s	Ref.
PbX_2 (X= Cl, Br and I)	Most frequently used halide and lead precursor	Difficult to control composition of the final NCs due to sub-stoichiometric amount of halogen and the formed halide-deficient NCs show poor stability and optical properties.	7, 16, 17
OAm^+X^- (X= Cl, Br and I)	All three all-inorganic $CsPbX_3$ NCs with near-unity PLQY can be prepared. Produces good quality $FAPbX_3$ (X= Br and I) NCs with high stability.	Highly hygroscopic and hence, special protection is needed for storing the samples. Systems like $MAPbX_3$ and $FAPbCl_3$ NCs are not reported yet. In some cases, the NCs are moderately stable under ambient condition (1-2 weeks).	1, 7, 18, 19
Benzoyl halides	All $APbX_3$ NCs can be obtained. The green-emitting $APbBr_3$ shows PLQY of ~92% and the violet/red-emitting$CsPbCl_3$and $CsPbI_3$ NCs show PLQY of ~65 and 58%, respectively.	The iodide-based NCs are moderately luminescent (PLQYbetween45-58%). Except $CsPbI_3$ NCs, stability of the other systems are not examined. Optical properties and	2

	The $CsPbI_3$ NCs are stable for over 20 days under ambient condition.	stability of the mixed-halide NCs are not explored. Benzoyl halides are highly toxic.	
NXI_m (X= Cl, Br)	High quality $APbBr_3$ NCs with near-unity PLQY can be prepared with exceptional stability under ambient condition. Blue-emitting NCs with PLQY of 85-97% and violet-emitting $CsPbCl_3$ NCs with second highest value of PLQY of 80% can be prepared.	Many systems like chloride and iodide-based hybrid NCs and yellow/orange-emitting mixed-halide NCs could not be obtained. The $CsPbI_3$ NCs are weakly luminescent (PLQY ~27%)and stable only for a few days.	4, 14
DBDMH	PLQY of the $APBr_3$ NCs between~91-95% can be prepared.	Only the green-emitting NCs are formed. Stability of the NCsis moderate.	20
DXDMH (X= Cl, Br and I)	$APbBr_3$ NCs exhibit near-unity PLQY with excellent stability. Red/NIR-emitting $APbI_3$ NCs exhibit high phase stability for several months and possess PLQY in the range of 67-96%, highest by any common method till date. PLQYs of the mixed-halide NCs are comparable or better than any previous method. Provides a common method of achieving high quality all $APbX_3$ NCs emitting across the visible (extendable to NIR) region.	Violet-emitting $MAPbCl_3$ and $FAPbCl_3$ NCs exhibit poor optical properties and stability. PLQY of $CsPbCl_3$, $MAPbI_3$ and $FAPbI_3$ NCs are less than unity. Size control of the NCs was unsuccessful.	**This work**

Table A3.11. *Atomic % ratio of the constituting elements (Cs, Pb and Br) and nitrogen (N) in $CsPbBr_3$ NCs obtained from XPS measurement.*

Samples	Area under the curve/ASF				Atomic % ratio (with respect to Pb)			
	Cs	Pb	Br	N	Cs	Pb	Br	N
$CsPbBr_3$	24948.45	29153.57	91152.43	53351.03	0.85	1.00	3.13	1.83
$CsPbBr_3$(II)	18149.36	19481.49	52471.89	28248.16	0.93	1.00	2.69	1.45

References:

1. A. Dutta, R. K. Behera, P. Pal, P. D. S. Baitalik and D. N. Pradhan, *Angew. Chem. Int. Ed.*, 2019, ***58***, 5552 –5556.
2. M. Imran, V. Caligiuri, M. Wang, L. Goldoni, M. Prato, R. Krahne, L. D. Trizio and L. Manna, *J. Am. Chem. Soc.*, 2018, ***140***, 2656–2664.
3. C. Zhang, Q. Wan, L. K. Ono, Y. Liu, W. Zheng, Q. Zhang, M. Liu, L. Kong, L. Li and Y. Qi, *ACS Energy Lett.*, 2021, ***6***, 3545−3554.
4. S. Paul, T. Ahmed, S. Das and A. Samanta, *J. Phys. Chem. C*, 2021, ***125***, 23539−23547.
5. X. Li, Y. Wu, S. Zhang, B. Cai, Y. Gu, J. Song and H. Zeng, *Adv. Funct. Mater.*, 2016, ***26***, 2435–2445.
6. Y. Shynkarenko, M. I. Bodnarchuk, C. Bernasconi, Y. Berezovska, V. Verteletskyi, S. T. Ochsenbein and M. V. Kovalenko, *ACS Energy Lett.*, 2019, ***4***, 2703–2711.
7. L. Protesescu, S. Yakunin, M. I. Bodnarchuk, F. Bertolotti, N. Masciocchi, A. Guagliardi and M. V. Kovalenko, *J. Am. Chem. Soc.*, 2016, ***138***, 14202–14205.
8. S. Wei, Y. Yang, X. Kang, L. Wang, L. Huang and D. Pan, *Chem. Commun.*, 2016, ***52***, 7265-7268.
9. E. Yassitepe, Z. Yang, O. Voznyy, Y. Kim, G. Walters, J. A. Castañeda, P. Kanjanaboos, M. Yuan, X. Gong, F. Fan, J. Pan, S. Hoogland, R. Comin, O. M. Bakr, L. A. Padilha, F. Nogueira and E. H. Sargent, *Adv. Funct. Mater.*, 2016, ***26***, 8757–8763.
10. P. Liu, W. Chen, W. Wang, B. Xu, D. Wu, J. Hao, W. Cao, F. Fang, Y. Li, Y. Zeng, R. Pan, S. Chen, W. Cao, X. W. Sun and K. Wang, *Chem. Mater.*, 2017, ***29***, 5168–5173.
11. Q. Li, H. Li, H. Shen, F. Wang, F. Zhao, F. Li, X. Zhang, D. Li, X. Jin and W. Sun, *ACS Photonics*, 2017, ***4***, 2504–2512.
12. F. Krieg, S. T. Ochsenbein, S. Yakunin, S. t. Brinck, P. Aellen, A. Süess, B. Clerc, D. Guggisberg, O. Nazarenko, Y. Shynkarenko, S. Kumar, C.-J. Shih, I. Infante and M. V. Kovalenko, *ACS Energy Lett.*, 2018, ***3***, 641–646.
13. M. Imran, P. Ijaz, D. Baranov, L. Goldoni, U. Petralanda, Q. Akkerman, A. L. Abdelhady, M. Prato, P. Bianchini, I. Infante and L. Manna, *Nano Lett.*, 2018, ***18***, 7822–7831.
14. S. Paul and A. Samanta, *ACS Energy Lett.*, 2020, ***5***, 64–69.
15. S. Akhil, V. G. V. Dutt and N. Mishra, *Nanoscale*, 2021, ***13***, 13142-13151.
16. L. Protesescu, S. Yakunin, M. I. Bodnarchuk, F. Krieg, R. Caputo, C. H. Hendon, R. X. Yang, A. Walsh and M. V. Kovalenko, *Nano Lett.*, 2015, ***15***, 3692–3696.

17. O. Vybornyi, S. Yakunin and M. V. Kovalenko, *Nanoscale*, 2016, ***8***, 6278-6283.
18. Q. A. Akkerman, L. Martínez-Sarti, L. Goldoni, M. Imran, D. Baranov, H. J. Bolink, F. Palazon and L. Manna, *Chem. Mater.*, 2018, ***30***, 6915–6921.
19. L. Protesescu, S. Yakunin, S. Kumar, J. Bär, F. Bertolotti, N. Masciocchi, A. Guagliardi, M. Grotevent, I. Shorubalko, M. I. Bodnarchuk, C.-J. Shih and M. V. Kovalenko, *ACS Nano*, 2017, ***11***, 3119–3134.
20. S. K. Mahankudo, A. Das, K. Mishra, M. Barai, P. Mal and S. Ghosh, *ACS Appl. Nano Mater.*, 2022, ***5***, 4360–4366.

Appendix 4

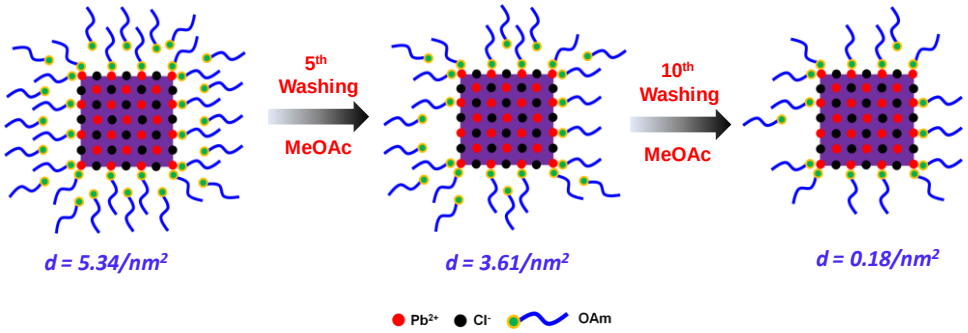

Scheme A4.1. *Schematic representation of the surface ligand content after 5 and 10 cycles of washing with MeOAc. For simplicity only OAm is shown here as surface capping ligand and ODE is not shown at the surface of the NCs.*

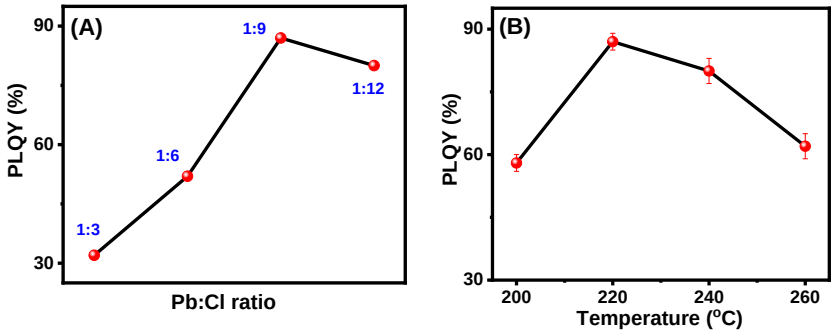

Figure A4.1. *Dependence of PLQY of the NCs on (A) Pb:Cl precursor molar ratio at reaction temperature of 220°C and (B) reaction temperature for a fixed Pb:Cl molar ratio of 1:9.*

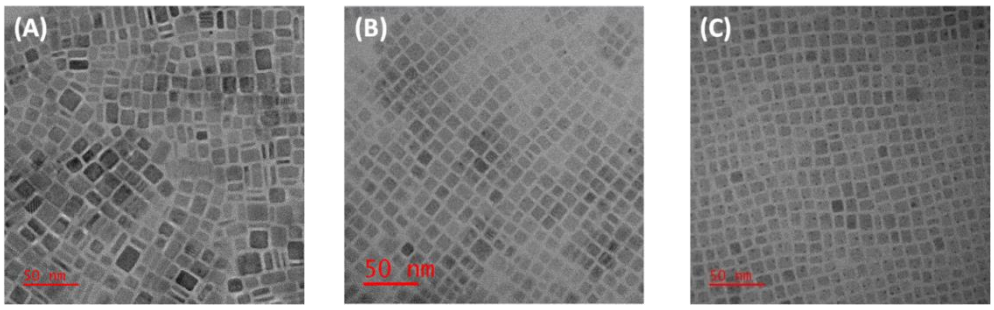

Figure A4.2. *Bright-field TEM images of the NCs obtained using Pb:Cl precursor molar ratio of (A) 1:3, (B) 1:6 and (C) 1:9. The scale bar is 50 nm in each image.*

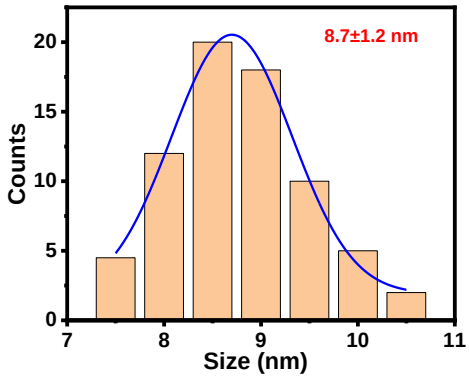

***Figure* A4.3.** *Size distribution histogram of the $CsPbCl_3$ NCs prepared at 220°C using Pb:Cl precursor ratio of 1:9. Inset shows average edge length of the NCs.*

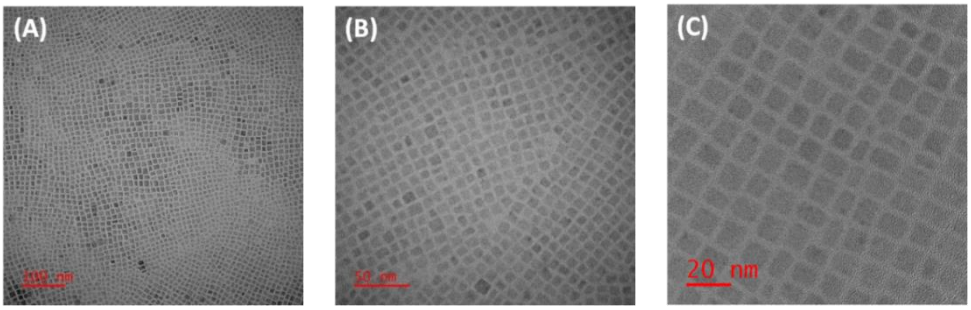

Figure A4.4. *Additional bright-field TEM images of the $CsPbCl_3$ NCs. The scale bar is indicated in the bottom left corner of each image.*

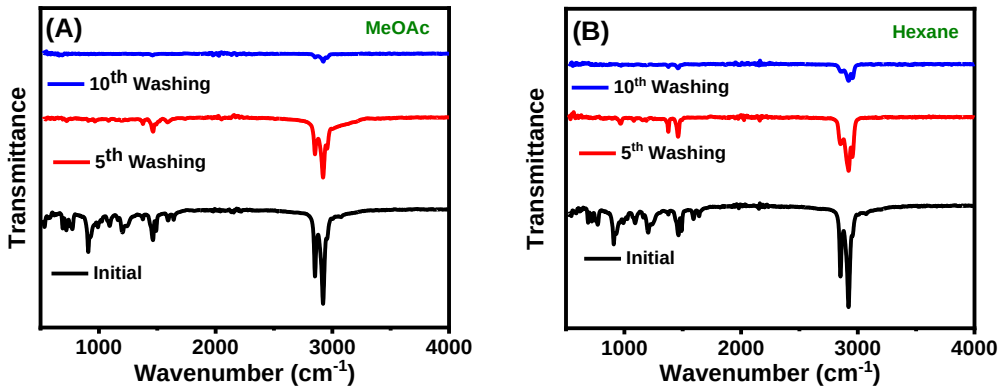

Figure A4.5. *FTIR spectra of the NCs before and after 5^{th} and 10^{th} cycle of washing with (A) MeOAc and (B) hexane.*

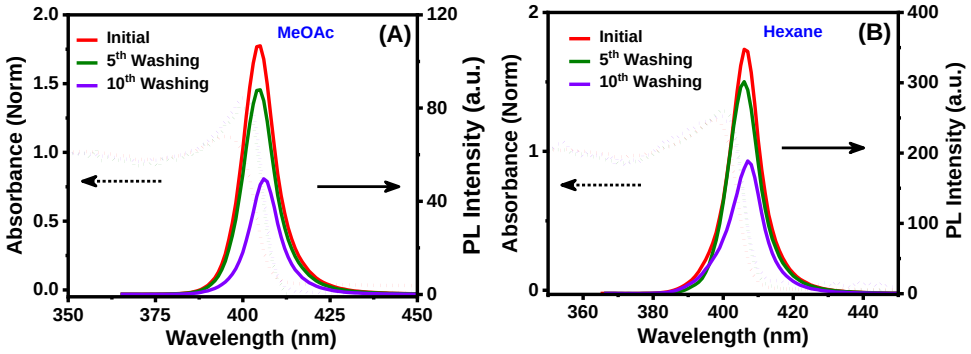

Figure A4.6. *UV-Vis absorption and PL spectra of the NCs before and after 5th and 10th cycle of washing with (A) MeOAc and (B) Hexane.*

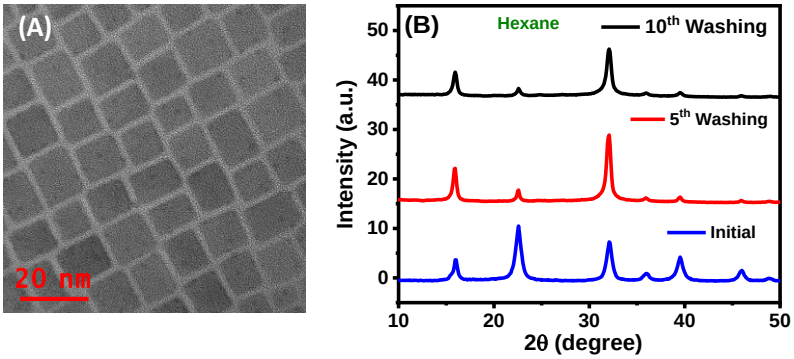

Figure A4.7. *(A) Bright-field TEM images of the NCs after 5th cycle of washing with hexane. (B) PXRD patterns of the NCs before and after 5th and 10th cycle of washing with hexane.*

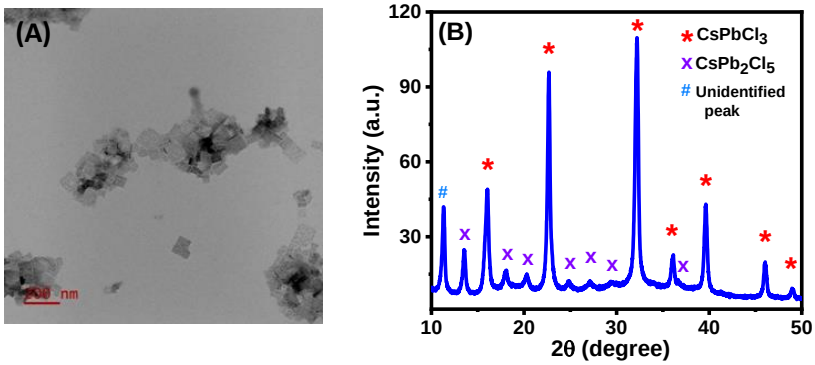

Figure A4.8. *(A) Bright-field TEM image and (B) PXRD pattern of the NCs after 14 cycles of washing with MeOAc. The unidentified peak at ~12 degrees possibly arises from 2D layered perovskite NCs.*

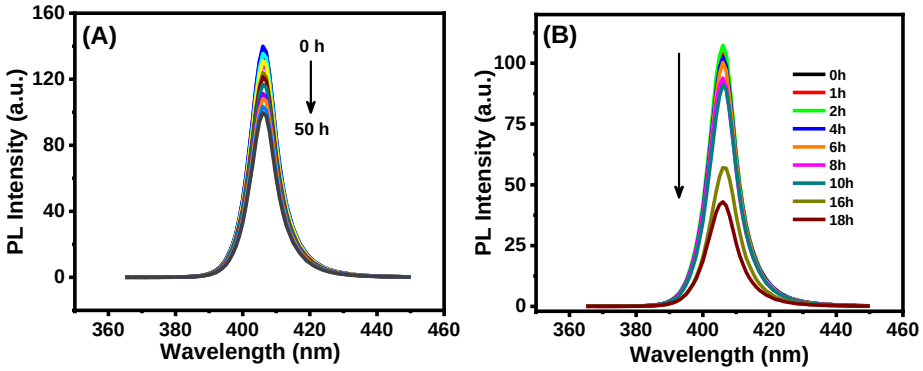

Figure A4.9. *Evolution of the PL spectrum of the NCs (A) in presence of water and (B) under continuous exposure to UV radiation (365 nm, 8W/cm^2).*

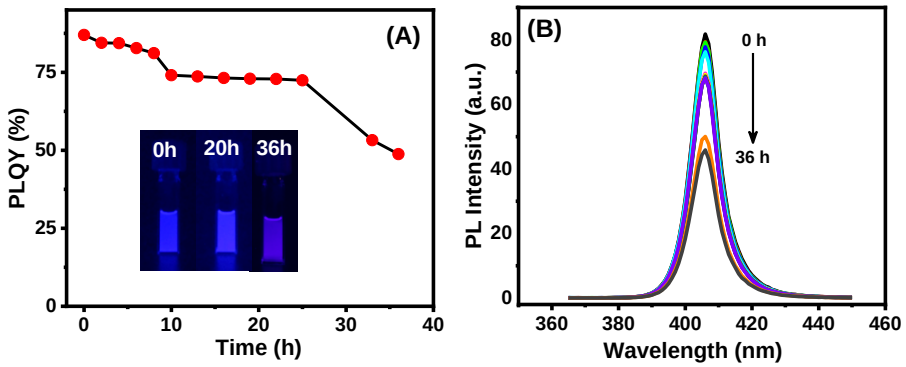

Figure A4.10. *(A) Change in PLQY and (B) evolution of the PL spectrum of the NCs in presence of ethanol under ambient condition.*

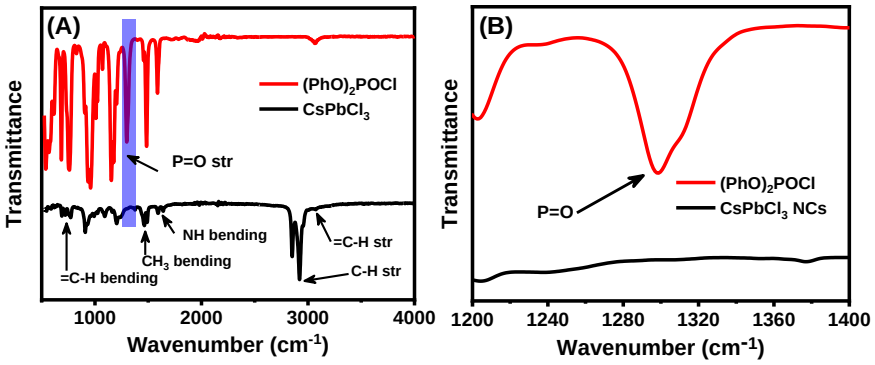

Figure A4.11. *(A) A comparison of the FTIR spectra of as-synthesized NCs and pure $(PhO)_2POCl$. (B) The highlighted region in Figure (A) shows no existence of P=O stretching band of $(PhO)_2POCl$ in the NCs.*

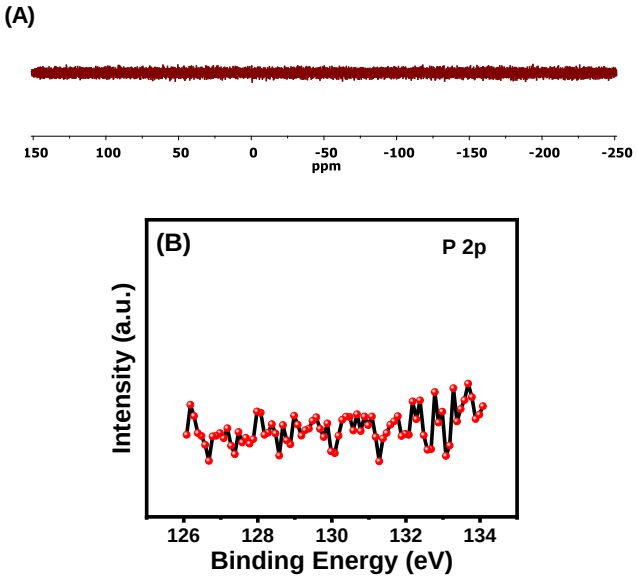

Figure A4.12. *(A) ^{31}P-NMR spectra of the as-synthesized NCs in $CDCl_3$ at RT. (B) High resolution XPS spectrum of the 'P 2p' region.*

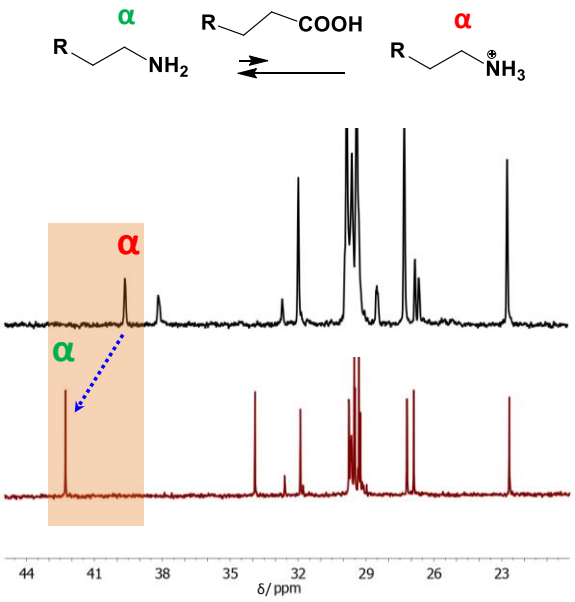

Figure A4.13. *A comparison of the ^{13}C-NMR spectra of the as-synthesized NCs capped with OAm (brick red) and conventional $OAmH^+$ capped NCs prepared with DCDMH as chloride precursor (black).*

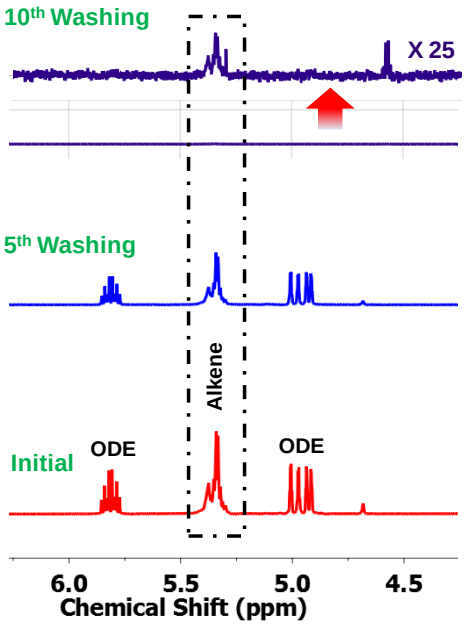

Figure A4.14. *^{1}H-NMR spectra of the NCs after different cycles of washing with MeOAc, indicating gradual reduction of oleyl due to both OAH and OAm ligands and ODE. After ten cycles of washing, ODE is completely removed from the surface and the oleyl content becomes so less that its presence is observed only after 25 times magnification of the ^{1}H-NMR data (top).*

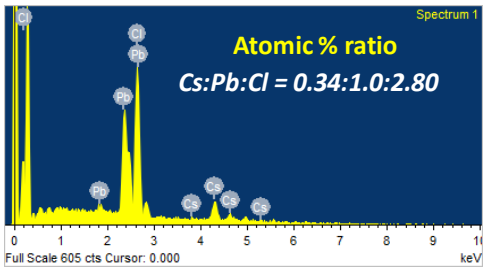

Figure A4.15. *EDX spectra of the as-synthesized NCs with atomic % ratio of the elements.*

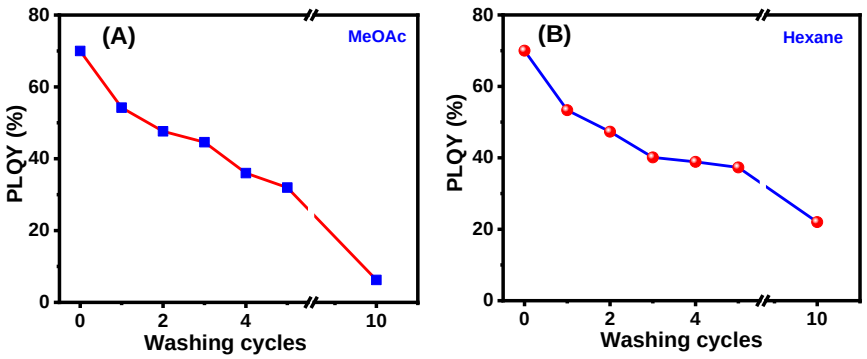

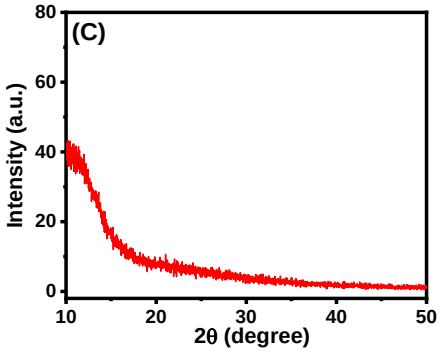

Figure A4.16. *The change in PLQY of $OAmH^+$ capped $CsPbCl_3$ NCs (prepared using DCDMH as chloride precursor) after multiple washing with (A) MeOAc and (B) hexane. (C) PXRD patterns of the NCs after ten cycles of washing with MeOAc.*

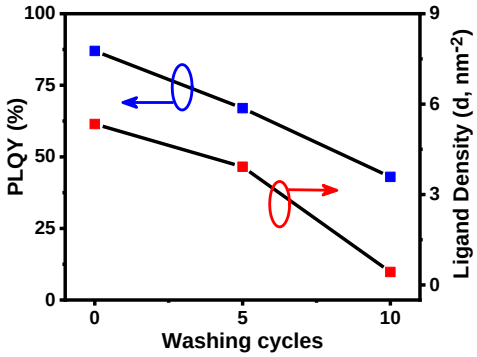

Figure A4.17. *Change in PLQY and ligand density of the NCs with successive washing using MeOAc.*

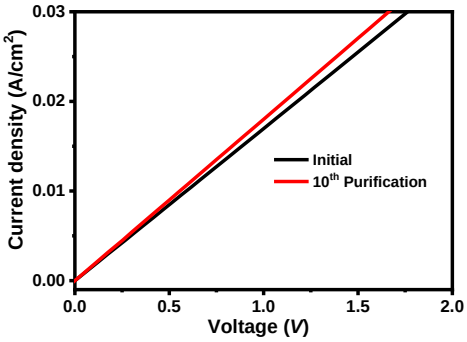

Figure A4.18. *Current (I) – Voltage (V) characteristics of the as-synthesized and ten times washed (with MeOAc) $CsPbCl_3$ NCs coated on a FTO plate.*

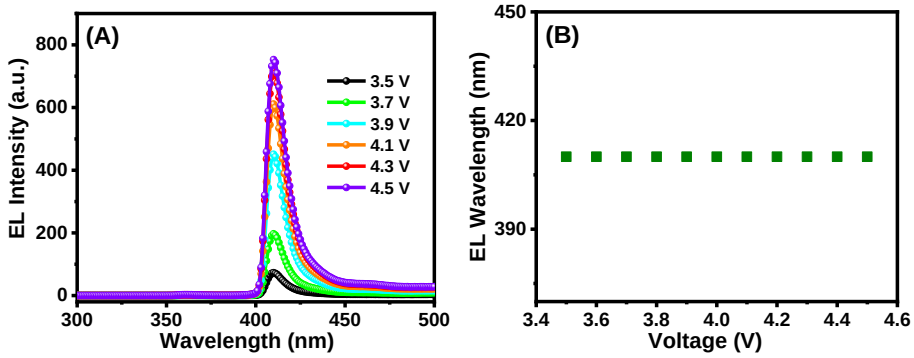

Figure A4.19. *(A) EL spectra of the LED at different bias voltages. (B) Unchanged peak maxima of the EL spectra over a wide range of applied voltages.*

Table A4.1. *A comparison of the optical properties of the $CsPbCl_3$ NCs prepared by different direct methods.*

Chloride precursor	Pb:Cl ratio used	λem (nm)	PLQY (%)	fwhm (nm)	Ref.
$OAmH^+Cl^-$	1:5.5-5.6	411	97	----	1
Benzoyl chloride	1:9	408	65	11	2
$PhPOCl_2$	1:4.5	404	71	12	3
NCP	1:9	404	80	9	4
DCDMH	1:3	406	70	10	5
$(PhO)_2POCl$	1:9	405	87	10	**This work**

Table A4.2. *Optical and phase stability of the $CsPbCl_3$ NCs prepared by different direct methods towards repeated washing.*

Sample	Chloride precursor/s	Stability toward washing	Ref.
$CsPbCl_3$	$PbCl_2$	***Optical stability:*** PL intensity almost completely quenched after 4th washing cycles. ***Phase stability:*** Phase transformation into non-emitting tetragonal phase starts after 2nd round of washing and completely converted into it after 4th round of washing.	6
$CsPbCl_3$	combination	***Optical stability:*** Retains ~50% of initial PL	

	of $PbCl_2$ and $OAmH^+Cl^-$	intensity after 4th round of washing ***Phase stability:*** The tetragonal phase arises after 4th round of washing.	6
$CsPbCl_3$	$PhPOCl_2$	***Optical stability:*** From an initial value of 71%, the PLQY decreases to 66.2 and 36.8% after 4th and 10th cycles of washing. ***Phase stability:*** Retains original phase and morphology after 10th cycles of washing.	3
Sr doped $CsPbCl_3$	combination of $PbCl_2$ and $SrCl_2$	***Optical stability:*** The initial PLQY (82.4%) decreases to only ~1% after 8th cycle of washing. However, their self assembled product remains bright with a PLQY of ~57% after the same cycles of washing. ***Phase stability:*** The tetragonal phase starts appearing after 5th washing cycles and completely converted to it after 8th such washing steps.	7
$CsPbCl_3$	$(PhO)_2POCl$	***Optical stability:*** The NCs exhibit ~67% and ~43% PLQY, respectively after 5th and 10th cycles of washing with MeOAc. An even better PLQY of ~71% and ~52% is observed after similar washing cycles with hexane. ***Phase stability:*** Original crystal phase and morphology is almost retained after 10th cycles of washing with both MeOAc and hexane. The tetragonal phase appears only after 14th such cycles of washing with MeOAc.	**This work**

Table A4.3. *A comparison of the PLQY and stability of the violet-emitting $CsPbCl_3$ NCs obtained by different three-precursor method of synthesis.*

Chloride precursor used	PLQY (%)	Stability parameters	Ref.
Benzoyl chloride	65	Not studied	2
$OAmH^+Cl^-$	97	***Ambient stability:*** PLQY reduced to	1

		~80% after 7 days of storage in air.	
$PhPOCl_2$	71	***Photostability:*** ~80% of initial PL intensity is retained after 5 h under continuous UV illumination.	3
NCP	80	***Ambient stability:*** ~85% of initial PL intensity is retained after 14 days of storage in ambient atmosphere.	4
DCDMH	70	***Ambient stability:*** ~80% of initial PLQY retained after 45 days in ambient conditions. ***Photostability:*** ~80% of the initial PLQY retained after 24h under continuous UV light illumination.	5
$(PhO)_2POCl$	87	***Ambient stability:*** The NCs shows ~79% PLQY even after 48 days of storage under ambient condition. ***Polar solvent stability:*** A PLQY of ~64% and ~48% is still obtained even after 2 days and 36 h of storage in water and ethanol, respectively. ***Photostability:*** A PLQY of ~80% is still retained after 10h continuous illumination of UV light. ***Thermal stability:*** Cubic phase and bright emission of the NCs remains intact even after continuous heating at 85°C for 10h.	**This work**

Table A4.4. *Ligand coverage of the $CsPbCl_3$ NCs after different cycles of washing with MeOAc.*

Washing steps with MeOAc	Concentration of alkene species (mM)	Concentration of the NCs (nM)	Size of the NCs (nm)	No. of ligands (nm^{-2})
0	25.00	10.3	8.7	5.34

5	12.68	6.8	8.9	3.92
10	0.49	2.1	9.5	0.43

Table A4.5. *Atomic % ratio of the constituting elements and N in $CsPbCl_3$ NCs calculated from core-level XPS data and atomic sensitivity factor of the elements.*

System	Atomic % ratio (with respect to Pb)			
	Cs	Pb	Cl	N
$CsPbCl_3$	0.53	1.00	2.73	1.64

Table A4.6. *Summary of the performance and operational stability of perovskite-based violet-LEDs.*

Systems	EL maxima (nm)	Fabrication Method	fwhm (nm)	EQE (%)	EL decay	Ref.
$(PEA)_2PbBr_4$ NPLs	410	Solution processed	14	0.038	---	8
$(PEA)_2PbBr_4$ NPLs	408.8	"	18	0.25	5% in 5h	9
$MAPbCl_{2.4}Br_{0.6}$ NCs	---	"	---	---	90% in 3h	
$Cs_3Sb_2Br_9$ QDs	408	"	55	0.206	10% in 6h	10
Mg^{2+} doped $CsPbCl_3$ NCs	402	"	---	0.1	---	11
$CsPbCl_3$ NCs	405	"	10.6	0.18	---	3
$CsPbCl_3$ NCs	410	"	12	0.16-0.19	30% in 3h	**This work**

References:

1. A. Dutta, R. K. Behera, P. Pal, P. D. S. Baitalik and D. N. Pradhan, *Angew. Chem. Int. Ed.*, 2019, ***58***, 5552 –5556.
2. M. Imran, V. Caligiuri, M. Wang, L. Goldoni, M. Prato, R. Krahne, L. D. Trizio and L. Manna, *J. Am. Chem. Soc*, 2018, ***140***, 2656–2664.
3. C. Zhang, Q. Wan, L. K. Ono, Y. Liu, W. Zheng, Q. Zhang, M. Liu, L. Kong, L. Li and Y. Qi, *ACS Energy Lett.*, 2021, ***6***, 3545–3554.
4. S. Paul, T. Ahmed, S. Das and A. Samanta, *J. Phys. Chem. C*, 2021, ***125***, 23539–23547.
5. S. Das and A. Samanta, *Nanoscale*, 2022, ***14***, 9349-9358.

6. R. K. Behera, S. D. Adhikari, S. K. Dutta, A. Dutta and N. Pradhan, *J. Phys. Chem. Lett.*, 2018, ***9***, 6884–6891.
7. Y. Ji, M. Wang, Z. Yang, H. Wang, M. A. Padhiar, H. Qiu, J. Dang, Y. Miao, Y. Zhou and A. S. Bhatti, *Nanoscale*, 2022, ***14***, 2359-2366.
8. D. Liang, Y. Peng, Y. Fu, M. J. Shearer, J. Zhang, J. Zhai, Y. Zhang, R. J. Hamers, T. L. Andrew and S. Jin, *ACS Nano*, 2016, ***10***, 6897−6904.
9. W. Deng, X. Jin, Y. Lv, X. Zhang, X. Zhang and J. Jie, *Adv. Funct. Mater.*, 2019, ***29***, 1903861.
10. Z. Ma, Z. Shi, D. Yang, F. Zhang, S. Li, L. Wang, D. Wu, Y. Zhang, G. Na, L. Zhang, X. Li, Y. Zhang and C. Shan, *ACS Energy Lett.*, 2020, ***5***, 385−394.
11. Q. Hu, J. Guo, M. Lu, P. Lu, Y. Zhang, W. W. Yu and X. Bai, *J. Phys. Chem. Lett.*, 2021, ***12***, 8203–8211.

Reprints of Publications

THE JOURNAL OF PHYSICAL CHEMISTRY Letters

pubs.acs.org/JPCL Letter

Ambient Condition Mg^{2+} Doping Producing Highly Luminescent Green- and Violet-Emitting Perovskite Nanocrystals with Reduced Toxicity and Enhanced Stability

Somnath Das, Apurba De, and Anunay Samanta*

Cite This: J. Phys. Chem. Lett. 2020, 11, 1178−1188 Read Online

ACCESS | Metrics & More | Article Recommendations | Supporting Information

ABSTRACT: The lack of long-term stability, the presence of toxic lead, and a low photoluminescence (PL) efficiency are the major obstacles to the commercialization of lead-halide perovskite-based optoelectronic and photovoltaic devices. Herein we report a facile ambient condition doping protocol that addresses all three issues of the $CsPbX_3$ perovskite nanocrystals (NCs) to a substantial extent. We show that the room-temperature treatment of these NCs with MgX_2 results in the partial (18−23%) replacement of toxic lead, enhances the PL quantum yield of green-emitting $CsPbBr_3$ (to ∼100% from ∼51%) and violet-emitting $CsPbCl_3$ NCs (to ∼79% from ∼1%), and improves the stability under ambient conditions and in the presence of light and a polar solvent. Ultrafast pump−probe and temperature-dependent PL studies reveal that curing of the intrinsic structural disorder, introduction of some shallow energy levels close to the conduction band edge, and effective passivation of the halide deficiency contribute to the improved properties of the doped systems.

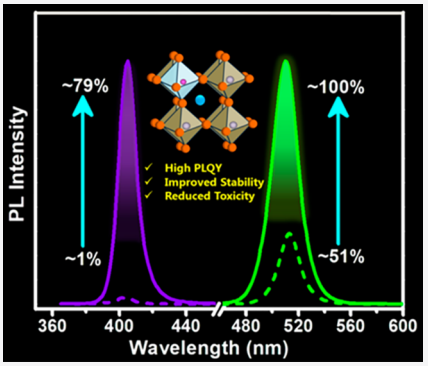

The outstanding potential of the lead halide perovskites (ABX_3-type, A = Cs, FA (formamidinium, $CH(NH_2)_2^+$) and MA (methylammonium, $CH_3NH_3^+$), B = Pb and X = Cl, Br, and I) in various photovoltaic and optoelectronic technologies such as solar cells,[1−4] light-emitting diodes (LEDs),[5,6] lasers[7,8] photodetectors, and nonlinear optics,[9−12] which has already been demonstrated, is owing to their unique optical and photophysical properties, namely, high luminescence efficiency,[6,13−15] high color purity,[13] large absorption coefficient,[16] defect-tolerant nature,[17] ease of tunability of the band gap throughout the entire visible region,[18,19] and facile low-cost synthesis.[13,20−22] Unlike the conventional metal chalcogenide semiconductor nanocrystals (NCs), the halide perovskites exhibit high photoluminescence (PL) due to their defect-tolerant nature.[17,23,24] However, in the nanodimension, a large surface to volume ratio has a detrimental effect on their optical properties and stability,[24−26] and the PL quantum yield (QY) and stability of these NCs under ambient conditions are often far from satisfactory.[25] For example, the violet-emitting $CsPbCl_3$ NCs are poorly luminescent with typical PLQYs of <5%, as deep trap centers generated by halide vacancies and distorted $[PbCl_6]^{4-}$ octahedral units facilitate the nonradiative recombination of photogenerated charge carriers.[27−36] Such a low PLQY is a major issue with this material in its practical utilization. In contrast, the green-emitting $CsPbBr_3$ NCs possess much higher PLQY because the defects are weakly localized and shallow in nature.[13,14,29,37] However, the subunity PLQY of the pristine $CsPbBr_3$ NCs implies a non-negligible contribution of the nonradiative recombination mediated by these shallow defect states that needs to be eliminated to obtain high-quality NCs with a near-unity PLQY.[37]

Although several successful strategies have been developed for enhancing the PLQY of these NCs, the presence of toxic lead has been a major concern for the commercialization of products based on these materials. In this regard, B-cation doping is an attractive approach because it not only enhances the PLQY of the system but also reduces the content of toxic lead in the NCs. The literature indicates that the PLQY of green-emitting $CsPbBr_3$ NCs is enhanced upon the doping of Ce^{3+}, Zn^{2+}, Sn^{2+}, Cd^{2+}, and Na^{+}[28],[38−42] and that of violet-emitting $CsPbCl_3$ NCs is enhanced by the doping of Ni^{2+}, Y^{3+}, La^{3+}, Cd^{2+}, Cu^{+}, and Ca^{2+}.[27,28,30,31,43−46] Although Cd^{2+} is one metal ion, which is effective for both green- and violet-emitting NCs,[28] its doping does not help reduce the toxicity of the NCs because cadmium compounds are also highly toxic.[47]

In the quest for a metal ion that will enhance the PLQY and the stability of both the blue- and green-emitting $CsPbX_3$ (X = Cl and Br) NCs and at the same time reduce the toxicity, we zeroed in on magnesium halides, MgX_2, considering their environmentally friendly nature, high natural abundance, strong preference for octahedral coordination,[48] and com-

Received: December 23, 2019
Accepted: January 24, 2020
Published: January 24, 2020

https://dx.doi.org/10.1021/acs.jpclett.9b03831
J. Phys. Chem. Lett. 2020, 11, 1178−1188

Scheme 1. (A) Schematic Representation of the Post-Synthetic Doping Strategy under Ambient Condition and (B) Illustration of Substitution of Pb^{2+} by Mg^{2+} and Passivation of the Halide Vacancy

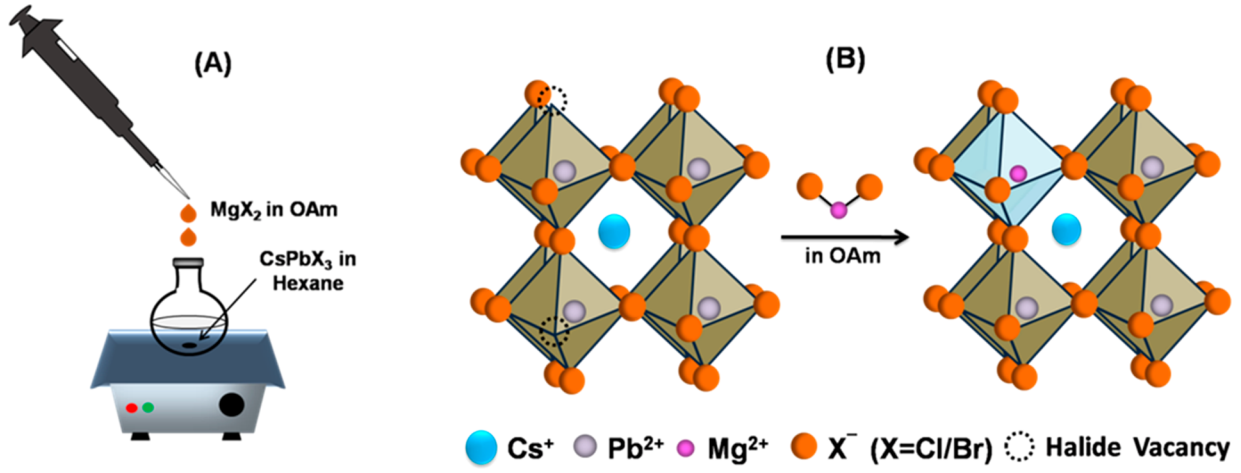

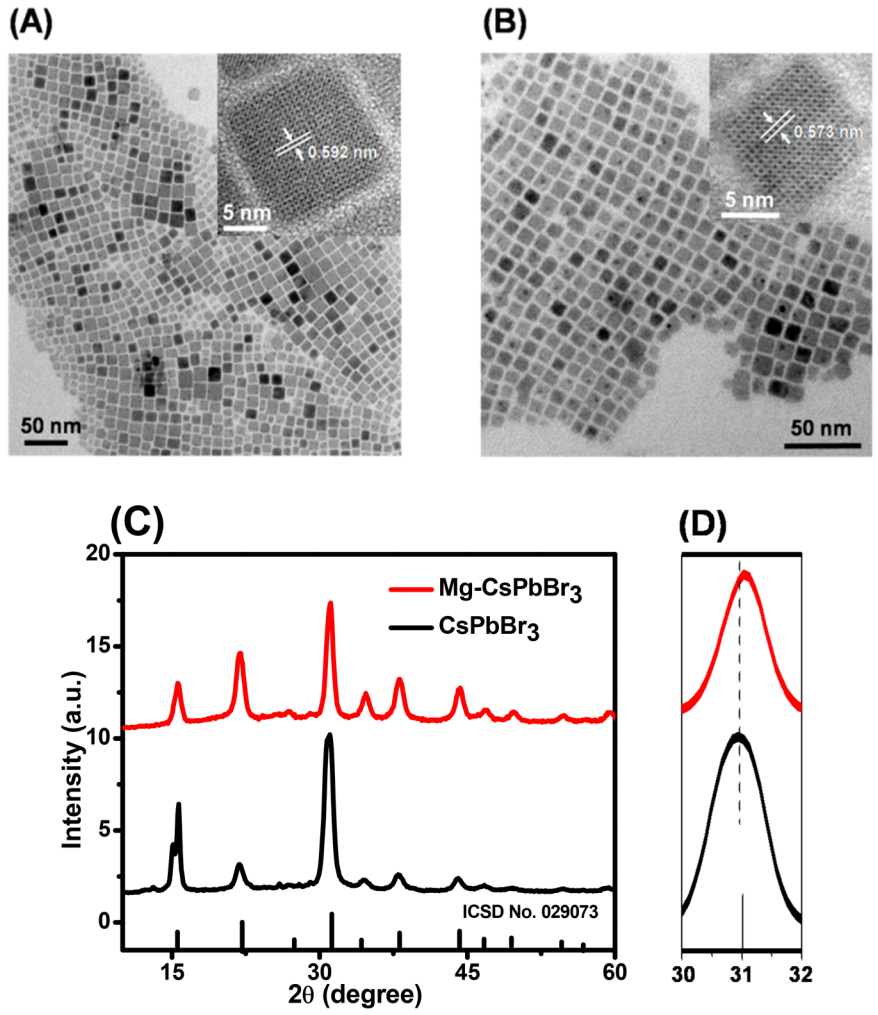

Figure 1. TEM images of (A) undoped and (B) Mg-doped $CsPbBr_3$ NCs with corresponding HRTEM images (inset) showing lattice spacing of the (100) planes. (C) PXRD patterns of the undoped and doped $CsPbBr_3$ NCs. (D) Zoomed view of the PXRD pattern shows the peak shift of the (200) plane to a higher angle upon Mg doping.

parable Mg−X and Pb−X bond dissociation energies.[49] Another factor that influenced our choice in favoring Mg^{2+} is a recent theoretical study that identified it as the best alternative to Pb^{2+} in the $CsPbX_3$ crystal lattice.[50] Two recent findings on the influence of Mg^{2+} on the PL of the $CsPbX_3$ film and NCs were, however, not encouraging because the reported PL enhancement was rather moderate.[27,51] Herein we report an entirely different strategy for introducing a significant

https://dx.doi.org/10.1021/acs.jpclett.9b03831
J. Phys. Chem. Lett. 2020, 11, 1178−1188

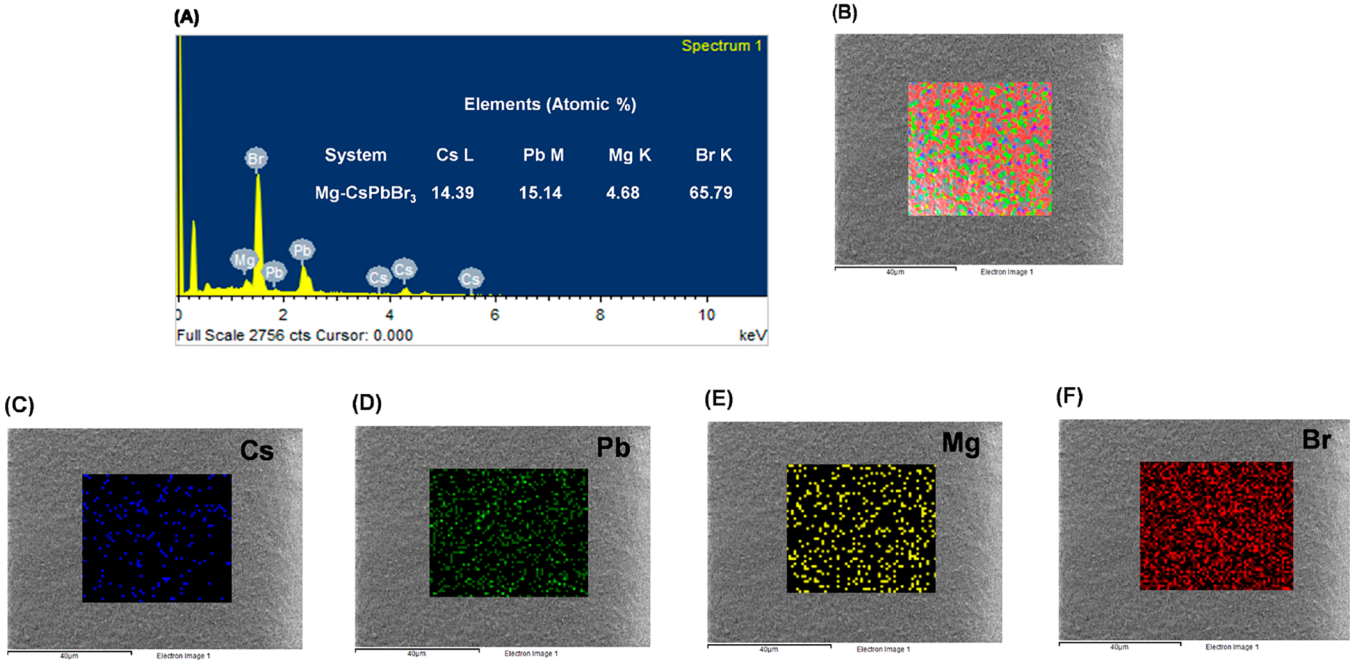

Figure 2. (A) EDX spectrum of the doped $CsPbBr_3$ NCs indicating the relative content of the individual elements. (B) FESEM image of the doped NCs. The center of the FESEM image, scanned for elemental mapping, indicates the homogeneous distribution of Cs, Pb, Mg, and Br throughout the scanned area of the doped NCs (C−F), respectively.

amount of Mg^{2+} under ambient conditions into the $CsPbX_3$ crystal, which reduces the lead content by ∼25%, dramatically improves the PLQY of both green- and violet-emitting perovskite NCs (near-unity for $CsPbBr_3$ and ∼79% for $CsPbCl_3$), and provides superior air- and photostability and robustness toward the polar solvent.

The undoped $CsPbX_3$ (X = Cl and Br) NCs were prepared following a conventional hot-injection method,[13] the details of which are provided as Supporting Information (SI). These NCs were dispersed in hexane and used for further investigation. For doping, MgX_2 (0.30 mmol) was dissolved in 4 mL of oleylamine (OAm) by heating to 100 °C for 2 h. The addition of 30 μL of this hexane-diluted solution to 0.50 mL of a colloidal dispersion (∼0.015 μM) of $CsPbX_3$ NCs, maintained under ambient conditions and stirring for 1 h (Scheme 1A), produced a brightly luminescent solution of $CsPbX_3$ NCs. This solution was mixed with methyl acetate in a 1:2 volume ratio and centrifuged at high speed (13 000 rpm) for 5 min. The supernatant liquid containing excess ligands and salts was discarded, and the residue at the bottom of the centrifuge tube was then collected and redispersed in hexane for further studies. Additional details of the method of synthesis are provided as SI.

The TEM images of the undoped and doped $CsPbBr_3$ NCs (Figure 1A,B) indicate the cubic morphology of both the samples. High-resolution TEM (HRTEM) images show an interplanar distance (100 lattice planes, d_{100}) of 0.592 nm in undoped NCs that is consistent with the literature.[14,29] A smaller interplanar distance of 0.573 nm in doped NCs is a reflection of the lattice contraction due to the smaller size of Mg^{2+} (72 pm, when hexa-coordinated) compared with Pb^{2+} (119 pm, hexa-coordinated).[52,53] It is to be noted that the stated d_{100} lattice spacings were obtained by the inspection of ∼40 NCs for both samples (Figure S1A,B). Although the cubic morphology of the $CsPbBr_3$ NCs was retained upon doping, the average edge length of the doped NCs is found to be noticeably smaller (11 ± 2 nm) compared with that of the undoped sample (14.5 ± 2 nm). A similar trend is observed for $CsPbCl_3$ NCs upon $MgCl_2$ treatment (Figure S2). The decrease in the edge length of the NCs upon doping is presumably due to the etching and smoothening of the doped NCs during the postsynthetic treatment.[54] Doping-induced lattice contraction (see later) can also contribute to this factor.

A careful inspection of the individual diffraction peaks of the powder X-ray diffraction (PXRD) patterns (Figure 1C) of the undoped and doped $CsPbBr_3$ NCs (Figure S3 for $CsPbCl_3$) shows a clear shift of the peaks toward a higher 2θ value, further confirming the lattice contraction upon doping. For example, the peak at 31.02° for undoped $CsPbBr_3$, which corresponds to the (200) plane, shifts to 31.12° for doped NCs (Figure 1D). Such a lattice-contraction-induced peak shift in the PXRD patterns is well-documented in the literature.[39,52,53,55,56] The estimated interplanar distance (d_{100} = 0.566 nm, see SI) from the PXRD data of the doped samples is very similar to that (0.573 nm) directly obtained from the HRTEM images, both confirming lattice contraction upon doping. The splitting of the (100) diffraction peak of the undoped $CsPbBr_3$ NCs is perhaps due to the existence of an orthorhombic phase as well, which, however, disappears upon Mg^{2+} incorporation into the lattice, indicating the pure cubic phase of the doped NCs.[57,58] Moreover, the absence of any new diffraction peak in doped NCs shows that no impure crystal phase is induced by Mg^{2+} doping.

The elemental analysis of a large area of the field-emission scanning electron microscopy (FESEM) images (Figure 2), obtained by energy-dispersive X-ray (EDX) measurements, allows a quantitative estimation of the dopant content. A characteristic peak of Mg at 1.3 keV only in the case of doped NCs (Figure 2A) confirms the presence of Mg^{2+}. The elemental analysis of the doped $CsPbBr_3$ NCs indicates a Cs/(Pb + Mg)/Br atomic ratio of ∼0.73:1.0:3.32 with overall ∼4.68% Mg, suggesting the replacement of ∼23.4% Pb^{2+} by

https://dx.doi.org/10.1021/acs.jpclett.9b03831
J. Phys. Chem. Lett. 2020, 11, 1178−1188

Mg^{2+} and a significant reduction in the toxicity of the pristine NCs. The Mg^{2+} content in doped NCs is also estimated through inductively coupled plasma optical emission spectroscopy (ICP-OES) measurements. The Mg^{2+} content (with respect to Pb^{2+}) is estimated to be ~23.13%. This value is very close to that obtained from the EDX measurement. Furthermore, elemental mapping (Figure 2B–F) shows a homogeneous distribution of all four elements throughout the scanned area of doped NCs. The EDX data and elemental mapping of undoped $CsPbBr_3$, $CsPbCl_3$, and doped $CsPbCl_3$ NCs are presented in Figures S4–S6.

An X-ray photoelectron spectroscopy (XPS) study of the samples provides insight into the chemical environment of the elements upon Mg^{2+} doping (Figure 3 and Figure S7). The high-resolution XPS spectrum of $CsPbBr_3$ shows that the intense peaks at ~138.1 and ~143 eV (Figure 3A) due to Pb $4f_{7/2}$ and Pb $4f_{5/2}$, respectively,[59] are shifted to a higher binding energy by ~0.2 eV upon doping. The Br $3d_{5/2}$ peak (Figure 3B) is also blue-shifted by ~0.2 to ~68.4 eV in doped $CsPbBr_3$ NCs.[42] The appearance of an additional peak at ~1305 eV only in doped NCs, which corresponds to Mg 1s (Figure 3C), re-establishes the presence of Mg^{2+}.[60] The blue shift of the Pb 4f and Br 3d peaks upon doping is due to the contraction of the $[PbBr_6]^{4-}$ units (and the consequent strengthening of the Pb–Br bonds) upon the incorporation of smaller Mg^{2+} ($r_{Mg^{2+}}$ = 72 pm versus $r_{Pb^{2+}}$ = 119 pm) at the B site.[28,53]

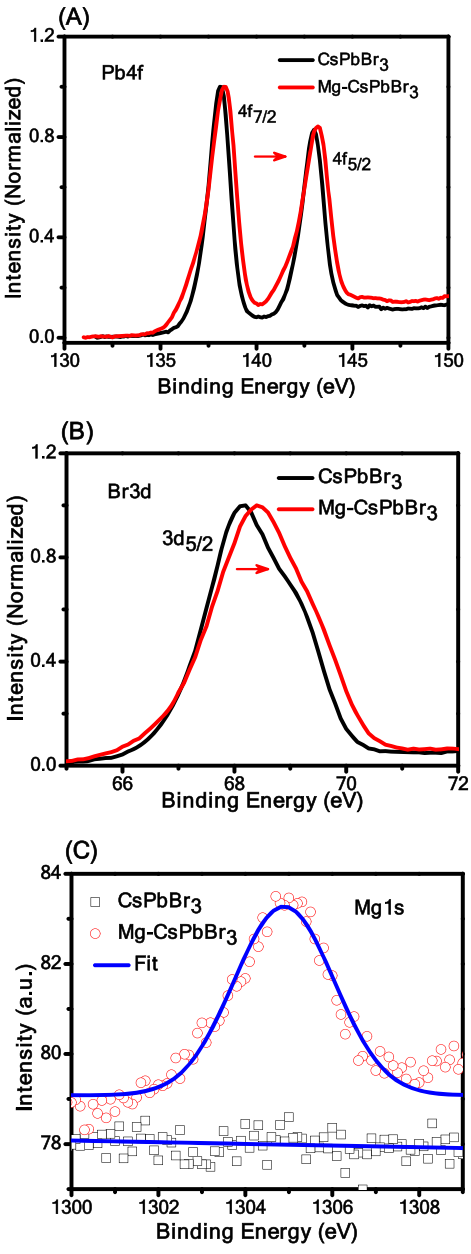

Figure 3. High-resolution XPS spectra of the undoped and doped $CsPbBr_3$ NCs showing signals due to (A) Pb 4f, (B) Br 3d, (C) Cs 3d, and (D) Mg 1s. All spectra were calibrated with respect to the C 1s peak at 285.0 eV.

A comparison of the FTIR spectra of the undoped and doped samples shows that except for some enhancement in the oleylammonium content (Figure S8), the surface ligand arrangement is not significantly changed upon doping. The observed change is not surprising because the oleylamine solution of MgX_2 has been used for the postsynthetic treatment.

We find that the peak positions of the UV–vis absorption and emission spectra of the $CsPbX_3$ NCs are not significantly changed upon doping, but the PL intensity of the systems is dramatically enhanced (Figure 4A). For example, the PLQY of the $CsPbBr_3$ NCs increases to ~100% from its initial value of ~51%, and that for $CsPbCl_3$ NCs increases to ~79% from an initial value of only ~1%. Careful inspection of the spectra reveals a small blue shift (~3 nm) of both absorption and PL maxima of $CsPbBr_3$ NCs upon doping (Figure S9 and Figure 4A, respectively) due to the lattice contraction induced by the smaller Mg^{2+} ion. In this context, we take note of a very recent work by Huang et al. on Mg doping of the $CsPbBr_3$ perovskite film (not NCs) improving its morphology, crystallinity, and PLQY and the external quantum efficiency (EQE) of the fabricated LEDs.[51] We also note the recent observation by Sun and coworkers of the increase in the PLQY of the violet-emitting $CsPbCl_3$ NCs from 0.8 to 36.6% upon the addition of $MgCl_2$ during the hot-injection synthesis of the NCs.[27] No doping of Mg was, however, observed like in our case. We surmise that the self-purification effect of NCs is dominant in the hot-injection synthesis and thus inhibits the doping of Mg^{2+} ions, whereas our postsynthetic doping strategy is based on the room-temperature reorganization of the perovskite lattice, which could feature the rather weak self-purification of NCs.

The PL decay behavior of undoped and Mg^{2+}-doped $CsPbBr_3$ NCs is shown in Figure 4B, and the decay parameters are presented in Table 1. Whereas $CsPbBr_3$ NCs exhibit three-component PL decay, the decay profile of Mg-doped samples is biexponential in nature. The contribution of the 2.91 ns component due to the band-edge excitonic recombination[28,29,61] is substantially enhanced from ~28 to ~70% upon treatment, and the fastest trapping component (0.64 ns), which has the largest contribution (~67%) in undoped NCs, vanishes completely in doped NCs. Another important point to note here is the increase in the contribution of the shallow trap-mediated radiative recombination component from ~5 to ~30% upon doping. An estimation of the rate constant (k_{nr}) of the nonradiative deactivation process using the measured PLQY and lifetime values of the systems before and after doping shows that the k_{nr} value decreases by a factor of ~128 after the treatment (Table 1). Likewise, Mg-doped $CsPbCl_3$ NCs also exhibit a much improved PL lifetime (Figure 4C) ($<\tau_{amp}>$ = 3.69 ns) compared with the undoped counterpart,

https://dx.doi.org/10.1021/acs.jpclett.9b03831
J. Phys. Chem. Lett. 2020, 11, 1178–1188

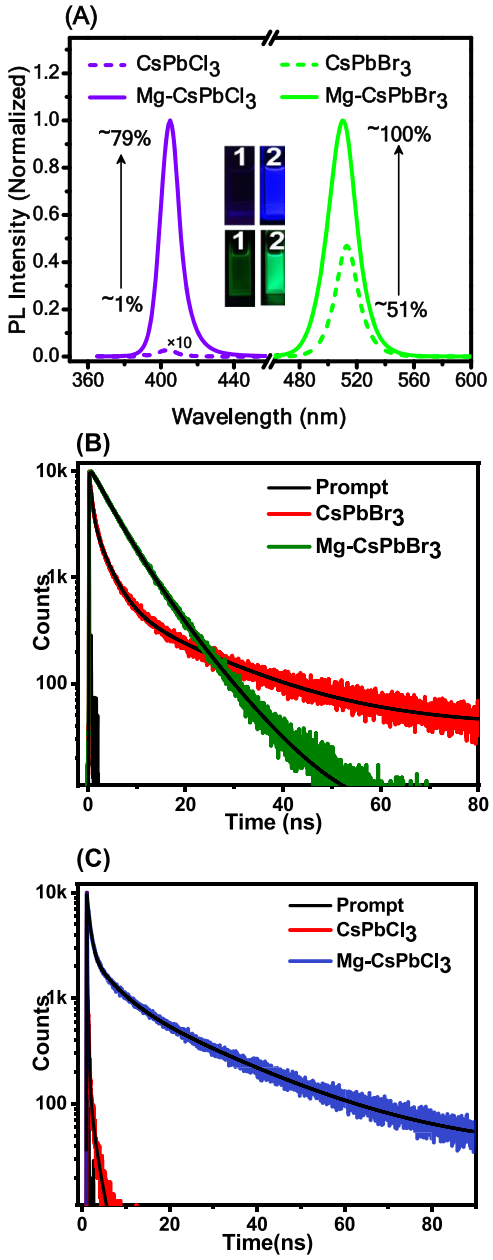

Figure 4. Effect of doping on (A) the PL spectra and (B,C) the decay profiles of $CsPbBr_3$ and $CsPbCl_3$ NCs. The inset in panel A shows the digital images of undoped (1) and doped (2) NCs under illumination by 365 nm radiation. The PL spectra were recorded by exciting the $CsPbCl_3$ and $CsPbBr_3$ NCs at 350 and 400 nm, respectively. For recording the PL decay curves, laser sources of 376 and 404 nm were used, and the PL was monitored at the respective peak wavelengths.

which is too short to be accurately estimated in our time-correlated single photon counting (TCSPC) setup, which has a time resolution of ~61 ps.

We have also studied the carrier dynamics in undoped and doped $CsPbBr_3$ NCs by transient absorption (TA) measurements with femtosecond time resolution. The TA spectral features (Figure 5A) are quite similar for both the undoped

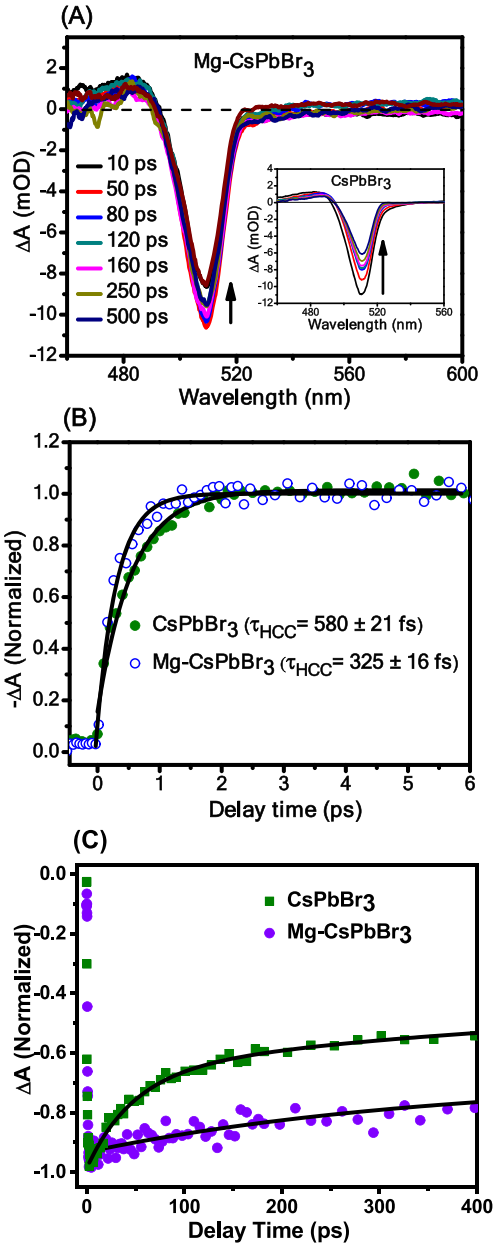

Figure 5. (A) TA spectra (λ_{ex} = 350 nm) of the doped and undoped NCs (inset). (B) Comparison of the HCC dynamics of the samples. (C) Bleach recovery dynamics of the two NCs. The kinetic parameters obtained upon biexponential fitting to the data are 47 ± 2.43 ps (0.55) and >850 ps (0.45) for the undoped $CsPbBr_3$ NCs. For the doped sample, the recovery dynamics is single-exponential with a time constant of >850 ps.

Table 1. PL Decay Parameters of Undoped and Doped $CsPbBr_3$ NCs

system	$\tau_1(a_1)$ (ns)[a]	$\tau_2(a_2)$ (ns)	$\tau_3(a_3)$ (ns)	$\langle\tau_{amp}\rangle$ (ns)[b]	k_r (ns^{-1})	k_{nr} (ns^{-1})
$CsPbBr_3$	2.91(0.28)	17.64(0.05)	0.64(0.67)	2.13	0.24	0.23
Mg-$CsPbBr_3$	4.32(0.70)	8.11(0.30)		5.46	0.18	0.0018

[a] a_i is the amplitude associated with ith lifetime component. [b] $\langle\tau_{amp}\rangle = \Sigma\tau_i a_i/\Sigma a_i$; k_r = PLQY/$\langle\tau_{amp}\rangle$; k_{nr} = (1 − PLQY)/$\langle\tau_{amp}\rangle$. PL decay parameters of undoped and doped $CsPbCl_3$ NCs are summarized in Table S1.

https://dx.doi.org/10.1021/acs.jpclett.9b03831
J. Phys. Chem. Lett. 2020, 11, 1178−1188

and doped systems and are characterized by a sharp negative (bleach) signal due to the ground-state depopulation of the NCs upon excitation by the pump pulse.[62,63]

Because the excitation wavelength (350 nm) corresponds to ~1.46E_g (where E_g corresponds to the band gap (~2.42 eV) of the undoped $CsPbBr_3$ NCs), photoexcitation of the NCs creates charge carriers much above the band-edge, which cool down to the band-edge excitonic state to initiate the bleach recovery process. The hot-carrier relaxation (hot-carrier cooling (HCC)) time estimated from the bleach formation dynamics in undoped NCs is 580 ± 21 fs, which is in good agreement with literature data.[62,63] The hot carriers, however, relax much faster (325 ± 16 fs) in doped system (Figure 5B) presumably due to the enhanced coupling of the conduction band states upon the introduction of the dopant states within the conduction band.[38,64,65] Because the conduction band is formed mainly by the Pb orbitals, the partial substitution of Pb with Mg is expected to change the distribution of energy levels in the conduction band. To validate that a faster HCC is due to the introduction of new energy levels within the conduction band upon doping, we have investigated the HCC dynamics of another undoped $CsPbBr_3$ NCs (λ_{ex} = 350 nm) with a comparable PLQY (92 ± 2%), synthesized following a reported three-precursor method.[21] A much slower HCC process (610 ± 20 fs) in these NCs (Figure S10) compared with the doped system (325 ± 16 fs) indeed proves the role of the higher density of the states in the conduction band of the doped NCs. A stronger electron−phonon coupling upon doping may also contribute to faster HCC dynamics, but we are not sure about this aspect. As far as bleach recovery is concerned (Figure 5C), the undoped $CsPbBr_3$ NCs exhibit a biexponential dynamics comprising one major ultrafast component (~47 ± 2.43 ps) due to carrier trapping and a much longer (>850 ps) recombination component.[38,62] However, estimation of the exact time constant for the longer component is not possible due to the time-window limitation of our experimental setup.[62] The presence of only a >850 ps component in the doped system indicates the effective elimination of the ultrafast nonradiative recombination routes for the carriers upon doping.

Further insight into carrier dynamics is obtained by examining the influence of temperature on the steady-state and time-resolved PL of the undoped and doped $CsPbBr_3$ NCs over a temperature window of 273−333 K. The PL intensity of undoped $CsPbBr_3$ NCs decreases by a factor of ~95 upon an increase in temperature from 273 to 333 K, but for the doped system, ~85% of its initial PL is retained even at 333 K (Figure 6A and Figure S11). This shows that carrier trapping, which is a thermally activated process and which decreases the PL of the undoped system at higher temperature, is almost eliminated upon doping. This conclusion is corroborated by the temperature dependence of the PL decay parameters (Table S2). With the increase in temperature, the contribution of the short trapping component increases from 45 to 68% (with a negligible change in the contribution of the longest time component) in the case of undoped $CsPbBr_3$ NCs, whereas the contribution of the longest time component, which represents the trapping−detrapping process, increases from 33 to 47% for the doped system. This increase in the contribution of the longest time component at higher temperature indicates the involvement of new energy states, which lie very close to the excitonic state and participate in the trapping−detrapping process, resulting in a prolonged PL

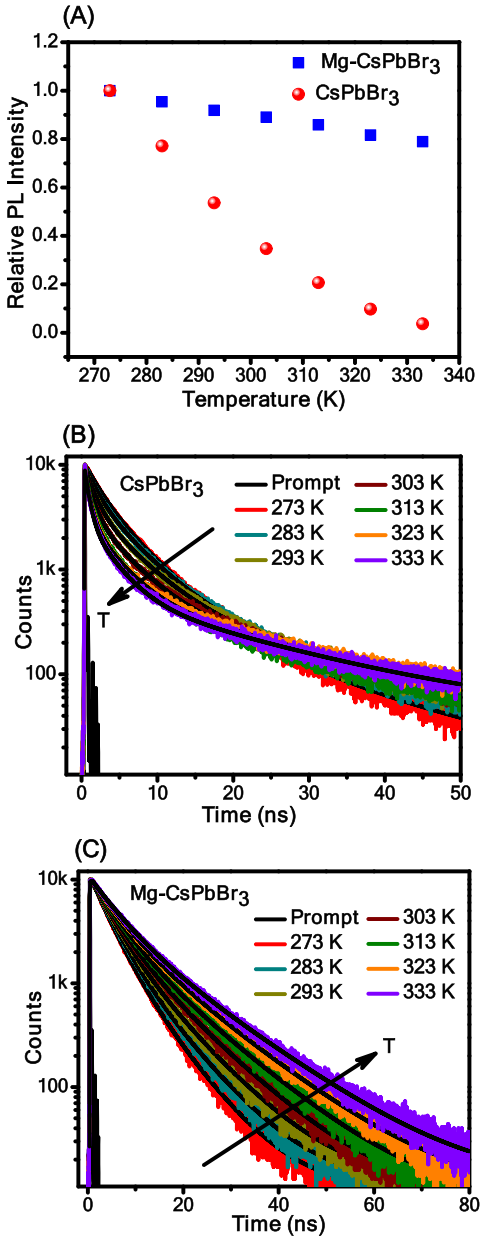

Figure 6. (A) Variation of the PL intensity of undoped and doped $CsPbBr_3$ NCs with temperature. (B,C) PL decay kinetics of the two samples over the same temperature window.

lifetime of the doped system (Figure S12).[61] Our ultrafast TA and these PL measurements show that the states, which facilitate the nonradiative deactivation of the carriers, are largely eliminated upon doping, but at the same time, doping can introduce new energy states that are distributed throughout the conduction band and a little below it (Scheme 2).

Halide-deficiency-associated point defects on the surface and distortion of the $[PbX_6]^{4-}$ octahedral units are the two main reasons for poor optical properties and low phase stability of the halide perovskite NCs.[37,66] The halide vacancies generate inter-band-gap trap states, which facilitate the nonradiative recombination of the photogenerated charge carriers, resulting in the poor PLQY of the NCs. The better optical properties and stability of the halide-rich NCs prove this point.[67] In the present case, the ratios of the atomic percentage Br/Pb and

https://dx.doi.org/10.1021/acs.jpclett.9b03831
J. Phys. Chem. Lett. 2020, 11, 1178−1188

Scheme 2. Schematic Illustration of Different Photophysical Processes in Undoped and Doped $CsPbBr_3$ NCs[a]

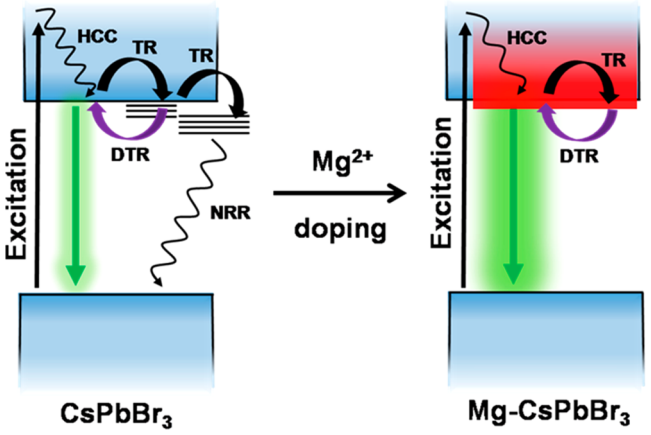

[a]VB, CB, HCC, TR, DTR, NRR, and TS are the acronyms for valence band, conduction band, hot carrier cooling, trapping, de-trapping, non-radiative recombination, and trap states. The red-shaded portion in the CB of the doped NCs indicates that Mg doping induced the introduction of energy states distributed throughout the CB and a little below it.

Br/(Pb + Mg) in undoped and doped $CsPbBr_3$ NCs (~2.98 and ~3.32, respectively, obtained from EDX study) indicate the effective removal of the halide-vacancy-related defects upon doping and the concomitant increase in the band-edge radiative excitonic recombination, as confirmed by the time-resolved PL decay (see Figure 4B) and TA studies (see Figure 5C). Apart from the halide vacancies, $[PbX_6]^{4-}$ octahedral distortion is also known to contribute to a poor PLQY and stability of the $CsPbX_3$ NCs.[43,66,68] Well-known octahedral distortion in $CsPbX_3$ NCs arises from the size-mismatch of the cuboctahedral void and the Cs^+ ion.[66] This distortion can be minimized either by replacing Cs^+ by a larger cation like formamidinium (FA^+)/methylammonium (MA^+) or by reducing the size of the octahedral unit by replacing the B-site Pb^{2+} with smaller cations.[28,66,68−70] Some very recent reports, however, suggest that the replacement of Pb^{2+} with smaller cations like Ni^{2+} (69 pm) and Cu^{2+} (73 pm) increases the defect formation energy of the resulting doped NC, endowing it with much improved optical properties and stability.[43,68,65,70] To determine the influence of Mg^{2+} alone on the PL properties of the NCs, when similar experiments were performed using MgO, a PLQY of ~87% was achieved (compared with 100% with $MgBr_2$) for $CsPbBr_3$ NCs, indicating that the doped NCs still suffered from halide vacancies, which is confirmed by the measured Br/(Pb + Mg) value of ~2.9 (Figure S13) in the doped sample. This was further proved by the PL decay behavior of the MgO-treated NCs. These NCs exhibited a short time component (0.86 ns, 42%), which could not be observed in $MgBr_2$-treated samples (Figure S14). However, in the case of $CsPbCl_3$ NCs, the

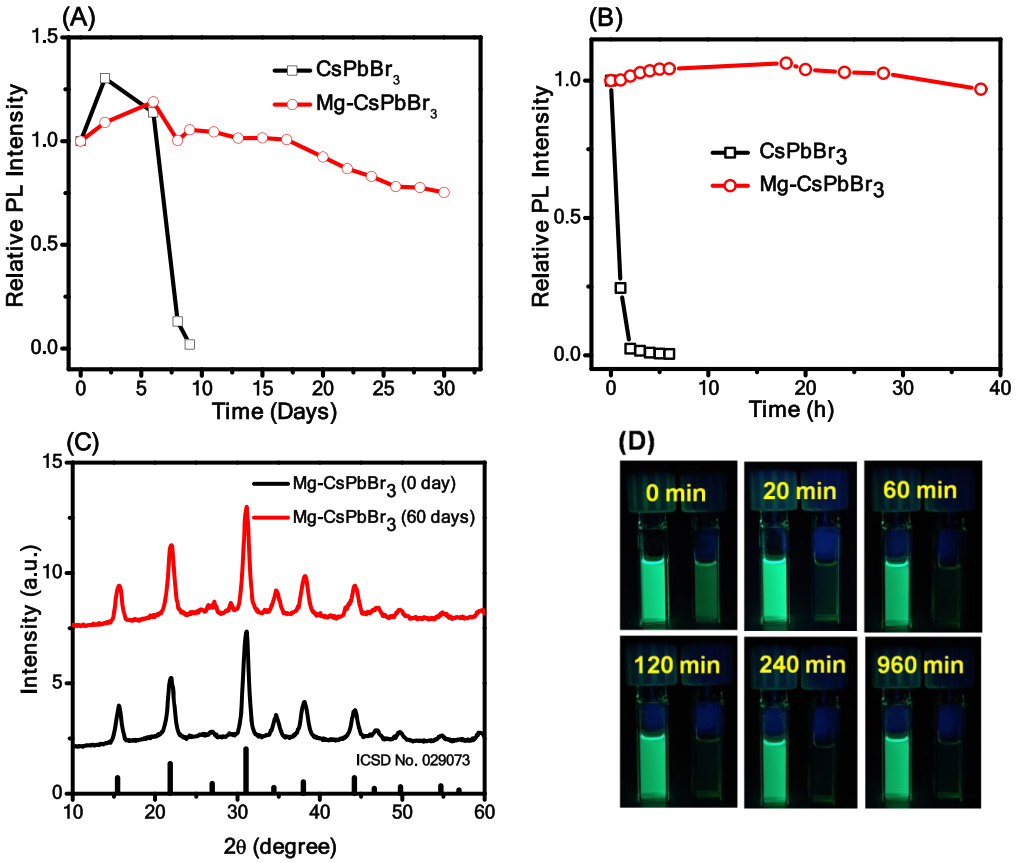

Figure 7. Comparison of the stability of undoped and doped $CsPbBr_3$ NCs. (A) Air stability under ambient conditions and (B) photostability under 365 nm (8 W) continuous UV illumination. (C) PXRD pattern of freshly prepared and 60 days aged samples kept under ambient conditions. (D) Digital images (under 365 nm UV illumination, 8 W) of the doped and undoped samples in the presence of 20 μL of ethanol at various time intervals.

https://dx.doi.org/10.1021/acs.jpclett.9b03831
J. Phys. Chem. Lett. 2020, 11, 1178−1188

PLQY was enhanced only up to ~28%, indicating the dominant role of the Cl^- vacancies in its low PLQY (Figure S12).[37] It is worth mentioning that addition of oleylamine solution alone enhances the PLQY of $CsPbBr_3$ NCs by only 8%, which is quite consistent with previous literature.[71] Thus it is evident that both Mg^{2+} and X^- play important roles in contributing to the superior optical properties of the Mg-doped $CsPbX_3$ NCs compared with their undoped cousins by rectification of the octahedral distortion and suppression of the halide-vacancy-related defects (Scheme 1B). An important point to note in this context is that B-cation doping is commonly executed under high-temperature reaction conditions because room-temperature exchange at the B site of perovskite NCs is considered to be quite challenging due to the high energy requirement to open up the rigid $[PbX_6]^{4-}$ octahedral units.[72] In our case, the room-temperature exchange is made possible, first by anchoring MgX_2 on the pre-existing halide vacancies of the NC surface and then by the elimination of the PbX_2 aided by OAm. This mechanism of the incorporation of Mg^{2+} into the crystal lattice is consistent with literature.[39,73]

Apart from reduced toxicity and high PLQY, these Mg-doped $CsPbX_3$ NCs are also characterized by remarkable stability, which is evident from Figure 7 (also Figure S15). As can be seen, under ambient conditions, the PL intensity of a freshly prepared Mg-doped $CsPbBr_3$ NCs remains unchanged for almost 20 days, and ~75% of its initial PL intensity is retained even after 2 months without any change in the band position or full width at half-maxima (fwhm) (Figure 7A, Figure S15). In contrast, under similar conditions, the PL of undoped NCs is quenched almost completely within 10 days. The doped NCs also exhibit excellent photostability. The initial PL intensity of doped $CsPbBr_3$ NCs remains unchanged for ~38 h (under 365 nm UV irradiation, 8 W), whereas for undoped NCs, the PL is lost almost completely in just 6 h (Figure 7B). The unchanged PXRD pattern recorded after storing the doped sample for 60 days under ambient conditions (Figure 7C) confirms the long-term stability of the sample. These measurements indicate the phenomenal air- and photostability of the doped NCs when compared with their undoped counterparts. The doped $CsPbBr_3$ NCs are also found to be significantly resistant toward polar solvents like ethanol, in which a bright emission can be observed for a long time (>960 min) without any change to the PL peak position or the fwhm (Figure 7D and Figures S16 and S17). In sharp contrast, the undoped NCs aggregate instantly in the presence of ethanol, and the PL intensity drops dramatically with a ~10 nm red shift of emission maxima (Figure S16). The enhanced stability of the doped NCs toward the polar solvent is most likely due to the protection provided by the long hydrocarbon chain of the surface-bound oleylammonium cations, which give a more hydrophobic nature to the doped NCs.[74] The $MgBr_2$ treatment provides a bromide-rich surface for the doped $CsPbBr_3$ NCs that attracts more oleylammonium cations.[75] A drop in the ratio of the Cs/Pb atomic percentage in the $CsPbBr_3$ NCs from ~0.81 to ~0.73 (as evident from the EDX data) upon doping confirms the replacement of some Cs ions from the surface by oleylammonium cations.[75−77] The presence of more oleylammonium ions at the surface is also evident from the FTIR spectra of the doped $CsPbBr_3$ NCs (Figure S8), as previously mentioned. Thus both an improved crystallinity and hydrophobicity play important roles in enhancing the stability of the doped NCs. The superior air- and photostability of the doped $CsPbCl_3$ NCs is evident from Figures S18 and S19. A table collecting the stability and optical properties of green- and violet-emitting perovskite NCs obtained through the B-site doping is provided as SI (Table S3). It highlights the air- and photostability and the robustness toward polar media of our doped NCs vis-à-vis the other samples.

It is shown that the room-temperature postsynthetic treatment of the $CsPbX_3$ (X = Cl and Br) NCs with MgX_2 leads to the incorporation of a significant quantity of Mg^{2+} into the NCs, yielding systems that are brightly luminescent, highly stable, less toxic, and more resistant to a polar environment. A model explaining the improved PL properties of the doped systems is proposed based on the findings of the ultrafast pump−probe and temperature-dependent PL measurements. The excellent optical properties, lower toxicity, and high stability of these NCs under different conditions make these systems promising for optoelectronic and photovoltaic applications.

■ ASSOCIATED CONTENT

Supporting Information

The Supporting Information is available free of charge at https://pubs.acs.org/doi/10.1021/acs.jpclett.9b03831.

Experimental section, TEM images and PXRD patterns of undoped and doped $CsPbCl_3$ NCs, EDX spectrum of undoped $CsPbBr_3$ and undoped and doped $CsPbCl_3$ NCs, elemental mapping of doped $CsPbCl_3$ NCs, FTIR and absorption spectra of undoped and doped $CsPbBr_3$/$CsPbCl_3$ NCs, EDX spectra of the NCs of control experiments, PL decay profile and HCC dynamics of $CsPbBr_3$ NCs, temperature-dependent PL spectra and average PL lifetime profiles, time-resolved PL decay of MgO-treated $CsPbBr_3$ NCs, PL spectra in air and under UV-light exposure, resistance plot of undoped and doped $CsPbBr_3$ NCs toward ethanol, stability comparison and PL decay parameters of undoped and doped $CsPbCl_3$ NCs, PL decay parameters of undoped and doped $CsPbBr_3$ NCs with the variation of temperature, and comparison of the stability and optical properties of green- and violet-emitting perovskite NCs (PDF)

■ AUTHOR INFORMATION

Corresponding Author

Anunay Samanta − *School of Chemistry, University of Hyderabad, Hyderabad 500046, India;* orcid.org/0000-0003-1551-0209; Email: anunay@uohyd.ac.in

Authors

Somnath Das − *School of Chemistry, University of Hyderabad, Hyderabad 500046, India*

Apurba De − *School of Chemistry, University of Hyderabad, Hyderabad 500046, India;* orcid.org/0000-0002-3042-0642

Complete contact information is available at: https://pubs.acs.org/10.1021/acs.jpclett.9b03831

Notes

The authors declare no competing financial interest.

https://dx.doi.org/10.1021/acs.jpclett.9b03831
J. Phys. Chem. Lett. 2020, 11, 1178−1188

■ ACKNOWLEDGMENTS

This work is supported by the J. C. Bose Fellowship (to A.S.) of the Science and Engineering Research Board (SERB), Department of Science and Technology (DST), India. We acknowledge the TEM facility of the Centre for Nanotechnology, University of Hyderabad and the femtosecond pump−probe facility of the School. The XPS measurements have been carried out at the National Chemical Laboratory, Pune. S.D. and A.D. thank the University Grants Commission (UGC) for fellowships.

■ REFERENCES

(1) Kojima, A.; Teshima, K.; Shirai, Y.; Miyasaka, T. Organometal Halide Perovskites as Visible-Light Sensitizers for Photovoltaic Cells. *J. Am. Chem. Soc.* **2009**, *131*, 6050−6051.
(2) Lee, M. M.; Teuscher, J.; Miyasaka, T.; Murakami, T. N.; Snaith, H. J. Efficient Hybrid Solar Cells Based on Meso-Superstructured Organometal Halide Perovskites. *Science* **2012**, *338*, 643−647.
(3) Jeon, N. J.; Na, H.; Jung, E. H.; Yang, T.-Y.; Lee, Y. G.; Kim, G.; Shin, H.-W.; Il Seok, S.; Lee, J.; Seo, J. A fluorene-terminated hole-transporting material for highly efficient and stable perovskite solar cells. *Nature Energy* **2018**, *3*, 682−689.
(4) Yang, W. S.; Park, B.-W.; Jung, E. H.; Jeon, N. J.; Kim, Y. C.; Lee, D. U.; Shin, S. S.; Seo, J.; Kim, E. K.; Noh, J. H.; Seok, S. I. Iodide management in formamidinium-lead-halide−based perovskite layers for efficient solar cells. *Science* **2017**, *356*, 1376−1379.
(5) Stranks, S. D.; Snaith, H. J. Metal-halide perovskites for photovoltaic and light-emitting devices. *Nat. Nanotechnol.* **2015**, *10*, 391−402.
(6) Du, X.; Wu, G.; Cheng, J.; Dang, H.; Ma, K.; Zhang, Y.-W.; Tan, P.-F.; Chen, S. High-quality $CsPbBr_3$ perovskite nanocrystals for quantum dot light-emitting diodes. *RSC Adv.* **2017**, *7*, 10391−10396.
(7) Wang, Y.; Li, X.; Song, J.; Xiao, L.; Zeng, H.; Sun, H. All Inorganic Colloidal Perovskite Quantum Dots: A New Class of Lasing Materials with Favorable Characteristics. *Adv. Mater.* **2015**, *27*, 7101−7108.
(8) Deschler, F.; Price, M.; Pathak, S.; Klintberg, L. E.; Jarausch, D.-D.; Higler, R.; Hüttner, S.; Leijtens, T.; Stranks, S. D.; Snaith, H. J.; Atatüre, M.; Phillips, R. T.; Friend, R. H. High Photoluminescence Efficiency and Optically Pumped Lasing in Solution-Processed Mixed Halide Perovskite Semiconductors. *J. Phys. Chem. Lett.* **2014**, *5*, 1421−1426.
(9) Yakunin, S.; Dirin, D. N.; Shynkarenko, Y.; Morad, V.; Cherniukh, I.; Nazarenko, O.; Kreil, D.; Nauser, T.; Kovalenko, M. V. Detection of gamma photons using solution-grown single crystals of hybrid lead halide perovskites. *Nat. Photonics* **2016**, *10*, 585−589.
(10) Ramasamy, P.; Lim, D.-H.; Kim, B.; Lee, S.-H.; Lee, M.-S.; Lee, J.-S. All-inorganic cesium lead halide perovskite nanocrystals for photodetector applications. *Chem. Commun.* **2016**, *52*, 2067−2070.
(11) Caligiuri, V.; Palei, M.; Imran, M.; Manna, L.; Krahne, R. Planar Double-Epsilon-Near-Zero Cavities for Spontaneous Emission and Purcell Effect Enhancement. *ACS Photonics* **2018**, *5*, 2287−2294.
(12) Zhang, R.; Fan, J.; Zhang, X.; Yu, H.; Zhang, H.; Mai, Y.; Xu, T.; Wang, J.; Snaith, H. J. Nonlinear Optical Response of Organic−Inorganic Halide Perovskites. *ACS Photonics* **2016**, *3*, 371−377.
(13) Protesescu, L.; Yakunin, S.; Bodnarchuk, M. I.; Krieg, F.; Caputo, R.; Hendon, C. H.; Yang, R. X.; Walsh, A.; Kovalenko, M. V. Nanocrystals of Cesium Lead Halide Perovskites ($CsPbX_3$, X = Cl, Br, and I): Novel Optoelectronic Materials Showing Bright Emission with Wide Color Gamut. *Nano Lett.* **2015**, *15*, 3692−3696.
(14) Koscher, B. A.; Swabeck, O. K.; Bronstein, O. D.; Alivisatos, A. P. Essentially Trap-Free CsPbBr3 Colloidal Nanocrystals by Postsynthetic Thiocyanate Surface Treatment. *J. Am. Chem. Soc.* **2017**, *139*, 6566−6569.
(15) Pan, J.; Shang, Y.; Yin, J.; De Bastiani, M.; Peng, W.; Dursun, I.; Sinatra, L.; El-Zohry, A. M.; Hedhili, M. N.; Emwas, A.-H.; Mohammed, O. F.; Ning, Z.; Bakr, O. M. Bidentate Ligand-Passivated $CsPbI_3$ Perovskite Nanocrystals for Stable Near-Unity Photoluminescence Quantum Yield and Efficient Red Light-Emitting Diodes. *J. Am. Chem. Soc.* **2018**, *140*, 562−565.
(16) Yin, W.-J.; Shi, T.; Yan, Y. Unique Properties of Halide Perovskites as Possible Origins of the Superior Solar Cell Performance. *Adv. Mater.* **2014**, *26*, 4653−4658.
(17) Kovalenko, M. V.; Protesescu, L.; Bodnarchuk, M. I. Properties and potential optoelectronic applications of lead halide perovskite nanocrystals. *Science* **2017**, *358*, 745−750.
(18) Nedelcu, G.; Protesescu, L.; Yakunin, S.; Bodnarchuk, M. I.; Grotevent, M. J.; Kovalenko, M. V. Fast Anion-Exchange in Highly Luminescent Nanocrystals of Cesium Lead Halide Perovskites ($CsPbX_3$, X = Cl, Br, I). *Nano Lett.* **2015**, *15*, 5635−5640.
(19) Akkerman, Q. A.; D'Innocenzo, V.; Accornero, S.; Scarpellini, A.; Petrozza, A.; Prato, M.; Manna, L. Tuning the Optical Properties of Cesium Lead Halide Perovskite Nanocrystals by Anion Exchange Reactions. *J. Am. Chem. Soc.* **2015**, *137*, 10276−10281.
(20) Zhang, F.; Zhong, H.; Chen, C.; Wu, X.-g.; Hu, X.; Huang, H.; Han, J.; Zou, B.; Dong, Y. Brightly Luminescent and Color-Tunable Colloidal $CH_3NH_3PbX_3$ (X = Br, I, Cl) Quantum Dots: Potential Alternatives for Display Technology. *ACS Nano* **2015**, *9*, 4533−4542.
(21) Imran, M.; Caligiuri, V.; Wang, M.; Goldoni, L.; Prato, M.; Krahne, R.; De Trizio, L.; Manna, L. Benzoyl Halides as Alternative Precursors for the Colloidal Synthesis of Lead-Based Halide Perovskite Nanocrystals. *J. Am. Chem. Soc.* **2018**, *140*, 2656−2664.
(22) Dutta, A.; Behera, R. K.; Pal, P.; Baitalik, P. D. S.; Pradhan, D. N. Near-Unity Photoluminescence Quantum Efficiency for All $CsPbX_3$ (X = Cl, Br, and I) Perovskite Nanocrystals: A Generic Synthesis Approach. *Angew. Chem., Int. Ed.* **2019**, *58*, 5552−5556.
(23) Akkerman, Q. A.; Rainò, G.; Kovalenko, M. V.; Manna, L. Genesis, challenges and opportunities for colloidal lead halide perovskite nanocrystals. *Nat. Mater.* **2018**, *17*, 394−405.
(24) Seth, S.; Ahmed, T.; De, A.; Samanta, A. Tackling the Defects, Stability, and Photoluminescence of $CsPbX_3$ Perovskite Nanocrystals. *ACS Energy Lett.* **2019**, *4*, 1610−1618.
(25) Tachikawa, T.; Karimata, I.; Kobori, Y. Surface Charge Trapping in Organolead Halide Perovskites Explored by Single-Particle Photoluminescence Imaging. *J. Phys. Chem. Lett.* **2015**, *6*, 3195−3201.
(26) Seth, S.; Mondal, N.; Patra, S.; Samanta, A. Fluorescence Blinking and Photoactivation of All-Inorganic Perovskite Nanocrystals $CsPbBr_3$ and $CsPbBr_2I$. *J. Phys. Chem. Lett.* **2016**, *7*, 266−271.
(27) Chen, J.-K.; Ma, J.-P.; Guo, S.-Q.; Chen, Y.-M.; Zhao, Q.; Zhang, B.-B.; Li, Z.-Y.; Zhou, Y.; Hou, J.; Kuroiwa, Y.; Moriyoshi, C.; Bakr, O. M.; Zhang, J.; Sun, o.-T. High-Efficiency Violet-Emitting All-Inorganic Perovskite Nanocrystals Enabled by Alkaline-Earth Metal Passivation. *Chem. Mater.* **2019**, *31*, 3974−3983.
(28) Mondal, N.; De, A.; Samanta, A. Achieving Near-Unity Photoluminescence Efficiency for Blue-Violet-Emitting Perovskite Nanocrystals. *ACS Energy Lett.* **2019**, *4*, 32−39.
(29) Ahmed, T.; Seth, S.; Samanta, A. Boosting the Photoluminescence of $CsPbX_3$ (X = Cl, Br, I) Perovskite Nanocrystals Covering a Wide Wavelength Range by Postsynthetic Treatment with Tetrafluoroborate Salts. *Chem. Mater.* **2018**, *30*, 3633−3637.
(30) Ahmed, G. H.; El-Demellawi, J. K.; Yin, J.; Pan, J.; Velusamy, D. B.; Hedhili, M. N.; Alarousu, E.; Bakr, O. M.; Alshareef, H. N.; Mohammed, O. F. Giant Photoluminescence Enhancement in $CsPbCl_3$ Perovskite Nanocrystals by Simultaneous Dual-Surface Passivation. *ACS Energy Lett.* **2018**, *3*, 2301−2307.
(31) De, A.; Das, S.; Mondal, N.; Samanta, A. Highly Luminescent Violet- and Blue-Emitting Stable Perovskite Nanocrystals. *ACS Materials Lett.* **2019**, *1*, 116−122.
(32) Ma, J.-P.; Chen, Y.-M.; Zhang, L.-M.; Guo, S.-Q.; Liu, J.-D.; Li, H.; Ye, B.-J.; Li, Z.-Y.; Zhou, Y.; Zhang, B.-B.; Bakr, O. M.; Zhang, J.-Y.; Sun, H.-T. Insights into the local structure of dopants, doping efficiency, and luminescence properties of lanthanide-doped $CsPbCl_3$ perovskite nanocrystals. *J. Mater. Chem. C* **2019**, *7*, 3037−3048.
(33) Ma, J.-P.; Yin, J.; Chen, Y.-M.; Zhao, Q.; Zhou, Y.; Li, H.; Kuroiwa, Y.; Moriyoshi, C.; Li, Z.-Y.; Bakr, O. M.; Mohammed, O. F.;

https://dx.doi.org/10.1021/acs.jpclett.9b03831
J. Phys. Chem. Lett. 2020, 11, 1178−1188

Sun, H.-T. Defect-Triggered Phase Transition in Cesium Lead Halide Perovskite Nanocrystals. *ACS Materials Lett.* **2019**, *1*, 185−191.
(34) Mandal, S.; Roy, D.; De, C. K.; Ghosh, S.; Mandal, M.; Das, A.; Mandal, P. K. Instantaneous, room-temperature, open-air atmosphere, solution-phase synthesis of perovskite quantum dots through halide exchange employing non-metal based inexpensive HCl/HI: ensemble and single particle spectroscopy. *Nanoscale Adv.* **2019**, *1*, 3506−3513.
(35) Dutta, A.; Behera, R. K.; Dutta, S. K.; Das Adhikari, S.; Pradhan, N. Annealing $CsPbX_3$ (X = Cl and Br) Perovskite Nanocrystals at High Reaction Temperatures: Phase Change and Its Prevention. *J. Phys. Chem. Lett.* **2018**, *9*, 6599−6604.
(36) Zheng, X.; Hou, Y.; Sun, H.-T.; Mohammed, O. F.; Sargent, E. H.; Bakr, O. M. Reducing Defects in Halide Perovskite Nanocrystals for Light-Emitting Applications. *J. Phys. Chem. Lett.* **2019**, *10*, 2629−2640.
(37) Nenon, D. P.; Pressler, K.; Kang, J.; Koscher, B. A.; Olshansky, J. H.; Osowiecki, W. T.; Koc, M. A.; Wang, L.-W.; Alivisatos, A. P. Design Principles for Trap-Free $CsPbX_3$ Nanocrystals: Enumerating and Eliminating Surface Halide Vacancies with Softer Lewis Bases. *J. Am. Chem. Soc.* **2018**, *140*, 17760−17772.
(38) Yao, J.-S.; Ge, J.; Han, B.-N.; Wang, K.-H.; Yao, H.-B.; Yu, H.-L.; Li, J.-H.; Zhu, B.-S.; Song, J.-Z.; Chen, C.; Zhang, Q.; Zeng, H.-B.; Luo, Y.; Yu, S.-H. Ce^{3+}-Doping to Modulate Photoluminescence Kinetics for Efficient $CsPbBr_3$ Nanocrystals Based Light-Emitting Diodes. *J. Am. Chem. Soc.* **2018**, *140*, 3626−3634.
(39) van der Stam, W.; Geuchies, J. J.; Altantzis, T.; van den Bos, K. H. W.; Meeldijk, J. D.; Van Aert, S.; Bals, S.; Vanmaekelbergh, D.; de Mello Donega, C. Highly Emissive Divalent-Ion-Doped Colloidal $CsPb_{1-x}M_xBr_3$ Perovskite Nanocrystals through Cation Exchange. *J. Am. Chem. Soc.* **2017**, *139*, 4087−4097.
(40) Vitoreti, A. B. F.; Agouram, S.; Solis de la Fuente, M.; Muñoz-Sanjosé, V.; Schiavon, M. A.; Mora-Seró. Study of the Partial Substitution of Pb by Sn in Cs−Pb−Sn−Br Nanocrystals Owing to Obtaining Stable Nanoparticles with Excellent Optical Properties. *J. Phys. Chem. C* **2018**, *122*, 14222−14231.
(41) Li, S.; Shi, Z.; Zhang, F.; Wang, L.; Ma, Z.; Yang, D.; Yao, Z.; Wu, D.; Xu, T.-T.; Tian, Y.; Zhang, Y.; Shan, C.; Li, X. J. Sodium Doping-Enhanced Emission Efficiency and Stability of $CsPbBr_3$ Nanocrystals for White Light-Emitting Devices. *Chem. Mater.* **2019**, *31*, 3917−3928.
(42) Woo, J. Y.; Kim, Y.; Bae, J.; Kim, T. G.; Kim, J. W.; Lee, D. C.; Jeong, S. Highly Stable Cesium Lead Halide Perovskite Nanocrystals through in Situ Lead Halide Inorganic Passivation. *Chem. Mater.* **2017**, *29*, 7088−7092.
(43) Yong, Z.-J.; Guo, S.-Q.; Ma, J.-P.; Zhang, J.-Y.; Li, Z.-Y.; Chen, Y.-M.; Zhang, B.-B.; Zhou, Y.; Shu, J.; Gu, J.-L.; Zheng, L.-R.; Bakr, O. M.; Sun, H.-T. Doping-Enhanced Short-Range Order of Perovskite Nanocrystals for Near-Unity Violet Luminescence Quantum Yield. *J. Am. Chem. Soc.* **2018**, *140*, 9942−9951.
(44) Zhai, Y.; Bai, X.; Pan, G.; Zhu, J.; Shao, H.; Dong, B.; Xu, L.; Song, H. Effective blue-violet photoluminescence through lanthanum and fluorine ions co-doping for $CsPbCl_3$ perovskite quantum dots. *Nanoscale* **2019**, *11*, 2484−2491.
(45) Behera, R. K.; Das Adhikari, S. D.; Dutta, S. K.; Dutta, A.; Pradhan, N. Blue-Emitting $CsPbCl_3$ Nanocrystals: Impact of Surface Passivation for Unprecedented Enhancement and Loss of Optical Emission. *J. Phys. Chem. Lett.* **2018**, *9*, 6884−6891.
(46) Das Adhikari, S.; Behera, R. K.; Bera, S.; Pradhan, N. Presence of Metal Chloride for Minimizing the Halide Deficiency and Maximizing the Doping Efficiency in Mn(II)-Doped $CsPbCl_3$ Nanocrystals. *J. Phys. Chem. Lett.* **2019**, *10*, 1530−1536.
(47) Rahimzadeh, M. R.; Rahimzadeh, M. R.; Kazemi, S.; Moghadamnia, A.-a. Cadmium toxicity and treatment: An update. *Caspian J. Intern Med.* **2017**, *8*, 135−145.
(48) Bock, C. W.; Kaufman, A.; Glusker, J. P. Coordination of Water to Magnesium Cations. *Inorg. Chem.* **1994**, *33*, 419−427.
(49) Lide, D. R. *CRC Handbook of Chemistry and Physics*, 87th ed.; CRC Press: Boca Raton, FL, 2007.
(50) Filip, M. R.; Giustino, F. Computational Screening of Homovalent Lead Substitution in Organic−Inorganic Halide Perovskites. *J. Phys. Chem. C* **2016**, *120*, 166−173.
(51) Huang, Q.; Zou, Y.; Bourelle, S. A.; Zhai, T.; Wu, T.; Tan, Y.; Li, Y.; Li, J.; Duhm, S.; Song, T.; Wang, L.; Deschler, F.; Sun, B. Suppressing defect states in $CsPbBr_3$ perovskite via magnesium substitution for efficient all-inorganic light-emitting diodes. *Nanoscale Horiz.* **2019**, *4*, 924−932.
(52) Shannon, R. D. Revised effective ionic radii and systematic studies of interatomic distances in halides and chalcogenides. *Acta Crystallogr., Sect. A: Cryst. Phys., Diffr., Theor. Gen. Crystallogr.* **1976**, *32*, 751−767.
(53) Liu, M.; Zhong, G.; Yin, Y.; Miao, J.; Li, K.; Wang, C.; Xu, X.; Shen, C.; Meng, H. Aluminum-Doped Cesium Lead Bromide Perovskite Nanocrystals with Stable Blue Photoluminescence Used for Display Backlight. *Adv. Sci.* **2017**, *4*, 1700335.
(54) Koscher, B. A.; Nett, Z.; Alivisatos, A. P. The Underlying Chemical Mechanism of Selective Chemical Etching in $CsPbBr_3$ Nanocrystals for Reliably Accessing Near-Unity Emitters. *ACS Nano* **2019**, *13*, 11825−11833.
(55) Liu, W.; Lin, Q.; Li, H.; Wu, K.; Robel, I.; Pietryga, J. M.; Klimov, V. I. Mn^{2+}-Doped Lead Halide Perovskite Nanocrystals with Dual-Color Emission Controlled by Halide Content. *J. Am. Chem. Soc.* **2016**, *138*, 14954−14961.
(56) De, A.; Mondal, N.; Samanta, A. Luminescence tuning and exciton dynamics of Mn-doped $CsPbCl_3$ nanocrystals. *Nanoscale* **2017**, *9*, 16722−16727.
(57) Eaton, S. W.; Lai, M.; Gibson, N. A.; Wong, A. B.; Dou, L.; Ma, J.; Wang, L.-W.; Leone, S. R.; Yang, P. Lasing in robust cesium lead halide perovskite nanowires. *Proc. Natl. Acad. Sci. U. S. A.* **2016**, *113*, 1993−1998.
(58) Zhang, M.; Zheng, Z.; Fu, Q.; Chen, Z.; He, J.; Zhang, S.; Yan, L.; Hu, Y.; Luo, W. Growth and characterization of all-inorganic lead halide perovskite semiconductor $CsPbBr_3$ single crystals. *CrystEngComm* **2017**, *19*, 6797−6803.
(59) Endres, J.; Kulbak, M.; Zhao, L.; Rand, B. P.; Cahen, D.; Hodes, G.; Kahn, A. Electronic structure of the $CsPbBr_3$/polytriarylamine (PTAA) system. *J. Appl. Phys.* **2017**, *121*, No. 035304.
(60) Yamada, Y.; Miura, M.; Tajima, K.; Okada, M.; Yoshimura, K. Pd distribution of switchable mirrors based on Mg−Y alloy thin films. *Sol. Energy Mater. Sol. Cells* **2014**, *120*, 631−634.
(61) Chirvony, V. S.; González-Carrero, S.; Suárez, I.; Galian, R. E.; Sessolo, M.; Bolink, H. J.; Martínez-Pastor, J. P.; Pérez-Prieto, J. Delayed Luminescence in Lead Halide Perovskite Nanocrystals. *J. Phys. Chem. C* **2017**, *121*, 13381−13390.
(62) Mondal, N.; Samanta, A. Complete ultrafast charge carrier dynamics in photo-excited all-inorganic perovskite nanocrystals ($CsPbX_3$). *Nanoscale* **2017**, *9*, 1878−1885.
(63) Mondal, N.; De, A.; Das, S.; Paul, S.; Samanta, A. Ultrafast carrier dynamics of metal halide perovskite nanocrystals and perovskite-composites. *Nanoscale* **2019**, *11*, 9796−9818.
(64) Begum, R.; Parida, M. R.; Abdelhady, A. L.; Murali, B.; Alyami, O. M.; Ahmed, G. H.; Hedhili, M. N.; Bakr, O. M.; Mohammed, O. F. Engineering Interfacial Charge Transfer in $CsPbBr_3$ Perovskite Nanocrystals by Heterovalent Doping. *J. Am. Chem. Soc.* **2017**, *139*, 731−737.
(65) Yao, J.-S.; Ge, J.; Wang, K.-H.; Zhang, G.; Zhu, B.-S.; Chen, C.; Zhang, Q.; Luo, Y.; Yu, S.-H.; Yao, H.-B. Few-Nanometer-Sized α-$CsPbI_3$ Quantum Dots Enabled by Strontium Substitution and Iodide Passivation for Efficient Red-Light Emitting Diodes. *J. Am. Chem. Soc.* **2019**, *141*, 2069−2079.
(66) Swarnkar, A.; Mir, W. J.; Nag, O. Can B-Site Doping or Alloying Improve Thermal- and Phase-Stability of All-Inorganic $CsPbX_3$ (X = Cl, Br, I) Perovskites? *ACS Energy Lett.* **2018**, *3*, 286−289.
(67) Liu, P.; Chen, W.; Wang, W.; Xu, B.; Wu, D.; Hao, J.; Cao, W.; Fang, F.; Li, Y.; Zeng, Y.; Pan, R.; Chen, S.; Cao, W.; Sun, X. W.; Wang, K. Halide-Rich Synthesized Cesium Lead Bromide Perovskite

https://dx.doi.org/10.1021/acs.jpclett.9b03831
J. Phys. Chem. Lett. 2020, 11, 1178−1188

Nanocrystals for Light-Emitting Diodes with Improved Performance. *Chem. Mater.* **2017**, *29*, 5168−5173.
(68) Bi, C.; Wang, S.; Li, Q.; Kershaw, S. V.; Tian, J.; Rogach, A. L. Thermally Stable Copper(II)-Doped Cesium Lead Halide Perovskite Quantum Dots with Strong Blue Emission. *J. Phys. Chem. Lett.* **2019**, *10*, 943−952.
(69) Protesescu, L.; Yakunin, S.; Kumar, S.; Bär, J.; Bertolotti, F.; Masciocchi, N.; Guagliardi, A.; Grotevent, M.; Shorubalko, I.; Bodnarchuk, M. I.; Shih, C.-J.; Kovalenko, M. V. Dismantling the "Red Wall" of Colloidal Perovskites: Highly Luminescent Formamidinium and Formamidinium−Cesium Lead Iodide Nanocrystals. *ACS Nano* **2017**, *11*, 3119−3134.
(70) Shamsi, J.; Urban, A. S.; Imran, M.; De Trizio, L.; Manna, L. Metal Halide Perovskite Nanocrystals: Synthesis, Post-Synthesis Modifications, and Their Optical Properties. *Chem. Rev.* **2019**, *119*, 3296−3348.
(71) Li, F.; Liu, Y.; Wang, H.; Zhan, Q.; Liu, Q.; Xia, Z. Postsynthetic Surface Trap Removal of $CsPbX_3$ (X = Cl, Br, or I) Quantum Dots via a ZnX2/Hexane Solution toward an Enhanced Luminescence Quantum Yield. *Chem. Mater.* **2018**, *30*, 8546−8554.
(72) Huang, G.; Wang, C.; Xu, S.; Zong, S.; Lu, J.; Wang, Z.; Lu, C.; Cui, Y. Postsynthetic Doping of $MnCl_2$ Molecules into Preformed CsPbBr3 Perovskite Nanocrystals via a Halide Exchange-Driven Cation Exchange. *Adv. Mater.* **2017**, *29*, 1700095.
(73) Yang, Z.; Wei, M.; Voznyy, O.; Todorovic, P.; Liu, M.; Quintero-Bermudez, R.; Chen, P.; Fan, J. Z.; Proppe, A. H.; Quan, L. N.; Walters, G.; Tan, H.; Chang, J.-W.; Jeng, U.-S.; Kelley, S. O.; Sargent, E. H. Anchored Ligands Facilitate Efficient B-Site Doping in Metal Halide Perovskites. *J. Am. Chem. Soc.* **2019**, *141*, 8296−8305.
(74) Zhong, Q.; Cao, M.; Xu, Y.; Li, P.; Zhang, Y.; Hu, H.; Yang, D.; Xu, Y.; Wang, L.; Li, Y.; Zhang, X.; Zhang, Q. L-Type Ligand-Assisted Acid-Free Synthesis of $CsPbBr_3$ Nanocrystals with Near-Unity Photoluminescence Quantum Yield and High Stability. *Nano Lett.* **2019**, *19*, 4151−4157.
(75) Cai, Y.; Wang, H.; Li, Y.; Wang, L.; Lv, Y.; Yang, X.; Xie, R.-J. Trimethylsilyl Iodine-Mediated Synthesis of Highly Bright Red-Emitting $CsPbI_3$ Perovskite Quantum Dots with Significantly Improved Stability. *Chem. Mater.* **2019**, *31*, 881−889.
(76) Ravi, V. K.; Santra, P. K.; Joshi, N.; Chugh, J.; Singh, S. K.; Rensmo, H.; Ghosh, P.; Nag, A. Origin of the Substitution Mechanism for the Binding of Organic Ligands on the Surface of $CsPbBr_3$ Perovskite Nanocubes. *J. Phys. Chem. Lett.* **2017**, *8*, 4988−4994.
(77) Paul, S.; Samanta, A. N-Bromosuccinimide as Bromide Precursor for Direct Synthesis of Stable and Highly Luminescent Green-Emitting Perovskite Nanocrystals. *ACS Energy Lett.* **2020**, *5*, 64−69.

https://dx.doi.org/10.1021/acs.jpclett.9b03831
J. Phys. Chem. Lett. 2020, 11, 1178−1188

ACS Energy LETTERS

http://pubs.acs.org/journal/aelccp

Highly Luminescent and Phase-Stable Red/NIR-Emitting All-Inorganic and Hybrid Perovskite Nanocrystals

Somnath Das and Anunay Samanta*

Cite This: ACS Energy Lett. 2021, 6, 3780−3787

Read Online

ACCESS | Metrics & More | Article Recommendations | Supporting Information

ABSTRACT: Because of their low band gap, iodide-based lead halide perovskite nanocrystals (NCs) with generic formula $APbI_3$ [A = Cs^+, methylammonium (MA^+), and formamidinium (FA^+)] are most suitable for solar photovoltaic applications. However, because of their poor phase stability, obtaining these NCs with stable red/NIR emission is a challenging task and is termed the "red wall". We report here a generic protocol for direct synthesis of all three NCs with extraordinary characteristics employing 1,3-diiodo-5,5-dimethylhydantoin (DIDMH) as iodide precursor. The as-synthesized NCs are phase-pure and monodispersed, and they exhibit phase stability for several months in ambient conditions and photoluminescence quantum yield (PLQY) of near-unity for the red-emitting $CsPbI_3$ NCs and ∼74 ± 2% and 67 ± 2% for NIR-emitting $(MA)PbI_3$ and $(FA)PbI_3$ NCs, respectively. The results highlight the greater efficacy of DIDMH over other iodide precursors, with which the present task could not be achieved earlier. The high-quality NCs for the red−NIR region may be useful for developing efficient perovskite-based solar photovoltaic devices.

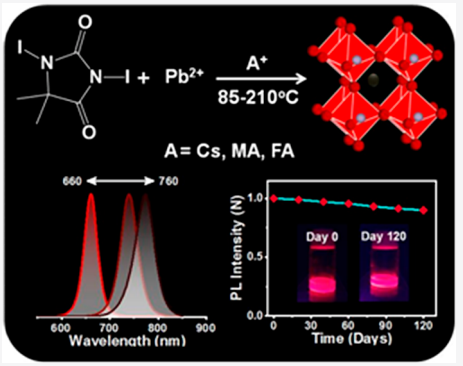

Among lead-halide perovskite nanocrystals (NCs), iodide-based $CsPbI_3$, $(MA)PbI_3$, and $(FA)PbI_3$ are most suitable for single-junction solar cells because of their narrow band gap.[1−10] However, unlike the widely explored bromide-based green-emitting $APbBr_3$ NCs, the poor phase stability of these iodide-based NCs leads to their rapid deterioration even under ambient conditions and prevents the practical utility of these otherwise promising substances.[6,11−17] The challenging task of obtaining small-sized and iodide-based perovskites emitting in the red and NIR region with high photoluminescence efficiency and stability, termed the "perovskite red wall",[18] needs to be accomplished for these substances to achieve their potential.

The stability and optical properties of the NCs depend to a great extent on their method of preparation.[5,19−23] The widely used two-precursor method of synthesis, in which PbI_2 is used as a source of both lead and iodine, produces NCs of poor quality.[5] For example, $(MA)PbI_3$ and $(FA)PbI_3$ NCs obtained by this method exhibit a broad size distribution and low photoluminescence quantum yield (PLQY),[24−26] and even $CsPbI_3$ NCs show a PLQY of only ∼30−70%.[11,17] The three-precursor method, which was developed later, employs a separate halide precursor for synthesis in a halide-rich condition and produces much better quality NCs.[27,28] However, despite great recent efforts to overcome the perovskite red wall, the success is rather limited and no generic method of preparation of all three NCs with high phase stability and PLQY is available to date.[8,18,29−31] For example, Kovalenko and co-workers prepared high-quality $FAPbI_3$ and mixed-cation $FA_{0.1}Cs_{0.9}PbI_3$ NCs with PLQY of ∼70% that retained its phase for several months.[18] Akkerman et al. succeeded in obtaining highly luminescent (PLQY ≈ 74−79%) $CsPbI_3$ and $FAPbI_3$ NCs, which were stable for at least 2 weeks.[29] Similarly, stable $CsPbI_3$ NCs with near-unity PLQY were also prepared by Pradhan and co-workers and later by Cai et al.[8,30,31] Interestingly, in none of these reports could all three red- and NIR-emitting $APbI_3$ NCs be obtained following a generic method. To the best of our knowledge, it was only Manna and co-workers who could obtain all three iodide-based NCs using benzoyl iodide as iodide precursor with a PLQY of 58% for $CsPbI_3$, 45% for $(MA)PbI_3$, and 55% for $(FA)PbI_3$ NCs.[32] While these $CsPbI_3$ NCs were reported to be stable for

Received: September 10, 2021
Accepted: October 4, 2021
Published: October 6, 2021

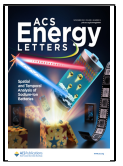

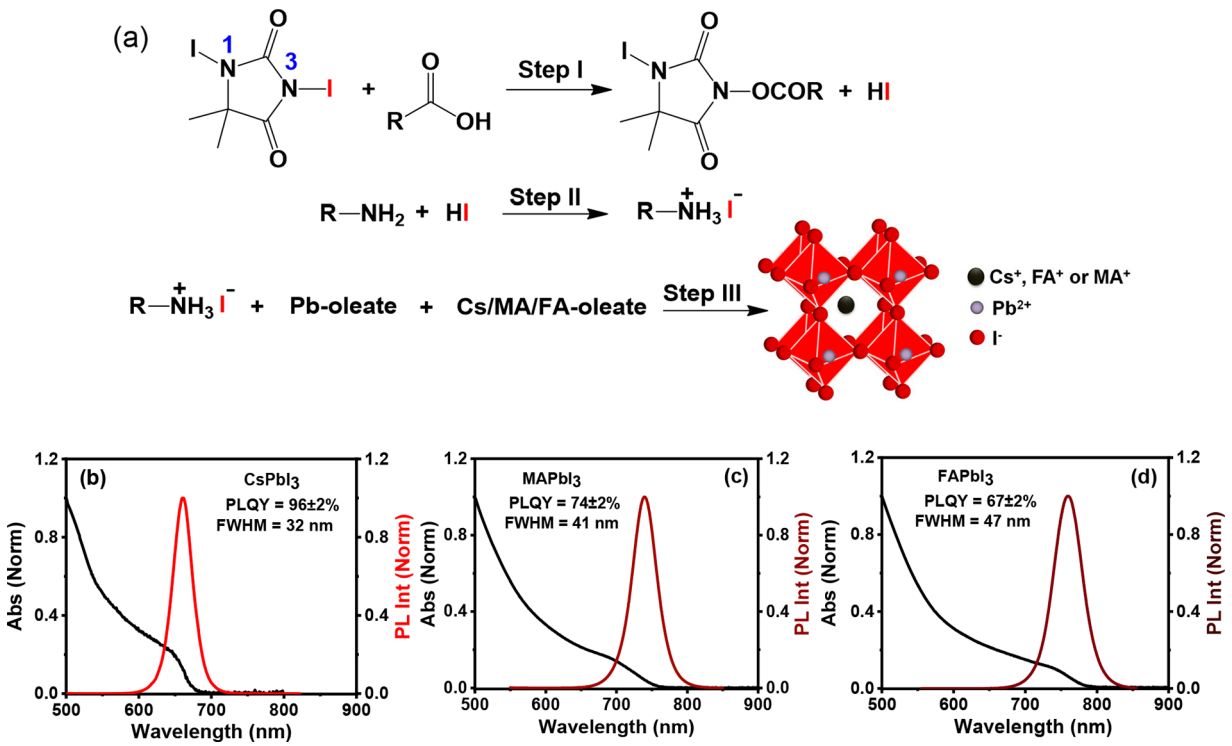

Figure 1. (a) Schematic representation of the steps in DIDMH-mediated synthesis of $APbI_3$ NCs. UV−vis absorption (black) and corresponding PL spectra (colored) of (b) $CsPbI_3$, (c) $(MA)PbI_3$, and (d) $(FA)PbI_3$ NCs. λ_{exc} = 540 nm.

~20 days, stability data for the two hybrid systems were not mentioned.

Recognizing the immense potential of the $CsPbI_3$, $(MA)PbI_3$, and $(FA)PbI_3$ NCs in solar photovoltaic and optoelectronic applications and the lack of any common method of preparation of these systems in their bright and stable form, we have been working for some time toward developing a generic method for the preparation of all three all-inorganic and hybrid systems to overcome the perovskite red wall. While it became clear to us that the iodide precursor chosen for synthesis was a key factor, we did not have much success with the iodo-analogues of the bromide precursors, which produced great quality green-emitting $APbBr_3$ NCs. For example, using N-bromosuccinamide (NBS) as bromide precursor, we obtained green-emitting $APbBr_3$ NCs with near-unity PLQY,[33] but using its iodo-analogue, N-iodosuccinamide (NIS), we could obtain only $CsPbI_3$ NCs, with PLQY of merely 27 ± 3%. The hybrid systems could not be prepared (Figure S1). Moreover, it was observed that phase transformation of the prepared $CsPbI_3$ NCs started within a day of synthesis (Figure S1c). Our continued work in this direction and careful search of the literature led us to 1,3-dichloro-5,5-dimethylhydantoin (DCDMH), which was reported to be a highly effective reagent for chloro-lactonization reaction even at −40 °C.[34,35] The N(1) halogen of DCDMH acts as an inductive activator of the N(3) halogen, which serves as the actual source of halogen. This important piece of information led us to explore the utility of its iodide analogue, 1,3-diiodo-5,5-dimethylhydantoin (DIDMH), as an iodinating agent for synthesis of the $APbI_3$ NCs.

The reaction of DIDMH with oleic acid produces HI (Scheme S1)[33,36] that reacts with oleylamine, generating oleylammonium iodide (OAm^+I^-),[29−32] which served as the active source of iodide in the reaction (Figure 1a).[30,31] The $APbI_3$ NCs were obtained using an optimum quantity of the oleate salt of the "A" cation followed by rapid quenching of the reaction mixture (Figure 1a, with details in the Supporting Information).

The formation of OAm^+I^- in the reaction medium was confirmed by the strong ~220 nm absorption in the UV spectrum and ~0.12 ppm down-shift of the ^1H NMR signal of the α-protons of OAm in the reaction mixture with respect to pure OAm (Figures S2 and S3).[29] It was also found that injection of OAm^+I^- (after preparing separately) into the reaction medium instead of its *in situ* generation produced only moderately luminescent $CsPbI_3$ NCs (PLQY of 38 ± 2%), which exhibited poor stability under ambient conditions (Figure S4). The phase transformation started within a day of synthesis. These results are consistent with the literature, which indicates *in situ* passivation of the perovskite NCs is much more effective in producing brightly luminescent well-passivated stable NCs.[33,37−39]

The Pb:I molar precursor ratio and reaction temperature were found to be the two most critical factors that influenced the quality of the NCs. A 1:3 molar precursor ratio of Pb:I and a temperature of 210 °C for all-inorganic $CsPbI_3$ and 85 °C for both $(MA)PbI_3$ and $(FA)PbI_3$ were found as the optimum conditions for obtaining strongly luminescent, monodispersed, and phase-stable NCs. When the reactions were performed below or above the optimum temperature, the obtained NCs consisted of multiple phases with inhomogeneous size distribution, and they exhibited broad PL bandwidth and substantially low PLQY (Figures S5−S8 and Table S1).

The excellent optical properties of all three $APbI_3$ NCs are evident from their high PLQY and narrow full width at half-maxima (fwhm) (Figure 1b-d and Table 1). The red-emitting $CsPbI_3$ NCs exhibit near-unity (96 ± 2%) PLQY. The NIR-emitting hybrid systems, $(MA)PbI_3$ and $(FA)PbI_3$ NCs, also

https://doi.org/10.1021/acsenergylett.1c01959
ACS Energy Lett. 2021, 6, 3780−3787

Table 1. Parameters of Synthesis and Optical Properties of the NCs

system	temp (°C)	OA (mL)	OAm (mL)	λ_{em} (nm)	fwhm (nm)	PLQY (%)
$CsPbI_3$	210	1	1	660 ± 1	32	96 ± 2
$(MA)PbI_3$	85	1.6	0.8	740 ± 1	41	74 ± 2
$(FA)PbI_3$	85	1.6	0.8	761 ± 2	47	67 ± 2

exhibit impressive PLQYs of 74 ± 2 and 67 ± 2%, respectively. These values are comparable with the best PLQY values reported to date.[18,23] We are not aware of any literature reporting such high PLQY values for both the hybrid and all-inorganic perovskite NCs prepared by a common procedure. These NCs not only exhibit excellent PL but also display a number of other extraordinary features like high phase-purity, monodispersity, and remarkable stability under a variety of conditions. Moreover, the method is also found to be highly reproducible (Figure S9).

Bright-field TEM images indicate the cubic shape and fairly narrow size distribution of all the $APbI_3$ NCs (Figures 2a−c and S10), and the mean edge lengths of $CsPbI_3$, $(MA)PbI_3$, and $(FA)PbI_3$ NCs are 8.8 ± 1.2, 12.2 ± 1.2, and 14.4 ± 2.6 nm, respectively, as obtained from different batches of the NCs. The cubic and tetragonal crystal phases of $CsPbI_3$ and $(MA)PbI_3$ NCs, respectively, are confirmed by comparing the PXRD patterns (Figure 2d,e) with the available ICSD codes (see insets). The diffraction peaks of the $(FA)PbI_3$ NCs (Figure 2f) suggest a cubic perovskite structure.[32,40] Moreover, the interplanar spacings of the NCs estimated from their high-resolution TEM (HRTEM) images (Figure 2a−c insets) are consistent with the literature values.[12,18,41] Notwithstanding two unidentified peaks in Figure 2d and one in Figure 2f, which is not uncommon,[9,10,29,42] the absence of any additional diffraction peak corresponding to other phases (as per ICSD data) eliminates the possibility of formation of any secondary undesired phase of the NCs, indicating high phase purity.

We have examined the PL decay characteristics of the $APbI_3$ NCs to understand the photophysical processes of these systems. The PL of the $CsPbI_3$ NCs decays biexponentially with time constants of 9.17 (68%) and 17.12 (32%) ns (Figure 3a and Table S2). The first component, which has a major contribution, is assigned to direct excitonic recombination, and the slower component is assigned to shallow trap-mediated band-edge recombination.[43−45] It is important to note here that the shallow trap states even in defect-tolerant $CsPbI_3$ NCs with near-unity PLQY arise from intrinsic point defects, which usually do not participate in the nonradiative recombination of the photogenerated charge carriers.[46] For $CsPbI_3$ NCs, a range of lifetimes including some large and short values are reported.[11,12,42,47,48] A short PL lifetime for good quality $CsPbI_3$ NCs is not uncommon[17,44] as the iodide-rich nature of the surface[49] and/or small size of the NCs (smaller than effective Bohr-diameter of ∼12 nm) can contribute to it.[50,51] The absence of any subnanosecond component suggests that the $CsPbI_3$ NCs are largely free from surface defect-related nonradiative recombination channels. A much higher value of the radiative rate constant (k_r) compared to the nonradiative one (k_{nr}) is consistent with high PLQY of the system (Table S2). The PL decay profiles of both $(MA)PbI_3$ (Figure 3b) and $(FA)PbI_3$ NCs (Figure 3c) are found to be triexponential, and the third (shortest) lifetime component is attributed to trapping (Table S2).[32]

We have studied the carrier dynamics of the NCs in the early time scale using ultrafast (femtosecond resolution) transient absorption (TA) technique. The strong bleach signal (ΔA =

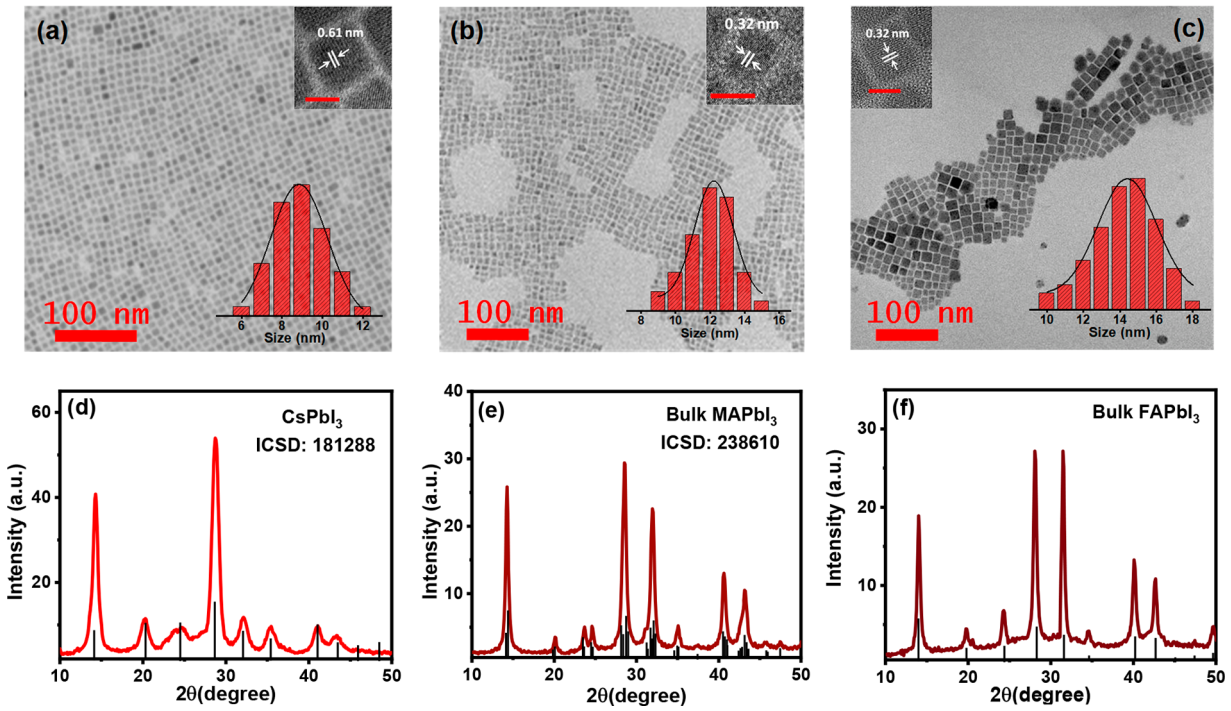

Figure 2. Bright-field TEM images of (a) $CsPbI_3$, (b) $(MA)PbI_3$, and (c) $(FA)PbI_3$ NCs. The scale bar is 100 nm for all samples. Insets show HRTEM images of the NCs (with scale bars of 5, 10, and 10 nm, respectively) with interplanar spacing corresponding to the (100), (220), and (200) planes of the $CsPbI_3$, $MAPbI_3$, and $FAPbI_3$ NCs, respectively. PXRD patterns of (d) $CsPbI_3$, (e) $(MA)PbI_3$, and (f) $(FA)PbI_3$ NCs. The absence of any additional diffraction peaks suggests that the $APbI_3$ NCs are highly phase-pure in nature.

https://doi.org/10.1021/acsenergylett.1c01959
ACS Energy Lett. 2021, 6, 3780−3787

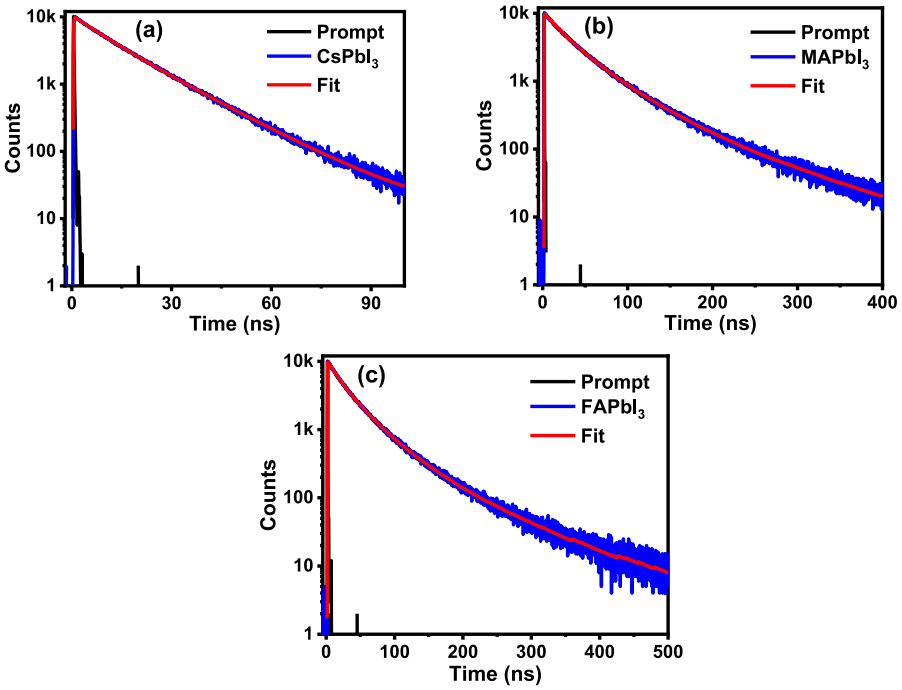

Figure 3. PL decay profiles of the (a) $CsPbI_3$, (b) $MAPbI_3$, and (c) $FAPbI_3$ NCs and bi/triexponential fits to the data. The samples were excited at 481 nm using a short laser pulse, and the decay was monitored at the respective PL maximum. The decay parameters are presented in Table S2.

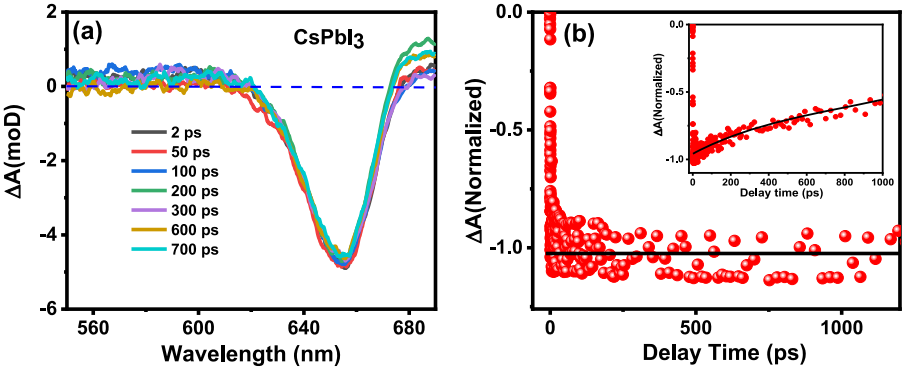

Figure 4. (a) TA spectra of $CsPbI_3$ NCs at different time intervals after excitation by a fs laser (λ_{ex} = 530 nm, ~100 fs). (b) Bleach recovery kinetics of the NCs (λ_{ex} = 530 nm), monitored at the bleach maxima ~656 nm. The inset shows bleach recovery kinetics of the $CsPbI_3$ NCs prepared using Pb:I molar ratio of 1:2.

−*ve*), which arises from the ground-state depopulation of the system,[52,53] exhibits very sluggish recovery even after ~700 ps (Figure 4a), which is more clearly observable from the nearly flat bleach recovery kinetic trace (Figure 4b and Table S3), indicating a long (>1000 ps) recombination component and negligible nonradiative carrier trapping in these NCs.[10,42] In contrast, the bleach recovery dynamics of samples of $CsPbI_3$ NCs, which are prepared using a lower Pb:I ratio of 1:2, exhibit clearly an ultrafast trapping component (243 ± 15 ps) (Figure 4b inset and Table S3).

As mentioned earlier, the biggest issue with the red/NIR-emitting perovskite NCs is their phase sensitivity under ambient conditions. For instance, the large ionic radius of iodine (~220 pm) induces octahedral distortion in $CsPbI_3$ NCs and triggers phase transformation from luminescent cubic (α) phase to nonluminescent orthorhombic (δ) phase within a few days.[11,12] The hybrid $(MA)PbI_3$ NCs, on the other hand, are thermally less stable because of volatile MA^+, and the $(FA)PbI_3$ NCs, which are best suited for single-absorber solar cell, transform into nonperovskite photoinactive hexagonal (δ) phase because of the hygroscopic nature of large FA^+.[13−16] Therefore, the stability of these important substances is a major issue that needs to be urgently addressed. Interestingly, all three $APbI_3$ NCs prepared following our protocol are exceptionally stable under ambient atmospheric conditions. For example, the $CsPbI_3$ NCs stored in a sealed bottle in air retain almost the original PL for several months (Figure S11 and Table S4). The excellent stability of the $CsPbI_3$ NCs is also evident from retention of >80% PLQY even after exposure in ambient conditions for 20 days with relative humidity of ~55−70% (Figure 5a). The unchanged PXRD pattern of a film of the sample kept on the benchtop for the same period also suggests superb phase stability of these NCs (Figure 5b). The excellent photostability and water resistivity of these NCs are also evident from their robustness toward continuous UV light exposure and in the presence of water (Figures S12 and S13).

https://doi.org/10.1021/acsenergylett.1c01959
ACS Energy Lett. 2021, 6, 3780−3787

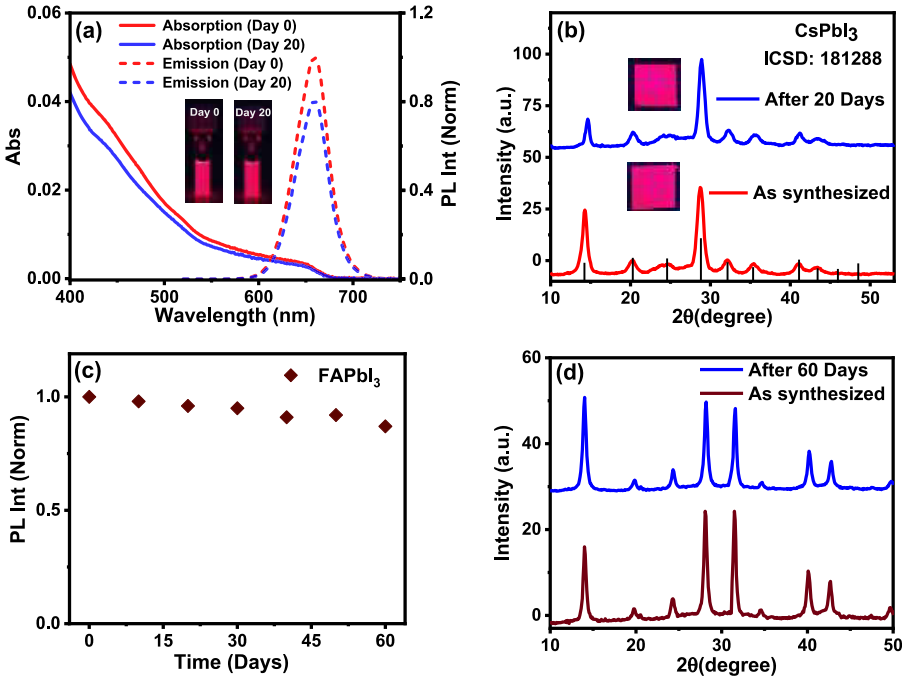

Figure 5. (a) UV−vis absorption and PL spectra of as-synthesized and 20 days old $CsPbI_3$ NCs kept under ambient conditions on benchtop. (b) PXRD patterns of the same samples. (c) Air stability of $(FA)PbI_3$ NCs colloidal dispersion stored in ambient conditions and (d) PXRD patterns of the corresponding as-synthesized and aged samples stored in air.

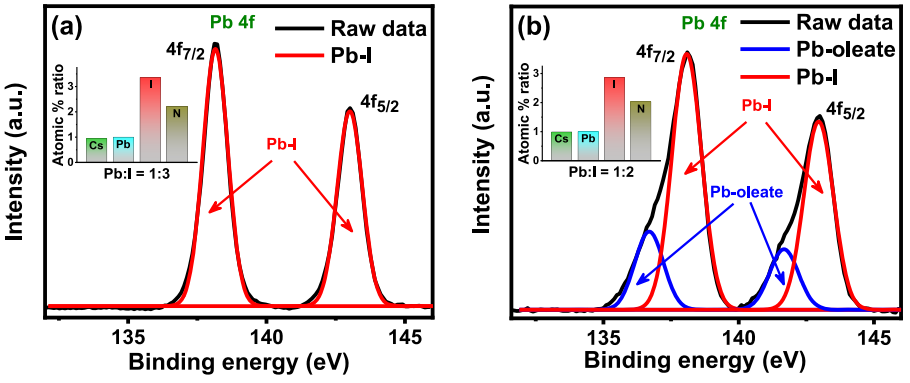

Figure 6. High-resolution XPS spectra of Pb 4f for $CsPbI_3$ NCs prepared using a Pb:I molar ratio of (a) 1:3 and (b) 1:2. Inset shows the estimated atomic percentage ratio (with respect to Pb) of the samples from the data.

The hybrid $(MA)PbI_3$ and $(FA)PbI_3$ NCs are also found to be highly stable and resistant to the environmental stresses. The unchanged PXRD pattern even after 2 months of storage in ambient conditions is a reflection of their phenomenal phase (black, α) stability in air (Figures 5d and S14b). Retention of ∼87−90% of the original PL during the same period further confirms the stability of these systems (Figures 5c and S14a). Retention of the cubic morphology of all three samples stored for 2 months under ambient conditions is also evident from the TEM images (Figure S15). The exceptional phase and optical stability of all three $APbI_3$ NCs under different external conditions are quite remarkable, considering that these are red/NIR-emitting promising candidates for both photovoltaic and optoelectronic applications. The outstanding characteristics of the NCs obtained by our method are clearly evident when they are compared with samples obtained by other methods (Table S5).

To determine the factors that impart exceptional qualities to these $APbI_3$ NCs, we closely inspect the analytical data using $CsPbI_3$ NCs as the model system. Elemental analysis of a large scanned area of the field emission scanning electron microscope (FESEM) images of the $CsPbI_3$ NCs (EDX measurements) shows a Cs:Pb:I ratio of 0.88:1.00:3.26, suggesting an iodide-rich surface of these NCs (Figure S16a,c) and hence the absence of iodide vacancy related surface defects, which facilitate nonradiative deactivation of the photogenerated carriers. Indeed, the iodide-deficient $CsPbI_3$ NCs prepared using 1:2 Pb:I molar ratio are poorly luminescent (Figure S16b) and exhibit an ultrafast bleach recovery component due to nonradiative transition through the iodide vacancy-mediated surface trap states (Figure 4b inset). X-ray photoelectron spectroscopy (XPS) measurements were performed to examine the chemical environment of the constituting elements of the $CsPbI_3$ NCs (Figures 6, S17, and S18). The Pb 4f core level XPS spectrum exhibits $4f_{7/2}$ (138.1 eV) and $4f_{5/2}$ (143.0 eV) peaks, which are assigned to the Pb−I bond in the NCs (Figure 6a).[31,37] For the $CsPbI_3$ NCs, which are prepared using a Pb:I molar ratio of 1:2, each band exhibits a hump

https://doi.org/10.1021/acsenergylett.1c01959
ACS Energy Lett. 2021, 6, 3780−3787

toward the lower binding energy region (~136.69 and ~141.67 eV), which is attributed to Pb-oleate species in these NCs (Figure 6b).[38,54−56] Appearance of the Pb-oleate signal for these NCs indicate iodide vacancy related surface defect,[38] and the absence of this signal for the $CsPbI_3$ NCs prepared using 1:3 molar ratio of Pb:I implies that use of a stoichiometric amount of DIDMH produces an iodide-rich surface. The latter is also evident from the calculated atomic % ratio of the NCs (insets of Figure 6 and Table S6). It is to be noted that the atomic % ratio estimated from the XPS measurements (Table S6) is in good agreemnt with that obtained from EDX studies (Figure S16c). This iodide-rich environment is a key element in providing better stability and bringing a desirable near-perfect surface structure of the $CsPbI_3$ NCs.[28,31,42,57] The surface ligand environment, which also influences the stability and PL properties of the perovskite NCs,[8,58−63] is assessed by ^{1}H NMR and FTIR studies. The ^{1}H NMR spectra (Figure S19) show two broad peaks (at ~6.9 and ~3.6 ppm), which are signatures of the α-protons (NH_3^+) and β-protons ($-CH_2-N$), respectively, of OAm^+.[58,60] Not only does this indicate the presence of OAm^+ on the surface of the $CsPbI_3$ NCs, but also the broadness of the two peaks suggests that OAm^+ is firmly anchored on the surface.[8,60] Interestingly, the ~2.4 ppm peak (marked a) characteristic of the oleate ion is quite sharp, indicating that unlike OAm^+ it is not bound to the NCs. The lack of surface-bound oleate indicates the absence of under-coordinated Pb^{2+} on the surface and reconfirms an iodide-rich surface of the NCs.[60] This observation is consistent with the XPS data, which did not show any signal due to Pb-oleate for the $CsPbI_3$ NCs obtained with a Pb:I ratio of 1:3 (Figure 6a). The asymmetric and symmetric bending absorption of N^+-H at ~1641 and 1554 cm^{-1}, respectively, in the FTIR spectrum further confirms the surface-bound nature of the OAm^+ (Figure S20).[8,58] A point to note here is that because of overlapping spectral signatures of OA, OAm, and ODE (both in ^{1}H NMR and FTIR), it is not possible to specify from these data whether DIDMH also acts as a protective surface ligand for the synthesized NCs (Figure S21). However, high solubility of DIDMH in polar solvents like MeOAc and ACN, which were used for purification of the NCs, indicates this possibility is very low. An iodide-rich surface attracts a greater number of OAm^+, giving them access to the surface sites occupied originally by Cs^+. Low Cs^+ content in the EDX and XPS data and a higher N/Pb ratio for $CsPbI_3$ NCs in XPS measurement support this point (Figures 6 inset, S18c, and Table S6). Substitution of some of these surface Cs^+ with alkylammonium ligand provides high stability to the perovskite NCs as the surface-bound ligand (OAm^+ in the present case) prevents crystal deformation through octahedral tilting (i.e., in maintaning the sensitive α-phase of the NCs).[8,64,65] The tightly bound hydrophobic envelope of OAm^+ also provides protection from moisture and polar media, thus preventing the decomposition of the sensitive cubic phase of the NCs.[61,66] Although OA does not bind to the surface of the NCs, it helps maintaining a ratio of OAm^+ and oleate (or OAm and OA) that is also crucial for the stability of the final product.[60] It is therefore evident that oleylammonium iodide produced *in situ* during the reaction helps to maintain an iodide-rich environment, which leads to the oleylammonium-lead iodide terminated surface by replacing some Cs^+ that provides the exceptional stability and optical properties to the NCs obtained by this method.

In summary, monodispersed, phase-pure, highly stable, and luminescent red−NIR-emitting $CsPbI_3$, $(MA)PbI_3$, and $(FA)PbI_3$ NCs have been obtained by a generic method employing DIDMH as iodide precursor. DIDMH-assisted formation of the oleylammonium-lead iodide-terminated surface is shown to impart the exceptional characteristics of these NCs. The outstanding phase durability and excellent PLQY of all three all-inorganic and hybrid systems obtained by a common procedure by breaching the so-called perovskite red wall significantly brightens the prospect of utilization of these narrow band gap materials for optoelectronic and photovoltaic applications, particularly in single-absorber solar cells. Development of blue/violet and green-emitting NCs using other halide analogues of DIDMH is currently underway.

■ ASSOCIATED CONTENT

Supporting Information

The Supporting Information is available free of charge at https://pubs.acs.org/doi/10.1021/acsenergylett.1c01959.

Experimental Section; reaction mechanism of formation of HI; dependence of PL spectra; PLQY and TEM images of the $APbI_3$ NCs on reaction temperature; Pb:I molar ratio-dependent PLQY of the NCs; optical reproducibility; additional TEM images; long-term air-, photo-, and water-stability data of $CsPbI_3$ NCs; air-stability of $MAPbI_3$ NCs; EDX studies; survey and core level XPS spectra; ^{1}H NMR and FTIR spectra of $CsPbI_3$ NCs and DIDMH; optical properties of the NCs in different conditions; PL decay parameters with k_r and k_{nr} values of the $APbI_3$ NCs; kinetic parameters of TA studies; comparison of PLQY and stability of our $APbI_3$ NCs with other reported methods; and atomic % ratio from XPS studies (PDF)

■ AUTHOR INFORMATION

Corresponding Author

Anunay Samanta − *School of Chemistry, University of Hyderabad, Hyderabad 500046, India;* orcid.org/0000-0003-1551-0209; Email: anunay@uohyd.ac.in

Author

Somnath Das − *School of Chemistry, University of Hyderabad, Hyderabad 500046, India;* orcid.org/0000-0002-3414-9597

Complete contact information is available at: https://pubs.acs.org/10.1021/acsenergylett.1c01959

Notes

The authors declare no competing financial interest.

■ ACKNOWLEDGMENTS

This work is supported by the J. C. Bose National Fellowship (to A.S.) of the Science and Engineering Research Board (SERB) and Institute of Eminence Grants (to University of Hyderabad) of the Ministry of Human Resource and Development (MHRD). The authors acknowledge the TEM and femtosecond laser facility of the School and thank Dr. M. Durga Prasad for TEM measurements. The XPS facility of the National Chemical Laboratory, Pune is also duly acknowledged. S.D. thanks University Grant Commission (UGC) for a Fellowship.

REFERENCES

(1) Stoumpos, C. C.; Kanatzidis, M. G. The Renaissance of Halide Perovskites and Their Evolution as Emerging Semiconductors. *Acc. Chem. Res.* **2015**, *48*, 2791−2802.

(2) Manser, J. S.; Christians, J. A.; Kamat, P. V. Intriguing Optoelectronic Properties of Metal Halide Perovskites. *Chem. Rev.* **2016**, *116*, 12956−13008.

(3) Kovalenko, M. V.; Protesescu, L.; Bodnarchuk, M. I. Properties and potential optoelectronic applications of lead halide perovskite nanocrystals. *Science* **2017**, *358*, 745−750.

(4) Huang, H.; Bodnarchuk, M. I.; Kershaw, S. V.; Kovalenko, M. V.; Rogach, A. L. Lead Halide Perovskite Nanocrystals in the Research Spotlight: Stability and Defect Tolerance. *ACS Energy Lett.* **2017**, *2*, 2071−2083.

(5) Shamsi, J.; Urban, A. S.; Imran, M.; De Trizio, L.; Manna, L. Metal Halide Perovskite Nanocrystals: Synthesis, Post-Synthesis Modifications, and Their Optical Properties. *Chem. Rev.* **2019**, *119*, 3296−3348.

(6) Dutta, A.; Pradhan, N. Phase-Stable Red-Emitting $CsPbI_3$ Nanocrystals: Successes and Challenges. *ACS Energy Lett.* **2019**, *4*, 709−719.

(7) Eperon, G. E.; Paternò, G. M.; Sutton, R. J.; Zampetti, A.; Haghighirad, A. A.; Cacialli, F.; Snaith, H. J. Inorganic caesium lead iodide perovskite solar cells. *J. Mater. Chem. A* **2015**, *3*, 19688−19695.

(8) Dutta, A.; Dutta, S. K.; Das Adhikari, S.; Pradhan, N. Phase-Stable $CsPbI_3$ Nanocrystals: The Reaction Temperature Matters. *Angew. Chem., Int. Ed.* **2018**, *57*, 9083−9087.

(9) Wang, C.; Chesman, A. S. R.; Jasieniak, J. J. Stabilizing the cubic perovskite phase of $CsPbI_3$ nanocrystals by using an alkyl phosphinic acid. *Chem. Commun.* **2017**, *53*, 232−235.

(10) Liu, F.; Zhang, Y.; Ding, C.; Kobayashi, S.; Izuishi, T.; Nakazawa, N.; Toyoda, T.; Ohta, T.; Hayase, S.; Minemoto, T.; Yoshino, K.; Dai, S.; Shen, Q. Highly Luminescent Phase-Stable $CsPbI_3$ Perovskite Quantum Dots Achieving Near 100% Absolute Photoluminescence Quantum Yield. *ACS Nano* **2017**, *11*, 10373−10383.

(11) Protesescu, L.; Yakunin, S.; Bodnarchuk, M. I.; Krieg, F.; Caputo, R.; Hendon, C. H.; Yang, R. X.; Walsh, A.; Kovalenko, M. V. Nanocrystals of Cesium Lead Halide Perovskites ($CsPbX_3$, X = Cl, Br, and I): Novel Optoelectronic Materials Showing Bright Emission with Wide Color Gamut. *Nano Lett.* **2015**, *15*, 3692−3696.

(12) Swarnkar, A.; Marshall, A. R.; Sanehira, E. M.; Chernomordik, B. D.; Moore, D. T.; Christians, J. A.; Chakrabarti, T.; Luther, J. M. Quantum dot−induced phase stabilization of α-$CsPbI_3$ perovskite for high-efficiency photovoltaics. *Science* **2016**, *354*, 92−95.

(13) Juarez-Perez, E. J.; Hawash, Z.; Raga, S. R.; Ono, L. K.; Qi, Y. Thermal degradation of $CH_3NH_3PbI_3$ perovskite into NH_3 and CH_3I gases observed by coupled thermogravimetry−mass spectrometry analysis. *Energy Environ. Sci.* **2016**, *9*, 3406−3410.

(14) Yang, J.; Siempelkamp, B. D.; Liu, D.; Kelly, T. L. Investigation of $CH_3NH_3PbI_3$ Degradation Rates and Mechanisms in Controlled Humidity Environments Using in Situ Techniques. *ACS Nano* **2015**, *9*, 1955−1963.

(15) Fabini, D. H.; Stoumpos, D. C. C.; Laurita, D. G.; Kaltzoglou, D. A.; Kontos, D. A. G.; Falaras, D. P.; Kanatzidis, P. D. M. G.; Seshadri, P. D. R. Reentrant Structural and Optical Properties and Large PositiveThermal Expansion in Perovskite Formamidinium Lead Iodide. *Angew. Chem., Int. Ed.* **2016**, *55*, 15392−15396.

(16) Masi, S.; Gualdrón-Reyes, A. s. F.; Mora-Seró, I. n. Stabilization of Black Perovskite Phase in $FAPbI_3$ and $CsPbI_3$. *ACS Energy Lett.* **2020**, *5*, 1974−1985.

(17) Pan, J.; Shang, Y.; Yin, J.; De Bastiani, M.; Peng, W.; Dursun, I.; Sinatra, L.; El-Zohry, A. M.; Hedhili, M. N.; Emwas, A.-H.; Mohammed, O. F.; Ning, Z.; Bakr, O. M. Bidentate Ligand-Passivated $CsPbI_3$ Perovskite Nanocrystals for Stable Near-Unity Photoluminescence Quantum Yield and Efficient Red Light-Emitting Diodes. *J. Am. Chem. Soc.* **2018**, *140*, 562−565.

(18) Protesescu, L.; Yakunin, S.; Kumar, S.; Bär, J.; Bertolotti, F.; Masciocchi, N.; Guagliardi, A.; Grotevent, M.; Shorubalko, I.; Bodnarchuk, M. I.; Shih, C.-J.; Kovalenko, M. V. Dismantling the "Red Wall" of Colloidal Perovskites: Highly Luminescent Formamidinium and Formamidinium−Cesium Lead Iodide Nanocrystals. *ACS Nano* **2017**, *11*, 3119−3134.

(19) Akkerman, Q. A.; Rainò, G.; Kovalenko, M. V.; Manna, L. Genesis, challenges and opportunities for colloidal lead halide perovskite nanocrystals. *Nat. Mater.* **2018**, *17*, 394−405.

(20) Huang, H.; Polavarapu, L.; Sichert, J. A.; Susha, A. S.; Urban, A. S.; Rogach, A. L. Colloidal lead halide perovskite nanocrystals: synthesis, optical properties and applications. *NPG Asia Mater.* **2016**, *8*, e328.

(21) Zheng, X.; Hou, Y.; Sun, H.-T.; Mohammed, O. F.; Sargent, E. H.; Bakr, O. M. Reducing Defects in Halide Perovskite Nanocrystals for Light- Emitting Applications. *J. Phys. Chem. Lett.* **2019**, *10*, 2629−2640.

(22) Pradhan, N. Tips and Twists in Making High Photoluminescence Quantum Yield Perovskite Nanocrystals. *ACS Energy Lett.* **2019**, *4*, 1634−1638.

(23) Liao, J.-F.; Chen, Y.-X.; Wei, J.-H.; Cai, Y.-T.; Wang, X.-D.; Xu, Y.-F.; Kuang, D.-B. A facile method to fabricate high-quality perovskite nanocrystals based on single crystal powder. *Nano Res.* **2019**, *12*, 2640−2645.

(24) Vybornyi, O.; Yakunin, S.; Kovalenko, M. V. Polar-solvent-free colloidal synthesis of highly luminescent alkylammonium lead halide perovskite nanocrystals. *Nanoscale* **2016**, *8*, 6278−6283.

(25) Levchuk, I.; Osvet, A.; Tang, X.; Brandl, M.; Perea, J. D.; Hoegl, F.; Matt, G. J.; Hock, R.; Batentschuk, M.; Brabec, C. J. Brightly Luminescent and Color-Tunable Formamidinium Lead Halide Perovskite $FAPbX_3$ (X = Cl, Br, I) Colloidal Nanocrystals. *Nano Lett.* **2017**, *17*, 2765−2770.

(26) Zhang, F.; Zhong, H.; Chen, C.; Wu, X.-g.; Hu, X.; Huang, H.; Han, J.; Zou, B.; Dong, Y. Brightly Luminescent and Color-Tunable Colloidal $CH_3NH_3PbX_3$ (X = Br, I, Cl) Quantum Dots: Potential Alternatives for Display Technology. *ACS Nano* **2015**, *9*, 4533−4542.

(27) Wei, S.; Yang, Y.; Kang, X.; Wang, L.; Huang, L.; Pan, D. Room-temperature and gram-scale synthesis of $CsPbX_3$ (X = Cl, Br, I) perovskite nanocrystals with 50−85% photoluminescence quantum yields. *Chem. Commun.* **2016**, *52*, 7265−7268.

(28) Liu, P.; Chen, W.; Wang, W.; Xu, B.; Wu, D.; Hao, J.; Cao, W.; Fang, F.; Li, Y.; Zeng, Y.; Pan, R.; Chen, S.; Cao, W.; Sun, X. W.; Wang, K. Halide-Rich Synthesized Cesium Lead Bromide Perovskite Nanocrystals for Light-Emitting Diodes with Improved Performance. *Chem. Mater.* **2017**, *29*, 5168−5173.

(29) Akkerman, Q. A.; Martínez-Sarti, L.; Goldoni, L.; Imran, M.; Baranov, D.; Bolink, H. J.; Palazon, F.; Manna, L. Molecular Iodine for a General Synthesis of Binary and Ternary Inorganic and Hybrid Organic−Inorganic Iodide Nanocrystals. *Chem. Mater.* **2018**, *30*, 6915−6921.

(30) Dutta, A.; Behera, R. K.; Pal, P.; Baitalik, S.; Pradhan, N. Near-Unity Photoluminescence Quantum Efficiency for All CsPbX3 (X = Cl, Br, and I) Perovskite Nanocrystals: A Generic Synthesis Approach. *Angew. Chem., Int. Ed.* **2019**, *58*, 5552−5556.

(31) Cai, Y.; Wang, H.; Li, Y.; Wang, L.; Lv, Y.; Yang, X.; Xie, R.-J. Trimethylsilyl Iodine-Mediated Synthesis of Highly Bright Red-Emitting $CsPbI_3$ Perovskite Quantum Dots with Significantly Improved Stability. *Chem. Mater.* **2019**, *31*, 881−889.

(32) Imran, M.; Caligiuri, V.; Wang, M.; Goldoni, L.; Prato, M.; Krahne, R.; De Trizio, L.; Manna, L. Benzoyl Halides as Alternative Precursors for the Colloidal Synthesis of Lead-Based Halide Perovskite Nanocrystals. *J. Am. Chem. Soc.* **2018**, *140*, 2656−2664.

(33) Paul, S.; Samanta, A. N-Bromosuccinimide as Bromide Precursor for Direct Synthesis of Stable and Highly Luminescent Green-Emitting Perovskite Nanocrystals. *ACS Energy Lett.* **2020**, *5*, 64−69.

(34) Whitehead, D. C.; Yousefi, R.; Jaganathan, A.; Borhan, B. An Organocatalytic Asymmetric Chlorolactonization. *J. Am. Chem. Soc.* **2010**, *132*, 3298−3300.

https://doi.org/10.1021/acsenergylett.1c01959
ACS Energy Lett. 2021, 6, 3780−3787

(35) Yousefi, R.; Whitehead, D. C.; Mueller, J. M.; Staples, R. J.; Borhan, B. On the Chlorenium Source in the Asymmetric Chlorolactonization Reaction. *Org. Lett.* **2011**, *13*, 608−611.
(36) Xue, H.; Tan, H.; Wei, D.; Wei, Y.; Lin, S.; Liang, F.; Zhao, B. N-Bromosuccinimide−carboxylic acid combination: mild and efficient access to dibromination of unsaturated carbonyl compounds. *RSC Adv.* **2013**, *3*, 5382−5385.
(37) Wu, Y.; Wei, C.; Li, X.; Li, Y.; Qiu, S.; Shen, W.; Cai, B.; Sun, Z.; Yang, D.; Deng, Z.; Zeng, H. In Situ Passivation of $PbBr_6^{4-}$ Octahedra toward Blue Luminescent $CsPbBr_3$ Nanoplatelets with Near 100% Absolute Quantum Yield. *ACS Energy Lett.* **2018**, *3*, 2030−2037.
(38) Woo, J. Y.; Kim, Y.; Bae, J.; Kim, T. G.; Kim, J. W.; Lee, D. C.; Jeong, S. Highly Stable Cesium Lead Halide Perovskite Nanocrystals through in Situ Lead Halide Inorganic Passivation. *Chem. Mater.* **2017**, *29*, 7088−7092.
(39) Zhang, F.; Huang, S.; Wang, P.; Chen, X.; Zhao, S.; Dong, Y.; Zhong, H. Colloidal Synthesis of Air-Stable $CH_3NH_3PbI_3$ Quantum Dots by Gaining Chemical Insight into the Solvent Effects. *Chem. Mater.* **2017**, *29*, 3793−3799.
(40) Zhumekenov, A. A.; Saidaminov, M. I.; Haque, M. A.; Alarousu, E.; Sarmah, S. P.; Murali, B.; Dursun, I.; Miao, X.-H.; Abdelhady, A. L.; Wu, T.; Mohammed, O. F.; Bakr, O. M. Formamidinium Lead Halide Perovskite Crystals with Unprecedented Long Carrier Dynamics and Diffusion Length. *ACS Energy Lett.* **2016**, *1*, 32−37.
(41) Liang, X.; Baker, R. W.; Wu, K.; Deng, W.; Ferdani, D.; Kubiak, P. S.; Marken, F.; Torrente-Murciano, L.; Cameron, P. J. Continuous low temperature synthesis of MAPbX3 perovskite nanocrystals in a flow reactor. *React. Chem. Eng.* **2018**, *3*, 640−644.
(42) Liu, F.; Ding, C.; Zhang, Y.; Kamisaka, T.; Zhao, Q.; Luther, J. M.; Toyoda, T.; Hayase, S.; Minemoto, T.; Yoshino, K.; Zhang, B.; Dai, S.; Jiang, J.; Tao, S.; Shen, Q. GeI2 Additive for High Optoelectronic Quality $CsPbI_3$ Quantum Dots and Their Application in Photovoltaic Devices. *Chem. Mater.* **2019**, *31*, 798−807.
(43) Chirvony, V. S.; González-Carrero, S.; Suárez, I.; Galian, R. E.; Sessolo, M.; Bolink, H. J.; Martínez-Pastor, J. P.; Pérez-Prieto, J. Delayed Luminescence in Lead Halide Perovskite Nanocrystals. *J. Phys. Chem. C* **2017**, *121*, 13381−13390.
(44) Yao, J.-S.; Ge, J.; Wang, K.-H.; Zhang, G.; Zhu, B.-S.; Chen, C.; Zhang, Q.; Luo, Y.; Yu, S.-H.; Yao, H.-B. Few-Nanometer-Sized α-$CsPbI_3$ Quantum Dots Enabled by Strontium Substitution and Iodide Passivation for Efficient Red-Light Emitting Diodes. *J. Am. Chem. Soc.* **2019**, *141*, 2069−2079.
(45) Zhang, X.; Lu, M.; Zhang, Y.; Wu, H.; Shen, X.; Zhang, W.; Zheng, W.; Colvin, V. L.; Yu, W. W. PbS Capped $CsPbI_3$ Nanocrystals for Efficient and Stable Light-Emitting Devices Using p−i−n Structures. *ACS Cent. Sci.* **2018**, *4*, 1352−1359.
(46) Kang, J.; Wang, L.-W. High Defect Tolerance in Lead Halide Perovskite $CsPbBr_3$. *J. Phys. Chem. Lett.* **2017**, *8*, 489−493.
(47) Mir, W. J.; Swarnkar, A.; Nag, A. Postsynthesis Mn-doping in $CsPbI_3$ nanocrystals to stabilize the black perovskite phase. *Nanoscale* **2019**, *11*, 4278−4286.
(48) Mondal, N.; De, A.; Das, S.; Paul, S.; Samanta, A. Ultrafast carrier dynamics of metal halide perovskite nanocrystals and perovskite-composites. *Nanoscale* **2019**, *11*, 9796−9818.
(49) Kong, W.; Ding, T.; Bi, G.; Wu, H. Optical characterizations of the surface states in hybrid lead−halide perovskites. *Phys. Chem. Chem. Phys.* **2016**, *18*, 12626−12632.
(50) Malgras, V.; Tominaka, S.; Ryan, J. W.; Henzie, J.; Takei, T.; Ohara, K.; Yamauchi, Y. Observation of Quantum Confinement in Monodisperse Methylammonium Lead Halide Perovskite Nanocrystals Embedded in Mesoporous Silica. *J. Am. Chem. Soc.* **2016**, *138*, 13874−13881.
(51) Zhang, D. X.; Bai, P. X.; Wu, H.; Zhang, X.; Sun, C.; Zhang, P. Y.; Zhang, P. W.; Zheng, P. W.; Yu, P. W. W.; Rogach, P. A. L. Water-Assisted Size and Shape Control of $CsPbBr_3$ Perovskite Nanocrystals. *Angew. Chem., Int. Ed.* **2018**, *57*, 3337−3342.
(52) Mondal, N.; Samanta, A. Complete ultrafast charge carrier dynamics in photo-excited all-inorganic perovskite nanocrystals ($CsPbX_3$). *Nanoscale* **2017**, *9*, 1878−1885.
(53) Dursun, I.; Maity, P.; Yin, J.; Turedi, B.; Zhumekenov, A. A.; Lee, K. J.; Mohammed, O. F.; Bakr, O. M. Why are Hot Holes Easier to Extract than Hot Electrons from Methylammonium Lead Iodide Perovskite? *Adv. Energy Mater.* **2019**, *9*, 1900084.
(54) Li, M.; Zhang, X.; Matras-Postolek, K.; Chen, H.-S.; Yang, P. An anion-driven Sn^{2+} exchange reaction in $CsPbBr_3$ nanocrystals towards tunable and high photoluminescence. *J. Mater. Chem. C* **2018**, *6*, 5506−5513.
(55) Pederson, L. R. Two-dimensional chemical-state plot for lead using XPS. *J. Electron Spectrosc. Relat. Phenom.* **1982**, *28*, 203−209.
(56) Morgan, W. E.; Van Wazer, J. R. Binding energy shifts in the x-ray photoelectron spectra of a series of related Group IVa compounds. *J. Phys. Chem.* **1973**, *77*, 964−969.
(57) Huang, Y.; Luan, W.; Liu, M.; Turyanska, L. DDAB-assisted synthesis of iodine-rich $CsPbI_3$ perovskite nanocrystals with improved stability in multiple environments. *J. Mater. Chem. C* **2020**, *8*, 2381−2387.
(58) De Roo, J.; Ibáñez, M.; Geiregat, P.; Nedelcu, G.; Walravens, W.; Maes, J.; Martins, J. C.; Van Driessche, I.; Kovalenko, M. V.; Hens, Z. Highly Dynamic Ligand Binding and Light Absorption Coefficient of Cesium Lead Bromide Perovskite Nanocrystals. *ACS Nano* **2016**, *10*, 2071−2081.
(59) Pan, A.; He, B.; Fan, X.; Liu, Z.; Urban, J. J.; Alivisatos, A. P.; He, L.; Liu, Y. Insight into the Ligand-Mediated Synthesis of Colloidal $CsPbBr_3$ Perovskite Nanocrystals: The Role of Organic Acid, Base, and Cesium Precursors. *ACS Nano* **2016**, *10*, 7943−7954.
(60) Ravi, V. K.; Santra, P. K.; Joshi, N.; Chugh, J.; Singh, S. K.; Rensmo, H.; Ghosh, P.; Nag, A. Origin of the Substitution Mechanism for the Binding of Organic Ligands on the Surface of $CsPbBr_3$ Perovskite Nanocubes. *J. Phys. Chem. Lett.* **2017**, *8*, 4988−4994.
(61) Das, S.; De, A.; Samanta, A. Ambient Condition Mg^{2+} Doping Producing Highly Luminescent Green- and Violet-Emitting Perovskite Nanocrystals with Reduced Toxicity and Enhanced Stability. *J. Phys. Chem. Lett.* **2020**, *11*, 1178−1188.
(62) Koh, D. W.-k.; Park, D. S.; Ham, Y. Phosphonic Acid Stabilized Colloidal $CsPbX_3$ (X = Br, I) Perovskite Nanocrystals and Their Surface Chemistry. *ChemistrySelect* **2016**, *1*, 3479−3482.
(63) Wu, L.; Zhong, Q.; Yang, D.; Chen, M.; Hu, H.; Pan, Q.; Liu, H.; Cao, M.; Xu, Y.; Sun, B.; Zhang, Q. Improving the Stability and Size Tunability of Cesium Lead Halide Perovskite Nanocrystals Using Trioctylphosphine Oxide as the Capping Ligand. *Langmuir* **2017**, *33*, 12689−12696.
(64) Chen, Y.; Smock, S. R.; Flintgruber, A. H.; Perras, F. A.; Brutchey, R. L.; Rossini, A. J. Surface Termination of $CsPbBr_3$ Perovskite Quantum Dots Determined by Solid-State NMR Spectroscopy. *J. Am. Chem. Soc.* **2020**, *142*, 6117−6127.
(65) Pan, L.; Zhang, L.; Qi, Y.; Conkle, K.; Han, F.; Zhu, X.; Box, D.; Shahbazyan, T. V.; Dai, Q. Stable $CsPbI_3$ Nanocrystals Modified by Tetra-n-butylammonium Iodide for Light-Emitting Diodes. *ACS Appl. Nano Mater.* **2020**, *3*, 9260−9267.
(66) Zhong, Q.; Cao, M.; Xu, Y.; Li, P.; Zhang, Y.; Hu, H.; Yang, D.; Xu, Y.; Wang, L.; Li, Y.; Zhang, X.; Zhang, Q. L-Type Ligand-Assisted Acid-Free Synthesis of $CsPbBr_3$ Nanocrystals with Near-Unity Photoluminescence Quantum Yield and High Stability. *Nano Lett.* **2019**, *19*, 4151−4157.

https://doi.org/10.1021/acsenergylett.1c01959
ACS Energy Lett. 2021, 6, 3780−3787

Nanoscale

PAPER

View Article Online
View Journal | View Issue

Cite this: *Nanoscale*, 2022, **14**, 9349

On direct synthesis of high quality $APbX_3$ ($A = Cs^+$, MA^+ and FA^+; $X = Cl^-$, Br^- and I^-) nanocrystals following a generic approach†

Somnath Das and Anunay Samanta *

Direct synthesis of $APbX_3$ [$A = Cs^+$, methylammonium (MA^+) or formamidinium (FA^+) and $X = Cl^-$, Br^- or I^-] perovskite nanocrystals (NCs) following a generic approach is a challenging task even today. Motivated by our recent success in obtaining directly high-quality red/NIR-emitting $APbI_3$ NCs employing 1,3-diiodo-5,5-dimethylhydantoin (DIDMH) as an iodide precursor, we explore here whether violet/green-emitting $APbCl_3$ and $APbBr_3$ NCs can also be obtained using the chloro- and bromo-analog of DIDMH keeping in mind that a positive outcome will provide the generic protocol for direct synthesis of all $APbX_3$ NCs using similar halide precursors. It is shown that green-emitting $APbBr_3$ NCs with near-unity PLQY and violet-emitting $CsPbCl_3$ NCs with an impressive PLQY of ~70%, mixed-halide NCs, $CsPb(Cl/Br)_3$ and $CsPb(Br/I)_3$, emitting in the blue and yellow-orange region with PLQYs of 87–95% and 68–98%, respectively can indeed be obtained employing the bromo- and chloro-analog of DIDMH. These NCs exhibit remarkable stability under different conditions including the polar environment. Femtosecond pump–probe studies show no ultrafast carrier trapping in these systems. The key elements of the halide precursors that facilitated the synthesis and the factors contributing to the excellent characteristics of the NCs are determined by careful analysis of the data. The results are of great significance because a direct method of obtaining highly luminescent and stable $APbX_3$ NCs (except violet-emitting hybrid NCs) is eventually identified and the work provides valuable insight into the selection of appropriate halide precursors for the development of superior systems.

Received 7th March 2022,
Accepted 23rd May 2022

DOI: 10.1039/d2nr01305c

rsc.li/nanoscale

1. Introduction

Owing to their fascinating optical properties,[1–8] the popularity of the lead-halide based perovskite nanocrystals (NCs) with the general chemical formula of $APbX_3$ [$A = Cs^+$, methylammonium (MA) or formamidinium (FA) and $X = Cl^-$, Br^- or I^-] in optoelectronic applications as LEDs, lasing medium and photodetectors has skyrocketed in recent years.[9–14] Increasing demand for various lighting and display technologies has generated huge interest in developing methodologies for the preparation of high quality perovskite NCs.[8,12,15,16] While these studies helped targeted synthesis of violet, green or red-emitting all-inorganic and/or hybrid NCs,[6,17–31] no generic method of obtaining all these systems with good optical properties and stability is reported to date despite intense efforts. For example, Pradhan and co-workers obtained $CsPbX_3$ (X = Cl, Br and I) NCs with near-unity PLQY, but not the hybrid systems.[6] Manna and co-workers succeeded in obtaining all $APbX_3$ NCs with high PLQYs of 65, 92 and 58% for the violet-, green- and red-emitting NCs, respectively using benzoyl halide as the halide precursor, but the stability of these systems (except for $CsPbI_3$) was not examined.[32]

The halide precursor chosen for the synthesis of the NCs is an important parameter that determines the yield, quality and even the stability. The halide precursor reacts with a nucleophile and generates HX.[32] The latter combines with oleylamine (OAm) forming an oleylammonium halide (OAm^+X^-), which not only serves as an active source of halogen, but also passivates the halide vacancies and protects the surface from its surrounding.[6] An understanding of the chemistry of the formation of HX from the halide precursor is key to identifying the right halide precursor for the synthesis of quality NCs. Our recent success in obtaining high quality red/NIR-emitting iodide-based $APbI_3$ (with A = Cs, MA and FA) NCs with unmatched optical properties and stability using 1,3-diiodo-5,5-dimethylhydantoin (DIDMH) as the iodide precursor[33] substantiates this statement. As the goal is to develop a generic strategy for the preparation of not only the iodides, but the

School of Chemistry, University of Hyderabad, Hyderabad-500 046, India.
E-mail: anunay@uohyd.ac.in

†Electronic supplementary information (ESI) available: Experimental section, instrumentation and additional characterization data of the $APbX_3$ NCs. See DOI: https://doi.org/10.1039/d2nr01305c

other halides as well, the next step naturally is to examine whether green-emitting $APbBr_3$ and violet-emitting $APbCl_3$ NCs can also be obtained using the bromo- and chloro-analog of DIDMH as the halide precursor. Herein we undertake this study, and the results show that the bromo- and chloro-analogs of DIDMH, namely, 1,3-dibromo-5,5-dimethylhydantoin (DBDMH) and 1,3-dichloro-5,5-dimethylhydantoin (DCDMH), are equally effective in producing highly luminescent and stable $APbBr_3$ and $APbCl_3$ NCs. This implies that we have eventually found a generic protocol for direct synthesis of phase pure, highly mono-disperse, stable and luminescent $APbX_3$ NCs (A = Cs, MA, and FA and X = Cl, Br, I or mixtures) emitting over the entire visible range using 1,3-dihalo-5,5-dimethylhydantoin (DXDMH) as a halide precursor.

2. Results and discussion

2.1. Reaction conditions

Scheme 1 depicts the preparation of the $APbX_3$ NCs by the hot-injection method using DXDMH (Fig. S1†) in the presence of oleic acid (OA) and OAm in octadecence (ODE). The mechanism of *in situ* generation of OAm^+X^- as an intermediate and subsequent formation of the NCs is shown in Scheme S1† and additional details can be found in our earlier work.[33] The quality of the as-synthesized NCs, as indicated by PLQY and size-uniformity, is found to depend on the Pb : X molar precursor ratio and reaction temperature. The 1 : 3 (Pb : X) molar precursor ratio was found optimum for all systems except for $MAPbCl_3$ NCs (discussed later). A lower content of the halide precursor yields NCs with a mixture of phases, broad size distribution and low PLQY (Fig. S2 and Table S1†). The optimum reaction temperatures for the synthesis of most luminescent, phase pure, homogeneous, and stable all-inorganic $CsPbX_3$ and mixed-halide NCs, green-emitting hybrid $APbBr_3$ and violet-emitting hybrid $APbCl_3$ NCs are found to be 210, 165 and 95 °C, respectively (Table 1). When reactions were carried out below the optimum temperature, the obtained NCs were of inhomogeneous size distribution displaying a higher PL bandwidth and a rapidly decreasing PLQY (Fig. S3 and S4 and Table S1†). The reproducibility of the present method is examined and found to be very good (Fig. S5†).

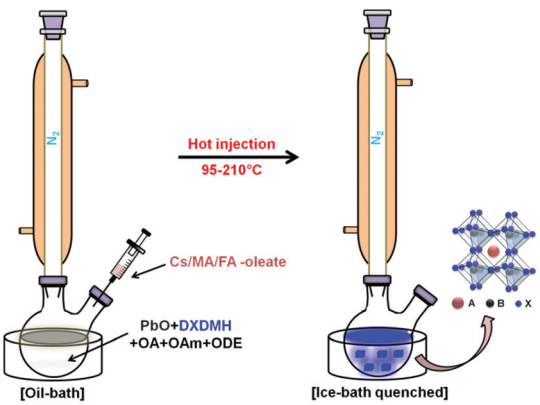

Scheme 1 DXDMH-mediated direct synthesis of the $APbX_3$.

2.2. Structural features

Bright-field transmission electron microscopy (TEM) images show cubic morphology and narrow size distribution of all $APbX_3$ NCs (Fig. 1A–C and S6A–C†), with average edge lengths of 8.03 ± 0.5, 10.06 ± 0.6 and 14.6 ± 1.3 nm for the $CsPbBr_3$, $MAPbBr_3$ and $FAPbBr_3$ NCs, respectively and 7.08 ± 0.05, 12.5 ± 1.15 and 10.4 ± 1.28 nm for the $CsPbCl_3$, $MAPbCl_3$ and $FAPbCl_3$ NCs, respectively (Fig. S6 and S7†). Additional TEM images of different resolutions are made available as ESI (Fig. S7 and S8†). The high crystallinity of the NCs allows clear observation of the lattice fringes in high-resolution TEM images (Fig. S9 and S10†). The powder X-ray diffraction (PXRD) patterns are also consistent with the cubic crystal structure of all $APbX_3$ NCs (X = Cl and Br) NCs (Fig. 1D–F and S6D–F†). Comparison of the measured PXRD patterns with available ICSD codes confirms the cubic perovskite structures for $CsPbBr_3$ (ICSD code: 29073), $MAPbBr_3$ (ICSD code: 252415) and $CsPbCl_3$ (ICSD code: 23108) NCs. The cubic crystal structure of the $FAPbBr_3$, $MAPbCl_3$ and $FAPbCl_3$ NCs is confirmed by comparing the diffraction peaks with the literature data.[32,34,35] The absence of any additional diffraction peaks in the PXRD spectra eliminates the possibility of formation of any secondary (undesired) phases in the prepared NCs and suggests high phase purity of the samples.

Table 1 Reaction conditions and PL characteristics of the $APbX_3$ NCs

Samples	Temp. (°C)	Pb : X	OA (mL)	OAm (mL)	PLQY (%)	FWHM (nm)	λ_{em} (nm)	Ref.
$CsPbBr_3$	210	1 : 3	2.0	2.0	99 ± 1	19	513 ± 1	This work
$MAPbBr_3$	165	1 : 3	1.5	0.5	99 ± 1	21	520 ± 2	
$FAPbBr_3$	165	1 : 3	1.5	0.5	99 ± 1	20	533 ± 2	
$CsPbCl_3$	210	1 : 3	2.0	2.0	70 ± 2	10	406 ± 1	
$MAPbCl_3$	95	1 : 1.5	2.0	0.4	3.3 ± 0.2	11	397 ± 1	
$FAPbCl_3$	95	1 : 3	2.0	0.8	1.2 ± 0.1	13	400 ± 1	
$CsPbI_3$	210	1 : 3	1	1	96 ± 2	32	660 ± 1	33
$MAPbI_3$	85	1 : 3	1.6	0.8	74 ± 2	41	740 ± 1	
$FAPbI_3$	85	1 : 3	1.6	0.8	67 ± 2	47	761 ± 2	

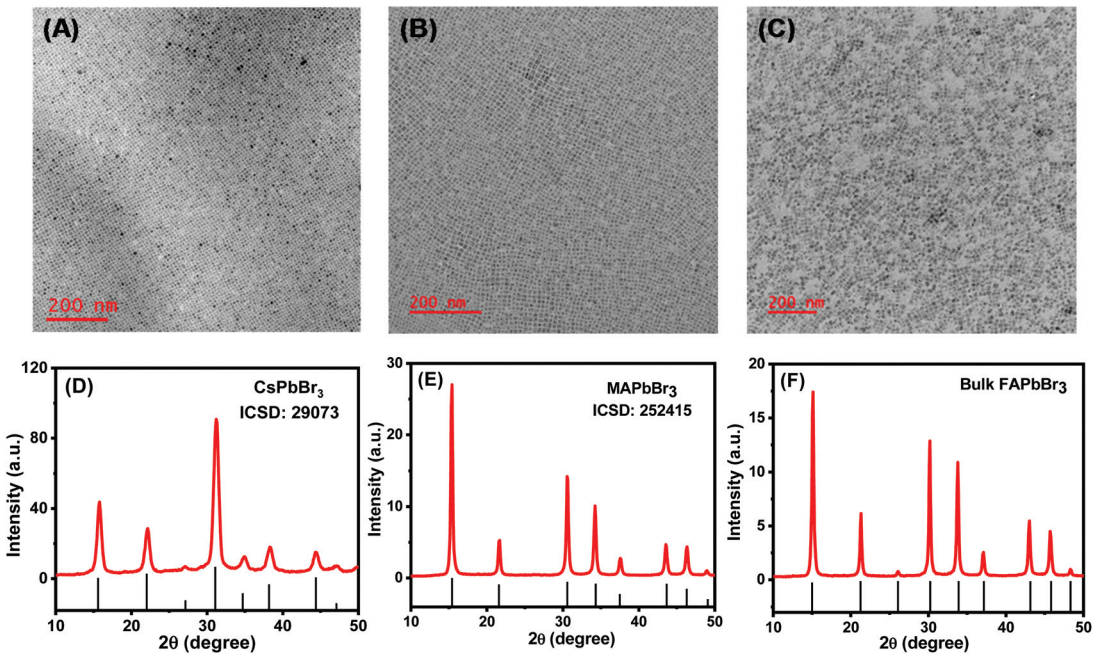

Fig. 1 Bright-field TEM images of (A) $CsPbBr_3$, (B) $MAPbBr_3$ and (C) $FAPbBr_3$ NCs. The scale bar is 200 nm for all the samples. PXRD patterns of (D) $CsPbBr_3$, (E) $MAPbBr_3$ and (F) $FAPbBr_3$ NCs with reference patterns obtained from their bulk cubic phases.

2.3. Photoluminescence and carrier relaxation dynamics

The excellent optical properties of the NCs obtained by the present method are evident from high PLQYs and narrow full widths at half-maxima (FWHM) of all three green-emitting $APbBr_3$ NCs emitting between 513 ± 1 and 533 ± 2 nm (Fig. 2). All $APbBr_3$ NCs exhibit near-unity (99 ± 1%) PLQY with narrow FWHM of 19, 21 and 20 nm for $CsPbBr_3$, $MAPbBr_3$ and

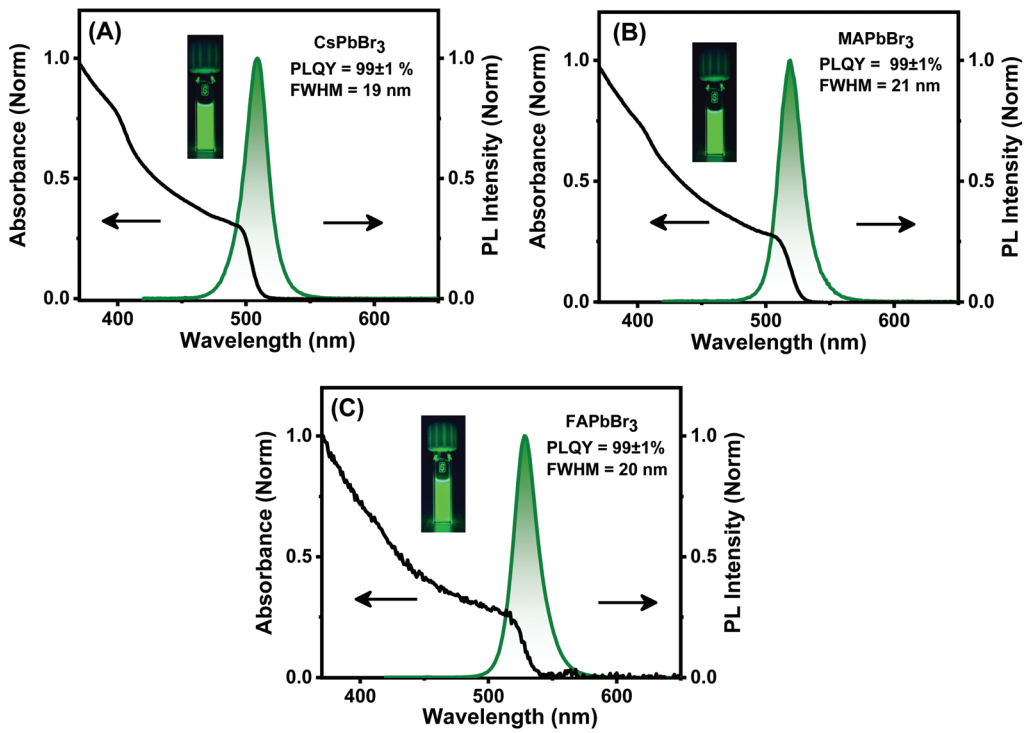

Fig. 2 UV-Vis absorption and PL spectra of (A) $CsPbBr_3$, (B) $MAPbBr_3$ and (C) $FAPbBr_3$ NCs. The excitation wavelength (λ_{ex}) was 400 nm in each case. Digital images of the respective NCs under 365 nm UV illumination are also shown in the insets.

$FAPbBr_3$ NCs, respectively (Fig. 2A–C and Table 1). These values are comparable to or better than the best PLQY reported for these systems by any method to date.[22,32] Similarly, the violet-emitting $APbCl_3$ NCs, especially all-inorganic $CsPbCl_3$ NCs display impressive optical properties (Fig. S6†). A PLQY of 70 ± 2% for violet-emitting $CsPbCl_3$ NCs (λ_{em} = 406 nm, Fig. S6G†) is quite remarkable as it represents one of the highest reported values for this system obtained by any direct method of synthesis (Table S2†).[6,24,25,32] An important point to note here is that a stoichiometric amount of DCDMH produces these brightly luminescent $CsPbCl_3$ NCs (Table S2†), unlike earlier cases, where a much higher amount of chloride precursor was necessary.[6,24,25,32] We found that an excess amount of DCDMH did not have much influence on the PLQY of the system initially, but the PLQY dropped for Pb : Cl precursor ratios exceeding 1 : 7 (Fig. S11†). The hybrid $MAPbCl_3$ and $FAPbCl_3$ NCs, which emit in the 396–400 nm region, are, however, found to be poorly luminescent with PLQYs of 3.3 ± 0.2% and 1.2 ± 0.1%, respectively (Fig. S6H and I,† Table 1). The violet-emitting $CsPbCl_3$, $MAPbCl_3$ and $FAPbCl_3$ NCs show narrow FWHMs of 10, 11 and 13 nm, respectively. Another point to note in this context is that, in the case of $MAPbCl_3$ NCs, 1 : 3 Pb : Cl molar precursor ratio results in the formation of undesired $PbCl_2$ (Fig. S12†), which is, however, not surprising as $PbCl_2$ formation during the preparation of $MAPbCl_3$ NCs is reported earlier.[32] To avoid this problem, a lower Pb : Cl ratio (1 : 1.5) is used for the synthesis of this system (Fig. S12B†). The reaction parameters and optical properties of all $APbX_3$ NCs (including the iodides obtained earlier[33]) are collected in Table 1.

We examined the PL decay characteristics of the NCs to understand the associated photophysical processes. All green-emitting ($APbBr_3$) NCs exhibit bi-exponential decay kinetics, but the violet-emitting ($APbCl_3$) NCs display a 3-component decay profile (Fig. 3 and S13†). Specifically, PL decay of the $CsPbBr_3$ NCs (Fig. 3A) consists of 4.97 (73%) and 12.50 (27%) ns lifetime components (Table S3†). While the major (4.97 ns) component arises from excitonic recombination, the longer component is assigned to shallow trap-mediated excitonic recombination.[6,22,36] The absence of any sub-nanosecond component indicates that these NCs are free from surface defect-related non-radiative recombination channels.[22] Indeed, $CsPbBr_3$(II) NCs, which are prepared using a lower bromide concentration (Pb : Br = 1 : 2), possess a sub-nanosecond component (0.61 ns, 12%) indicating the presence of surface defect states (Fig. S14 and Table S3†). The PL decay of the $CsPbCl_3$ NCs consists of 4.63 (19%), 20.72 (5%) and 0.47 (76%) ns lifetime components (Fig. 3B). The shortest and major component (0.47 ns, 76%) is due to the rapid non-radiative relaxation of the carriers through the trap states.[25,37] The absence of this trapping component for the $CsPbBr_3$ NCs explains its higher PLQY compared to the $CsPbCl_3$ NCs. The calculated radiative (k_r) and non-radiative (k_{nr}) rate constants of the systems give further insight into the charge carrier recombination processes. A much higher k_r/k_{nr} value for $CsPbBr_3$ NCs compared to $CsPbCl_3$ NCs (140 *vs.* 2.33) is in line with the PLQY values of the systems. The PL decay profiles and associated decay parameters of other $APbX_3$ NCs are presented in Fig. S13 and S14 and Table S3.†

The early-time photophysical processes in these systems have been studied by femtosecond transient absorption (fs-TA) measurements (details are provided in the ESI†) and for a clear understanding of these events, we have compared the ultrafast carrier dynamics of the $CsPbBr_3$ NCs and $CsPbBr_3$(II) NCs. As can be seen (Fig. 4), the TA spectra comprising excitonic bleach (ΔA = −ve) at ~509 nm and transient absorption (ΔA =

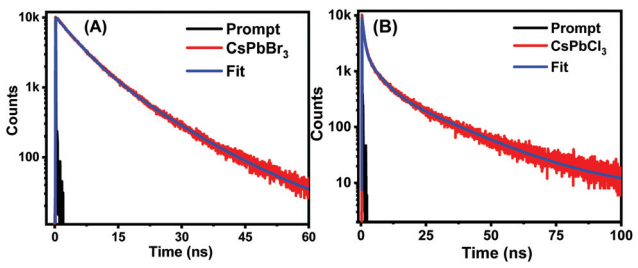

Fig. 3 PL decay profiles of (A) $CsPbBr_3$ and (B) $CsPbCl_3$ NCs. For recording the PL decay curves, laser sources of 404 and 376 nm were used, and the PL was monitored at 513 and 406 nm for the $CsPbBr_3$ and $CsPbCl_3$ NCs, respectively.

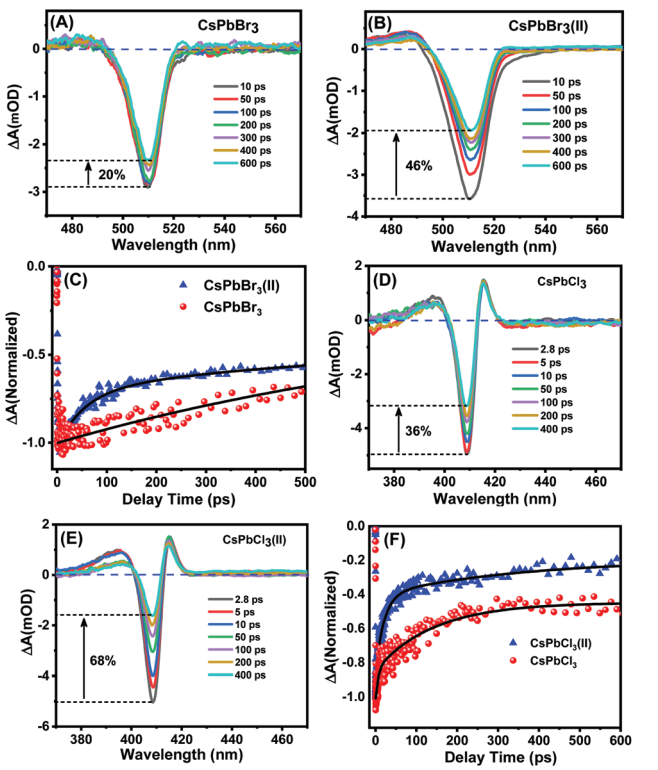

Fig. 4 TA spectra of (A) $CsPbBr_3$ and (B) $CsPbBr_3$(II) NCs. (C) A comparison of the bleach recovery dynamics of the two samples. TA spectra of (D) $CsPbCl_3$, (E) $CsPbCl_3$(II) and (F) bleach recovery dynamics of the two NCs. The NCs were excited at 350 nm by fs-laser pulses and the bleach recovery dynamics were monitored at respective bleach maxima.

+ve) in the lower wavelength region (470–490 nm) are quite similar for both samples.[38,39] However, the recovery of bleach in $CsPbBr_3$ NCs is substantially smaller than that in $CsPbBr_3$(II) NCs (~20% *vs.* ~46% in initial ~600 ps, Fig. 4A and B) due to slower bleach recovery kinetics in the former system and this is clearly seen in Fig. 4C. Moreover, while the bleach recovery is bi-exponential for the $CsPbBr_3$(II) NCs comprising a 53.2 ± 5 ps component due to carrier trapping and a >1000 ps due to direct recombination (Table S4†),[39–41] the dynamics is single exponential comprising only the long component in the case of $CsPbBr_3$ NCs (Fig. 4C). Similarly, though the TA spectra of $CsPbCl_3$ and $CsPbCl_3$(II) NCs are similar (Fig. 4D and E), the bleach recovery kinetics of the $CsPbCl_3$ NCs (Fig. 4F) are found to be bi-exponential comprising a trapping component of 5.9 ± 1.6 ps (27%, Table S4†) unlike a 3-component decay of the $CsPbCl_3$(II) NCs consisting of two dominant (total 85%) ultrafast trapping components (5.8 ± 0.3 and 74.8 ± 5 ps) and a long direct recombination component (>1000 ps).[42] We have also performed an fs-TA experiment on the violet-emitting hybrid NCs (Fig. S15†) for the first time. The bleach recovery kinetics of these NCs are tri-exponential with a large contribution (~86–89%) of the ultrafast trapping component (Table S4†) consistent with poor PLQY of these samples.

2.4. Mixed-halide systems

The universality of the present method is examined by extending the synthesis to mixed-halide $CsPb(Cl/Br)_3$ and $CsPb(Br/I)_3$ NCs as well. The mixed-halide NCs were obtained readily using appropriate quantities of two halide precursors during the reaction (Table S5†). The blue-emitting $CsPbCl_2Br$, $CsPbCl_{1.5}Br_{1.5}$ and $CsPbClBr_2$ NCs exhibit outstanding PLQYs of 87 ± 1%, 95 ± 1%, 96 ± 1% with a PL peak between 431 and 478 nm and narrow FWHM (Fig. 5A, Table S6†), as compared to a commonly observed PLQY of <40% of these systems.[43–45] These values are impressive as they are comparable to or better than the PLQY of previously reported blue-emitting NCs obtained by other direct methods (Table S7†).[25,46] The yellow-orange emitting $CsPb(Br/I)_3$ NCs also display excellent PL properties as exemplified by narrow FWHM and PLQY of 68 ± 2 to 98 ± 1%, respectively (Fig. 5B, Table S6†). We are not aware of any literature reporting this high PLQY of these mixed-halide NCs emitting in the 531–635 nm region by any direct synthesis method. PL decay profiles of the mixed-halide NCs are mostly tri-exponential with a major contribution from the band-edge radiative recombination process (Fig. S16 and Table S8†). Thus, a wide 430–635 nm range is covered by these directly synthesized mixed-halide NCs (Fig. S17†). This wavelength range extends much wider (395–760 nm, Fig. 6) when the results of our recent work following this generic strategy are taken into consideration.[33]

Bright-field TEM images indicate the cubic morphology of these mixed-halide NCs with an average size of ~6.9–10 nm depending on the halide compositions (Fig. S18†). Furthermore, a linear shift of the PXRD diffraction peak toward a lower angle, while moving from chloride- to iodide-based NCs (*via* the bromide ones), also indicates the uniform cubic crystal structure of all these mixed-halide NCs (Fig. S19†).

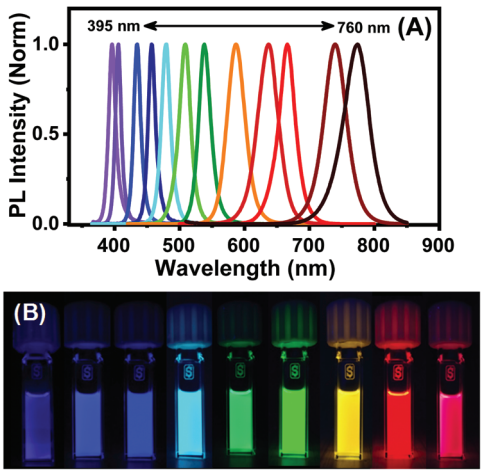

Fig. 6 (A) PL spectra of all $APbX_3$ (X = Cl, Br and I) and mixed-halide NCs prepared by our method (including data from our previous work[33] on $APbI_3$ NCs) showing the wide window of PL. (B) Digital photographs of the colloidal solutions of the $CsPbX_3$ NCs under UV illumination.

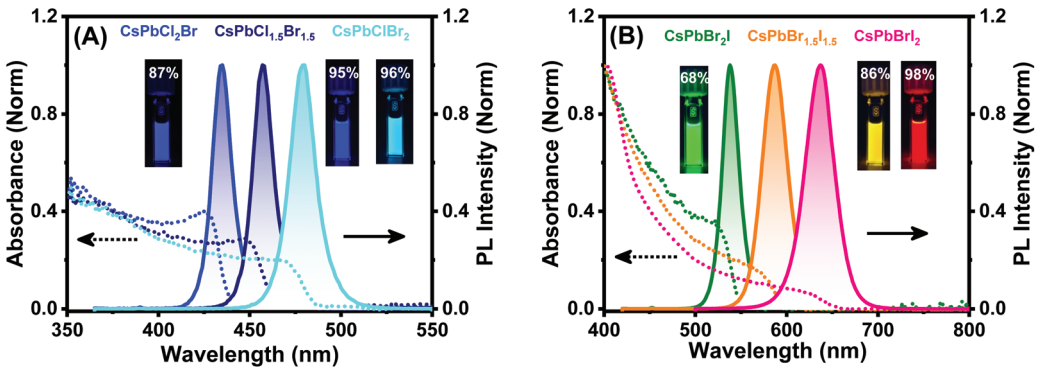

Fig. 5 UV-Vis absorption and PL spectra of (A) blue-emitting $CsPb(Cl/Br)_3$ and (B) yellow-orange-emitting $CsPb(Br/I)_3$ NCs obtained by using a mixture of different DXDMH. The insets show digital photographs of the respective NCs under 365 nm UV light with their PLQY values.

2.5. Post-synthetic cation and anion exchange reactions

The great effectiveness of DXDMH as a halide precursor even at room-temperature (RT) is evident from instantaneous post-synthetic halide exchange reactions on the as-synthesized NCs. For example, a green colloidal dispersion of pre-synthesized $CsPbBr_3$ NCs turns violet (or red) instantly on the addition of a small amount of hexane solution of DCDMH (or DIDMH) in OA and OAm due to rapid anion exchange reactions under ambient conditions (Fig. S20†). This allows tuning of the PL peak position of the NCs post-synthetically over a wide range (~410 to 660 nm) using appropriate DXDMH. The high reactivity of these halide precursors even at RT is quite impressive considering that commonly used metal halide solutions for halide-exchange are not very effective in non-polar media or they induce phase transformation of the system.[47] We have also examined post-synthetic A-site cation (Cs^+ here) exchange at RT by treating the $CsPbBr_3$ NCs with dilute FA–oleate solution in hexane. A gradual red-shift of the PL maximum from ~513 to ~530 nm in 15 min suggests partial replacement for Cs^+ with FA^+. The PLQY of the system is however not affected by this exchange (Fig. S21†).

2.6. Stability of the NCs

Lack of long-term stability of the perovskite NCs is a major issue and a variety of methods, which include a protective coating of the surface with an inert layer,[48–50] ligand engineering,[20,24,51] *in situ* modification,[52,53] doping,[40,42] *etc.* have been attempted for enhancing their stability. The NCs obtained by our method are found to be exceptionally stable under atmospheric conditions and in the presence of polar solvents like water. For example, the PLQY of the $CsPbBr_3$ NCs decreases only ~16% after 70 days under ambient conditions (Fig. 7A) with no change in the PL peak position (Fig. S22A†). Unchanged PXRD patterns and TEM images recorded after storing the sample for 60 days under ambient conditions suggest excellent phase stability of these NCs (Fig. 7B and C). The excellent photostability of these NCs is evident from only a 15% reduction of PLQY after ~38 h of continuous UV illumination (Fig. S22B†). The perovskite NCs readily degrade in a polar environment due to their ionic nature. However, the $CsPbBr_3$ NCs obtained by this method display significant resistance to water retaining ~75% PLQY in the presence of water even after a day of storage under ambient conditions (Fig. 7D). The hybrid $MAPbBr_3$ and $FAPbBr_3$ NCs too are highly stable under atmospheric conditions. The impressive air stability of these systems is evident from 80–82% PLQY and cubic morphology even after 80 days of storage under ambient conditions (Fig. S23–S25†). The hybrid systems are generally not very stable; they undergo rapid photo-degradation with a concomitant shift of the PL peak wavelength.[54] A PLQY of 82–87% of the hybrid systems after a long time under continuous illumination of UV light without any shift of PL peak and change of FWHM indicates much better photostability of these NCs (Fig. S23 and S24†). The stability of the violet-emitting $CsPbCl_3$ NCs is also quite impressive. A PLQY of 55% and 58% is still

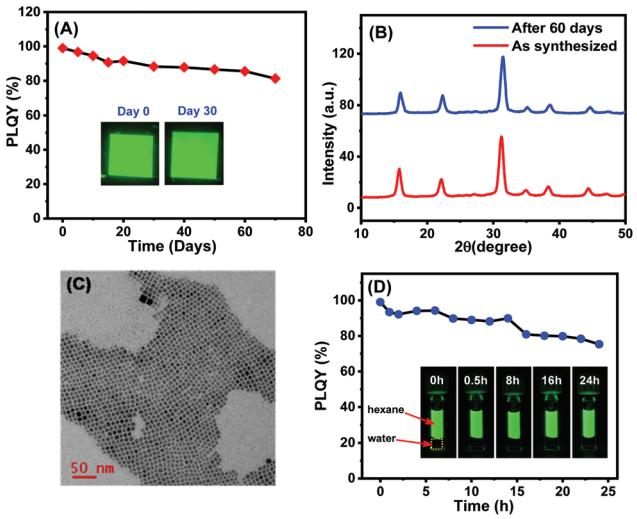

Fig. 7 (A) Stability of colloidal $CsPbBr_3$ NCs stored under ambient conditions. The inset shows digital images of films of the NCs under UV light stored under ambient conditions for one month. (B) PXRD patterns of the NCs after 60 days. (C) TEM images of the NCs after the same period of time. The scale bar is 50 nm. (D) Time-dependent change of PLQY of the $CsPbBr_3$ NCs in the presence of polar solvent (water). Digital images at different time intervals under UV light are shown in the inset.

maintained after ~45 days of storage under ambient conditions and 24 h under continuous illumination at 365 nm by a UV lamp, respectively (Fig. S26†). A major problem with the mixed-halide systems is halide migration, which causes continuous drifting of the PL peak.[55] However, our mixed-halide systems show distinctive stability with a PLQY of 85–90% without any change in the PL peak position and FWHM even after 25 days of storage under ambient conditions (Fig. S27†). However, the violet-emitting $MAPbCl_3$ and $FAPbCl_3$ NCs show poor stability under ambient conditions with a PLQY of only 1.6% and 0.2%, respectively after ~7 days of storage (Fig. S28†). The exceptional characteristics of the NCs obtained by the present method become clear when these are compared to different green- and violet-emitting samples obtained by other direct synthesis methods (Table S9†).

2.7. Effectivity of the halide precursor

A separate halide precursor is used in the three-precursor method of synthesis of the lead-halide perovskite NCs. Under the reaction condition, the halide precursor generates HX that reacts with oleylamine to form the oleylammonium halide (OAm^+X^-), which serves as the active source of halide in the reaction medium (Scheme S1†). Benzoyl halides are a good choice as halide precursors[32] as they readily produce HX upon nucleophilic attack by OA and OAm at the electron-deficient carbonyl carbon.[56] On the other hand, the *N*-haloimides (NXI_m, Scheme 2) like *N*-halosuccinimide or *N*-halophthalimide produce HX by protonation of one of the carbonyl oxygens followed by nucleophilic (oleate ion) attack at the halogen center.[22,57] A key point to note here is that in

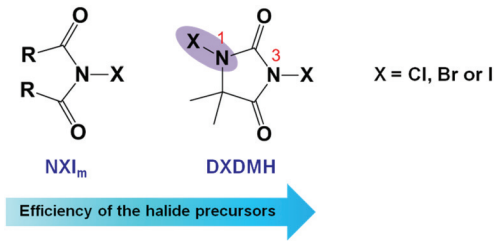

Scheme 2 Increased effectiveness of DXDMH over NXI$_m$ towards nucleophilic attack leading to the formation of HX. The N(1) halogen in DXDMH is marked for convenience.

NXI$_m$, X is electrophilic due to the presence of two electron withdrawing carbonyl groups linked to the nitrogen with which X is attached. Protonation of the carbonyl oxygen further enhances the electrophilicity of X making its release as HX easier upon nucleophilic attack by oleate.[57] This explains the effectiveness of NXI$_m$ as a halogenating agent for all green and selective violet-emitting NCs. However, the chloro/iodo-based hybrid systems are not formed or of poor quality (like $CsPbI_3$) using NXI$_m$. In the case of DXDMH, HX formation is much more facile because of the presence of an additional halogen at N(1), which acts as an inductive activator of the N(3) halogen (the actual source of halogen) and makes it much more electrophilic than that in NXI$_m$ (Scheme 2).[58,59] Facile formation of HX in the reaction medium generates *in situ* OAm^+X^-, which acts as a source of active halide and also, a surface passivating ligand for the $APbX_3$ NCs. Instantaneous post-synthetic halide exchange reactions at RT (Fig. S20†) show the ease of formation of HX (and OAm^+X^-) from DXDMH. Therefore, when the halogen atom of the halide precursor is electron deficient (like in DXDMH) or directly attached to an electron withdrawing group (EWG) (like C=O in benzoyl halides[32] or P=O in $PhPOCl_2$[24]), nucleophilic attack at the halogen center or electrophilic center of the EWG, leads to the facile generation of HX and subsequent formation of OAm^+X^- and high quality perovskite NCs. Table S10† summarizes the advantages and disadvantages of popular halide precursors used in the hot-injection method of synthesis.

2.8. Factors contributing to the optical properties and stability

The factors responsible for the exceptional characteristics of the present NCs are identified as follows using the $CsPbBr_3$ NCs as a model system. The energy dispersive X-ray (EDX) measurements, which show a Cs : Pb : Br ratio of 0.80 : 1.00 : 3.15 in these NCs (Fig. 8A), indicate a bromide-rich surface of these NCs as compared to the bromide deficient $CsPbBr_3$(II) NCs (Fig. 8A and S29†), which exhibit poor stability under ambient conditions (Fig. S30†). The X-ray photoelectron spectroscopy (XPS) measurements provide additional insight into the chemical environment of the elements. The XPS survey spectra confirm the presence of all constituent elements of $CsPbBr_3$ NCs (Fig. S31†). The Pb 4f XPS core-level spectrum shows characteristics Pb $4f_{5/2}$ and Pb $4f_{7/2}$ peaks at 143.17 and

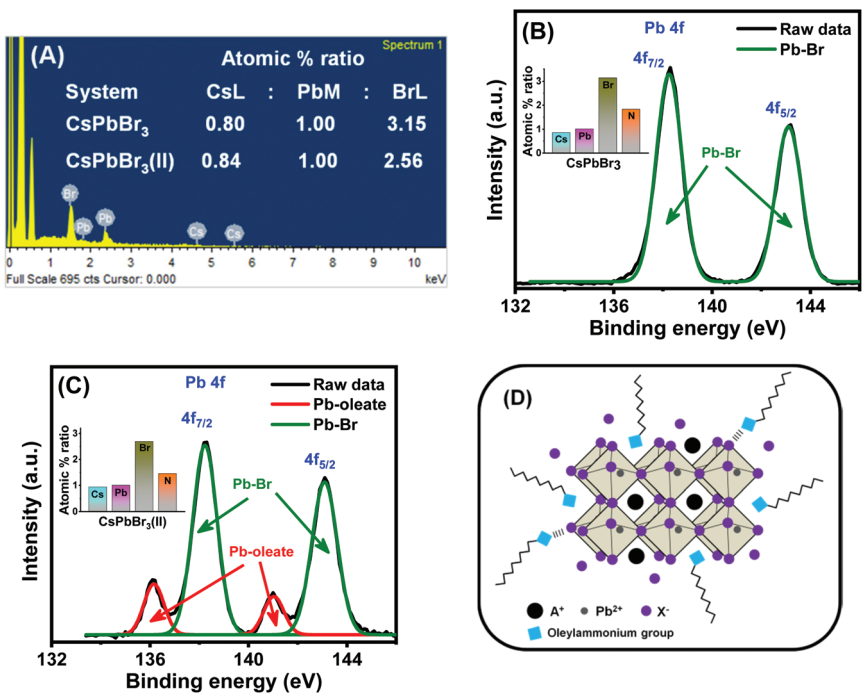

Fig. 8 (A) EDX spectra of $CsPbBr_3$ NCs. The calculated atomic % ratios of the $CsPbBr_3$ and $CsPbBr_3$(II) NCs obtained from the EDX measurements are provided in the inset. High-resolution Pb 4f XPS signal of the (B) $CsPbBr_3$ and (C) $CsPbBr_3$(II) NCs. The inset shows the atomic % ratio (with respect to lead) of the respective samples calculated based on the XPS results. (D) Schematic representation of a halide rich surface of the synthesized $APbX_3$ NCs, showing direct binding of oleylammonium on the surface.

138.27 eV, respectively (Fig. 8B),[52] but, for $CsPbBr_3$(II) NCs, each signal consists of two clearly resolvable peaks representing two different chemical environments of Pb (Fig. 8C); the signals with higher and lower binding energy are assigned to Pb–Br (138.23 and 143.09 eV) and Pb–oleate (136.14 and 141.02 eV), respectively.[60,61] The latter is a reflection of bromide vacancy related surface defect in $CsPbBr_3$(II) NCs, which is absent in $CsPbBr_3$ NCs. The atomic percentage ratio calculated from the XPS data (insets of Fig. 8B and C and Table S11†) matches that obtained from EDX measurements (Fig. 8A) and further confirm bromide rich surface of the $CsPbBr_3$ NCs.[52] The core-level Br 3d XPS spectrum (Fig. S32†) shows Br $3d_{3/2}$ and Br $3d_{5/2}$ signals, representing the bromide ions at the surface and core, respectively.[62] The much intense and blue-shifted (~0.12 eV) Br $3d_{3/2}$ peak of the $CsPbBr_3$ NCs compared to $CsPbBr_3$(II) NCs corroborates the bromide rich surface of the $CsPbBr_3$ NCs (Fig. S32A†).[52,62] Similarly, a chloride rich surface of the $CsPbCl_3$ NCs compared to the $CsPbCl_3$(II) NCs is also observed (Fig. S33†).

A point to note in this context is that the atomic % of chloride in $CsPbCl_3$ NCs is very similar to the Pb : Cl precursor molar ratio between 1 : 3 and 1 : 7 (Table S12†). However, for ratios >1 : 7, the formation of $PbCl_2$ as a byproduct (Fig. S34†) decreases the effective amount of chloride in the reaction medium and the $CsPbCl_3$ NCs formed under this condition contain a lower atomic % of chloride and are weakly luminescent (Fig. S11A†).

The surface ligand environment, which influences the optical properties and stability of the perovskite NCs,[63,64] is determined by ^{1}H NMR and FTIR studies. The ^{1}H NMR spectrum of purified $CsPbBr_3$ NCs (Fig. S35†) shows two broad signature peaks of the α-protons ($-NH_3^+$) and β-protons ($-CH_2-NH_3^+$) of OAm^+ at ~7 and ~3.6 ppm,[64] respectively, indicating the presence of OAm^+ at the surface of the NCs and the broadness of these two peaks (denoted as a and b) suggests firm anchoring of OAm^+ on the surface.[33,64] In this context, it may be noted that the NMR signal for the three α-protons of OAm^+ in the present case appears as a broad singlet,[63,64] not as a multiplet.[27] In contrast, the sharp nature of the characteristic peak of the oleate ion at ~2.4 ppm (labeled as c) indicates that the oleate ion is not bound to the surface, but present in solution,[33,64] suggesting a bromide rich surface and the absence of uncoordinated surface Pb^{2+} of the NCs. This finding is consistent with the XPS data presented earlier, where no signature of Pb–oleate was observed for $CsPbBr_3$ NCs (Fig. 8B). The asymmetric and symmetric bending absorption of the N^+–H bond at ~1641 and 1548 cm^{-1} in the FTIR spectrum further establishes the anchoring of OAm^+ on the surface (Fig. S36†).[27] A halide-rich surface attracts a greater number of OAm^+ and provides them access to some of the surface exposed A-sites and allows replacement for some Cs^+ ions.[26] A higher N/Pb ratio and low Cs^+ content in $CsPbBr_3$ NCs (Fig. 8B inset and Table S11†) support this picture. It is thus evident that strongly bound OAm^+ provides a robust ligand environment at the surface that contributes to the exceptional stability of the NCs.[27,33] Moreover, the hydrophobic environment of OAm^+ protects the NCs from moisture and polar solvents preventing or slowing down the decomposition of the optically active inorganic framework.[33] Although OA is not bound to the surface, it maintains an optimum concentration of oleate and OAm^+ ligands and provides colloidal stability.[64] Therefore, OAm^+X^- produced *in situ* creates a halide-rich surface of the NCs that eventually turns into an oleylammonium-lead halide terminated surface by replacing some of the surface Cs^+ that endows exceptional characteristics to the NCs (Fig. 8D).

3. Conclusions

It is shown that high quality all-inorganic and hybrid lead halide perovskite $APbX_3$ NCs (where A = Cs^+, MA^+ or FA^+ and X = Cl^-, Br^- or I^-) emitting in the 395–760 nm region can be obtained via direct synthesis by a generic method using DXDMH as halide precursors. The high phase purity, narrow size distribution, high PLQY and excellent stability (except for $MAPbCl_3$ and $FAPbCl_3$ NCs) of such a large collection of NCs obtained by a common method are attributed to the efficacy of this class of halide precursors facilitating the formation of oleylammonium-lead halide terminated surface, which passivates the defect states and provides necessary protection to the NCs. The present work not only provides a generic methodology for the direct synthesis of good quality $APbX_3$ NCs, but also provides useful insight for the design and development of even better $APbX_3$ NCs.

Conflicts of interest

The authors declare no conflict of interest.

Acknowledgements

This work is supported by the J. C. Bose National Fellowship (to A. S.) of the Science and Engineering Research Board (SERB) and the Institute of Eminence Grants (to the University of Hyderabad) of the Ministry of Human Resource and Development (MHRD). The National Chemical Laboratory (NCL), Pune is thanked for the XPS measurements. S. D. thanks the University Grant Commission (UGC) for a Fellowship.

Notes and references

1 L. Protesescu, S. Yakunin, M. I. Bodnarchuk, F. Krieg, R. Caputo, C. H. Hendon, R. X. Yang, A. Walsh and M. V. Kovalenko, *Nano Lett.*, 2015, **15**, 3692–3696.
2 F. Zhang, H. Zhong, C. Chen, X.-G. Wu, X. Hu, H. Huang, J. Han, B. Zou and Y. Dong, *ACS Nano*, 2015, **9**, 4533–4542.
3 Q. A. Akkerman, V. D'Innocenzo, S. Accornero, A. Scarpellini, A. Petrozza, M. Prato and L. Manna, *J. Am. Chem. Soc.*, 2015, **137**, 10276–10281.

4 G. Nedelcu, L. Protesescu, S. Yakunin, M. I. Bodnarchuk, M. J. Grotevent and M. V. Kovalenko, *Nano Lett.*, 2015, **15**, 5635–5640.
5 V. G. V. Dutt, S. Akhil and N. Mishra, *CrystEngComm*, 2020, **22**, 5022–5030.
6 A. Dutta, R. K. Behera, P. Pal, P. D. S. Baitalik and D. N. Pradhan, *Angew. Chem., Int. Ed.*, 2019, **58**, 5552–5556.
7 G. H. Ahmed, J. Yin, O. M. Bakr and O. F. Mohammed, *J. Chem. Phys.*, 2020, **152**, 020902.
8 J. Shamsi, A. S. Urban, M. Imran, L. D. Trizio and L. Manna, *Chem. Rev.*, 2019, **119**, 3296–3348.
9 J. Song, J. Li, X. Li, L. Xu, Y. Dong and H. Zeng, *Adv. Mater.*, 2015, **27**, 7162–7167.
10 S. Yakunin, L. Protesescu, F. Krieg, M. I. Bodnarchuk, G. Nedelcu, M. Humer, G. D. Luca, M. Fiebig, W. Heiss and M. V. Kovalenko, *Nat. Commun.*, 2015, **6**, 8056.
11 J. Pan, S. P. Sarmah, B. Murali, I. Dursun, W. Peng, M. R. Parida, J. Liu, L. Sinatra, N. Alyami, C. Zhao, E. Alarousu, T. K. Ng, B. S. Ooi, O. M. Bakr and O. F. Mohammed, *J. Phys. Chem. Lett.*, 2015, **6**, 5027–5033.
12 A. Dey, J. Ye, A. De, E. Debroye, S. K. Ha, E. Bladt, A. S. Kshirsagar, Z. Wang, J. Yin and Y. Wang, *ACS Nano*, 2021, **15**, 10775–10981.
13 Y. Wei, Z. Cheng and J. Lin, *Chem. Soc. Rev.*, 2019, **48**, 310–350.
14 H. Huang, L. Polavarapu, J. A. Sichert, A. S. Susha, A. S. Urban and A. L. Rogach, *NPG Asia Mater.*, 2016, **8**, e328–e328.
15 J. Ye, M. M. Byranvand, C. O. Martínez, R. L. Z. Hoye, D. M. Saliba and D. L. Polavarapu, *Angew. Chem., Int. Ed.*, 2021, **60**, 21636–21660.
16 N. Pradhan, *ACS Energy Lett.*, 2019, **4**, 1634–1638.
17 L. Protesescu, S. Yakunin, M. I. Bodnarchuk, F. Bertolotti, N. Masciocchi, A. Guagliardi and M. V. Kovalenko, *J. Am. Chem. Soc.*, 2016, **138**, 14202–14205.
18 P. Liu, W. Chen, W. Wang, B. Xu, D. Wu, J. Hao, W. Cao, F. Fang, Y. Li, Y. Zeng, R. Pan, S. Chen, W. Cao, X. W. Sun and K. Wang, *Chem. Mater.*, 2017, **29**, 5168–5173.
19 E. Yassitepe, Z. Yang, O. Voznyy, Y. Kim, G. Walters, J. A. Castañeda, P. Kanjanaboos, M. Yuan, X. Gong, F. Fan, J. Pan, S. Hoogland, R. Comin, O. M. Bakr, L. A. Padilha, A. F. Nogueira and E. H. Sargent, *Adv. Funct. Mater.*, 2016, **26**, 8757–8763.
20 F. Krieg, S. T. Ochsenbein, S. Yakunin, S. T. Brinck, P. Aellen, A. Süess, B. Clerc, D. Guggisberg, O. Nazarenko, Y. Shynkarenko, S. Kumar, C.-J. Shih, I. Infante and M. V. Kovalenko, *ACS Energy Lett.*, 2018, **3**, 641–646.
21 M. Imran, P. Ijaz, D. Baranov, L. Goldoni, U. Petralanda, Q. Akkerman, A. L. Abdelhady, M. Prato, P. Bianchini, I. Infante and L. Manna, *Nano Lett.*, 2018, **18**, 7822–7831.
22 S. Paul and A. Samanta, *ACS Energy Lett.*, 2020, **5**, 64–69.
23 S. Akhil, V. G. V. Dutt and N. Mishra, *Nanoscale*, 2021, **13**, 13142–13151.
24 C. Zhang, Q. Wan, L. K. Ono, Y. Liu, W. Zheng, Q. Zhang, M. Liu, L. Kong, L. Li and Y. Qi, *ACS Energy Lett.*, 2021, **6**, 3545–3554.
25 S. Paul, T. Ahmed, S. Das and A. Samanta, *J. Phys. Chem. C*, 2021, **125**, 23539–23547.
26 Y. Cai, H. Wang, Y. Li, L. Wang, Y. Lv, X. Yang and R.-J. Xie, *Chem. Mater.*, 2019, **31**, 881–889.
27 A. Dutta, S. K. Dutta, S. D. Adhikari and D. N. Pradhan, *Angew. Chem., Int. Ed.*, 2018, **57**, 9083–9087.
28 L. Protesescu, S. Yakunin, S. Kumar, J. Bär, F. Bertolotti, N. Masciocchi, A. Guagliardi, M. Grotevent, I. Shorubalko, M. I. Bodnarchuk, C.-J. Shih and M. V. Kovalenko, *ACS Nano*, 2017, **11**, 3119–3134.
29 Q. A. Akkerman, L. Martínez-Sarti, L. Goldoni, M. Imran, D. Baranov, H. J. Bolink, F. Palazon and L. Manna, *Chem. Mater.*, 2018, **30**, 6915–6921.
30 S. K. Mahankudo, A. Das, K. Mishra, M. Barai, P. Mal and S. Ghosh, *ACS Appl. Nano Mater.*, 2022, **5**, 4360–4366.
31 I. Levchuk, A. Osvet, X. Tang, M. Brandl, J. D. Perea, F. Hoegl, G. J. Matt, R. Hock, M. Batentschuk and C. J. Brabec, *Nano Lett.*, 2017, **17**, 2765–2770.
32 M. Imran, V. Caligiuri, M. Wang, L. Goldoni, M. Prato, R. Krahne, L. D. Trizio and L. Manna, *J. Am. Chem. Soc.*, 2018, **140**, 2656–2664.
33 S. Das and A. Samanta, *ACS Energy Lett.*, 2021, **6**, 3780–3787.
34 G. Maculan, A. D. Sheikh, A. L. Abdelhady, M. I. Saidaminov, M. A. Haque, B. Murali, E. Alarousu, O. F. Mohammed, T. Wu and O. M. Bakr, *J. Phys. Chem. Lett.*, 2015, **6**, 3781–3786.
35 A. A. Zhumekenov, M. I. Saidaminov, M. A. Haque, E. Alarousu, S. P. Sarmah, B. Murali, I. Dursun, X.-H. Miao, A. L. Abdelhady, T. Wu, O. F. Mohammed and O. M. Bakr, *ACS Energy Lett.*, 2016, **1**, 32–37.
36 V. G. V. Dutt, S. Akhil and N. Mishra, *Nanoscale*, 2021, **13**, 14442–14449.
37 A. De, S. Das, N. Mondal and A. Samanta, *ACS Mater. Lett.*, 2019, **1**, 116–122.
38 N. Mondal and A. Samanta, *Nanoscale*, 2017, **9**, 1878–1885.
39 R. K. Gautam, S. Das and A. Samanta, *J. Phys. Chem. C*, 2021, **125**, 24170–24179.
40 S. Das, A. De and A. Samanta, *J. Phys. Chem. Lett.*, 2020, **11**, 1178–1188.
41 A. De, S. Das and A. Samanta, *ACS Energy Lett.*, 2020, **5**, 2246–2252.
42 N. Mondal, A. De and A. Samanta, *ACS Energy Lett.*, 2019, **4**, 32–39.
43 D. P. Nenon, K. Pressler, J. Kang, B. A. Koscher, J. H. Olshansky, W. T. Osowiecki, M. A. Koc, L.-W. Wang and A. P. Alivisatos, *J. Am. Chem. Soc.*, 2018, **140**, 17760–17772.
44 X. Zheng, S. Yuan, J. Liu, J. Yin, F. Yuan, W.-S. Shen, K. Yao, M. Wei, C. Zhou, K. Song, B.-B. Zhang, Y. Lin, M. N. Hedhili, N. Wehbe, Y. Han, H.-T. Sun, Z.-H. Lu, T. D. Anthopoulos, O. F. Mohammed, E. H. Sargent, L.-S. Liao and O. M. Bakr, *ACS Energy Lett.*, 2020, **5**, 793–798.
45 R. K. Gautam, S. Das and A. Samanta, *ChemNanoMat*, 2022, **8**, e20220002.

46 Y. Shynkarenko, M. I. Bodnarchuk, C. Bernasconi, Y. Berezovska, V. Verteletskyi, S. T. Ochsenbein and M. V. Kovalenko, *ACS Energy Lett.*, 2019, **4**, 2703–2711.
47 S. E. Creutz, E. N. Crites, M. C. D. Siena and D. R. Gamelin, *Chem. Mater.*, 2018, **30**, 4887–4891.
48 H. Huang, B. Chen, Z. Wang, T. F. Hung, A. S. Susha, H. Zhong and A. L. Rogach, *Chem. Sci.*, 2016, **7**, 5699–5703.
49 S. Wang, C. Bi, J. Yuan, L. Zhang and J. Tian, *ACS Energy Lett.*, 2018, **3**, 245–251.
50 V. K. Ravi, S. Saikia, S. Yadav, V. V. Nawale and A. Nag, *ACS Energy Lett.*, 2020, **5**, 1794–1796.
51 Q. Zhong, M. Cao, Y. Xu, P. Li, Y. Zhang, H. Hu, D. Yang, Y. Xu, L. Wang, Y. Li, X. Zhang and Q. Zhang, *Nano Lett.*, 2019, **19**, 4151–4157.
52 J. Y. Woo, Y. Kim, J. Bae, T. G. Kim, J. W. Kim, D. C. Lee and S. Jeong, *Chem. Mater.*, 2017, **29**, 7088–7092.
53 Y. Wu, C. Wei, X. Li, Y. Li, S. Qiu, W. Shen, B. Cai, Z. Sun, D. Yang, Z. Deng and H. Zeng, *ACS Energy Lett.*, 2018, **3**, 2030–2037.
54 L. Liu, L. Deng, S. Huang, P. Zhang, J. Linnros, H. Zhong and I. Sychugov, *J. Phys. Chem. Lett.*, 2019, **10**, 864–869.
55 P. V. Kamat and M. Kuno, *Acc. Chem. Res.*, 2021, **54**, 520–531.
56 *Preparation of acyl halides*, ed. M. F. Ansell, John Wiley & Sons Ltd. UK, London, 1972.
57 H. Xue, H. Tan, D. Wei, Y. Wei, S. Lin, F. Liang and B. Zhao, *RSC Adv.*, 2013, **3**, 5382–5385.
58 D. C. Whitehead, R. Yousefi, A. Jaganathan and B. Borhan, *J. Am. Chem. Soc.*, 2010, **132**, 3298–3300.
59 R. Yousefi, D. C. Whitehead, J. M. Mueller, R. J. Staples and B. Borhan, *Org. Lett.*, 2011, **13**, 608–611.
60 M. Li, X. Zhang, K. Matras-Postolek, H.-S. Chen and P. Yang, *J. Mater. Chem. C*, 2018, **6**, 5506–5513.
61 W. E. Morgan and J. R. V. Wazer, *J. Phys. Chem.*, 1973, **77**, 964–969.
62 T. Cai, F. Li, Y. Jiang, X. Liu, X. Xia, X. Wang, J. Peng, L. Wang and W. A. Daoud, *Nanoscale*, 2019, **11**, 1319–1325.
63 J. D. Roo, M. Ibáñez, P. Geiregat, G. Nedelcu, W. Walravens, J. Maes, J. C. Martins, I. V. Driessche, M. V. Kovalenko and Z. Hens, *ACS Nano*, 2016, **10**, 2071–2081.
64 V. K. Ravi, P. K. Santra, N. Joshi, J. Chugh, S. K. Singh, H. Rensmo, P. Ghosh and A. Nag, *J. Phys. Chem. Lett.*, 2017, **8**, 4988–4994.

Photoluminescence and charge carrier dynamics of perovskite nanocrystals

by Somnath Das

Submission date: 30-Nov-2022 02:10PM (UTC+0530)
Submission ID: 1967104497
File name: Thesis_for_Plagarism.pdf (4.67M)
Word count: 31910
Character count: 164543

Photoluminescence and charge carrier dynamics of perovskite nanocrystals

ORIGINALITY REPORT

42%	18%	40%	5%
SIMILARITY INDEX	INTERNET SOURCES	PUBLICATIONS	STUDENT PAPERS

PRIMARY SOURCES

1	pubs.acs.org Internet Source	12%
2	Somnath Das, Anunay Samanta. " On direct synthesis of high quality APbX (A = Cs , MA and FA ; X = Cl , Br and I) nanocrystals following a generic approach ", Nanoscale, 2022 Publication	10%
3	Somnath Das, Anunay Samanta. "Highly Luminescent and Phase-Stable Red/NIR-Emitting All-Inorganic and Hybrid Perovskite Nanocrystals", ACS Energy Letters, 2021 Publication	9%
4	Submitted to University of Hyderabad, Hyderabad Student Paper	2%
5	Somnath Das, Anunay Samanta. "On Direct Synthesis of High Quality APbX3 (A= Cs+, MA+ and FA+; X= Cl-, Br- and I-) Nanocrystals.	2%

own publication

own publication

own publication

Wall" of Colloidal Perovskites: Highly Luminescent Formamidinium and Formamidinium–Cesium Lead Iodide Nanocrystals", ACS Nano, 2017
Publication

16 Submitted to Indian Institute of Technology, Ropar
Student Paper
<1 %

17 Margherita Maiuri, Marco Garavelli, Giulio Cerullo. "Ultrafast Spectroscopy: State of the Art and Open Challenges", Journal of the American Chemical Society, 2019
Publication
<1 %

18 Tasnim Ahmed, Apurba De, Sumanta Paul, Anunay Samanta. " Individual Particle-Level Picture of Charge Carrier Recombination in Bi-Doped CsPbBr Nanocrystals ", The Journal of Physical Chemistry C, 2021
Publication
<1 %

19 Somnath Das, Apurba De, Anunay Samanta. " Ambient Condition Mg Doping Producing Highly Luminescent Green- and Violet-Emitting Perovskite Nanocrystals with Reduced Toxicity and Enhanced Stability ", The Journal of Physical Chemistry Letters, 2020
Publication
<1 %

Our publication.

47	ir.canterbury.ac.nz Internet Source	<1%

Exclude quotes	On	Exclude matches	< 14 words
Exclude bibliography	On		